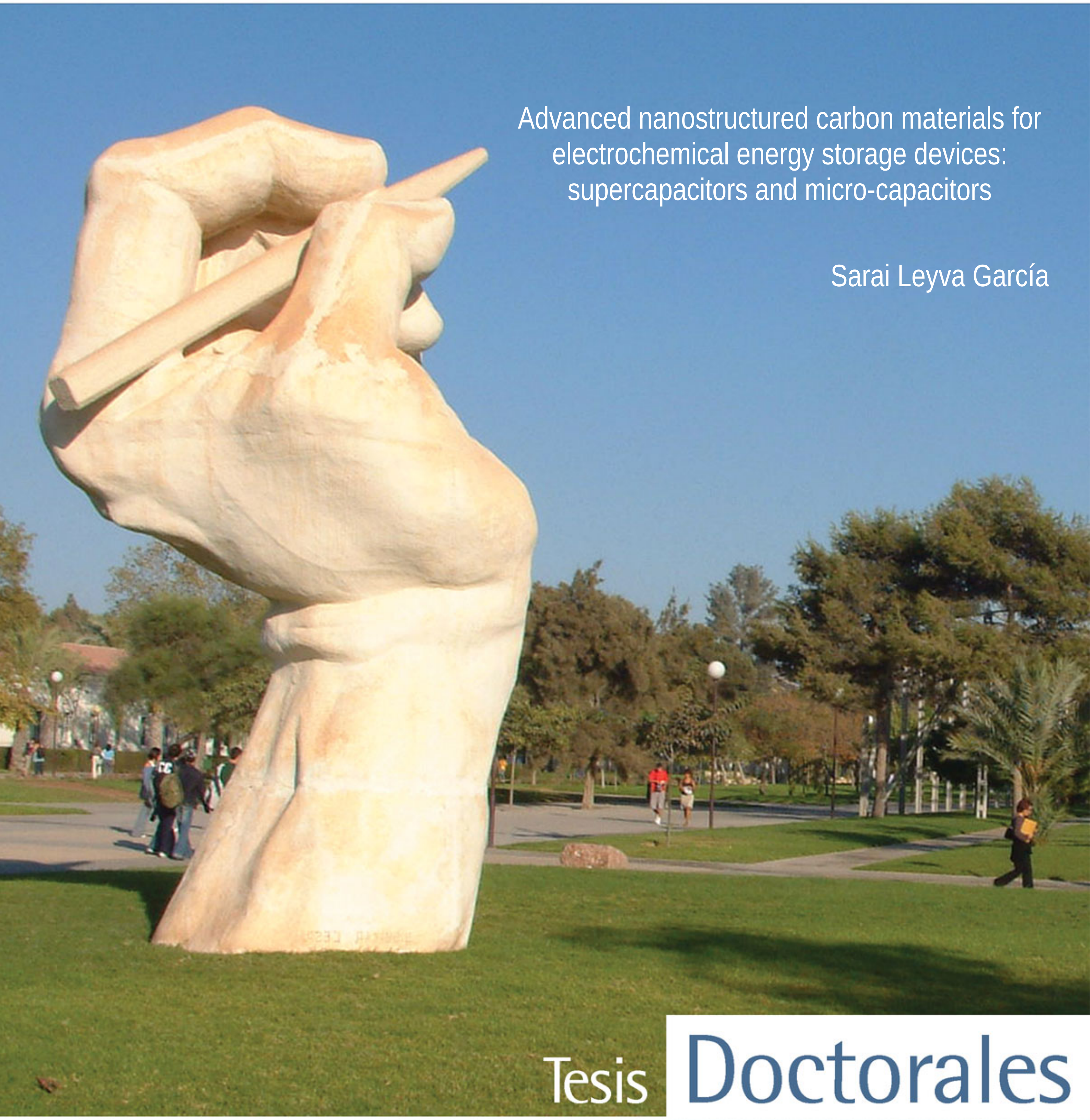

# Advanced nanostructured carbon materials for electrochemical energy storage devices: supercapacitors and micro-capacitors

Sarai Leyva García

Universitat d'Alacant
Universidad de Alicante

*Grupo de Materiales Carbonosos y Medio Ambiente*
*Departamento de Química Inorgánica (Facultad de Ciencias) e*
*Instituto Universitario de Materiales de Alicante*

# ADVANCED NANOSTRUCTURED CARBON MATERIALS FOR ELECTROCHEMICAL ENERGY STORAGE DEVICES: SUPERCAPACITORS AND MICRO-CAPACITORS

**SARAI LEYVA GARCÍA**

*Doctorado en Ciencia de Materiales*

Tesis presentada para aspirar al
grado de DOCTORA POR LA UNIVERSIDAD DE ALICANTE
MENCIÓN DE DOCTORA INTERNACIONAL

Dirigida por:

| | |
|---|---|
| Diego Cazorla Amorós | Dolores Lozano Castelló |
| Catedrático de Química Inorgánica | Profesora Titular de Química Inorgánica |

Alicante, noviembre 2016

DIEGO CAZORLA AMORÓS, Catedrático de Química Inorgánica y DOLORES LOZANO CASTELLÓ, Profesora Titular de Química Inorgánica, ambos de la Universidad de Alicante.

CERTIFICAN QUE:

Dña. **Sarai Leyva García,** Licenciada en Química, ha realizado en el Grupo de Materiales Carbonosos y Medio Ambiente, del Departamento de Química Inorgánica (Facultad de Ciencias) e Instituto Universitario de Materiales de Alicante, bajo nuestra dirección, el trabajo que lleva por título: **Advanced nanostructured carbon materials for electrochemical energy storage devices: supercapacitors and micro-capacitors**, que constituye su memoria para aspirar al grado de doctora, reuniendo, a nuestro juicio, las condiciones necesarias para ser presentada y defendida ante el tribunal correspondiente.

Y para que conste a los efectos oportunos, en cumplimiento de la legislación vigente, firmamos el presente certificado en Alicante a 21 de octubre de 2016.

Diego Cazorla Amorós
Catedrático de Química Inorgánica

Dolores Lozano Castelló
Profesora Titular de Química Inorgánica

## *Agradecimientos*

En primer lugar, quisiera agradecer a mis directores de Tesis, el Profesor Diego Cazorla Amorós y la Profesora Dolores Lozano Castelló la oportunidad otorgada para realizar la presente Tesis Doctoral bajo su supervisión, así como por la dedicación y paciencia mostrada durante el desarrollo de este trabajo. Merece especial mención, asimismo, la Profesora Emilia Morallón Núñez, por sus aportaciones al trabajo presentado.

Quisiera agradecer al Ministerio Español de Educación, Cultura y Deporte (MECD) la beca de Formación de Profesorado Universitario (FPU) recibida (referencia: AP-2012-5071), así como al Servicio Alemán de Intercambio Académico (DAAD) por otorgarme una beca de investigación de corta duración (referencia: 91590114).

I would also like to thank Professor Andrea Balducci and Professor Stefano Passerini for their kind attention during my short-term research in Germany.

A mis compañeros y amigos, por el apoyo y los ánimos recibidos durante estos años.

Y, finalmente, agradecer a mi madre que me haya acompañado siempre en el camino.

*A MI MADRE*

# GENERAL INDEX

CAPÍTULO I Objetivos y estructura general de la Tesis Doctoral

CAPÍTULO II Introducción general

CAPÍTULO III Experimental

CHAPTER IV New insights on electrochemical hydrogen storage in nanoporous carbons by *in situ* Raman spectroscopy

CHAPTER V Characterization of a zeolite-templated carbon by electrochemical quartz crystal microbalance and *in situ* Raman spectroscopy

CHAPTER VI Silica-templated ordered mesoporous carbon thin films as electrodes for micro-capacitors

CHAPTER VII Electrochemical performance of a superporous activated carbon in ionic liquid-based electrolytes

CHAPTER VIII General conclusions

CAPÍTULO VIII Conclusiones generales

SUMMARY

RESUMEN

# SUMMARY OF CONTENTS

GENERAL INDEX

TABLE INDEX

FIGURE INDEX

## CAPÍTULO I. Objetivos y estructura general de la Tesis Doctoral

I.1. Introducción........................................3

I.2. Objetivos de la Tesis Doctoral........................................3

I.3. Estructura de la Tesis Doctoral........................................5

## CAPÍTULO II. Introducción general

II.1. Introducción........................................13

II.2. Formas de almacenamiento de energía eléctrica........................................14

- II.2.1. Procesos farádicos y electrostáticos........................................14
- II.2.2. Baterías y pilas de combustible........................................15
- II.2.3. Condensadores........................................17

II.3. Condensadores electroquímicos basados en materiales carbonosos de elevada área superficial........................................19

- II.3.1. Modelos de la doble capa eléctrica........................................21
- II.3.2. Características de los condensadores electroquímicos........................................25
  - II.3.2.1. Energía almacenada........................................25

II.3.2.2. Resistencia equivalente en serie .................................... 27

II.3.2.3. Voltaje .................................................................... 28

II.3.2.4. Capacidad ................................................................ 29

II.3.2.5. Tipos de configuraciones de condensador electroquímico ................................................................................ 29

II.3.2.6. Tipos de electrolitos ...................................................... 31

II.3.3. Micro-condensadores .......................................................... 34

II.4. Materiales carbonosos con porosidad diseñada .......................... 37

II.4.1. Almacenamiento de energía en materiales carbonosos ........ 37

II.4.2. Contribución a la capacidad de la doble capa eléctrica: influencia de la textura porosa ...................................................... 40

II.4.2.1. Carbones activados ...................................................... 43

II.4.2.2. Materiales carbonosos nanomoldeados .......................... 46

II.4.3. Contribución de la química superficial ................................. 52

II.4.3.1. Grupos funcionales oxigenados ..................................... 53

II.4.3.2. Grupos funcionales nitrogenados .................................. 55

Referencias ............................................................................ 57

**CAPÍTULO III. Experimental**

III.1. Introducción ............................................................ 73

III.2. Materiales ................................................................. 73

III.2.1. Materiales comerciales ......................................... 73

III.2.2. Materiales sintetizados ......................................... 74

III.3. Técnicas de caracterización........................................................76

III.3.1. Adsorción física de gases....................................................76

III.3.1.1. Teoría de Brunauer–Emmett–Teller................................79

III.3.1.2. Ecuación de Dubinin–Radushkevich...............................81

III.3.1.3. Teoría del funcional de densidad no localizada...............82

III.3.2. Desorción a temperatura programada...................................83

III.3.3. Técnicas de caracterización electroquímica...........................85

III.3.3.1. Voltamperometría cíclica ...............................................85

III.3.3.2. Cronopotenciometría ....................................................89

III.3.3.3. Cronoamperometría......................................................92

III.3.3.3. Microbalanza electroquímica de cristal de cuarzo...........93

III.3.4. Espectroscopía Raman *in situ*.............................................96

III.3.5. Microscopía electrónica de barrido y espectroscopía de fluorescencia de rayos-X mediante análisis por dispersión de energía ......................................................................................100

III.3.6. Microscopía electrónica de transmisión.............................102

Referencias ..........................................................................104

## CHAPTER IV. New insights on electrochemical hydrogen storage in nanoporous carbons by *in situ* Raman spectroscopy

IV.1. Introduction ......................................................................111

IV.2. Experimental ......................................................................112

IV.2.1. Synthesis of the activated carbon .......................................113

IV.2.2. Porous texture characterization........................................ 113

IV.2.3. Surface chemistry characterization .................................... 114

IV.2.3. Electrochemical characterization...................................... 114

IV.2.4. *In situ* Raman characterization......................................... 116

IV.3. Results and discussion........................................................... 117

IV.3.1. Porous texture and surface chemistry characterization results ............................................................................................ 117

IV.3.2. Electrochemical characterization results ............................ 118

IV.3.3. *In situ* Raman characterization results ............................... 125

IV.4. Conclusions............................................................................ 130

References ..................................................................................... 132

**CHAPTER V. Characterization of a zeolite-templated carbon by electrochemical quartz crystal microbalance and *in situ* Raman spectroscopy**

V.1.Introduction ............................................................................ 139

V.2. Experimental .......................................................................... 141

V.2.1. Synthesis of the zeolite-templated carbon........................... 141

V.2.2. Porous texture characterization........................................... 142

V.2.3. Electrochemical and gravimetric characterization................ 142

V.2.4. Surface chemistry characterization .................................... 145

V.2.5. *In situ* Raman characterization........................................... 146

V.3. Results and discussion............................................................ 147

V.3.1. Porous texture and surface chemistry characterization results of powder ZTC ....................................................................147

V.3.2. Electrochemical and gravimetric characterization results .....148

V.3.3. *In situ* Raman characterization results ................................159

V.4. Conclusions..........................................................................166

References ..............................................................................168

## CHAPTER VI. Silica-templated ordered mesoporous carbon thin films as electrodes for micro-capacitors

VI.1. Introduction .......................................................................177

VI.2. Experimental ......................................................................179

VI.2.1. Synthesis of ordered mesoporous silica thin films ..............179

VI.2.2. Synthesis of mesoporous carbon thin films .........................180

VI.2.3. SEM, TEM and Raman characterization ............................181

VI.2.4. Electrochemical characterization.......................................182

VI.3. Results and discussion.........................................................183

VI.3.1. SEM, TEM and Raman characterization results..................183

VI.3.2. Three-electrode cell electrochemical characterization results ..........................................................................................188

VI.3.3. Two-electrode cell electrochemical characterization results 199

VI.4. Conclusions.........................................................................205

References ..............................................................................207

## CHAPTER VII. Electrochemical performance of a superporous activated carbon in ionic liquid-based electrolytes

VII.1. Introduction........................................................................ 217

VII.2. Experimental ........................................................................ 220

VII.2.1. Synthesis of the activated carbon...................................... 220

VII.2.2. Porous texture characterization........................................ 220

VII.2.3. Surface chemistry characterization .................................. 220

VII.2.4. Electrolytes preparation .................................................... 221

VII.2.5. Electrochemical characterization....................................... 221

VII.3. Results and discussion......................................................... 224

VII.3.1. Porous texture and surface chemistry characterization ..... 224

VII.3.2. Electrochemical characterization in three-electrode configuration ......................................................................... 226

VII.3.3. EDLC characterization ...................................................... 235

VII.4. Conclusions.......................................................................... 238

References........................................................................................ 239

**CHAPTER VIII. General conclusions** ............................................ 245

**CAPÍTULO VIII. Conclusiones generales** ..................................... 251

**SUMMARY** ........................................................................... 259

**RESUMEN**........................................................................... 265

# TABLE INDEX

- Tabla III.1. Textura porosa y química superficial del carbón activado MWV-E510A.
- Tabla III.2. Textura porosa y química superficial del carbón activado DLC Super 30.
- Table IV.1. Porous texture and surface chemistry characterization results.
- Table IV.2. Specific capacitance values obtained from the cyclic voltammograms at 1 mV $s^{-1}$.
- Table IV.3. Hydrogen storage capacity estimated from the GCD experiments. Charge -500 mA $g_{electrode}^{-1}$ during 1 hour, discharge +50 mA $g_{electrode}^{-1}$ until initial open circuit potential.
- Table V.1. Porous texture and surface chemistry characterization results of powdered ZTC.
- Table VII.1. Porous texture and surface chemistry characterization results of ANK3.
- Table VII.2. Capacitance values calculated for the ions of the three electrolytes (1M $Et_4N$ $BF_4$/PC, 1M $PYR_{14}$ $BF_4$/PC and 1M $PYR_{14}$ TFSI/PC) in three-electrode configuration.
- Table VII.3. Viscosity and conductivity of the electrolytes at 20 ºC [1].
- Table VII.4. Capacitance values calculated for the ions of $PYR_{14}$ TFSI in three-electrode configuration.

# FIGURE INDEX

- Figura II.1. Esquema de un condensador electroquímico o supercondensador basado en electrodos de carbón activado.
- Figura II.2. Diagrama de Ragone. Adaptado de [9].
- Figura II.3. Modelo de Helmholtz (a) y variación del potencial eléctrico con la distancia al electrodo (b).
- Figura II.4. Modelo de Gouy-Chapman (a) y variación del potencial eléctrico con la distancia al electrodo (b).
- Figura II.5. Modelo de Stern (a) y variación del potencial eléctrico con la distancia al electrodo (b).
- Figura II.6. Modelo de Grahame.
- Figura II.7. Esquema de la tortuosidad de los iones al entrar en la porosidad de una fibra de carbón activada y un carbón activado.
- Figura II.8. Esquema general de los procesos de activación física y activación química. Adaptado de [74].
- Figura II.9.Esquema de la estructura de un ZTC [73].
- Figura II.10.Sitios activos y grupos funcionales oxigenados más frecuentes representados en una lámina grafénica. Adaptado de [123].
- Figura II.11. Grupos funcionales nitrogenados más frecuentes representados en una lámina grafénica. Adaptado de [127].
- Figura III.1. Tipos de isotermas de fisisorción según la IUPAC. Adaptado de [4].

- Figura III.2. Grupos funcionales oxigenados y gases emitidos por su descomposición. Adaptado de [22].
- Figura III.3. Esquema de la variación del potencial (E) frente al tiempo (t).
- Figura III.4. Esquema de una celda electroquímica en configuración de tres electrodos y su circuito equivalente.
- Figura III.5. Voltamperogramas cíclicos típicos donde se representa: un comportamiento puramente capacitivo (a) y de formación de la doble capa eléctrica con un proceso farádico (b).
- Figura III.6. Esquema de una celda electroquímica en configuración de dos electrodos y su circuito equivalente.
- Figura III.7. Esquema de un salto galvanostático.
- Figura III.8. Esquema de cronopotenciograma típico obtenido para un material con comportamiento capacitivo en configuración de tres electrodos (a) y variación de la intensidad de corriente eléctrica (b).
- Figura III.9. Esquema de un salto potenciostático.
- Figura III.10. Esquema de un electrodo de cuarzo en corte AT de 9 MHz.
- Figura III.11. Esquema de la celda electroquímica utilizada para los experimentos realizados con la EQCM.
- Figura III.12. Esquema energético de la dispersión Rayleigh y Raman no resonante.
- Figura III.13. Esquema de la celda espectro-electroquímica empleada para los experimentos de espectroscopía Raman *in situ*.

- Figure IV.1. Cyclic voltammograms (1 mV $s^{-1}$) of ANK3 in 6 M KOH solution. Red line (-0.67 V / -0.27 V), green line (-0.87 V / 0.13 V), blue line (-1.07 V / 0.13 V), black line (-1.27 V / 0.13 V).

- Figure IV.2. Cyclic voltammograms (1 mV $s^{-1}$) of MWV-E510A in 6 M KOH solution. Red line (-0.67 V / -0.27 V), green line (-0.87 V / 0.13 V), blue line (-1.07 V / 0.13 V), black line (-1.27 V / 0.13 V).

- Figure IV.3. Cyclic voltammograms (1 mV $s^{-1}$) of ANK3 in 0.5 M $Na_2SO_4$ solution. Red line (-0.14 V / 0.26 V), green line (-0.79 V / 1.21 V), blue line (-1.14 V / 1.21 V), black line (-1.34 V / 1.21 V).

- Figure IV.4. Cyclic voltammograms (1 mV $s^{-1}$) of MWV-E510A in 0.5 M $Na_2SO_4$ solution. Red line (-0.14 V / 0.26 V), green line (-0.79 V / 1.21 V), blue line (-1.14 V / 1.21 V), black line (-1.34 V / 1.21 V).

- Figure IV.5. GCD curves in 6 M KOH solution. Charge -500 mA $g_{electrode}^{-1}$ during 1 hour, discharge +50 mA $g_{electrode}^{-1}$ until initial open circuit potential.

- Figure IV.6. GCD curves in 0.5 M $Na_2SO_4$ solution. Charge -500 mA $g_{electrode}^{-1}$ during 1 hour, discharge +50 mA $g_{electrode}^{-1}$ until initial open circuit potential.

- Figure IV.7. Raman spectra for the sample ANK3 at different potentials referred to NHE in 6 M KOH solution. Spectra normalized versus the D band.

- Figure IV.8. Raman spectra for the sample MWV-E510A at different potentials referred to NHE in 6 M KOH solution. Spectra normalized versus the D band.

- Figure IV.9. Raman spectra for sample ANK3 at different potentials referred to NHE in 0.5 M $Na_2SO_4$ solution. Spectra normalized versus the D band.
- Figure IV.10. Raman spectra for sample MWV-E510A at different potentials referred to NHE in 0.5 M $Na_2SO_4$ solution. Spectra normalized versus the D band.
- Figure V.1. Cyclic voltammograms obtained between -0.10 V and 0.30 V of ZTC at 5 mV $s^{-1}$ in 1M $H_2SO_4$ solution.
- Figure V.2. Cyclic voltammograms (a) and gravimetric response (b) simultaneously obtained between -0.10 V and 0.80 V of ZTC at 5 mV $s^{-1}$ in 1M $H_2SO_4$ solution.
- Figure V.3. Cyclic voltammograms (a) and gravimetric response (b) simultaneously obtained between -0.10 V and 0.60 V of ZTC at 5 mV $s^{-1}$ in 1M $H_2SO_4$ solution, after the electrochemical oxidation between -0.10 V and 0.80 V.
- Figure V.4. Cyclic voltammograms (a) and gravimetric response (b) simultaneously obtained between -0.10 V and 1.20 V of ZTC at 5 mV $s^{-1}$ in 1M $H_2SO_4$ solution.
- Figure V.5. Cyclic voltammograms between -0.10 V and 1.40 V of ZTC at 5 mV $s^{-1}$ in 1M $H_2SO_4$ solution. Dashed line (3rd scan of the 2nd CV experiment), solid line (22nd scan of the 4th CV experiment).
- Figure V.6. Gravimetric response between -0.10 V and 1.40 V of ZTC at 5 mV $s^{-1}$ in 1M $H_2SO_4$ solution during the 22 cycles of the 4th CV experiment.

- Figure V.7. Gravimetric response between -0.10 V and 1.40 V of ZTC at 5 mV $s^{-1}$ in 1M $H_2SO_4$ solution of the 22nd scan of the 4th CV experiment.

- Figure V.8. Raman spectra recorded with He-Ne laser of the ZTC sample at different potentials referred to Ag/AgCl (KCl 3 M) in 1 M $H_2SO_4$ solution. Spectra normalized versus the D band.

- Figure V.9. Raman spectra recorded with Diode laser of the ZTC sample at different potentials referred to Ag/AgCl (KCl 3 M) in 1 M $H_2SO_4$ solution. Spectra normalized versus the D band.

- Figure V.10. ID/IG for He–Ne laser of the ZTC sample. Square symbol (■) going to more positive potential, circle symbol (●) going to more negative potential after the scan to positive potential.

- Figure VI.1. FE-SEM image (a) and corresponding EDX silicon mapping analysis (b) of the mesoporous silica thin film deposited onto the graphite current collector.

- Figure VI.2. TEM image of: mesoporous silica thin film (a), composite silica/carbon thin film (b) and mesoporous carbon thin film (c).

- Figure. VI.3. Raman spectra of the graphite plate and the mesoporous silica, composite silica/carbon and mesoporous carbon thin films. Spectra normalized versus the D band.

- Figure VI.4. Cyclic voltammograms of the mesoporous carbon thin film in 1M $H_2SO_4$ solution: between 0.00 V and 0.60 V at 2, 5, 10, 20, 50, 100, 200, 500, 1000, 2000, 5000 mV $s^{-1}$ (a); between -0.20 and 0.80 V (blue line), between -0.40 V and 1.00 V (red line) and between -0.60 and 1.00 V (black line) at 5 mV $s^{-1}$ (b); between 0.00 V

and 0.60 V at 2, 5, 10, 20, 50, 100, 200, 500, 1000, 2000, 5000 mV $s^{-1}$ after opening the potential window (c).

- Figure VI.5. 4th chage-discharge cycle of the mesoporous carbon thin film in 1M $H_2SO_4$ solution at: 2 (blue line), 4 (red line), 6 (black line), 8 (green line), 10 (purple line), 20 (orange line), 40 (dark blue line) mA $cm^{-2}$.
- Figure VI.6. Cyclic voltammograms of the composite silica/carbon thin film in 1M $H_2SO_4$ solution: between 0.00 V and 0.60 V at 2, 5, 10, 20, 50, 100, 200, 500, 1000, 2000, 5000 mV $s^{-1}$ (a); between -0.20 and 0.80 V (blue line), between -0.40 V and 1.00 V (red line) and between -0.60 and 1.00 V (black line) at 5 mV $s^{-1}$ (b); between 0.00 V and 0.60 V at 2, 5, 10, 20, 50, 100, 200, 500, 1000, 2000, 5000 mV $s^{-1}$ after opening the potential window (c).
- Figure VI.7. 4th chage-discharge cycle of the composite silica/carbon thin film in 1M $H_2SO_4$ solution at: 2 (blue line), 4 (red line), 6 (black line), 8 (green line), 10 (purple line), 20 (orange line), 40 (dark blue line) mA $cm^{-2}$.
- Figure VI.8. Specific capacitance *versus* scan rate plot for: graphite current collector after opening the potential window (-Δ- empty triangle symbols) and mesoporous carbon thin film before (-○-empty circle symbols) and after (-□-empty square symbols) opening the potential window. Note: the secondary axis of capacitance retention applies only to the mesoporous carbon thin film after opening the potential window.
- Figure VI.9. Specific capacitance *versus* scan rate plot for: mesoporous carbon thin film (-□- empty square symbols) and

composite silica/carbon thin film (-■- full square symbols) after opening the potential window. Note: the secondary axis of capacitance retention applies only to the composite silica/carbon thin film.

- Figure VI.10. Specific capacitance *versus* current density plot for: mesoporous carbon thin film (-◊- empty rhombus symbols) and composite silica/carbon thin film (-♦- full rhombus symbols).
- Figure VI.11. Cyclic voltammograms of the symmetric electrochemical capacitor from the mesoporous carbon thin film in 1M $H_2SO_4$ solution between 0.00 V and 1.00 V at: 5, 10, 20, 50, 100, 200, 500, 1000, 2000, 5000 mV $s^{-1}$.
- Figure VI.12. Cyclic voltammograms of the symmetric electrochemical capacitor from the composite silica/carbon thin film in 1M $H_2SO_4$ solution between 0.00 V and 1.00 V at: 5, 10, 20, 50, 100, 200, 500, 1000, 2000, 5000 mV $s^{-1}$.
- Figure VI.13. Specific capacitance *versus* scan rate plot for the symmetric electrochemical capacitor made from: the mesoporous carbon thin film (-□- empty square symbols) and the composite silica/carbon thin film (-■- full square symbols).
- Figure VI.14. Specific capacitance *versus* current density plot for the symmetric electrochemical capacitor made from: the mesoporous carbon thin film (-◊- empty rhombus symbols) and the composite silica/carbon thin film (-♦- full rhombus symbols).
- Figure VI.15. Specific capacitance versus cycle number plot for the symmetric electrochemical capacitor made from the mesoporous carbon thin film: between 0.00 V and 1.00 V (-■- black square

symbols) and between 0.00 V and 1.20 V (-🟥- red square symbols).Current density: 10 mA $cm^{-2}$.

- Figure VII.1. $N_2$ adsorption isotherm at 77 K of ANK3.
- Figure VII.2. PSD of ANK3 obtained from the $N_2$ isotherm at 77 K by applying NLDFT method.
- Figure VII.3. Cyclic voltammograms in three-electrode configuration in: 1M $Et_4N$ $BF_4$/PC, 1M $PYR_{14}$ $BF_4$/PC and 1M $PYR_{14}$ TFSI/PC. 1 mV $s^{-1}$ scan rate. 20 ºC.
- Figure VII.4. Avogadro software model of the structure of $PYR_{14}^+$.
- Figure VII.5. Cyclic voltammograms in three-electrode configuration in $PYR_{14}$ TFSI at 20, 40 and 60 ºC. 1 mV $s^{-1}$ scan rate.
- Figure VII.6. Cyclic voltammograms at 5 mV $s^{-1}$ in two-electrode configuration in: 1M $Et_4N$ $BF_4$/PC, 1M $PYR_{14}$ $BF_4$/PC and 1M $PYR_{14}$ TFSI/PC.
- Figure VII.7. $C_s$ values versus scan rate plot for: 1M $Et_4N$ $BF_4$/PC, 1M $PYR_{14}$ $BF_4$/PC and 1M $PYR_{14}$ TFSI/PC.

# *Capítulo I*

# Objetivos y estructura general de la Tesis Doctoral

## I.1. Introducción

La investigación en el campo de la producción y el almacenamiento de energía se ha convertido en un tema puntero debido al crecimiento de la población y a la creciente industrialización de la sociedad. Se están realizando grandes esfuerzos en conseguir que la producción y el almacenamiento de energía sean procesos eficientes y medioambientalmente sostenibles.

En los últimos años se ha incrementado el estudio de nuevos sistemas de almacenamiento de energía, principalmente baterías y condensadores electroquímicos. El uso de materiales carbonosos ha sido y continúa siendo ampliamente estudiado para su aplicación en este campo.

El grupo de investigación Materiales Carbonosos y Medio Ambiente, en el que se ha realizado la presente Tesis Doctoral, tiene una amplia experiencia en la síntesis de materiales carbonosos avanzados. Dentro de las distintas áreas de investigación que abarcan, el estudio del almacenamiento electroquímico de energía eficiente está teniendo cada vez más importancia. La presente Tesis Doctoral se enmarca en el campo de la síntesis de materiales carbonosos avanzados para aplicaciones en el almacenamiento de energía.

## I.2. Objetivos de la Tesis Doctoral

Los objetivos generales de la presente Tesis Doctoral comprenden los siguientes puntos:

(i) Diseño y síntesis de materiales carbonosos nanoestructurados con porosidad diseñada para su uso como electrodos en micro-condensadores.

Dada la creciente demanda de dispositivos de almacenamiento de energía miniaturizados, y teniendo en cuenta las desventajas asociadas a la preparación de electrodos a partir de materiales carbonosos en polvo, el primer objetivo de la presente Tesis Doctoral se centra en el estudio de la síntesis de una película delgada continua de un material carbonoso nanoestructurado directamente sobre el colector de corriente para su uso como electrodo en micro-condensadores.

(ii) Caracterización química y electroquímica de materiales carbonosos nanoestructurados para su uso como electrodos en supercondensadores.

Cabe destacar que, además de las películas delgadas sintetizadas del material carbonoso nanoestructurado, se han utilizado otros materiales carbonosos con porosidad diseñada.

El segundo objetivo de la presente Tesis Doctoral está centrado en el estudio del comportamiento electroquímico del material carbonoso (configuración de tres electrodos) y del supercondensador (configuración de dos electrodos) desde el punto de vista de su estabilidad electroquímica, los mecanismos de almacenamiento de energía y la ventana de estabilidad del electrolito.

Además, el conocimiento de las propiedades de los materiales electródicos resulta esencial para la explicación de su comportamiento electroquímico en sistemas de almacenamiento de energía. Es por ello que el segundo objetivo de la presente Tesis Doctoral incluye, también, la caracterización química, textural y estructural de los materiales carbonosos avanzados empleados.

Cabe destacar que se emplearán, además de electrolitos acuosos habituales, otros electrolitos no convencionales (incluyendo líquidos iónicos y sales disueltas en disolventes orgánicos). Estos electrolitos están despertando gran interés en la actualidad, ya que permiten aumentar el voltaje de trabajo, respecto a los electrolitos acuosos, lo que se traduce en mayores valores de densidad de energía almacenada.

## I.3. Estructura de la Tesis Doctoral

La presente Tesis Doctoral ha sido realizada en el grupo de Materiales Carbonosos y Medio Ambiente perteneciente al Departamento de Química Inorgánica de la Universidad de Alicante y al Instituto Universitario de Materiales de Alicante. Además, parte del trabajo de investigación presentado se ha desarrollado en el Helmholtz Institute Ulm perteneciente al Karlsruhe Institute of Technology (Alemania) bajo la supervisión del Doctor Andrea Balducci durante la realización de una estancia de investigación.

Dado que la memoria de Tesis Doctoral se presenta para aspirar al grado de doctora por la Universidad de Alicante con “mención de doctora internacional”, los capítulos correspondientes a los resultados obtenidos han sido redactados exclusivamente en inglés. Además, tanto las conclusiones generales como el resumen final adjunto han sido redactados tanto en castellano como en inglés. Cumpliendo, de esta forma, con la normativa vigente.

La Tesis Doctoral se encuentra dividida en ocho capítulos, en los cuales se desarrollan los contenidos que se presentan a continuación.

### ❖ Capítulo I. Objetivos y estructura general de la Tesis Doctoral

En este capítulo se exponen, en primer lugar, los objetivos de la presente Tesis Doctoral. Además, se expone la estructura general de la misma.

### ❖ Capítulo II. Introducción general

En este capítulo se presenta una breve introducción sobre los dispositivos de almacenamiento electroquímico de energía, centrada en los supercondensadores o condensadores electroquímicos. Se abordan temas tales como: electrolitos empleados y tipos de materiales carbonosos porosos utilizados como electrodos. Además, se presenta la influencia que tienen las propiedades de dichos materiales (textura porosa y química superficial) en su comportamiento electroquímico como electrodos en supercondensadores.

### ❖ Capítulo III. Experimental

En este capítulo se incluye una breve explicación acerca de los materiales carbonosos empleados en la presente Tesis Doctoral.

Además, se resumen los fundamentos básicos de las técnicas experimentales utilizadas para la caracterización de dichos materiales.

### ❖ Chapter IV. New insights on electrochemical hydrogen storage in nanoporous carbons by *in situ* Raman spectroscopy

El trabajo presentado en el Capítulo IV se centra en profundizar en el mecanismo de almacenamiento electroquímico de hidrógeno en condiciones catódicas utilizando dos carbones activados con diferente porosidad, química superficial y reactividad. Además, se ha utilizado la técnica de espectroscopía Raman *in situ* para analizar los cambios estructurales que tienen lugar en dichos carbones activados en función del potencial, estudiándose el efecto del tipo de material carbonoso y el electrolito.

Los resultados de dicho estudio han dado lugar a la publicación de un artículo en la revista *Carbon*, cuyo índice de impacto es 6,198:

*Leyva-García S, Morallón E, Cazorla-Amorós D, Béguin F, Lozano-Castelló D. New insights on electrochemical hydrogen storage in nanoporous carbons by in situ Raman spectroscopy. Carbon 2014;69:401–8.*

### ❖ Chapter V. Characterization of a zeolite-templated carbon by electrochemical quartz crystal microbalance and *in situ* Raman spectroscopy

Los materiales carbonosos sintetizados por nanomoldeo utilizando como plantilla zeolita Y (ZTC) son materiales prometedores para su uso como electrodos en condensadores electroquímicos. En el trabajo presentado en este capítulo se analiza el comportamiento electroquímico del ZTC, bajo diferentes condiciones en medio 1 M $H_2SO_4$, prestando especial atención a los cambios químicos y estructurales que se producen.

Este estudio ha dado lugar a la publicación de un artículo en la revista *Carbon*, cuyo índice de impacto es 6,198:

*Leyva-García S, Nueangnoraj K, Lozano-Castelló D, Nishihara H, Kyotani T, Morallón E, Cazorla-Amorós D. Characterization of a zeolite-templated carbon by electrochemical quartz crystal microbalance and in situ Raman spectroscopy. Carbon 2015;89:63-73.*

### ❖ Chapter VI. Silica-templated ordered mesoporous carbon thin films as electrodes for micro-capacitors

A lo largo de la presente memoria de Tesis Doctoral, se verá la importancia de los materiales carbonosos porosos para su uso como electrodos en supercondensadores. Dado que en la actualidad existe una creciente demanda de dispositivos de almacenamiento de energía miniaturizados, en el Capítulo VI se presenta la síntesis y caracterización de películas delgadas de materiales carbonosos mesoporosos directamente sobre un colector de corriente de grafito para su uso como electrodos en micro-condensadores, lo cual permite solventar algunas de las desventajas asociadas al procedimiento estándar de preparación de electrodos carbonosos porosos a partir de materiales en polvo. Para la síntesis del material carbonoso nanoestructurado se ha utilizado como plantilla una lámina de sílice mesoporosa sintetizada directamente sobre el colector de grafito. Las películas delgadas sintetizadas se han caracterizado mediante diferentes técnicas microscópicas y espectroscópicas así como electroquímicas (en medio 1M $H_2SO_4$).

Los resultados del estudio desarrollado en este capítulo se han publicado en un artículo en la revista *Journal of Materials Chemistry A*, cuyo índice de impacto es 8,262:

*Leyva-García S, Lozano-Castelló S, Morallón E and Cazorla-Amorós D. Silica-templated ordered mesoporous carbon thin films as electrodes for micro-capacitors. J. Mater. Chem. A, 2016,4, 4570-4579.*

### ❖ Chapter VII. Electrochemical performance of a superporous activated carbon in ionic liquid-based electrolytes

Los electrolitos basados en líquidos iónicos o sales disueltas en disolventes orgánicos están siendo ampliamente estudiados en la actualidad para su uso en supercondensadores debido a que permiten aumentar el voltaje de trabajo, respecto a los electrolitos acuosos, lo que se traduce en un aumento de la densidad de energía almacenada. En el trabajo presentado en el Capítulo VII, se estudia el comportamiento electroquímico de un carbón activado superporoso en diferentes electrolitos no acuosos. Los resultados han permitido destacar la importancia no sólo de la textura porosa del material carbonoso en el comportamiento electroquímico mostrado por éste, sino también de otros parámetros característicos del electrolito.

Los interesantes resultados extraídos de éste estudio han permitido enviar un artículo a la revista *Journal of Power Sources*, cuyo índice de impacto es 6,333, que se encuentra, actualmente, en revisión:

*Leyva-García S, Lozano-Castelló D, Morallón E, Vogl T, Schütter C, Passerini S, Balducci A and Cazorla-Amorós D. Electrochemical performance of a superporous activated carbon in ionic liquid-based electrolytes.*

### ❖ Chapter VIII. General conclusions/Capítulo VIII. Conclusiones generales

En este capítulo se recogen las conclusiones generales extraídas del trabajo de investigación realizado en la presente Tesis Doctoral. Se ha redactado tanto en inglés como en castellano.

### ❖ Summary/Resumen

Por último, se incluye un resumen general redactado, también, en inglés y castellano.

# Capítulo II

## Introducción general

## II.1. Introducción

El consumo energético mundial ha experimentado un considerable aumento desde el pasado siglo XX hasta la actualidad, como consecuencia del crecimiento de la población y de la creciente industrialización de la sociedad. La investigación en el campo de la producción y el almacenamiento de energía mediante tecnologías alternativas se ha convertido en un tema puntero, como consecuencia del cambio climático (producido por la contaminación atmosférica) y del incremento del coste de combustibles fósiles. Las investigaciones se centran en conseguir una menor dependencia de combustibles fósiles, incrementar la eficiencia energética, así como aumentar la implicación de las energías renovables en la producción energética. Los dispositivos electroquímicos de generación y almacenamiento de energía (como baterías y condensadores electroquímicos o supercondensadores) son una opción muy prometedora, incluso para aplicaciones que requieren densidades elevadas de potencia y energía, tales como vehículos eléctricos, telefonía móvil, ordenadores portátiles, etc. En la actualidad, existe un gran interés en el desarrollo de supercondensadores que puedan almacenar una cantidad de energía comparable a las baterías pero manteniendo la potencia característica de los condensadores convencionales [1]. Estos sistemas funcionan de forma similar a estos condensadores pero utilizando como electrodos materiales de elevada área específica y un electrolito como transportador de carga [2,3]. La disponibilidad de una mayor superficie permite alcanzar valores de capacidad específica varios órdenes de magnitud por encima de los condensadores convencionales, con la ventaja de que muestran, también, un elevado valor de potencia específica, del que carecen las baterías y que es imprescindible para numerosas aplicaciones como el coche eléctrico o dispositivos alimentados con pilas de combustible [3]. Los materiales carbonosos porosos están siendo ampliamente investigados para su uso como electrodos en supercondensadores debido a su elevada conductividad, bajo coste y versatilidad de su textura/estructura [4]. A lo largo de la introducción se va a profundizar en la explicación de estos dispositivos de almacenamiento de energía, centrando la atención, tanto en los materiales carbonosos utilizados como electrodos, como en los electrolitos usados habitualmente.

## II.2. Formas de almacenamiento de energía eléctrica

### II.2.1. Procesos farádicos y electrostáticos

Los mecanismos de almacenamiento de energía que se producen en baterías y supercondensadores se pueden clasificar de manera general en [2,5]:

(i) Procesos farádicos que involucran reacciones redox que se producen en la interfase electrodo/electrolito. Este mecanismo de almacenamiento de energía predomina principalmente en baterías, aunque puede producirse también en supercondensadores. Las baterías son capaces de almacenar grandes cantidades de energía, pero no son capaces de proporcionar elevadas potencias, debido a que están condicionadas por la propia cinética de la reacción electroquímica.

(ii) Procesos capacitivos. Consiste en la acumulación de cargas electrostáticas entre dos placas conductoras paralelas. Es el mecanismo de almacenamiento de energía que predomina en los condensadores. La principal ventaja de esta forma de almacenamiento de energía es la elevada velocidad de propagación de la carga, no sujeta a la cinética propia de una reacción electroquímica, por lo que la carga y descarga suceden en intervalos cortos de tiempo, pudiendo proporcionar elevadas potencias eléctricas.

### II.2.2. Baterías y pilas de combustible

Las baterías se pueden definir de manera simple como unidades que emplean una reacción electroquímica (energía química) para producir una corriente eléctrica (energía eléctrica). Estos dispositivos están constituidos generalmente por dos electrodos, uno donde se produce la reacción de oxidación (ánodo) y otro electrodo donde se produce la reacción de reducción (cátodo) en presencia de un electrolito. Durante el proceso de descarga, se produce un flujo de electrones desde el electrodo negativo al positivo a través del circuito exterior (como consecuencia de conectar la batería a un consumo o resistencia). En el electrodo negativo se produce la reacción de oxidación, generándose cationes que migran al electrodo positivo a través del electrolito. El proceso de carga implica que el flujo de electrones va desde el electrodo positivo al negativo a través del circuito exterior al conectar la batería a una fuente de corriente continua que actúa como alimentación. En este caso es en el electrodo positivo donde se produce la reacción de oxidación, generándose iones que migran al electrodo negativo a través del electrolito.

Las baterías se pueden clasificar, de forma general, en los siguientes tipos:

(i) Primarias: emplean especies redox que no pueden regresar a su estado original recargándolas debido a la irreversibilidad de la reacción redox, de modo que cuando los reactivos se consumen, la batería queda agotada y debe desecharse. Dentro de esta categoría se encuentran, entre otras, la batería seca de Leclanché, la celda alcalina, la de plata-zinc y la de zinc-aire.

(ii) Secundarias: estas presentan similitudes con las primarias, aunque pueden ser descargadas y restauradas hasta su carga inicial, debido a la reversibilidad de las reacciones [6]. En este apartado podemos destacar el acumulador de plomo, la batería de níquel-cadmio o níquel-hidrógeno.

Dentro de esta categoría están las baterías de ion-litio que son las más utilizadas en el campo de los dispositivos electrónicos (teléfonos móviles, portátiles, reproductores de música, etc.). Estas baterías están constituidas por un electrodo de un material carbonoso (ej. grafito), que actúa como electrodo negativo, y un óxido de litio (ej. $LiMO_2$), que actúa como electrodo positivo. El electrolito utilizado es una mezcla de una sal de litio ($LiPF_6$, $LiBF_4$, etc.) con un disolvente orgánico (carbonato de etileno o carbonato de dimetilo, entre otros). El funcionamiento de esta batería consiste en el proceso de extracción-inserción de iones litio en los electrodos, que produce el movimiento de electrones de un electrodo a otro.

La elección de la batería dependerá del tipo de aplicación. Si se necesitan periodos de vida útil elevados, se recurrirá a las baterías primarias o secundarias basadas en litio. Sin embargo, además del valor de energía, es importante tener en cuenta el valor de potencia. Este es el motivo por el que en determinados casos, como en el coche eléctrico, se tiene que recurrir a sistemas híbridos combinando condensadores convencionales o condensadores electroquímicos con baterías, ya que estas últimas presentan, generalmente, valores bajos de potencia.

Las pilas de combustible constituyen, también, un importante dispositivo electroquímico de generación de energía eléctrica. En este caso, los reactivos se van alimentando de forma continua durante la generación de energía eléctrica. El combustible se oxida en el ánodo, y en el cátodo se produce la reducción de oxígeno. Entre los posibles combustibles empleados, el que mayor interés presenta es el hidrógeno, aunque también han suscitado gran interés las pilas que utilizan el metanol como combustible. En todos estos casos, el ánodo de la celda de combustible está formado por un material carbonoso (negro de carbón, nanofibras de carbono, nanotubos de carbono, grafito, etc.) sobre el que se soportan nanopartículas de platino o aleaciones de éste (que actúan como catalizador).

Las celdas de combustible presentan una elevada eficiencia y una elevada densidad de energía, además, no producen sustancias tóxicas. Sin embargo, entre sus principales desventajas cabe destacar la poca estabilidad, su elevado coste, etc.

### II.2.3. Condensadores

Los condensadores eléctricos son sistemas de almacenamiento y liberación de energía, cuya estructura tipo sándwich contiene normalmente dos electrodos separados por un material dieléctrico (mica, material cerámico, aire, etc.). Entre estos electrodos se aplica una diferencia de potencial externo, produciendo un proceso de carga que da lugar a la acumulación gradual de carga positiva en un electrodo y carga negativa en el otro. Una vez finalizado el proceso de carga, cada electrodo tiene un valor de carga eléctrica igual y de signo opuesto (siendo la carga neta del condensador igual a cero).

$$Q = C \cdot V$$ **Ecuación II.1**

Donde *Q* es la carga eléctrica, *V* es la diferencia de potencial aplicada y *C* es la capacidad eléctrica.

La capacidad proporciona información sobre la cantidad de culombios necesarios para producir una determinada diferencia de potencial entre las placas del condensador. Este valor depende del material dieléctrico utilizado como separador, así como del área de los electrodos y de la distancia entre placas del dispositivo, tal y como se muestra en la Ecuación II.2:

$$C = \frac{Q}{V} = \frac{(\varepsilon_0 \cdot A)}{d}$$ **Ecuación II.2**

Donde *A* es el área de los electrodos, *d* es la separación entre ambos electrodos y $\varepsilon_0$ es la constante dieléctrica del material dieléctrico.

Esta ecuación es aplicable a condensadores plano-paralelos, puesto que si la configuración fuera esférica o cilíndrica habría que tener en cuenta el parámetro del radio externo e interno [7].

## II.3. Condensadores electroquímicos basados en materiales carbonosos de elevada área superficial

Los condensadores electroquímicos o supercondensadores son sistemas de almacenamiento de energía eléctrica compuestos por dos electrodos de elevada área superficial en contacto con un electrolito y separados mediante una membrana porosa. Al introducir un electrodo en una disolución electrolítica se genera una separación de cargas que se denomina doble capa eléctrica. La formación de la doble capa eléctrica da lugar a una distancia de separación entre las cargas muy pequeña, lo que constituye un factor importante en el valor de capacidad específica y, por tanto, en el valor de energía final del dispositivo.

La Figura II.1 muestra el esquema de un supercondensador cuyos electrodos están basados en carbón activado, donde puede observarse un electrodo negativo, donde se produce la adsorción de los cationes y otro positivo, sobre el que se adsorben los aniones.

En estos dispositivos, el sistema de almacenamiento de energía está basado en interacciones electrostáticas, por lo que el tiempo de respuesta es corto y, por lo tanto, muestran valores de potencia mayores que las baterías. Además, el uso de electrodos con elevadas áreas en los supercondensadores permite la obtención de valores de densidad de energía varios órdenes de magnitud superiores que los de los condensadores convencionales. En este sentido, los materiales carbonosos porosos están siendo ampliamente investigados para su uso como electrodos en supercondensadores. En particular, el carbón activado es el material más utilizado como electrodo, ya que presenta propiedades como alta conductividad eléctrica, versatilidad de estructura y textura porosa, buena resistencia a la corrosión, estabilidad térmica y bajo coste.

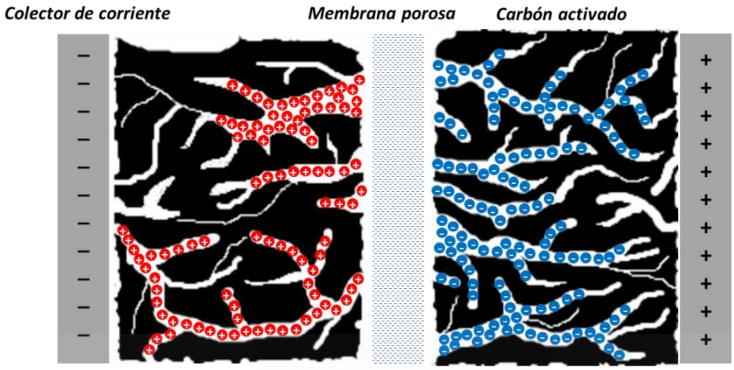

Figura II.1. Esquema de un condensador electroquímico o supercondensador basado en electrodos de carbón activado.

La vida media de los supercondensadores es muy elevada, pudiendo acumular hasta cientos de miles de ciclos de carga y descarga sin sufrir pérdidas notorias de su capacidad de almacenamiento y de conductividad [8]. Además, la reversibilidad del sistema, medida por la eficiencia culómbica o energética, es superior al 95%. Otra de sus ventajas es que los tiempos de carga son bajos, pudiéndose completar en minutos, e incluso segundos.

Dos parámetros importantes a la hora de valorar los posibles usos de un dispositivo de almacenamiento de energía son la energía y la potencia específicas. En la Figura II.2 se presenta un diagrama de Ragone, donde se comparan los valores de energía y potencia específicas suministrables por distintos dispositivos de almacenamiento y generación de energía. Los condensadores electroquímicos están situados entre las baterías, las pilas de combustibles y los condensadores convencionales.

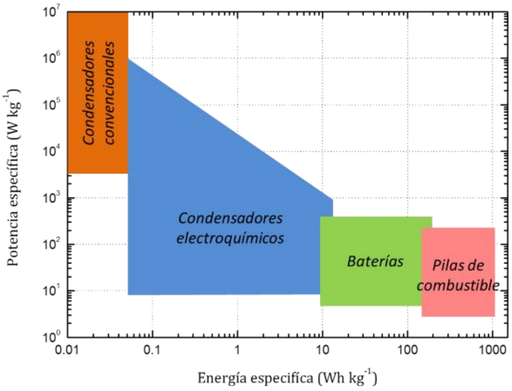

Figura II.2. Diagrama de Ragone. Adaptado de [9].

### II.3.1. Modelos de la doble capa eléctrica

Para una mayor comprensión de los procesos que ocurren en los condensadores electroquímicos es necesario explicar el fenómeno de la doble capa eléctrica que tiene lugar en la interfase electrodo/electrolito. Este fenómeno consiste en la separación de cargas entre dos fases, causada por la diferencia de potencial que se produce al poner en contacto dos fases con diferente composición química.

Existen diferentes modelos que explican el fenómeno de la doble capa eléctrica. El esquema del modelo propuesto por Helmholtz, en 1874, se muestra en la Figura II.3.a. Este modelo está basado en la formación de dos láminas paralelas cargadas de signo opuesto, una localizada en la superficie del electrodo y otra en la disolución (capa rígida); la separación entre ambas capas sería de unos pocos Angstroms. La capa de contraiones de la disolución neutraliza la carga superficial del electrodo por interacción electrostática (análogamente al condensador plano paralelo). En este modelo, el potencial eléctrico disminuye linealmente con el aumento de la distancia al electrodo, hasta hacerse nulo en el plano de la capa rígida (Figura II.3.b).

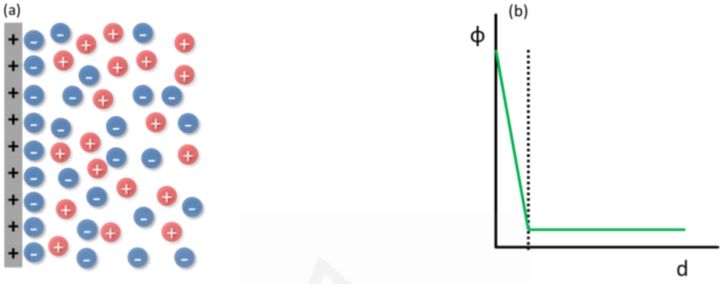

Figura II.3. Modelo de Helmholtz (a) y variación del potencial eléctrico con la distancia al electrodo (b).

El modelo de Gouy-Chapman propuesto en 1913 (Figura II.4.a), muestra ciertas similitudes con el modelo de Helmholtz, aunque no se habla de la formación de una capa rígida de iones, ya que se considera que están sujetos a agitación térmica, sino de una capa difusa que, en su conjunto, neutraliza la carga sobre el electrodo. En este caso, el potencial eléctrico varía de forma exponencial con la distancia al electrodo (Figura II.4.b).

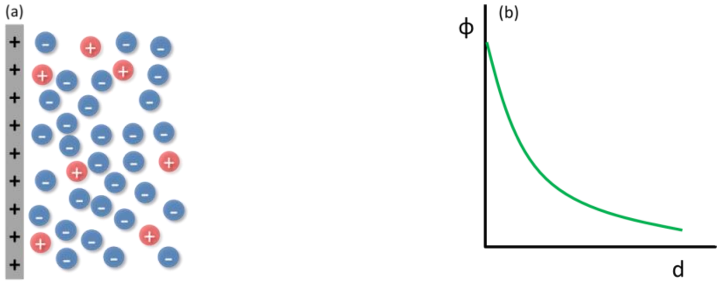

Figura II.4. Modelo de Gouy-Chapman (a) y variación del potencial eléctrico con la distancia al electrodo (b).

El modelo de Stern, propuesto en 1924 (Figura II.5.a), combina los modelos de Helmholtz y Gouy-Chapman. Se basa en la existencia de algunos iones «inmovilizados» en la superficie del electrodo, pero sin la formación de una capa rígida. La carga del electrodo es compensada tanto por los iones que se encuentran más cerca de éste como los que se distribuyen en la capa difusa. En este caso, el potencial varía de forma lineal en las cercanías del electrodo, por la contribución de los iones «inmovilizados», y disminuye de forma exponencial con el aumento de la distancia al electrodo en la zona de la capa difusa (Figura II.5.b).

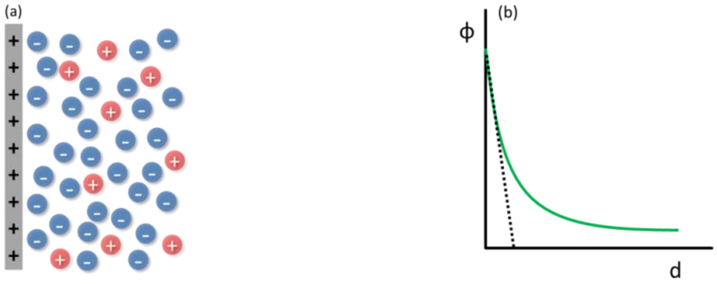

Figura II.5. Modelo de Stern (a) y variación del potencial eléctrico con la distancia al electrodo (b).

Por último, Grahame propuso en 1947 (Figura II.6) la adaptación al modelo de interfase electrodo/electrolito, teniendo en cuenta la estructura de las disoluciones de los electrolitos, es decir, considerando la solvatación de los iones que se encuentran en disolución y el carácter dipolar de las moléculas de agua. En este caso, se supone la existencia de diferentes planos de acercamiento a la superficie del electrodo, dependiendo de si el ión está solvatado o interacciona directamente con el electrodo. Por lo tanto, el modelo propone la existencia de: (i) una capa real, correspondiente al electrodo, (ii) una segunda capa virtual, constituida por el plano interno de Helmholtz (IHP, del inglés *inner Helmholtz plane*) en la disolución, donde se supone que los iones han perdido su esfera de solvatación y se encuentran adsorbidos de forma específica (en este caso, la interacción entre el electrodo y el ion compensaría la fuerza de repulsión electrostática) y (iii) una tercera capa que se denomina plano externo de Helmholtz (OHP, del inglés *outer Helmholtz plane*), donde se encuentran los contraiones solvatados [10,11]. La distribución de cargas se establece a través de la denominada zona compacta, cuyo espesor está en torno a 0,5 nm (correspondiente a los diámetros de las moléculas del disolvente e iones) y una zona difusa que va de 1 a 100 nm, correspondiente a iones térmicamente distribuidos [11]. El tamaño de la zona difusa depende de la concentración del electrolito, de forma que para concentraciones muy elevadas (superiores a 0,1 M), el tamaño de la zona difusa es inferior a 1 nm.

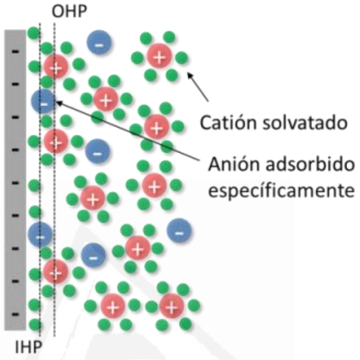

Figura II.6. Modelo de Grahame.

### II.3.2. Características de los condensadores electroquímicos

#### II.3.2.1. Energía almacenada

Cuando se aplica un voltaje a un supercondensador durante un período diferencial de tiempo, se realiza un diferencial de trabajo para mover una cantidad diferencial de carga que se acumula en la interfase electrodo/electrolito, lo que viene expresado por la Ecuación II.3:

$$dW = V.dQ$$ **Ecuación II.3**

Donde *dW* es el diferencial de trabajo, *V* es el voltaje y *dQ* el diferencial de carga.

Asumiendo que no hay pérdidas por disipación de calor, el trabajo será equivalente a la energía almacenada en el condensador, y considerando que el voltaje está relacionado con la carga desplazada y la capacidad, es posible integrar la ecuación anterior como se muestra a continuación:

$$W = E = \int_0^Q V.dQ = \int_0^Q \frac{Q}{C}.dQ = \frac{1}{2}.C.V^2$$ **Ecuación II.4**

Donde *W* es el trabajo, *E* es la energía y *C* la capacidad.

Por lo tanto, la energía acumulada en el condensador depende del potencial aplicado y de su capacidad. La energía suele medirse en Wh·kg$^{-1}$, aunque para aplicaciones donde el espacio ocupado por el supercondensador tiene gran importancia (como en dispositivos móviles) la energía volumétrica es también un factor relevante.

Por otro lado, la potencia máxima suministrable por el condensador viene determinada por la resistencia equivalente en serie de la celda:

$$P = \frac{V^2}{4.ESR}$$ **Ecuación II.5**

Donde *P* es la potencia máxima y *ESR* la resistencia equivalente en serie.

Una resistencia equivalente en serie muy elevada limita la potencia que puede suministrar el supercondensador y por tanto, sus posibles aplicaciones.

Por lo tanto, las tres propiedades principales que determinan la energía y potencia específicas de un supercondensador son el voltaje máximo, la capacidad y la resistencia equivalente en serie.

### II.3.2.2. Resistencia equivalente en serie

La resistencia equivalente en serie de un condensador engloba la resistencia del material usado como electrodo, la resistencia interfacial entre el electrodo y el colector de corriente, la resistencia iónica relacionada con la difusividad de los iones que se desplazan en la red porosa y la resistencia iónica relacionada con la difusividad de los iones que se desplazan a través de la membrana porosa situada entre los electrodos [2]. El espesor del electrodo influye, también, en la resistencia de la celda, ya que un mayor espesor del electrodo implica mayor resistencia a la transferencia electrónica desde el electrodo hasta el colector de corriente [12].

En el caso de electrodos carbonosos sintetizados, típicamente, a partir de carbón activado, es habitual mejorar su conductividad mediante el uso de aglomerantes (que empaqueta las partículas del material carbonoso) y aditivos conductores. Entre los aglomerantes más usados se encuentran el politetrafluoroetileno (PTFE, del inglés *polytetrafluoroethylene*) o teflón y el fluoruro de polivinilideno (PVDF, del inglés *polyvinylidene fluoride*). Como promotor de conductividad se utiliza, normalmente, negro de carbón, aunque se pueden usar otros materiales más avanzados como los nanotubos de carbono [13].

Por otro lado, la conductividad del electrolito y la movilidad de los iones encargados de transportar la corriente también influyen en la resistencia equivalente en serie.

Otras estrategias para la reducción de la resistencia equivalente en serie de una celda son: (i) el uso de electrodos basados en materiales avanzados de elevada conductividad, como los nanotubos de carbono [14]; (ii) la reducción de los caminos difusionales de los iones en la red porosa de los electrodos, lo cual se consigue mediante el uso de materiales nanoestructurados ordenados como nanotubos de carbono orientados [13] o materiales carbonosos de porosidad jerarquizada [15]; (iii) la mejora del contacto entre el electrodo y el colector de corriente, por ejemplo, sintetizando el material carbonoso (que ejerce de electrodo) directamente sobre el colector de corriente [16,17]; o (iv) la preparación de materiales carbonosos continuos en forma de monolitos, cuya estructura tridimensional y continua aumenta, notablemente, los puntos de contacto eléctrico respecto a un carbón activado en polvo [18], haciendo innecesario el uso de aglomerantes y promotores de conductividad.

### II.3.2.3. Voltaje

El voltaje máximo de trabajo depende, principalmente, de la estabilidad del electrolito usado. En medio acuoso, el potencial termodinámico de descomposición del agua (1,23 V) limita el voltaje de celda en torno a 1 V [19-21]. Los electrolitos orgánicos, basados en sales orgánicas disueltas en disolventes como el carbonato de propileno (PC, del ingés *propylene carbonate*) o el acetonitrilo (ACN, del ingés *acetonitrile*) permiten alcanzar potenciales en torno a 2,5-2,7 V [19]. En la actualidad, se está investigando ampliamente el uso de líquidos iónicos como electrolitos, ya que permiten alcanzar voltajes de hasta 5,5 V [22]. Las ventajas e inconvenientes de estos electrolitos se discutirán más adelante.

### II.3.2.4. Capacidad

Los mecanismos a través de los cuales se almacena energía en un supercondensador son: formación de la doble capa eléctrica por adsorción de los iones del electrolito en la porosidad del electrodo (proceso capacitivo) y reacciones redox, rápidas y reversibles, que suceden en la interfase electrodo/electrolito (mecanismo pseudocapacitivo). En supercondensadores basados en carbones activados, la formación de la doble capa es el mecanismo principal a través del cual se produce el almacenamiento de energía, aunque los grupos funcionales presentes en materiales carbonosos pueden participar en reacciones redox, contribuyendo al almacenamiento de energía a través de un mecanismo pseudocapacitivo [19,23,24], lo cual se detallará más adelante. Además, el almacenamiento de energía a través del mecanismo pseudocapacitivo se puede promover con el uso de materiales activos, como polímeros conductores y óxidos metálicos, de forma másica o bien nanoestructurados sobre la superficie de un material poroso [8,25].

### II.3.2.5. Tipos de configuraciones de condensador electroquímico

#### II.3.2.5.1. Condensador simétrico

En este caso, el supercondensador está compuesto por dos electrodos iguales, tanto en el tipo de material como en cantidad de masa. Este es el formato más frecuente y de más sencilla implementación industrial que, sin embargo, no es necesariamente el montaje óptimo, en cuanto a densidades de energía y potencia, para el material usado como electrodo.

### II.3.2.5.2. Condensador asimétrico

Los materiales usados como electrodos en supercondensadores pueden mostrar diferentes valores de capacidad en función de la ventana de potencial de trabajo. Esto es especialmente notable en el caso de materiales que muestren un comportamiento pseudocapacitivo, ya que las reacciones redox se producen a un valor de potencial determinado y, por tanto, la capacidad del material depende del potencial aplicado. Esto sucede, también, cuando los tamaños del catión y del anión son muy diferentes y cuando el tamaño medio de los poros del material carbonoso es similar al tamaño efectivo de uno de los iones [26]. En estos casos en los que los electrodos presentan distintas capacidades, el condensador se construye usando masas distintas de los electrodos positivo y negativo, buscándose una relación de masas que permita optimizar el funcionamiento del supercondensador. Se ha demostrado que la relación de masas que maximiza la densidad de energía de un supercondensador para electrodos de distinta capacidad gravimétrica es [27]:

$$\frac{m_+}{m_-} = \sqrt{\frac{C_-}{C_+}} \quad \textbf{Ecuación II.6}$$

Donde $m_+$ y $m_-$ son las masas de los electrodos positivo y negativo, respectivamente, y $C_+$ y $C_-$ son las capacidades de los electrodos positivo y negativo, respectivamente.

También se puede ajustar la masa de fase activa con el objetivo de que ambos electrodos se usen en su ventana de potencial de trabajo máxima, la cual está limitada por los potenciales de descomposición del electrolito sobre el electrodo o por el valor de potencial al que el electrodo comienza a degradarse. En electrolitos en fase acuosa, el material usado como electrodo positivo tiene una ventana operativa máxima, habitualmente, menor que la del electrodo negativo, por lo que limita el voltaje máximo que se puede alcanzar en configuración simétrica, ya que el electrodo negativo deja sin usar parte de su ventana de estabilidad. En este caso, la relación másica se calcula igualando la cantidad de carga almacenada o suministrada por cada electrodo:

$$Q = Q_+ = Q_- \quad \textbf{Ecuación II.7}$$

$$Q = m_+ \cdot C_+ \cdot \Delta\mathrm{E}_+ = \mathrm{m}_- \cdot \mathrm{C}_- \cdot \Delta\mathrm{E}_- \quad \textbf{Ecuación II.8}$$

$$\frac{m_+}{m_-} = \frac{C_- \cdot \Delta E_-}{C_+ \cdot \Delta E_+} \quad \textbf{Ecuación II.9}$$

Donde *Q* es la carga del supercondensador (siendo $Q_+$ y $Q_-$ la carga del electrodo positivo y negativo, respetivamente) y $\Delta E_+$ y $\Delta E_-$ son las ventanas de potencial de trabajo del electrodo positivo y negativo, respetivamente.

II.3.2.5.3. Condensador híbrido

En este caso se utilizan distintos materiales como electrodos positivo y negativo; usualmente, uno de ellos muestra comportamiento de batería y otro de supercondensador. La principal ventaja de estos sistemas es que permiten operar a voltajes más elevados.

### II.3.2.6. Tipos de electrolitos

La elección del electrolito es clave para optimizar el funcionamiento del supercondensador, ya que la ventana de potencial de estabilidad del electrolito determina el voltaje máximo operativo alcanzado en el dispositivo y, por tanto, influye en la energía y potencia máxima alcanzadas. Los tipos de electrolitos utilizados habitualmente en supercondensadores basados en materiales carbonosos de elevada área superficial se describen a continuación.

#### II.3.2.6.1. Electrolitos acuosos

El uso de electrolitos acuosos, como el $H_2SO_4$ o KOH, permite que los electrodos muestren valores elevados de capacidad (hasta 300 $F{\cdot}g^{-1}$ para carbones activados de elevada área superficial [23,28]). Sin embargo, debido a que el potencial termodinámico de descomposición del agua es 1,23 V, el voltaje de trabajo del supercondensador está limitado a alrededor de 1 V [19-21]. No obstante, se ha demostrado que es posible incrementar el voltaje de trabajo hasta 1,6 V, en medio 1M $H_2SO_4$, utilizando diferentes carbones activados como electrodos y/o balanceando las masas de los mismos [29]. Se ha visto, además, que en electrolitos acuosos neutros, basados en $Na_2SO_4$ o $Li_2SO_4$, se pueden alcanzar valores de voltaje de trabajo de hasta 2 V [30,31].

Es importante mencionar que el coste de los electrolitos acuosos es bastante inferior al de los electrolitos orgánicos y líquidos iónicos. Además, los electrolitos acuosos son relativamente respetuosos con el medio ambiente. Otra ventaja es que la fabricación de este tipo de supercondensadores no requiere el uso de cámaras de atmósfera controlada y se pueden alcanzar potencias mayores en el condensador.

### II.3.2.6.2. Electrolitos orgánicos

Los electrolitos orgánicos usados típicamente suelen estar basados en sales cuaternarias de amonio disueltas en un disolvente orgánico como el PC o el ACN. A pesar de que la capacidad específica mostrada por electrodos carbonosos en disolventes orgánicos es menor que en electrolitos acuosos (entre 150 y 200 $F \cdot g^{-1}$ [19,24]), los dispositivos basados en electrolitos orgánicos muestran, como principal ventaja, elevados valores de voltaje de trabajo, entre 2,5 y 2,7 V [19]. Esto permite que los supercondensadores presenten valores de energía mayores que los dispositivos que utilizan electrolitos acuosos y, es por ello, que son los más usados en la fabricación de supercondensadores comerciales [21]. Se ha publicado, sin embargo, que a estos valores tan elevados de voltaje se puede producir la descomposición de los electrolitos orgánicos basados en PC [32] y ACN [33] que puede dar lugar al bloqueo de la porosidad del material carbonoso, que actúa como electrodo, como consecuencia de los productos de descomposición del electrolito [32].

### II.3.2.6.3. Líquidos iónicos

Los líquidos iónicos pueden definirse como sales que son líquidas a temperaturas inferiores a 100 ºC [22]. Están compuestos, únicamente, por cationes y aniones, generalmente grandes y asimétricos, cuya naturaleza química determina las propiedades físicas y químicas del líquido iónico. Presentan bajas presiones de vapor, baja inflamabilidad y elevada estabilidad térmica [34] siendo considerados, por lo tanto, más seguros que los disolventes orgánicos. La combinación de distintos tipos de iones y cationes permite obtener líquidos iónicos con propiedades químicas distintas [22]. Las propiedades de los líquidos iónicos han despertado un gran interés en los últimos años para ser utilizados en dispositivos de almacenamiento de energía [34]. Los supercondensadores que utilizan líquidos iónicos como electrolitos permiten alcanzar valores de capacidad específica similares a los mostrados en disolventes orgánicos [35] con la ventaja de que se alcanzan voltajes de trabajo de más de 3,5 V, lo que permite que los supercondensadores muestren valores de energía superiores [22,34]. Sin embargo, el principal inconveniente respecto a los electrolitos orgánicos basados en PC y ACN es que muestran mayores valores de viscosidad y, por lo tanto, menores valores de conductividad, lo que puede limitar los valores de potencia alcanzados [34] (de hecho la conductividad iónica de los electrolitos acuosos (~1 $S \cdot cm^{-1}$) es muy superior a la de los electrolitos orgánicos (~0,02 $S \cdot cm^{-1}$) y a la de los líquidos iónicos (<0,01 $S \cdot cm^{-1}$) [19,22]).

Dado que algunas aplicaciones requieren el funcionamiento de supercondensadores en un amplio intervalo de temperaturas (entre -30 ºC y +60 ºC) [36] pueden encontrarse numerosos estudios sobre el comportamiento de dichos dispositivos basados en líquidos iónicos a diferentes temperaturas [32,37,38].

### II.3.3. Micro-condensadores

El creciente desarrollo de dispositivos tecnológicos portátiles demanda la miniaturización de los sistemas de almacenamiento de energía. Los supercondensadores usados habitualmente utilizan como electrodos unos discos o láminas obtenidas tras el prensado de un material compuesto formado por el material carbonoso poroso en polvo, un polímero que actúa como aglomerante y un aditivo conductor. Debido a la forma de preparación, el electrodo contiene macroporos en el espacio entre partículas y presenta una resistividad eléctrica interpartícula importante. Además, la cantidad de material activo presente está en torno al 80-90 % en masa, lo cual es también una importante desventaja. Los condensadores basados en películas delgadas (o micro-condensadores) se presentan como una interesante opción para ser usados como sistemas de almacenamiento de energía en dispositivos miniaturizados. Películas delgadas continuas de un material carbonoso con la textura porosa apropiada directamente sintetizadas sobre el colector de corriente, constituyen una aproximación atractiva para la mejora de las prestaciones de estos dispositivos. El espesor de los electrodos juega un importante papel en el camino que han de recorrer los iones del electrolito para llegar al electrodo por lo que el espesor de los micro-electrodos (que va desde los nm [39] hasta unos pocos µm [40]) es una importante ventaja respecto a los electrodos convencionales, que tienen un espesor de hasta unos cientos de µm [21]. De acuerdo con lo dicho anteriormente, los micro-condensadores deben mostrar elevados valores de capacidad, así como de retención de capacidad, que se requieren para dispositivos que han de proporcionar elevados valores de densidad de energía y de potencia.

En la bibliografía, se pueden encontrar numerosos estudios sobre diferentes métodos de síntesis y configuraciones de micro-condensadores, basados en distintos materiales activos y utilizando diferentes electrolitos.

Se ha reportado la síntesis de películas delgadas de grafeno (por depósito químico en fase vapor), y de óxido de grafeno reducido (por reducción química de óxido de grafeno) [39]. Los micro-condensadores basados en estos materiales se han probado utilizando un electrolito sólido basado en un polímero (polivinilalcohol-$H_3PO_4$) mostrando valores de capacidad de 80 $\mu F \cdot cm^{-2}$ para los electrodos sintetizados con grafeno, y de hasta 394 $\mu F \cdot cm^{-2}$ para los basados en óxido de grafeno reducido. Se ha publicado la síntesis de otros tipos de micro-condensadores que utilizan diferentes electrolitos y cuyos electrodos están basados, también, en películas delgadas de: (i) nanotubos de carbono de pared única, utilizando electrolitos sólidos poliméricos (tanto en medio acuoso como orgánico) consiguiendo, así, dispositivos flexibles [41]; (ii) nanohilos de silicio poroso (sintetizados por depósito químico en fase vapor) y utilizando electrolitos basados en sales orgánicas [42]; y (iii) polímeros conductores como el polipirrol [43]. También se ha reportado la síntesis de películas delgadas de un material carbonoso nanomoldeado utilizando zeolita como plantilla (ZTC, del inglés *zeolite-templated carbon*) mediante depósito químico en fase vapor de acetileno, dichos electrodos han mostrado valores de capacidad de hasta 12 $mF \cdot cm^{-2}$ en medio 1 M $H_2SO_4$ [16].

Además, existen estudios sobre la fabricación de micro-condensadores interdigitados basados en diferentes materiales [40,44-46]. En estos dispositivos un número variable de electrodos (en torno a 20) se disponen paralelamente. Dichos electrodos presentan una anchura de unas decenas de µm, y separación similar entre ellos. La longitud es de unos cientos de µm y su espesor de tan sólo algunos µm (1-7 µm), lo que permite obtener dispositivos con unas dimensiones finales de unos pocos $cm^2$. Se han utilizado diferentes materiales para la fabricación de estos dispositivos interdigitados: (i) óxidos metálicos porosos (por ejemplo, $RuO_2$ [44] y $MnO_2$ [47], sintetizados por electrodepósito), lo que ha permitido alcanzar capacidades de hasta 12,6 $mF \cdot cm^{-2}$ para el caso de los dispositivos basados en $RuO_2$ [44]; (ii) carbón activado en polvo (síntesis basada en el depósito de tinta de carbón), donde los dispositivos han mostrado valores de capacidad de hasta 2,1 $mF \cdot cm^{-2}$ en medio orgánico (1 M tetrafluoroborato de tetraetilamonio en PC) [40]; (iii) *onion-like carbon*, que han mostrado un buen comportamiento electroquímico incluso a elevados valores de velocidad de barrido, de hasta 200 $V \cdot s^{-1}$ [46]; y (iv) materiales compuestos de óxido de grafeno reducido y nanotubos de carbono (sintetizados por depósito de spray electrostático) que han permitido alcanzar valores de capacidad de 5,1 $mF \cdot cm^{-2}$ en electrolito acuoso neutro (3 M KCl) [45].

## II.4. Materiales carbonosos con porosidad diseñada

### II.4.1. Almacenamiento de energía en materiales carbonosos

El almacenamiento de energía electroquímicamente se ha estudiado utilizando una gran variedad de materiales carbonosos, como: carbones activados, nanotubos de carbono, fibras de carbón, aerogeles de carbón, xerogeles de carbón, materiales carbonosos nanoestructurados, etc.

La textura porosa y la química superficial influyen de manera determinante en el comportamiento electroquímico de los materiales carbonosos porosos para su uso como electrodo en supercondensadores. Esto es debido a los mecanismos a través de los cuales se produce el almacenamiento electroquímico de energía en dichos materiales [19]:

(i) Proceso capacitivo, donde la energía se almacena de forma electrostática, a través de la formación de la doble capa eléctrica. En este caso, el área superficial específica y la distribución del tamaño de poros son parámetros clave para el incremento de la capacidad mostrada por el material [19,24,28,48], como se verá en detalle más adelante.

(ii) Procesos farádico y capacitivo combinados. Los materiales carbonosos porosos presentan grupos superficiales basados, principalmente, en oxígeno y nitrógeno, que pueden generarse debido al propio precursor carbonoso y al proceso de síntesis del material, así como a partir de tratamientos posteriores. Estos grupos superficiales pueden participar en reacciones redox, contribuyendo al aumento de la capacidad mostrada por el material (lo que se denomina, pseudocapacidad) [23,24,49,50].

(iii) El almacenamiento electroquímico de hidrógeno es un proceso farádico que contribuye, también, al almacenamiento electroquímico de energía. Se produce como consecuencia de la descomposición del agua en condiciones catódicas. La energía se almacena en forma de carga eléctrica en el material a través de la adsorción y desorción de hidrógeno (reducción del agua y posterior oxidación del hidrógeno adsorbido). El mecanismo de almacenamiento de hidrógeno ha sido estudiado por Béguin y colaboradores en diferentes trabajos [51-55]. Las reacciones que han propuesto son:

$H_2O + e^- \rightarrow H + OH^-$ **Etapa de Volmer**

$C + H \rightarrow CH_{ad}$ **Etapa de adsorción**

Donde la reducción electroquímica del agua da lugar a la formación de un átomo de hidrógeno (que denominan «hidrógeno naciente») que rápidamente se adsorbe sobre la superficie del material carbonoso.

En estos mismos trabajos, se proponen otra serie de reacciones que pueden producirse durante el proceso de almacenamiento:

$CH_{ad} + H_2O + e^- \rightarrow H_2 + OH^- + C$ **Etapa de Heyrovsky**

$2H \rightarrow H_2$ **Etapa de Tafel**

$CH_{ad} + CH_{ad} \rightarrow H_2 + 2C$ **Recombinación**

Diferentes estudios muestran que el hidrógeno se encuentra formando un enlace químico reversible [51,54,55]; de hecho, se ha estimado la energía de enlace, obteniéndose un valor de 110 kJ $mol^{-1}$ (que se correspondería con un verdadero enlace químico) [54]. Además, el incremento del tiempo de carga conduce a la adsorción de hidrógeno en sitios de mayor energía [52,54,55]. Por otro lado, parece existir una fuerte influencia del pH del medio: el almacenamiento electroquímico de hidrógeno es mayor en medio básico que en ácido [53], y algo superior en medio neutro que en básico [51].

Respecto a la influencia de la porosidad en el almacenamiento electroquímico de hidrógeno, se ha visto que cuando la cantidad de grupos oxigenados superficiales no es muy elevada, la cantidad de hidrógeno almacenado electroquímicamente se incrementa de forma lineal con el aumento de la porosidad del material [56] y, en concreto, se ha reportado el aumento de la cantidad de hidrógeno almacenado con el volumen de microporos [52]. Sin embargo, se han encontrado desviaciones en esta tendencia [57] que se han asociado a la distribución del tamaño de poros. Parece que la porosidad estrecha (entre 0,6 y 0,7 nm) es la responsable del almacenamiento electroquímico de hidrógeno [57] mientras que la porosidad más ancha parece no mejorar el comportamiento de los materiales carbonosos para el almacenamiento de hidrógeno. Aunque la respuesta no es del todo satisfactoria, ya que la relación lineal entre la porosidad estrecha y la cantidad del hidrógeno almacenado no pasa por el origen de coordenadas [57]. Además, se ha visto que manteniendo la porosidad casi constante y variando la química superficial del material carbonoso, la cantidad de hidrógeno almacenado varía significativamente. En concreto, la cantidad de hidrógeno almacenado disminuye con el aumento de grupos oxigenados, lo que puede deberse a que los sitios activos (para el almacenamiento de hidrógeno) están saturados por los grupos oxigenados superficiales [56].

### II.4.2. Contribución a la capacidad de la doble capa eléctrica: influencia de la textura porosa

El área superficial específica y la distribución del tamaño de poros del material carbonoso son parámetros clave que determinan el comportamiento electroquímico mostrado por éste cuando es utilizado como electrodo [19,28,48].

Teniendo en cuenta la Ecuación II.2 (mostrada anteriormente) cabría esperar una relación lineal entre la capacidad y el área superficial del material carbonoso. Sin embargo, se ha demostrado que esta relación muestra un límite para un valor determinado de área superficial específica, para el cual, el valor de la capacidad, se hace casi constante [58]. Algunos autores han propuesto que la desviación de la tendencia para áreas superficiales específicas elevadas podría deberse a que el espesor de las paredes es tan pequeño que no es capaz de apantallar la carga en poros contiguos, disminuyendo la adsorción [58,59]. Otros parámetros que deben tenerse en cuenta para explicar esta tendencia son la relación entre el tamaño de los poros y los iones, así como la accesibilidad a la estructura porosa, es decir, como de interconectados están los poros del material.

Según la IUPAC, la porosidad se puede clasificar dependiendo del tamaño de los poros en [60]: microporos (< 2 nm), mesoporos (2-50 nm) y macroporos (> 50 nm). La presencia de microporos permite alcanzar elevados valores de capacidad [24,28,61-63]. En contra de lo que cabría esperar, se ha visto que tamaños de poro similares a los de los iones sin solvatar se traducen en grandes capacidades específicas, debido al efecto de confinamiento del ion en el interior del poro [64,65]. Sin embargo, la presencia de microporos muy estrechos puede dar lugar a efectos tamiz molecular, y en consecuencia, no intervienen en la formación de la doble capa eléctrica [21,23,24,26]. La presencia de mesoporos puede ser beneficioso para la interconexión de la red porosa, promoviendo, de esta manera, una rápida difusión del electrolito [66-69]. No obstante, si el material carbonoso presenta unos microporos con tamaño adecuado para permitir la formación de la doble capa eléctrica, la presencia de mesoporosidad dejaría de ser beneficiosa ya que se traduce en una pérdida de área superficial específica.

Por otro lado, hay que tener en cuenta que los tamaños del catión y anión empleados en el electrolito son diferentes. Esto implica que la velocidad con la que se transporta la carga será mayor para el ion solvatado de menor tamaño y que, además, pueden producirse fenómenos de tamiz molecular relacionados con uno de los iones [70,71].

Por último, además de la distribución de tamaño de poros, la interconectividad de los mismos, su disposición y el tamaño de la partícula donde se encuentran juegan también un papel esencial en la cinética de la formación de la doble capa y, por tanto, de la capacidad del material. Bleda-Martínez y col. [28] demostraron la importancia de la disposición de los poros en cuanto a la accesibilidad del electrolito. Observaron que la pérdida de capacidad (en medio 1 M $Na_2SO_4$) era mucho mayor para un carbón activado (que posee una red porosa altamente desordenada, con una tortuosidad elevada) que en fibras de carbón activadas (donde la microporosidad se encuentra dispuesta fundamentalmente de forma perpendicular al eje, siendo baja su tortuosidad) (ver Figura II.7).

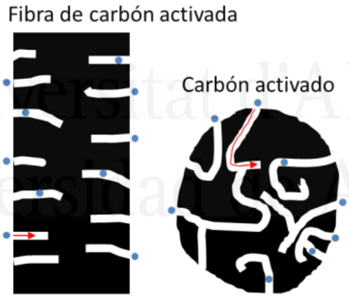

Figura II.7. Esquema de la tortuosidad de los iones al entrar en la porosidad de una fibra de carbón activada y un carbón activado.

Por tanto, materiales con una porosidad más accesible serán adecuados para aplicaciones donde se requiera elevada potencia. En este sentido, los materiales carbonosos con porosidad jerarquizada, donde los macroporos, mesoporos y microporos están dispuestos de tal forma que minimizan el camino difusional de los iones en la partícula carbonosa [72] y los materiales carbonosos nanomoldeados donde la red porosa ordenada e interconectada posee distribuciones de tamaños de poro muy homogéneas [73], pueden ser muy útiles para preparar supercondensadores que permitan alcanzar elevados valores de energía y potencia específicas.

### II.4.2.1. Carbones activados

El nombre de carbón activado se aplica a una serie de materiales de carbón porosos preparados artificialmente para que exhiban un elevado grado de porosidad y una elevada área superficial. Desde el punto de vista estructural, el carbón activado está constituido por un conjunto irregular de capas de carbono, siendo los espacios entre las mismas los que constituyen la porosidad del material [74].

Los carbones activados son unos de los materiales carbonosos más empleados para la fabricación de electrodos para supercondensadores debido a que presentan: alta conductividad eléctrica, versatilidad de estructura y textura porosa, buena resistencia a la corrosión, estabilidad térmica y bajo coste. El comportamiento electroquímico de los carbones activados viene determinado, especialmente, por su textura porosa y su química superficial [21,23,24,75].

Los carbones activados pueden sintetizarse mediante procesos de activación física o activación química. La principal diferencia entre los dos métodos es que la activación física implica, en general, una etapa previa de carbonización del material de partida, mientras que el proceso de activación química se lleva a cabo en una sola etapa [74,76] (ver Figura II.8). Los precursores para la síntesis de carbones activados son muy variados: madera, huesos de frutas (aceitunas, cerezas, etc.), cáscaras (coco, almendra, etc.), carbones minerales, breas, alquitranes, etc. Las características de los carbones activados sintetizados dependen tanto del precursor utilizado como del proceso de activación.

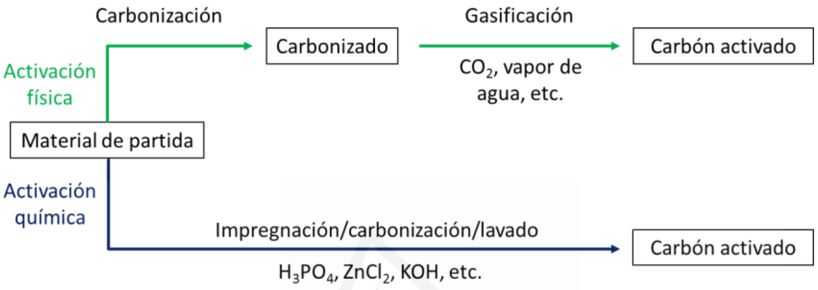

Figura II.8. Esquema general de los procesos de activación física y activación química. Adaptado de [74].

El proceso de activación física implica, generalmente (aunque no necesariamente), un proceso previo de carbonización del material de partida (entre 400 y 850 ºC, aunque pueden alcanzarse hasta 1000 ºC) [76,77]. Las muestras carbonizadas se tratan térmicamente entre 800-1100 ºC bajo atmósfera oxidante, principalmente $CO_2$, vapor de agua o mezcla de ambos [74,76,77]. El control del proceso de activación física permite obtener materiales muy activados. Sin embargo, se produce no sólo un desarrollo de la microporosidad, sino también un ensanchamiento de la distribución de tamaño de poros, por lo que no es posible obtener carbones activados con una distribución estrecha de microporos a través de la activación física [23,76,78].

El proceso de activación química implica la mezcla del agente activante (NaOH, KOH, $H_3PO_4$ o $ZnCl_2$) con el precursor carbonoso y su calentamiento a elevadas temperaturas (entre 400 y 900 ºC) bajo atmósfera inerte. El material obtenido requiere una etapa adicional de lavado para la eliminación del agente activante que no haya reaccionado, así como de productos inorgánicos de reacción [76,77]. La activación química presenta ventajas respecto a la activación física [76,78-80] que pueden resumirse en: (i) se lleva a cabo empleando temperaturas más bajas y tiempos de pirólisis menores, (ii) se suele llevar a cabo en una sola etapa, (iii) los rendimientos conseguidos son mayores y (iv) permite obtener carbones activados muy microporosos. No obstante, también presenta una serie de desventajas ya que se necesita una etapa adicional de lavado (tras el tratamiento térmico) y el uso de agentes químicos más corrosivos (en comparación con el $CO_2$ o el vapor de agua, usados en la activación física).

La activación química con $H_3PO_4$ se ha llevado a cabo utilizando, generalmente, precursores lignocelulósicos [77,81,82]. Bajos grados de activación producen carbones activados esencialmente microporosos y con un desarrollo no muy elevado del área superficial, mientras que mayores grados de activación producen el incremento del área superficial y un ensanchamiento de la distribución del tamaño de microporos. Por lo tanto, los procesos de activación química donde se utiliza $H_3PO_4$ como agente activante, no permiten la obtención de carbones activados con elevada área superficial y distribución estrecha de tamaño de microporos. Los carbones activados preparados con $ZnCl_2$ son esencialmente microporosos [79,83] y, aunque se pueden obtener carbones activados con mayores volúmenes de microporos, esto va acompañado, también, de un ensanchamiento de la microporosidad. Respecto a la activación con hidróxidos de metales alcalinos (KOH y NaOH) se ha estudiado la influencia en la textura porosa de variables como: tiempo de activación, temperatura de activación, velocidad de calentamiento, flujo de $N_2$ y proporción entre agente activante y precursor carbonoso [76,80]. Se ha visto que la activación con hidróxidos permite un mayor desarrollo de la porosidad y, por tanto, la obtención de carbones activados con áreas superficiales muy elevadas, siendo el KOH el que permite la obtención de una distribución de tamaño de microporos más estrecha [23,76,78,80,84].

El comportamiento electroquímico de materiales carbonosos con porosidad desarrollada ha sido ampliamente estudiado en la bibliografía. Se han reportado valores de 220 F $g^{-1}$ en medio orgánico (1 M $LiClO_4$ en PC) y de 250-300 F $g^{-1}$ en medio ácido (1 M $H_2SO_4$) para carbones activados químicamente con KOH debido, no sólo a la excelente textura porosa (área superficial específica, volumen de microporos y distribución de tamaño de microporos) sino también a la química superficial desarrollada [24,50,75] (lo que se verá más adelante).

### II.4.2.2. Materiales carbonosos nanomoldeados

En apartados anteriores, se ha remarcado la importancia de la textura porosa en el comportamiento electroquímico de los materiales carbonosos para ser usados como electrodos en supercondensadores. En este sentido, la síntesis de materiales carbonosos nanomoldeados es una importante herramienta para producir materiales carbonosos con estructuras y texturas controladas a nivel nanométrico. Los materiales carbonosos sintetizados por nanomoldeo exhiben una estructura porosa única, con un tamaño de poro bien definido, elevada área superficial específica y red porosa interconectada, que hace que sean candidatos prometedores para ser usados en aplicaciones como:

adsorbentes, soportes de catalizadores, biosensores, pilas de combustible y, en concreto, han despertado un gran interés como electrodos en supercondensadores. En general, el proceso de nanomoldeo incluye la infiltración del precursor carbonoso en los espacios que quedan en los materiales que se usan como plantilla, la polimerización/carbonización del precursor carbonoso y, finalmente, la eliminación de la plantilla (para obtener el material carbonoso diseñado) [73,85]. Se ha descrito en la bibliografía la síntesis de numerosos materiales nanomoldeados utilizando diferentes plantillas. Algunos ejemplos son:

(i) Materiales carbonosos sintetizados utilizando óxido de aluminio anodizado como plantilla. El óxido de aluminio anodizado consiste en una lámina porosa con estructura de panal de abeja, preparada a partir de la oxidación anódica de aluminio en medio ácido. Utilizando este material como plantilla se han sintetizado nanotubos de carbono (tanto por depósito químico en fase vapor como a través de la polimerización y carbonización de un polímero orgánico) [86]. También se han sintetizado fibras de carbón mesoporosas en el interior de los canales del óxido de aluminio anodizado utilizando un copolímero tribloque como surfactante, Pluronic® F127 ($EO_{106}PO_{70}EO_{106}$) y un precursor carbonoso polimérico (fenol y formaldehído) [87].

(ii) Materiales preparados como réplica de cristales coloidales u ópalos. Usualmente, se utilizan partículas de sílice como plantilla que pueden ser, además, de diferente tamaño. Estas partículas se pueden combinar con otros materiales «blandos» como plantillas (por ejemplo polímeros). La impregnación de dichos materiales plantilla con precursores carbonosos (como resinas fenólicas), la carbonización de éstos y la posterior eliminación de la plantilla permiten la obtención de materiales carbonosos con textura porosa bimodal [88,89]. Estos materiales carbonosos presentan estructuras porosas tridimensionales ordenadas, cuyos poros esféricos están interconectados y tienen tamaños correspondientes a las plantillas utilizadas (entre 20 y 1000 nm).

(iii) Materiales carbonosos mesoporosos ordenados utilizando sílices como plantilla. En la bibliografía pueden encontrarse numerosos trabajos sobre el uso de sílices mesoporosas, con estructura porosa tridimensional ordenada y conectada (por ejemplo, MCM-48, SBA-15 o SBA-16), como plantilla para la síntesis de materiales carbonosos nanomoldeados [67,90-94]. Los precursores carbonosos utilizados incluyen: sacarosa [92,93,95], alcohol furfurílico [67,96], resorcinol y formaldehído [97], fenol y formaldehído [98] o 2,3-dihidroxinaftaleno [94], entre otros. Tras la polimerización y carbonización de dichos precursores carbonosos, la plantilla de sílice se elimina utilizando, comúnmente, HF [67,93].

Los materiales carbonosos sintetizados utilizando este tipo de materiales «duros» como plantilla presentan tamaños de poro entre 2 y 10 nm. Cabe destacar, sin embargo, que la carbonización del propio precursor carbonoso puede conducir a la aparición de microporosidad [99]. Además, se puede generar microporosidad en el carbón mesoporoso nanomoldeado llevando a cabo una etapa posterior de activación (por ejemplo, activación química con KOH) [90,100]. Por otro lado, pueden formarse materiales nanomoldeados con poros de mayor tamaño debido a la coalescencia de los poros no impregnados de la sílice cuando se ésta se disuelve [99].

Los materiales carbonosos mesoporosos ordenados presentan una elevada área superficial específica, entre 1200-2400 $m^2·g^{-1}$, debido, en parte, a la presencia de microporos [66,99,101,102].

Son de especial relevancia los materiales carbonosos con porosidad jerarquizada. Este tipo de materiales carbonosos no sólo hace referencia a aquellos que presentan microporosidad, debida a la propia carbonización del precursor carbonoso o introducida con procesos posteriores de activación, como se ha visto anteriormente, sino también a aquellos donde la combinación de diferentes tipos de plantilla permite la obtención de poros de diferentes tamaños (por ejemplo, el uso conjunto de polímeros como Pluronic® F127 y partículas de sílice [97]).

La funcionalización/modificación de los materiales carbonosos mesoporosos ordenados permite la obtención, por ejemplo, de materiales dopados con nitrógeno, utilizando poliacrilonitrilo como precursor carbonoso [103] o melamina [104], entre otros.

(iv) ZTC. Diferentes tipos de zeolitas se han utilizado para fabricar materiales carbonosos microporosos nanomoldeados, utilizando rutas de síntesis como: (i) depósito químico en fase vapor de propileno o acetileno [105] y (ii) combinación de los procesos de impregnación (y posterior carbonización) de alcohol furfurílico, seguido de una etapa de depósito químico en fase vapor de propileno [106] o ACN [107]. Finalmente, es necesario eliminar la plantilla de zeolita, para lo que se emplea, usualmente HF [16,105].

En concreto, los ZTC sintetizados utilizando como plantilla zeolita Y son especialmente interesantes debido a su elevada área superficial (hasta 4000 $m^2·g^{-1}$ [108,109]) y volumen de microporos [108-110], un tamaño de poro bien definido de 1,2 nm [109,111] y una estructura porosa tridimensional y ordenada [108,112] (Figura II.9). A pesar de no poseer mesoporos, los ZTC presentan un transporte de materia eficiente debido a la conexión tridimensional de la porosidad [113]. También se ha reportado la síntesis de ZTC dopados con nitrógeno [107] y con boro y nitrógeno [114].

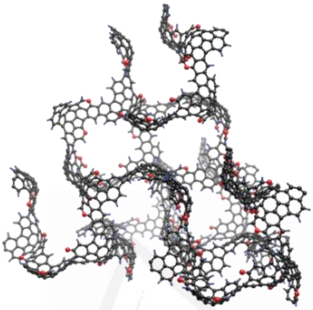

Figura II.9. Esquema de la estructura de un ZTC [73].

(v) Otros tipos de plantillas utilizadas incluyen: estructuras metal-orgánicas (MOFs) [115], MgO [116] y citrato de magnesio [117] o arcillas [118].

Cabe añadir que, en algunos trabajos, se ha realizado un post-tratamiento a elevadas temperaturas en atmósfera inerte con el objetivo de incrementar la conductividad eléctrica del material carbonoso sintetizado [67,99,106,108].

Como se ha visto, las ventajas de los procesos de nanomoldeo de materiales carbonosos son numerosas, ya que permiten la obtención de materiales carbonosos con una estructura única, uniforme y ordenada. Estos materiales carbonosos muestran una elevada área superficial específica y un elevado volumen de poros de un tamaño determinado, e incluso con porosidad jerarquizada. Por todos estos motivos, los materiales nanomoldeados se están investigando ampliamente para su uso en aplicaciones en el campo del almacenamiento de energía. Sin embargo, también presentan algunas desventajas entre las que cabe destacar el elevado coste de producción y la producción en bajas cantidades. Además, el proceso de eliminación de plantillas «duras» (por ejemplo, sílice y zeolitas) requiere el uso de HF que es un producto especialmente peligroso.

En cuanto al comportamiento electroquímico de materiales carbonosos namomoldeados se ha visto que una relación de mesoporos/microporos apropiada y la interconexión de la porosidad promueve la rápida difusión del electrolito a través de la red porosa [67,119]. Ello ha permitido que utilizando sílices mesoporosas como plantilla (por ejemplo SBA-16) se hayan sintetizado materiales carbonosos mesoporosos nanomoldeados con un área superficial específica de 1880 $m^2 \cdot g^{-1}$ y se hayan alcanzado valores de capacidad específica de: ~200 $F \cdot g^{-1}$ en medio ácido (1 M $H_2SO_4$), ~200 $F \cdot g^{-1}$ en medio básico (6M KOH) y ~110 $F \cdot g^{-1}$ en medio orgánico (1 M tetrafluoroborato de tetraetilamonio en ACN) [67]. Se han sintetizado materiales carbonosos con porosidad jerarquizada y dopados con nitrógeno, con un área superficial específica de 2255 $m^2 \cdot g^{-1}$ que, además de mostrar valores de capacidad específica en medio 6 M KOH tan elevados como 258 $F \cdot g^{-1}$, muestran un excelente comportamiento electroquímico a elevadas densidades de corriente y velocidades de barrido, debido, precisamente, a la adecuada proporción entre micro y mesoporosidad y a la interconexión de la red porosa [104]. En el caso del ZTC se han reportado valores de capacidad específica en medio 1 M $H_2SO_4$ extremadamente altos (~500 $F \cdot g^{-1}$) [112] debido, no sólo a la estructura microporosa ordenada tridimensional que presenta, sino también a la contribución de la pseudocapacidad derivada de los grupos oxigenados que se generan en los bordes de las láminas grafénicas que lo componen [108,112].

### II.4.3. Contribución de la química superficial

La química superficial de los materiales carbonosos juega un papel importante en sus propiedades físico-químicas y, por tanto, determina en gran medida las posibles aplicaciones de los mismos. La química superficial está definida por la presencia de distintos heteroátomos formando diferentes grupos funcionales en la superficie del material carbonoso y, en particular, en los bordes de los planos basales. Los heteroátomos que se encuentran más frecuentemente son oxígeno y nitrógeno, aunque también es posible encontrar fósforo, azufre o boro, entre otros. Estos heteroátomos pueden ser introducidos a través de tratamientos durante la síntesis de los materiales carbonosos o bien por medio de tratamientos posteriores, aunque también pueden ser inherentes a los mismos (por ejemplo, los bordes de los planos de la estructura de los materiales carbonosos presentan una fuerte propensión a quimisorber oxígeno y este oxígeno molecular quimisorbido puede disociarse en átomos que reaccionen químicamente con átomos de carbono para formar compuestos oxigenados superficiales).

La investigación sobre materiales carbonosos para su uso como electrodos en supercondensadores ha prestado especial atención al papel de la química superficial. Como se ha visto anteriormente, el almacenamiento de energía en materiales carbonosos puede producirse a través de procesos capacitivos (formación de la doble capa eléctrica) y que dependen, por tanto, de la textura porosa del material, pero también a través de procesos farádicos (es decir, reacciones redox entre el electrodo y el electrolito), lo que estaría directamente relacionado con el tipo y cantidad de grupos superficiales que presente el material carbonoso. Además de contribuir a la capacidad del material (a través de la pseudocapacidad), los grupos superficiales producen un aumento de la mojabilidad del material y, por tanto, un incremento del área accesible al electrolito [23,24]. No obstante, pueden producir efectos no deseados como reducción de la estabilidad del material y disminución de la conductividad eléctrica [120] además de promover la descomposición del electrolito [32,121].

### II.4.3.1. Grupos funcionales oxigenados

Tradicionalmente, los grupos superficiales oxigenados están divididos en dos grupos dependiendo de la naturaleza ácida y básica (o neutra) de los mismos [122]. En esta clasificación, los grupos carboxílicos, anhídridos y lactonas corresponden a grupos ácidos, mientras que los fenoles, quinonas, carbonilos y éteres son considerados grupos ligeramente básicos. En la Figura II.10 se presenta un esquema de una lámina de grafeno con los grupos superficiales oxigenados más frecuentes, además se incluyen sitios activos, como radicales en borde o centro de lámina o enlaces tipo carbino en borde de lámina, que son también de notable importancia cuando se analiza la química superficial de los materiales carbonosos [123]

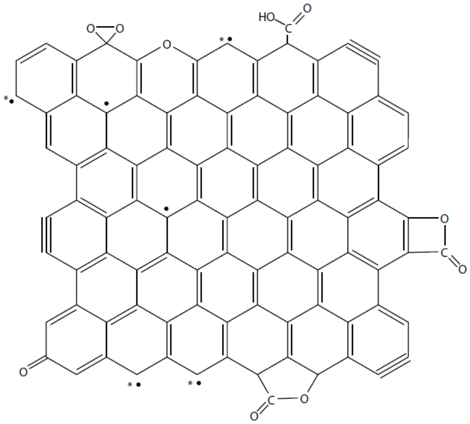

Figura II.10.Sitios activos y grupos funcionales oxigenados más frecuentes representados en una lámina grafénica. Adaptado de [123].

Como ya se ha dicho, los motivos más importantes por los que los grupos funcionales oxigenados pueden tener un efecto positivo en el comportamiento de un material carbonoso como electrodo en supercondensadores son el aumento de la mojabilidad y la contribución a la pseudocapadidad [23,112]. En concreto, se ha visto que existe una buena correlación entre la capacidad mostrada por el material carbonoso en medio acuoso y el número de grupos oxigenados superficiales que desorben como CO [23].

El efecto de los grupos superficiales en la capacidad depende, además, del pH del medio en el que se realice el proceso, ya que los mecanismos reversibles de oxidación-reducción implican el intercambio de protones. Se ha visto que en medio básico, la contribución farádica de este tipo de grupos es mucho menor que en medio ácido [124].

En concreto, la química superficial de los carbones activados viene determinada tanto por el precursor carbonoso como por las condiciones de activación. Se ha visto que la activación química con KOH produce mayor cantidad de grupos oxigenados que la activación química con NaOH y que la activación física con $CO_2$ [23]. Además, el tipo y cantidad de grupos oxigenados puede variarse con diferentes tratamientos posteriores como: (i) oxidación con ácidos oxidantes, como $HNO_3$ (que permite generar gran cantidad de grupos oxigenados) y posterior tratamiento térmico con $N_2$ (para eliminar parte de los grupos oxigenados creados) o (ii) tratamiento térmico con $H_2$ (que permite eliminar gran parte de los grupos oxigenados que se producen como consecuencia del propio proceso de activación) y posterior oxidación en aire (para introducir algunos grupos oxigenados) [23].

El contenido de grupos oxigenados superficiales de materiales carbonosos nanomoldeados viene determinado por el precursor carbonoso, el método de síntesis, así como por la propia nanoestructura final del material sintetizado.

### II.4.3.2. Grupos funcionales nitrogenados

El nitrógeno es uno de los heteroátomos, junto con el oxígeno, que se encuentra más frecuentemente en la superficie de los materiales carbonosos. En general, el nitrógeno puede encontrarse enlazado a uno (grupo amino) o dos (grupos piridínicos y pirrólicos) átomos de carbono y pueden también sustituir un átomo de carbono del centro de la lámina grafénica (nitrógeno cuaternario) [125,126]. También existen grupos funcionales nitrogenados que involucran funcionalidades oxigenadas (grupos piridonas). En la Figura II.11 se presentan los diferentes grupos funcionales nitrogenados que se pueden generar en la superficie de los materiales carbonosos.

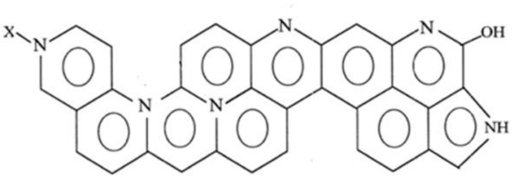

Figura II.11. Grupos funcionales nitrogenados más frecuentes representados en una lámina grafénica. Adaptado de [127].

Los grupos funcionales nitrogenados pueden aumentar el carácter básico del material carbonoso. Estos grupos funcionales tienen una contribución importante en aplicaciones energéticas ya que pueden incrementar la capacidad del material por fenómenos de pseudocapacidad, mejorar la mojabilidad, facilitar los procesos de transferencia electrónica y elevar la estabilidad del material carbonoso [49,128-131].

Las funcionalidades nitrogenadas pueden generarse en la superficie de los materiales carbonosos mediante el uso de diversos métodos, como [49,50,126,129-131]: (i) carbonización seguida, o no, de activación química o activación física de un material rico en nitrógeno, por ejemplo, materiales poliméricos como melamina, poliacrilonitrilo, polipirrol, etc.; (ii) reacción entre un compuesto nitrogenado (amoníaco, urea, etc.) y un material carbonoso poroso; (iii) carbonización hidrotérmica de un precursor adecuado como, por ejemplo, glucosamina; y (iv) conversión de los grupos funcionales carboxilos en grupos amida.

## Referencias

[1] Miller JR, Simon P. Materials science - Electrochemical capacitors for energy management. Science 2008;321:651-2.

[2] Conway BE. Electrochemical supercapacitors. New York: Plenum Publishers, 1999.

[3] Winter M, Brodd RJ. What are batteries, fuel cells, and supercapacitors? Chem Rev 2004;104:4245-70.

[4] Zhang LL, Zhao XS. Carbon-based materials as supercapacitor electrodes. Chem Soc Rev 2009;38:2520-31.

[5] Subramaniam C, Maiyalagan T. Double layer energy storage in graphene-a study. Micro and Nanosystems 2012;4:180-5.

[6] Hamann CH, Hamnett A, Vielstich W. Electrochemistry. 2nd ed. Toronto: Wiley-VCH, 1998.

[7] Yu A, Chabot V, Zhang J. Electrochemical supercapacitors for energy storage and delivery: fundamentals and applications. New York: CRC Press, 2013.

[8] Pandolfo A, Hollenkamp A. Carbon properties and their role in supercapacitors. J Power Sources 2006;157:11-27.

[9] Kotz R, Carlen M. Principles and applications of electrochemical capacitors. Electrochim Acta 2000;45:2483-98.

[10] Atkins P. Physical chemistry. 6th ed. Oxford: Oxford University Press, 1998.

[11] Bertrán J, Núñez J. Química física. Barcelona: Ariel, 2002.

[12] Hu L, Choi JW, Yang Y, Jeong S, La Mantia F, Cui LF et al. Highly conductive paper for energy-storage devices. Proc Natl Acad Sci U S A 2009;106:21490-4.

[13] Chen Q, Xue K, Shen W, Tao F, Yin S, Xu W. Fabrication and electrochemical properties of carbon nanotube array electrode for supercapacitors. Electrochim Acta 2004;49:4157-61.

[14] Sherrill SA, Banerjee P, Rubloff GW, Lee SB. High to ultra-high power electrical energy storage. Phys Chem Chem Phys 2011;13:20714-23.

[15] Jiang H, Lee PS, Li C. 3D carbon based nanostructures for advanced supercapacitors. Energ Environ Sci 2013;6:41-53.

[16] Berenguer-Murcia A, Ruiz-Rosas RR, Garcia-Aguilar J, Nueangnoraj K, Nishihara H, Morallon E et al. Binderless thin films of zeolite-templated carbon electrodes useful for electrochemical microcapacitors with ultrahigh rate performance. Phys Chem Chem Phys 2013;15:10331-4.

[17] Leyva-García S, Lozano-Castelló D, Morallón E, Cazorla-Amorós D. Silica-templated ordered mesoporous carbon thin films as electrodes for micro-capacitors. J Mater Chem A 2016;4:4570-9.

[18] Shiraishi S, Yukiko E, Onda K, Tsukada H. Electric double layer capacitor using seamless activated carbon electrode. Carbon2013 Extended Abstracts 2013.

[19] Béguin F, Raymundo-Piñero E, Frackowiak E. Electrical double-layer capacitors and pseudocapacitors. In: Béguin F, Frackowiak E, editors. Carbons for electrochemical energy storage and conversion systems, Boca Raton (USA): CRC Press,Taylor & Francis Group; 2010, p. 329.

[20] Frackowiak E, Béguin F. Carbon materials for the electrochemical storage of energy in capacitors. Carbon 2001;39:937-50.

[21] Béguin F, Presser V, Balducci A, Frackowiak E. Carbons and electrolytes for advanced supercapacitors. Adv Mater 2014;26:2219-51.

[22] Galinski M, Lewandowski A, Stepniak I. Ionic liquids as electrolytes. Electrochim Acta 2006;51:5567-80.

[23] Bleda-Martínez MJ, Maciá-Agulló JA, Lozano-Castelló D, Morallón E, Cazorla-Amorós D, Linares-Solano A. Role of surface chemistry on electric double layer capacitance of carbon materials. Carbon 2005;43:2677-84.

[24] Lozano-Castelló D, Cazorla-Amorós D, Linares-Solano A, Shiraishi S, Kurihara H, Oya A. Influence of pore structure and surface chemistry

on electric double layer capacitance in non-aqueous electrolyte. Carbon 2003;41:1765-75.

[25] Inagaki M, Konno H, Tanaike O. Carbon materials for electrochemical capacitors. J Power Sources 2010;195:7880-903.

[26] Salitra G, Soffer A, Eliad L, Cohen Y, Aurbach D. Carbon electrodes for double layer capacitors I. Relations between ion and pore dimensions. J Electrochem Soc 2000;147:2486-93.

[27] Snook GA, Wilson GJ, Pandolfo AG. Mathematical functions for optimisation of conducting polymer/activated carbon asymmetric supercapacitors. J Power Sources 2009;186:216-23.

[28] Bleda-Martínez MJ, Lozano-Castelló D, Cazorla-Amorós D, Morallón E. Kinetics of double-layer formation: influence of porous structure and pore size distribution. Energ Fuel 2010;24:3378-84.

[29] Khomenko V, Raymundo-Pinero E, Frackowiak E, Béguin F. High-voltage asymmetric supercapacitors operating in aqueous electrolyte. Appl Phys A:Mater Sci Process 2006;82:567-73.

[30] Demarconnay L, Raymundo-Piñero E, Béguin F. A symmetric carbon/carbon supercapacitor operating at 1.6 V by using a neutral aqueous solution. Electrochem Commun 2010;12:1275-8.

[31] Fic K, Lota G, Meller M, Frackowiak E. Novel insight into neutral medium as electrolyte for high-voltage supercapacitors. Energ Environ Sci 2012;5:5842-50.

[32] Cazorla-Amorós D, Lozano-Castelló D, Morallón E, Bleda-Martínez MJ, Linares-Solano A, Shiraishi S. Measuring cycle efficiency and capacitance of chemically activated carbons in propylene carbonate. Carbon 2010;48:1451-6.

[33] Azais P, Duclaux L, Florian P, Massiot D, Lillo-Ródenas M, Linares-Solano A et al. Causes of supercapacitors ageing in organic electrolyte. J Power Sources 2007;171:1046-53.

[34] Brandt A, Pohlmann S, Varzi A, Balducci A, Passerini S. Ionic liquids in supercapacitors. MRS Bull 2013;38:554-9.

[35] Pohlmann S, Lobato B, Centeno TA, Balducci A. The influence of pore size and surface area of activated carbons on the performance of ionic liquid based supercapacitors. Phys Chem Chem Phys 2013;15:17287-94.

[36] Simon P, Gogotsi Y. Materials for electrochemical capacitors. Nat Mater 2008;7:845-54.

[37] Huang P, Pech D, Lin R, McDonough JK, Brunet M, Taberna P et al. On-chip micro-supercapacitors for operation in a wide temperature range. Electrochem Commun 2013;36:53-6.

[38] Kado Y, Imoto K, Soneda Y, Yoshizawa N. Highly enhanced capacitance of MgO-templated mesoporous carbons in low temperature ionic liquids. J Power Sources 2014;271:377-81.

[39] Yoo JJ, Balakrishnan K, Huang J, Meunier V, Sumpter BG, Srivastava A et al. Ultrathin planar graphene supercapacitors. Nano Lett 2011;11:1423-7.

[40] Pech D, Brunet M, Taberna P, Simon P, Fabre N, Mesnilgrente F et al. Elaboration of a microstructured inkjet-printed carbon electrochemical capacitor. J Power Sources 2010;195:1266-9.

[41] Kaempgen M, Chan CK, Ma J, Cui Y, Gruner G. Printable thin film supercapacitors using single-walled carbon nanotubes. Nano Lett 2009;9:1872-6.

[42] Thissandier F, Pauc N, Brousse T, Gentile P, Sadki S. Micro-ultracapacitors with highly doped silicon nanowires electrodes. Nanoscale Res Lett 2013;8:1-5.

[43] Sun W, Zheng R, Chen X. Symmetric redox supercapacitor based on micro-fabrication with three-dimensional polypyrrole electrodes. J Power Sources 2010;195:7120-5.

[44] Makino S, Yamauchi Y, Sugimoto W. Synthesis of electro-deposited ordered mesoporous RuOx using lyotropic liquid crystal and application toward micro-supercapacitors. J Power Sources 2013;227:153-60.

[45] Beidaghi M, Wang C. Micro-supercapacitors based on interdigital electrodes of reduced graphene oxide and carbon nanotube composites

with ultrahigh power handling performance. Adv Func Mater 2012;22:4501-10.

[46] Pech D, Brunet M, Durou H, Huang P, Mochalin V, Gogotsi Y et al. Ultrahigh-power micrometre-sized supercapacitors based on onion-like carbon. Nat Nanotechnol 2010;5:651-4.

[47] Nam I, Kim G, Park S, Park J, Kim ND, Yi J. Fabrication and design equation of film-type large-scale interdigitated supercapacitor chips. Nanoscale 2012;4:7350-3.

[48] Zhang LL, Lei Z, Zhang J, Tian X, Zhao XS. Supercapacitors: electrode materials aspects. In: Crabtree RH, editor. Energy production and storage. Inorganic chemical strategies for a warming world, New Haven: John Wiley & Sons; 2010, p. 341.

[49] Salinas-Torres D, Shiraishi S, Morallón E, Cazorla-Amorós D. Improvement of carbon materials performance by nitrogen functional groups in electrochemical capacitors in organic electrolyte at severe conditions. Carbon 2015;82:205-13.

[50] Mostazo-Lopez MJ, Ruiz-Rosas R, Morallón E, Cazorla-Amorós D. Generation of nitrogen functionalities on activated carbons by amidation reactions and Hofmann rearrangement: Chemical and electrochemical characterization. Carbon 2015;91:252-65.

[51] Demarconnay L, Raymundo-Piñero E, Béguin F. Highly effective hydrogen sorption on graphene edge planes through electroreduction of aqueous electrolytes. 2010:1-2.

[52] Vix-Guterl C, Frackowiak E, Jurewicz K, Friebe M, Parmentier J, Béguin F. Electrochemical energy storage in ordered porous carbon materials. Carbon 2005;43:1293-302.

[53] Jurewicz K, Frackowiak E, Béguin F. Towards the mechanism of electrochemical hydrogen storage in nanostructured carbon materials. Appl Phys A 2004;78:981-7.

[54] Béguin F, Friebe M, Jurewicz K, Vix-Guterl C, Dentzer J, Frackowiak E. State of hydrogen electrochemically stored using nanoporous carbons as negative electrode materials in an aqueous medium. Carbon 2006;44:2392-8.

[55] Lota G, Fic K, Jurewicz K, Frackowiak E. Correlation of hydrogen capacity in carbon material with the parameters of electrosorption. Cent Eur J Chem 2011;9:20-4.

[56] Bleda-Martínez MJ, Pérez JM, Linares-Solano A, Morallón E, Cazorla-Amorós D. Effect of surface chemistry on electrochemical storage of hydrogen in porous carbon materials. Carbon 2008;46:1053-9.

[57] Béguin F, Kierzek K, Friebe M, Jankowska A, Machnikowski J, Jurewicz K et al. Effect of various porous nanotextures on the reversible electrochemical sorption of hydrogen in activated carbons. Electrochim Acta 2006;51:2161-7.

[58] Barbieri O, Hahn M, Herzog A, Kotz R. Capacitance limits of high surface area activated carbons for double layer capacitors. Carbon 2005;43:1303-10.

[59] Stoller MD, Magnuson CW, Zhu Y, Murali S, Suk JW, Piner R et al. Interfacial capacitance of single layer graphene. Energy Environ Sci 2011;4:4685-9.

[60] Sing KSW, Everett DH, Haul RAW, Moscou L, Pierotti RA, Rouquerol J et al. Reporting physisorption data for gas solid systems with special reference to the determination of surface-area and porosity. Pure Appl Chem 1985;57(4):603-19.

[61] Liu M, Qian J, Zhao Y, Zhu D, Gan L, Chen L. Core-shell ultramicroporous@microporous carbon nanospheres as advanced supercapacitor electrodes. J Mater Chem A 2015;3:11517-26.

[62] Zhao Y, Liu M, Deng X, Miao L, Tripathi PK, Ma X et al. Nitrogen-functionalized microporous carbon nanoparticles for high performance supercapacitor electrode. Electrochim Acta 2015;153:448-55.

[63] Zhao Y, Liu M, Gan L, Ma X, Zhu D, Xu Z et al. Ultramicroporous carbon nanoparticles for the high-performance electrical double-layer capacitor electrode. Energ Fuel 2014;28:1561-8.

[64] Largeot C, Portet C, Chmiola J, Taberna P, Gogotsi Y, Simon P. Relation between the ion size and pore size for an electric double-layer capacitor. J Am Chem Soc 2008;130:2730.

[65] Chmiola J, Yushin G, Gogotsi Y, Portet C, Simon P, Taberna PL. Anomalous increase in carbon capacitance at pore sizes less than 1 nanometer. Science 2006;313:1760-3.

[66] Liu H, Wang K, Teng H. A simplified preparation of mesoporous carbon and the examination of the carbon accessibility for electric double layer formation. Carbon 2005;43:559-66.

[67] Fuertes A, Lota G, Centeno T, Frackowiak E. Templated mesoporous carbons for supercapacitor application. Electrochim Acta 2005;50:2799-805.

[68] Kim K, Choi M, Ryoo R. Ethanol-based synthesis of hierarchically porous carbon using nanocrystalline beta zeolite template for high-rate electrical double layer capacitor. Carbon 2013;60:175-85.

[69] Yoon S, Lee J, Hyeon T, Oh SM. Electric double-layer capacitor performance of a new mesoporous carbon. J Electrochem Soc 2000;147:2507-12.

[70] Shiraishi S, Kurihara H, Shi L, Nakayama T, Oya A. Electric double-layer capacitance of meso/macroporous activated carbon fibers prepared by the blending method - I. Nickel-loaded activated carbon fibers in propylene carbonate solution containing $LiClO_4$ salt. J Electrochem Soc 2002;149:A855-61.

[71] Eliad L, Salitra G, Soffer A, Aurbach D. Ion sieving effects in the electrical double layer of porous carbon electrodes: Estimating effective ion size in electrolytic solutions. J Phys Chem B 2001;105:6880-7.

[72] Li Y, Fu Z, Su B. Hierarchically structured porous materials for energy conversion and storage. Adv Funct Mater 2012;22:4634-67.

[73] Nishihara H, Kyotani T. Templated nanocarbons for energy storage. Adv Mater 2012;24:4473-98.

[74] Reinoso Rodríguez F. Activated carbon: structure, characterization, preparation and applications. In: Marsh H, Heintz EA, Reinoso Rodríguez F, editors. Introduction to carbon technologies, Alicante (España): Universidad de Alicante; 1997, p. 35-102.

[75] Bleda-Martínez MJ, Lozano-Castelló D, Morallón E, Cazorla-Amorós D, Linares-Solano A. Chemical and electrochemical characterization of porous carbon materials. Carbon 2006;44:2642-51.

[76] Linares-Solano A, Lozano-Castelló D, Lillo-Ródenas MA, Cazorla-Amorós D. Carbon activation by alkaline hydroxides: preparation and reactions, porosity and performance. In: Radovic L, editor. Chemistry and physics of carbon, Boca Raton (USA): CRC Press-Taylor & Francis Group; 2008, p. 1-62.

[77] Ioannidou O, Zabaniotou A. Agricultural residues as precursors for activated carbon production-A review. Renewable and Sustainable Energy Reviews 2007;11:1966-2005.

[78] Maciá-Agulló JA, Moore BC, Cazorla-Amorós D, Linares-Solano A. Activation of coal tar pitch carbon fibres: Physical activation vs. chemical activation. Carbon 2004;42:1367-70.

[79] Ahmadpour A, Do DD. The preparation of active carbons from coal by chemical and physical activation. Carbon 1996;34:471-9.

[80] Lozano-Castelló D, Lillo-Ródenas MA, Cazorla-Amorós D, Linares-Solano A. Preparation of activated carbons from Spanish anthracite: I. Activation by KOH. Carbon 2001;39:741-9.

[81] Molina-Sabio M, RodRíguez-Reinoso F, Caturla F, Sellés MJ. Porosity in granular carbons activated with phosphoric acid. Carbon 1995;33:1105-13.

[82] Romero-Anaya AJ, Molina A, Garcia P, Ruiz-Colorado AA, Linares-Solano A, Salinas-Martínez de Lecea C. Phosphoric acid activation of recalcitrant biomass originated in ethanol production from banana plants. Biomass Bioenergy 2011;35:1196-204.

[83] Caturla F, Molina-Sabio M, Rodríguez-Reinoso F. Preparation of activated carbon by chemical activation with $ZnCl_2$. Carbon 1991;29:999-1007.

[84] Lillo-Ródenas MA, Lozano-Castelló D, Cazorla-Amorós D, Linares-Solano A. Preparation of activated carbons from Spanish anthracite: II. Activation by NaOH. Carbon 2001;39:751-9.

[85] Lee J, Kim J, Hyeon T. Recent progress in the synthesis of porous carbon materials. Adv Mater 2006;18:2073-94.

[86] Kyotani T, Tsai L, Tomita A. Preparation of ultrafine carbon tubes in nanochannels of an anodic aluminum oxide film. Chem Mat 1996;8:2109-13.

[87] Kaixue Wang, Birjukovs P, Erts D, Phelan R, Morris MA, Haoshen Zhou et al. Synthesis and characterisation of ordered arrays of mesoporous carbon nanofibres. Journal of Materials Chemistry 2009;19:1331-8.

[88] Woo S, Dokko K, Nakano H, Kanamura K. Preparation of three dimensionally ordered macroporous carbon with mesoporous walls for electric double-layer capacitors. J Mater Chem 2008;18:1674-80.

[89] Deng Y, Liu C, Yu T, Liu F, Zhang F, Wan Y et al. Facile synthesis of hierarchically porous carbons from dual colloidal crystal/block copolymer template approach. Chem Mat 2007;19:3271-7.

[90] Gorka J, Zawislak A, Choma J, Jaroniec M. Adsorption and structural properties of soft-templated mesoporous carbons obtained by carbonization at different temperatures and KOH activation. Appl Surf Sci 2010;256:5187-90.

[91] Lee J, Yoon S, Hyeon T, Oh S, Kim K. Synthesis of a new mesoporous carbon and its application to electrochemical double-layer capacitors. Chem Commun 1999:2177-8.

[92] Jun S, Joo S, Ryoo R, Kruk M, Jaroniec M, Liu Z et al. Synthesis of new, nanoporous carbon with hexagonally ordered mesostructure. J Am Chem Soc 2000;122:10712-3.

[93] Xia K, Gao Q, Jiang J, Hu J. Hierarchical porous carbons with controlled micropores and mesopores for supercapacitor electrode materials. Carbon 2008;46:1718-26.

[94] Nishihara H, Fukuraa Y, Inde K, Tsuji K, Takeuchi M, Kyotani T. Carbon-coated mesoporous silica with hydrophobicity and electrical conductivity. Carbon 2008;46:48-53.

[95] Joo S, Jun S, Ryoo R. Synthesis of ordered mesoporous carbon molecular sieves CMK-1. Micropor Mesopor Mat 2001;44:153-8.

[96] Fuertes A, Nevskaia D. Control of mesoporous structure of carbons synthesised using a mesostructured silica as template. Micropor Mesopor Mat 2003;62:177-90.

[97] Gorka J, Jaroniec M. Hierarchically porous phenolic resin-based carbons obtained by block copolymer-colloidal silica templating and post-synthesis activation with carbon dioxide and water vapor. Carbon 2011;49:154-60.

[98] Meng Y, Gu D, Zhang F, Shi Y, Yang H, Li Z et al. Ordered mesoporous polymers and homologous carbon frameworks: Amphiphilic surfactant templating and direct transformation. Angew Chem -Int Edit 2005;44:7053-9.

[99] Fuertes A, Pico F, Rojo J. Influence of pore structure on electric double-layer capacitance of template mesoporous carbons. J Power Sources 2004;133:329-36.

[100] Górka J, Zawislak A, Choma J, Jaroniec M. KOH activation of mesoporous carbons obtained by soft-templating. Carbon 2008;46:1159-61.

[101] Gadiou R, Saadallah S, Piquero T, David P, Parmentier J, Vix-Guterl C. The influence of textural properties on the adsorption of hydrogen on ordered nanostructured carbons. Micropor Mesopor Mat 2005;79:121-8.

[102] Xing W, Qiao SZ, Ding RG, Li F, Lu GQ, Yan ZF et al. Superior electric double layer capacitors using ordered mesoporous carbons. Carbon 2006;44:216-24.

[103] Lu A, Kiefer A, Schmidt W, Schuth F. Synthesis of polyacrylonitrile-based ordered mesoporous carbon with tunable pore structures. Chem Mat 2004;16:100-3.

[104] Wang G, Zhang J, Kuang S, Zhou J, Xing W, Zhuo S. Nitrogen-doped hierarchical porous carbon as an efficient electrode material for supercapacitors. Electrochim Acta 2015;153:273-9.

[105] Hou P, Yamazaki T, Orikasa H, Kyotani T. An easy method for the synthesis of ordered microporous carbons by the template technique. Carbon 2005;43:2624-7.

[106] Kyotani T, Ma Z, Tomita A. Template synthesis of novel porous carbons using various types of zeolites. Carbon 2003;41:1451-9.

[107] Hou P, Orikasa H, Yamazaki T, Matsuoka K, Tomita A, Setoyama N et al. Synthesis of nitrogen-containing microporous carbon with a highly ordered structure and effect of nitrogen doping on $H_2O$ adsorption. Chem Mat 2005;17:5187-93.

[108] Nishihara H, Yang Q, Hou P, Unno M, Yamauchi S, Saito R et al. A possible buckybowl-like structure of zeolite templated carbon. Carbon 2009;47:1220-30.

[109] Matsuoka K, Yamagishi Y, Yamazaki T, Setoyama N, Tomita A, Kyotani T. Extremely high microporosity and sharp pore size distribution of a large surface area carbon prepared in the nanochannels of zeolite Y. Carbon 2005;43:876-9.

[110] Ma Z, Kyotani T, Tomita A. Synthesis methods for preparing microporous carbons with a structural regularity of zeolite Y. Carbon 2002;40:2367-74.

[111] Nishihara H, Itoi H, Kogure T, Hou P, Touhara H, Okino F et al. Investigation of the ion storage/transfer behavior in an electrical double-layer capacitor by using ordered microporous carbons as model materials. Chem Eur J 2009;15:5355-63.

[112] Itoi H, Nishihara H, Ishii T, Nueangnoraj K, Berenguer-Betrián R, Kyotani T. Large pseudocapacitance in quinone-functionalized zeolite-templated carbon. Bull Chem Soc Jpn 2014;87:250-7.

[113] Itoi H, Nishihara H, Kogure T, Kyotani T. Three-dimensionally arrayed and mutually connected 1.2-nm nanopores for high-performance electric double layer capacitor. J Am Chem Soc 2011;133:1165-7.

[114] Wang L, Yang FH, Yang RT. Hydrogen storage properties of B- and N-doped microporous carbon. J Phys Chem C 2009;55:1823-33.

[115] Liu B, Shioyama H, Akita T, Xu Q. Metal-organic framework as a template for porous carbon synthesis. J Am Chem Soc 2008;130:5390.

[116] Morishita T, Soneda Y, Tsumura T, Inagaki M. Preparation of porous carbons from thermoplastic precursors and their performance for electric double layer capacitors. Carbon 2006;44:2360-7.

[117] Soneda Y, Kodama M. Effect of mesopore in MgO templated mesoporous carbon electrode on capacitor performance. Electrochemistry 2013;81:845-8.

[118] Meyers C, Shah S, Patel S, Sneeringer R, Bessel C, Dollahon N et al. Templated synthesis of carbon materials from zeolites (Y, beta, and ZSM-5) and a montmorillonite clay (K10): Physical and electrochemical characterization. J Phys Chem B 2001;105:2143-52.

[119] Jurewicz K, Vix-Guterl C, Frackowiak E, Saadallah S, Reda M, Parmentier J et al. Capacitance properties of ordered porous carbon materials prepared by a templating procedure. J Phys Chem Solids 2004;65:287-93.

[120] Pantea D, Darmstadt H, Kaliaguine S, Summchen L, Roy C. Electrical conductivity of thermal carbon blacks. Influence of surface chemistry. Carbon 2001;39:1147-58.

[121] Zhai Y, Dou Y, Zhao D, Fulvio PF, Mayes RT, Dai S. Carbon Materials for Chemical Capacitive Energy Storage. Adv Mater 2011;23:4828-50.

[122] Boehm H. Some Aspects of the Surface-Chemistry of Carbon-Blacks and Other Carbons. Carbon 1994;32:759-69.

[123] Radovic LR. Surface chemical and electrochemical properties of carbons. In: Beguin F, Frackowiak E, editors. Carbons for electrochemical energy storage and conversion systems, Boca Raton, US: CRC Press Taylor & Francis Group; 2010, p. 163-220.

[124] Andreas HA, Conway BE. Examination of the double-layer capacitance of an high specific-area C-cloth electrode as titrated from acidic to alkaline pHs. Electrochim Acta 2006;51:6510-20.

[125] Biniak S, Szymański G, Siedlewski J, Świtkowski A. The characterization of activated carbons with oxygen and nitrogen surface groups. Carbon 1997;35:1799-810.

[126] Raymundo-Piñero E, Cazorla-Amorós D, Linares-Solano A, Find J, Wild U, Schlögl R. Structural characterization of N-containing activated carbon fibers prepared from a low softening point petroleum pitch and a melamine resin. Carbon 2002;40:597-608.

[127] Salinas-Torres D, Ornelas O, Ruiz-Rosas R, Cazorla-Amorós D, Morallón E. Almacenamiento de energía eléctrica en materiales carbonosos. In: Álvarez Merino MA, Carrasco Marín F, Maldonado Hódar FJ, editors. Desarrollo y aplicaciones de materiales avanzados de carbón, Sevilla: Universidad Internacional de Andalucía; 2014, p. 325-368.

[128] Jeong HM, Lee JW, Shin WH, Choi YJ, Shin HJ, Kang JK et al. Nitrogen-doped graphene for high-performance ultracapacitors and the importance of nitrogen-doped sites at basal planes. Nano Lett 2011;11:2472-7.

[129] Shen W, Fan W. Nitrogen-containing porous carbons: synthesis and application. J Mater Chem A 2013;1:999-1013.

[130] Chen L, Zhang X, Liang H, Kong M, Guan Q, Chen P et al. Synthesis of nitrogen-doped porous carbon nanofibers as an efficient electrode material for supercapacitors. ACS Nano 2012;6:7092-102.

[131] Zhao L, Fan L, Zhou M, Guan H, Qiao S, Antonietti M et al. Nitrogen-containing hydrothermal carbons with superior performance in supercapacitors. Adv Mater 2010;22:5202.

# Capítulo III

## Experimental

## III.1. Introducción

En este capítulo se presentan: (i) los materiales carbonosos utilizados (tanto comerciales como sintetizados); y (ii) los fundamentos de las técnicas de caracterización empleadas. Los detalles de la síntesis de los materiales carbonosos y de los electrodos basados en éstos, así como de las condiciones experimentales específicas empleadas en la caracterización, se incluyen en los capítulos donde se presentan los resultados correspondientes.

## III.2. Materiales

### III.2.1. Materiales comerciales

En la presente Tesis Doctoral se han utilizado dos carbones activados comerciales, cuya caracterización se presenta a continuación.

**(i) MWV-E510A** producido por MeadWestvaco. Es un carbón activado sintetizado por activación química de madera con $H_3PO_4$. Los resultados de caracterización de textura porosa y química superficial se muestran en la Tabla III.1.

Tabla III.1. Textura porosa y química superficial del carbón activado MWV-E510A.

| $S_{BET}$ ($m^2$ $g^{-1}$) | $V_{DR}(N_2)$ ($cm^3$ $g^{-1}$) | $V_{DR}(CO_2)$ ($cm^3$ $g^{-1}$) | µmolCO $g^{-1}$ | µmol$CO_2$ $g^{-1}$ | µmolO $g^{-1}$ [a] |
|---|---|---|---|---|---|
| 2240 | 0,79 | 0,83 | 460 | 160 | 780 |

[a] µmolO $g^{-1}$ = µmolCO $g^{-1}$ + 2 · µmol$CO_2$ $g^{-1}$

**(ii) DLC Super 30** producido por NORIT. Es un carbón activado sintetizado a partir de residuos lignocelulósicos mediante activación física con vapor de agua. En la Tabla III.2 se muestran los resultados de la caracterización de textura porosa y química superficial.

Tabla III.2. Textura porosa y química superficial del carbón activado DLC Super 30.

| $S_{BET}$ ($m^2$ $g^{-1}$) | $L_0$ [b] (nm) | $S_{DR}$ ($N_2$) ($m^2$ $g^{-1}$) | μmolO $g^{-1}$ |
|---|---|---|---|
| 1618 | 1,24 | 977 | 540 |

[b] Tamaño medio de microporos

### III.2.2. Materiales sintetizados

Los materiales que se han sintetizado para ser utilizados en la presente Tesis Doctoral se presentan a continuación.

**(i) ANK3**. Es un carbón activado químicamente utilizando una antracita española como precursor carbonoso y KOH como agente activante. El grupo de investigación Materiales Carbonosos y Medio Ambiente cuenta con una amplia experiencia en la preparación y caracterización de carbones activados a partir de distintos precursores y con diferentes métodos de activación. El procedimiento de síntesis del ANK3 ha sido seleccionado con el objetivo de obtener un carbón activado con una textura porosa apropiada para el almacenamiento electroquímico de energía. Los detalles de preparación y caracterización de este carbón activado se presentan en los Capítulos de IV y VII.

**(ii) ZTC**. Carbón nanomoldeado con zeolita. Este carbón ha sido preparado en el Institute of Multidisciplinary Research for Advanced

Materials de la Universidad de Tohoku (Japón), bajo la coordinación del Profesor Takashi Kyotani, con quien se ha llevado a cabo un trabajo en colaboración. Los detalles de la síntesis y caracterización del ZTC se presentan en el Capítulo V.

**(iii) Películas delgadas de carbón mesoporoso y películas delgadas de material compuesto sílice/carbón.** La síntesis de las películas delgadas de carbón mesoporoso y sílice mesoporosa ha requerido un estudio sistemático previo de síntesis de sílices mesoporosas ordenadas en polvo y en forma de películas delgadas, así como de preparación de materiales carbonosos a partir de diferentes precursores carbonosos (citrato de magnesio, alcohol polivinílico, alcohol furfurílico, caramelo, sacarosa). También se ha estudiado el efecto del número de impregnaciones y tiempo de impregnación de la plantilla con el precursor carbonoso, el flujo de $N_2$ durante la carbonización, etc.

Además, se ha llevado a cabo la síntesis de carbones mesoporosos a partir de precursores como el citrato de magnesio (la formación de partículas de MgO permite la obtención de carbones mesoporosos [1]). Incluso se ha probado la posible obtención de materiales carbonosos a partir de la carbonización del surfactante utilizado para la síntesis de las sílices mesoporosas ordenadas (por ejemplo, el copolímero tribloque Pluronic® F127).

Este estudio previo ha permitido la elección de las condiciones óptimas de síntesis de las películas delgadas de material carbonoso nanoestructurado utilizando como plantilla una película delgada de sílice mesoporosa sintetizada directamente sobre un colector de corriente de grafito. Los detalles de preparación y caracterización de las películas delgadas sintetizadas se presentan en el Capítulo VI.

## III.3. Técnicas de caracterización

A continuación, se presentan los fundamentos generales de las técnicas de caracterización utilizadas en la presente Tesis Doctoral. Tal y como se ha dicho en la introducción, los detalles experimentales se incluyen en los capítulos donde se presentan los resultados correspondientes.

### III.3.1. Adsorción física de gases

La textura porosa de los materiales carbonosos determina, en gran medida, su comportamiento en diferentes aplicaciones, de ahí la importancia de su caracterización. La técnica más utilizada para ello es la adsorción física de gases o vapores [2,3].

El fenómeno de adsorción consiste en poner un sólido (adsorbente) en contacto con un gas o vapor (adsortivo), a una presión y temperatura dadas (en un recipiente cerrado). Las moléculas del gas o vapor se acumulan en la interfase, como consecuencia de las fuerzas de atracción entre el adsorbente y el adsorbato (que es como se denomina al adsortivo cuando está adsorbido), provocando una disminución de presión en el recipiente así como un «aumento» de la masa del sólido. Después de un determinado tiempo, se alcanza el equilibrio y la presión permanece, entonces, constante. La cantidad de gas o vapor adsorbido se puede calcular de forma gravimétrica (midiendo el incremento de masa del sólido) o de forma volumétrica (que, en un recipiente cerrado, se calcula indirectamente a través de la disminución de presión).

La representación de la cantidad de gas o vapor adsorbido frente a la presión absoluta (P) o a la presión relativa (P $P_0^{-1}$) permite obtener la isoterma de adsorción.

Diferentes tipos de adsorbentes y gases o vapores dan lugar a la obtención de isotermas con diferentes formas. La IUPAC ha clasificado los tipos de isotermas de adsorción-desorción física en seis grupos principales [4] (Figura III.1).

- Tipo I: isotermas características de sólidos microporosos que tienen una superficie externa relativamente pequeña.
- Tipo II: isotermas características de sólidos macroporosos o no porosos. El punto «B» es indicativo del momento en que la monocapa se ha completado y comienza la adsorción en multicapa.
- Tipo III: son isotermas poco comunes. Son características de atracciones muy débiles entre adsorbente y adsorbato.
- Tipo IV: isotermas caracterizadas por la presencia de un ciclo de histéresis, debido a la condensación capilar en los mesoporos.
- Tipo V: isotermas relacionadas con las Tipo III, es decir, también características de interacciones débiles entre el adsorbato y el adsorbente.
- Tipo VI: isotermas de sólidos que tienen una superficie no porosa uniforme.

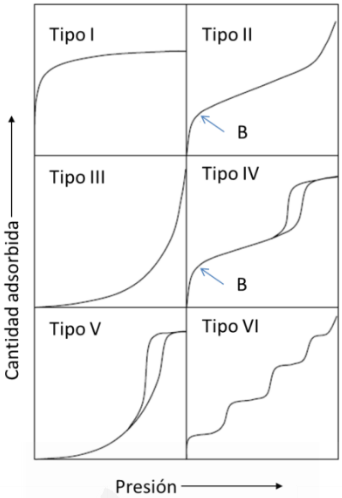

Figura III.1. Tipos de isotermas de fisisorción según la IUPAC. Adaptado de [4].

Entre los adsorbatos más utilizados se encuentran el $N_2$ y el $CO_2$, aunque también se emplean otros gases como el $CH_4$, Ar, He, etc.

La temperatura de análisis de isotermas de $N_2$ es de -196 ºC y, a esta temperatura, el $N_2$ se adsorbe en un amplio intervalo de presiones relativas (desde $10^{-8}$ hasta 1) lo que permite la adsorción en todo el intervalo de porosidad. La principal desventaja se presenta, sin embargo, en la caracterización de sólidos microporosos, ya que el $N_2$ puede presentar problemas difusionales en la microporosidad estrecha (es decir, con tamaños de poro menores a 0,7 nm); la cinética de adsorción es muy lenta por lo que el tiempo de equilibrio es muy elevado.

La realización de isotermas de adsorción de $CO_2$, tanto a 0 como a 25 ºC) es una interesante alternativa para la caracterización de la porosidad estrecha [5-7]. En este caso, y aunque las dimensiones de la molécula son similares a las dimensiones del $N_2$, la mayor temperatura usada para la realización de la isoterma de $CO_2$ resulta en una mayor energía cinética de las moléculas. La principal desventaja del uso del $CO_2$ es que, debido a que su presión de saturación es elevada a las temperaturas de análisis, sería necesario llevar a cabo la adsorción a elevadas presiones para cubrir todo el intervalo de porosidad.

La caracterización de la textura porosa de las muestras empleadas en la Tesis Doctoral se ha realizado utilizando el equipo de adsorción volumétrico Autosorb–6B de Quantachrome. El sistema consta de una unidad de desgasificación independiente donde se desgasifican las muestras a vacío y a temperatura controlada.

Las isotermas de adsorción se han analizado utilizando diferentes teorías y métodos a fin de deducir los parámetros texturales del adsorbente.

### III.3.1.1. Teoría de Brunauer–Emmett–Teller

La teoría de Brunauer–Emmett–Teller (BET) es una de las teorías de fisisorción más ampliamente utilizada para la caracterización de materiales porosos [8]. La ecuación de BET está basada en el modelo cinético de adsorción propuesto por Langmuir. Esta teoría parte del punto de que se alcanza un equilibrio dinámico en el cual la velocidad con la que las moléculas de adsortivo se condensan en los sitios vacíos es igual que la velocidad con que se evaporan de los sitios ocupados [2,8-10]. Otras asunciones en las que se basa el modelo de Langmuir son [2,8-10]: (i) sólo se puede adsorber una molécula por sitio libre del adsorbente; (ii) la superficie del sólido está formada por sitios energéticamente homogéneos; (iii) la saturación se alcanza cuando se completa la monocapa; (iv) la fuerzas (repulsivas o atractivas) entre las moléculas de adsorbato son despreciables (en comparación con las fuerzas de interacción entre el adsorbato y el adsorbente).

La teoría de BET extiende la teoría de Langmuir a la adsorción en multicapa, con la introducción de las siguientes asunciones: (i) la primera capa adsorbida es similar a la propuesta por el modelo de Langmuir; (ii) en todas las capas, excepto en la primera, el calor de adsorción es igual que el calor de licuefacción del adsortivo a la temperatura de adsorción; (iii) en todas las capas, salvo en la primera, las condiciones de evaporación-condensación son idénticas; (iv) cuando $P P_0^{-1} = 1$, el adsortivo condensa como líquido en la superficie del adsorbente (el número de capas adsorbidas es infinito).

La isoterma de adsorción según el modelo de BET se puede expresar mediante la Ecuación III.1.

$$\frac{\frac{P}{P_0}}{n\left(1-\frac{P}{P_0}\right)} = \frac{1}{n_m C} + \frac{(C-1)}{n_m C}\left(\frac{P}{P_0}\right)$$ **Ecuación III.1**

Donde $n$ y $n_m$ son la cantidad de gas adsorbido a una determinada $P P_0^{-1}$ y la cantidad de gas adsorbido en la monocapa superficial, respectivamente y $C$ es un parámetro relacionado con el calor de adsorción.

La representación gráfica del cociente $\frac{\frac{P}{P_0}}{n\left(1-\frac{P}{P_0}\right)}$ frente a $\frac{P}{P_0}$ da lugar a la obtención de una recta cuya pendiente y ordenada en el origen permiten el cálculo de los parámetros $n_m$ y $C$.

Normalmente, el intervalo de presiones relativas en el que se puede aplicar la ecuación de BET va desde 0,05 hasta 0,35 [3], aunque dicho intervalo puede variar mucho dependiendo de las características del adsorbente. La ecuación de BET no es aplicable por debajo de presiones relativas de 0,05, por la presencia de heterogeneidades superficiales, ni por encima de 0,35, debido a la posible existencia de fenómenos de condensación capilar (aspectos que no se contemplan en las bases de la teoría).

El área superficial específica del adsorbente puede calcularse a partir de los datos de adsorción. Teniendo en cuenta los moles de gas adsorbidos por gramo de adsorbente para completar una monocapa ($n_m$) se puede obtener la superficie específica del adsorbente aplicando la Ecuación III.2:

$$S = n_m \cdot a_m \cdot N_A \cdot 10^{-18}$$ **Ecuación III.2**

Donde $S$ es la superficie aparente del adsorbente ($m^2 \cdot g^{-1}$), $N_a$ es el número de Avogadro y $a_m$ es el área media ocupada por la molécula de adsorbato ($nm^2$), que en el caso del $N_2$ a -196 ºC es de 0,162 $nm^2$ [2,9,10].

### III.3.1.2. Ecuación de Dubinin–Radushkevich

La ecuación de Dubinin–Radushkevich (DR) es de las más empleadas para el análisis de materiales microporosos [11]. Esta ecuación está basada en la teoría del potencial de Polanyi, que supone la condensación del adsorbato en los microporos en capas equipotenciales [2].

La ecuación basada en el modelo de DR se puede describir como:

$$\frac{V}{V_0} = \exp\left[\frac{-1}{(E_0\beta)^2}\left(RT\ln\left(\frac{P_0}{P}\right)\right)^2\right] \quad \textbf{Ecuación III.3}$$

Donde *V* es el volumen adsorbido a una presión *P*, $V_0$ es el volumen de microporos del sólido, $E_0$ es la energía característica dependiente de la estructura del poro, $\beta$ es el coeficiente de afinidad característico del adsortivo y $P_0$ es la presión de saturación del adsortivo a la temperatura de trabajo.

La representación gráfica del $\ln V$ frente al $\ln\left(\frac{P_0}{P}\right)^2$ permite obtener el volumen de microporos ($V_0$).

En la práctica, se suele aplicar la ecuación DR a las isotermas de $N_2$ y $CO_2$ para la el cálculo del volumen total de microporos (< 2 nm) y de microporos estrechos (aproximadamente < 0,7 nm), respectivamente.

### III.3.1.3. Teoría del funcional de densidad no localizada

Aunque la teoría BET es ampliamente utilizada para el cálculo de áreas superficiales de sólidos porosos, las limitaciones de dicha teoría han sido puestas de manifiesto en diferentes estudios [12,13]. De hecho, la propia IUPAC establece que el área BET no debería utilizarse en el caso de sólidos microporosos [4]. Para sólidos microporosos, el análisis BET generalmente sobreestima el valor de área total respecto a otros cálculos.

En la actualidad, la teoría del funcional de densidad (DFT, del inglés *density functional theory*) y su versión más reciente, la teoría del funcional de densidad no localizada (NLDFT, del inglés *non local density functional theory*) [14-16], se han convertido en una importante herramienta para la caracterización textural de sólidos porosos (área superficial y distribución de tamaño de poros) [3,17,18].

Los cálculos utilizados en DFT se basan en la termodinámica de la interacción entre moléculas de adsorbato y de adsorbente utilizando las ecuaciones de la mecánica estadística, considerando un modelo de poro, y evaluando la densidad de partículas a medida que cambia la distancia a la superficie con la que están interactuando.

### III.3.2. Desorción a temperatura programada

La química superficial de los materiales carbonosos tiene especial importancia para su aplicación como electrodos en supercondensadores, como se ha descrito en el Capítulo de Introducción. Principalmente, son los grupos oxigenados superficiales los que tienen un papel importante en la capacidad mostrada por los materiales carbonosos [19].

La desorción a temperatura programada (TPD, del inglés *temperature programmed desorption*) es una técnica que permite la caracterización de la química superficial de materiales carbonosos. Dicha técnica consiste en el análisis de los gases emitidos por el material carbonoso cuando se aplica un programa de temperatura en atmósfera inerte. El seguimiento de los gases emitidos es analizado por un detector (suele utilizarse un espectrómetro de masas). El análisis de los gases emitidos por la muestra, en función de la temperatura, proporciona información sobre la composición química y la estabilidad de los grupos superficiales.

En el caso concreto de los grupos funcionales oxigenados, además de presentar diferente grado de estabilidad, desorben emitiendo diferentes gases (CO, $CO_2$ y $H_2O$) dependiendo del grupo funcional [20-22]. En la Figura III.2 se muestra un esquema en el que se indican los gases que emiten los diferentes grupos oxigenados superficiales presentes en los materiales carbonosos. El desprendimiento de CO ocurre a elevadas temperaturas (600-980 ºC) como consecuencia de la descomposición de grupos básicos o neutros, como fenoles, éteres, carbonilos y quinonas. La emisión de $CO_2$ tiene lugar, generalmente, a menores temperaturas (hasta, aproximadamente, 627 ºC) y es debida a la descomposición de grupos carboxílicos y lactonas. Los grupos anhidrido descomponen a partir de unos 350 ºC produciendo tanto CO como $CO_2$.

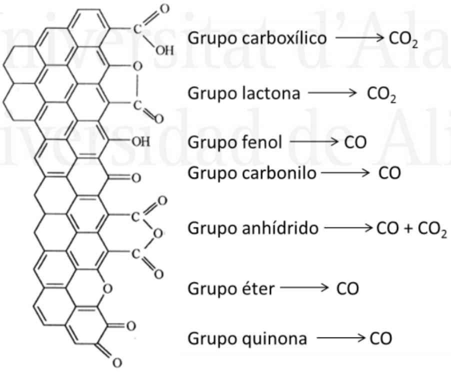

Figura III.2. Grupos funcionales oxigenados y gases emitidos por su descomposición. Adaptado de [21].

El dispositivo experimental utilizado en la presente Tesis Doctoral consta de un equipo de termogravimetría (TA Intruments, SDT 2960) acoplado a un espectrómetro de masas (Thermostar, Balzers, GSD 300 T3).

### III.3.3. Técnicas de caracterización electroquímica

La caracterización electroquímica puede llevarse a cabo en configuración de tres electrodos y de dos electrodos. La configuración de tres electrodos es apropiada para la caracterización del material electródico, mientras que la configuración de dos electrodos permite estudiar el comportamiento como supercondensador.

Los detalles referentes al: (i) tipo de celda electroquímica, (ii) configuración electródica, (iii) síntesis del electrodo de trabajo y (iv) tipo de electrodo de referencia y contraelectrodo empleados, vienen descritos en cada capítulo.

Las técnicas de caracterización electroquímica utilizadas en la presente Tesis Doctoral han sido muy variadas, y se presentan en los siguientes apartados.

#### III.3.3.1. Voltamperometría cíclica

La voltamperometría cíclica es una técnica electroquímica en la que el electrodo es sometido a una variación lineal del potencial con el tiempo (Figura III.3), registrándose la corriente que circula entre el electrodo de trabajo y el contraelectrodo con el tiempo [23] (configuración de tres electrodos) (Figura III.4).

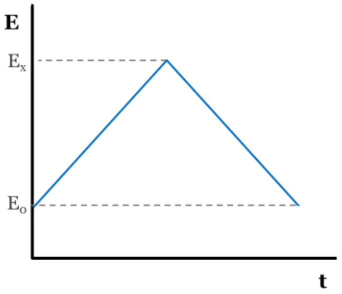

Figura III.3. Esquema de la variación del potencial (E) frente al tiempo (t).

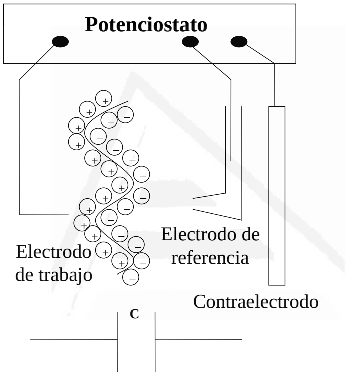

Figura III.4. Esquema de una celda electroquímica en configuración de tres electrodos y su circuito equivalente.

La Ecuación III.4 permite estimar la capacidad específica del electrodo en la ventana de potencial seleccionada.

$$C_{esp,3E} = \frac{Q/_2}{m \cdot \Delta E} \quad \textbf{Ecuación III.4}$$

Donde $C_{esp,3E}$ es la capacidad específica del material activo del electrodo (F·g$^{-1}$), $Q$ es la carga eléctrica total obtenida de la integración del voltamperograma cíclico (C), $m$ es la masa activa del electrodo (g), y $\Delta E$ es la ventana de potencial (V).

Además de la capacidad del material, también se pueden detectar los procesos redox relacionados con procesos pseudocapacitivos, así como con la degradación tanto del electrodo como del electrolito.

En la Figura III.5. se muestran dos esquemas de voltamperogramas cíclicos típicos que se obtendrían en configuración de tres electrodos. En el esquema (a) se representa el comportamiento puramente capacitivo de un electrodo (muestra una forma rectangular). En el esquema (b) aparece representado el esquema de un voltamperograma cíclico donde, además de la formación de la doble capa eléctrica, tiene lugar proceso farádico.

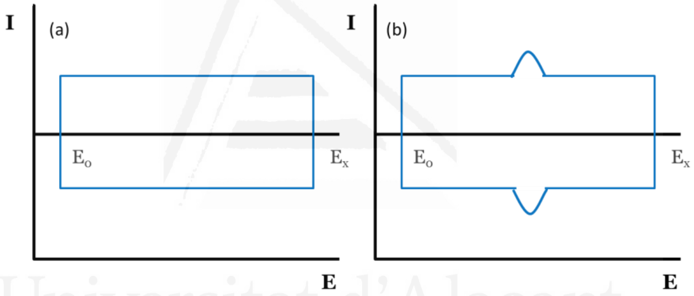

Figura III.5. Voltamperogramas cíclicos típicos donde se representa: un comportamiento puramente capacitivo (a) y de formación de la doble capa eléctrica con un proceso farádico (b).

Para el caso de la caracterización del supercondensador (configuración de dos electrodos) lo que se varía es el voltaje de la celda, es decir, la diferencia de potencial entre electrodo positivo y electrodo negativo. En este caso, el esquema del condensador electroquímico y su circuito equivalente aparece en la Figura III.6.

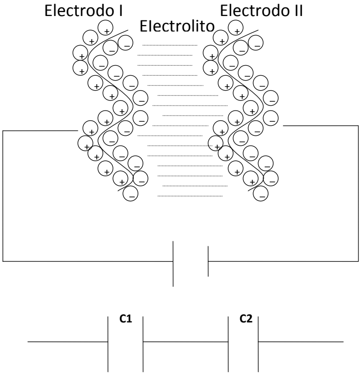

Figura III.6. Esquema de una celda electroquímica en configuración de dos electrodos y su circuito equivalente.

La voltamperometría cíclica permite estudiar el comportamiento del supercondensador y calcular la capacidad específica con la Ecuación III.5 (equivalente a la Ecuación III.4):

$$C_{esp,2E} = \frac{Q/_{2}}{m_{total} \cdot V} \quad \textbf{Ecuación III.5}$$

Donde $C_{esp,2E}$ es la capacidad específica del supercondensador ($F \cdot g^{-1}$), $m_{total}$ es la suma de las masas activas de los electrodos positivo y negativo (g) y V el voltaje de trabajo (V).

La Ecuación III.6 expresa la relación entre los valores de capacidad del supercondensador y de cada uno de los electrodos:

$$\frac{1}{C_{2E}} = \frac{1}{C_1} + \frac{1}{C_2} \quad \textbf{Ecuación III.6}$$

Donde $C_{2E}$ es la capacidad del supercondensador (F), y $C_1$ y $C_2$ son las capacidades de cada uno de los electrodos (F).

Además, en el caso de supercondensadores simétricos, se pueden comparar los resultados de capacidad específica del material electródico obtenidos utilizando sistemas dos electrodos y de tres electrodos:

Si las masas de cada uno de los electrodos son iguales:

$$C = C_1 = C_2$$ **Ecuación III.7**

La capacidad medida para el sistema de dos electrodos es:

$$C_{2E} = \frac{1}{2} \cdot C$$ **Ecuación III.8**

Y la capacidad específica pasa a ser:

$$C_{esp,2E} = \frac{C_{2E}}{2m} = \frac{1}{4} \cdot \left(\frac{C}{m}\right)$$ **Ecuación III.9**

Sin embargo, para un sistema de tres electrodos, la capacidad del material electródico se mide directamente, por lo que:

$$C_{3E} = C$$ **Ecuación III.10**

Y la capacidad específica:

$$C_{esp,3E} = \frac{C_{3E}}{m} = \frac{C}{m}$$ **Ecuación III.11**

Combinando las Ecuaciones III.9 y III.11 se obtiene que:

$$C_{esp,3E} = 4 \cdot C_{esp,2E}$$ **Ecuación III.12**

### III.3.3.2. Cronopotenciometría

La cronopotenciometría es una técnica electroquímica que se basa en la medida del potencial de un sistema en función del tiempo durante la aplicación de una intensidad de corriente constante (Figura III.7).

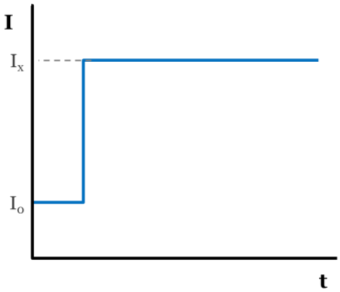

Figura III.7. Esquema de un salto galvanostático.

En la Figura III.8.a se presenta un esquema de un ciclo de carga y descarga, de un electrodo en celda de tres electrodos, en la Figura III.8.b se muestra la variación de la intensidad de corriente eléctrica que se aplicaría. En estos análisis, se aplica una corriente constante, produciéndose una variación del potencial con el tiempo. Cuando se alcanza un determinado valor de potencial, se invierte la polaridad de la corriente aplicada (hasta alcanzar, de nuevo, el potencial inicial). El proceso donde se incrementa el potencial del electrodo es denominado carga, mientras que el inverso es la descarga (constituyendo, los dos procesos, un ciclo). En el ejemplo mostrado en la Figura III.8.a, el comportamiento del electrodo es capacitivo, ya que si hubiera contribución farádica la representación de la carga y la descarga no se ajustarían a una línea recta, sino que se observaría una zona de potencial casi constante en el cronopotenciograma.

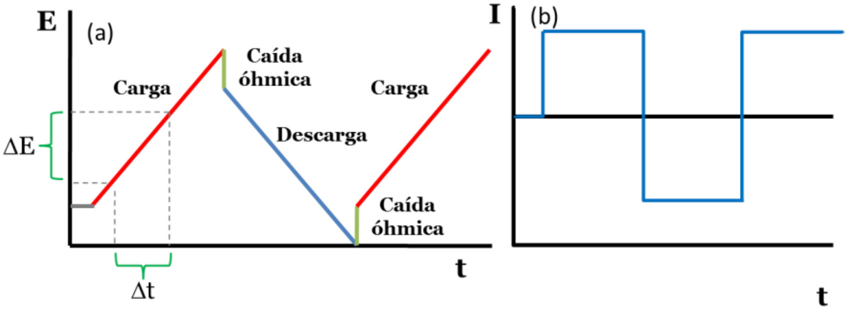

Figura III.8. Esquema de cronopotenciograma típico obtenido para un material con comportamiento capacitivo en configuración de tres electrodos (a) y variación de la intensidad de corriente eléctrica (b).

De los experimentos de cronopotenciometría, realizados en configuración tres y dos electrodos, se puede determinar la caída óhmica que corresponde a la resistencia de material electródico o del condensador electroquímico, respectivamente. Esta caída óhmica debe ser descontada cuando se calcule la capacidad específica, tanto del material como del supercondensador.

$$C_{esp,3E} = \frac{I.\Delta t}{\Delta E - \Delta E_{\Omega}}$$ **Ecuación III.13**

Donde $C_{esp,3E}$ es la capacidad específica del material activo electródico (F·g$^{-1}$), $I$ es la intensidad de corriente eléctrica aplicada (A·g$^{-1}$), $\Delta t$ es el tiempo de descarga (s), $\Delta E$ es la ventana de potencial (V), y $\Delta E_{\Omega}$ la caída óhmica (V).

De la misma manera que en el caso de los experimentos de voltamperometría cíclica, los resultados de capacidad específica del material activo electródico obtenidos utilizando sistemas dos electrodos y de tres electrodos se relacionan a través de la Ecuación III.12.

La realización de un número elevado de ciclos de carga-descarga galvanostática en configuración de dos electrodos es uno de los métodos más extendidos para estudiar la durabilidad de los condensadores electroquímicos, lo cual es un parámetro muy importante a la hora de determinar su posible aplicabilidad [24].

En la presente Tesis Doctoral, esta técnica ha sido utilizada, también, para el cálculo de la cantidad de hidrógeno almacenado electroquímicamente en un material carbonoso (lo cual se explicará, detalladamente, en el Capítulo IV).

Dado que se han utilizado diferentes potenciostatos para la realización de las medidas experimentales de voltamperometría cíclica y cronopotenciometría, los modelos específicos en cada caso vendrán especificados en cada capítulo.

### III.3.3.3. Cronoamperometría

En esta técnica electroquímica se mide el cambio de la intensidad de corriente eléctrica como consecuencia de la aplicación de un potencial constante durante un tiempo determinado (Figura III.9).

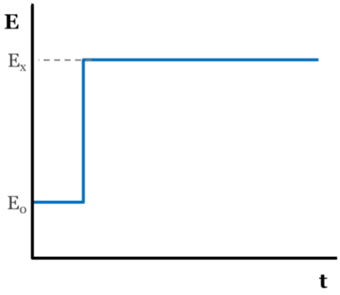

Figura III.9. Esquema de un salto potenciostático.

Se han llevado a cabo experimentos de cronoamperometría para la caracterización de diferentes materiales electródicos con las técnicas: microbalanza electroquímica de cristal de cuarzo y espectroscopía Raman *in situ* (cuyos fundamentos se explicarán detalladamente en los siguientes apartados).

### III.3.3.3. Microbalanza electroquímica de cristal de cuarzo

La microbalanza electroquímica de cristal de cuarzo (EQCM, del inglés *electrochemical quartz crystal microbalance*) es una técnica que permite la medida simultánea de parámetros electroquímicos (como potencial, corriente y carga) y la variación de masa, en la escala de los nanogramos [25].

El fundamento de la EQCM es la excitación mediante corriente alterna de un elemento piezoeléctrico, en este caso, un cristal de cuarzo, produciéndose una onda acústica que interacciona con el medio en contacto con ese cristal. La onda acústica sólo se propaga durante una pequeña distancia en el medio en contacto, por lo que la respuesta está determinada predominantemente por las propiedades interfaciales, lo que resulta ideal para sistemas electroquímicos [26].

Los electrodos de cuarzo, utilizados más comúnmente, constan de una oblea de cuarzo cristalino (con un modo fundamental de vibración entre 1 y 10 MHz) sobre cuyas caras planas se depositan finas capas de metal (Au, Pt, etc.) [27] que constituyen los electrodos entre los cuales se aplica la diferencia de potencial que forma el campo eléctrico variable que provoca la oscilación del cristal. El cristal de cuarzo puede cortarse en placas finas según determinadas orientaciones. El tipo de corte empleado define aspectos del resonador como el efecto que tiene la temperatura sobre la frecuencia de vibración o la cantidad de modos de vibración indeseados que se generan al aplicar el campo eléctrico. Es por ello que, el tipo de corte más adecuado cuando pretende conseguirse el doble objetivo de reducir el efecto de la temperatura sobre la frecuencia, así como los modos de vibración acoplados (no deseados), es el denominado AT [25,27]. En esta Tesis Doctoral se han utilizado cristales de cuarzo en corte AT de 9 MHz de frecuencia fundamental, donde se ha depositado una fina capa de Ti y, sobre éste, una fina capa de Pt (Figura III.10).

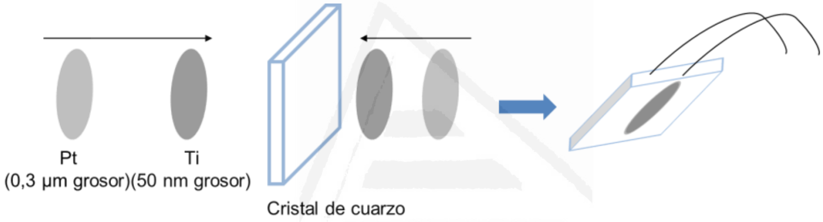

Figura III.10. Esquema de un electrodo de cuarzo en corte AT de 9 MHz.

Los resonadores de cristal de cuarzo son muy sensibles a los cambios de masa en su superficie. Para películas finas uniformemente depositadas sobre el cristal, la desviación de frecuencia de resonancia del mismo es proporcional a la masa añadida. La ecuación de Sauerbrey establece una relación matemática entre los incrementos de frecuencia y los de masa, la cual sólo es válida cuando la capa depositada es muy fina. En estas condiciones, el material depositado queda rígidamente acoplado a la superficie del cuarzo, sufriendo una deformación despreciable cuando es atravesado por la onda acústica [28]:

$$\Delta f = \frac{-2nf^2}{\sqrt{\mu_Q \rho_Q}} \frac{\Delta m}{A} \quad \textbf{Ecuación III.14}$$

Donde $\Delta f$ es el cambio en la frecuencia de resonancia medido (Hz), $n$ es el modo fundamental del cristal de cuarzo, $f$ es la frecuencia de resonancia del cristal antes del depósito (Hz), $\mu_Q$ es el módulo de cizalladura del cristal de cuarzo de ($2{,}947 \cdot 10^{10}$ N $m^{-2}$), $\rho_Q$ densidad del cristal de cuarzo (2651 kg $m^{-3}$), $\Delta m$ es el cambio de masa (kg), y $A$ es el área piezoeléctricamente activa ($m^2$).

En la Figura III.11 se presenta un esquema de la celda electroquímica de teflón empleada en la presente Tesis Doctoral para los análisis realizados con la EQCM.

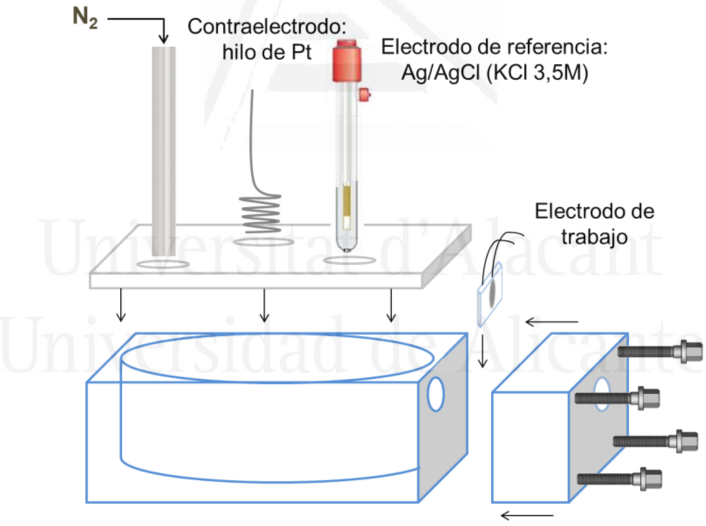

Figura III.11. Esquema de la celda electroquímica utilizada para los experimentos realizados con la EQCM.

Se ha utilizado una EQCM marca EG&G PAR modelo QCA 917. Se ha usado un potenciostato modelo Wenking ST72 con un generador de señal EG&G PARC 175.

### III.3.4. Espectroscopía Raman *in situ*

La espectroscopía Raman constituye una excelente herramienta para la identificación de compuestos y caracterización de la estructura molecular, aplicada en numerosos campos de investigación.

Cuando una molécula es irradiada por luz monocromática se produce una interacción entre el campo magnético oscilante y la molécula. El campo eléctrico produce una perturbación en la distribución de carga de la molécula y, por lo tanto, induce un momento dipolar en la misma. La suma de los momentos dipolares inducidos constituye la segunda fuente de campo eléctrico que actúa, a su vez, como fuente de radiación originando las dispersiones Rayleigh y Raman [29].

En la Figura III.12 se presenta un esquema energético de la dispersión Rayleigh y Raman. El estado energético intermedio que alcanza una molécula en un proceso de dispersión Rayleigh y Raman es un estado virtual, que no necesariamente coincide con ningún estado propio de la molécula. La mayor parte de la luz es elásticamente dispersada dando lugar a la dispersión Rayleigh, es decir, la radiación emitida tiene la misma energía que la incidente. Algunos fotones intercambian energía con la muestra, y son dispersados inelásticamente, produciendo la dispersión Raman, en este caso la radiación emitida tiene diferente energía que la radiación incidente. La dispersión Raman puede ser: (i) Stokes, si la radiación dispersada tiene una energía menor que la incidente y (ii) Anti-Stokes, cuando la energía de la radiación dispersada es mayor que la del haz incidente [30]. La emisión Raman Anti-Stokes es mucho más débil que la Stokes, a temperatura ambiente, debido a que la proporción de moléculas en estados vibracionales excitados, que sigue la distribución de Boltzman, es mucho menor que las moléculas en el estado vibracional fundamental [29]. Es por ello, que se suele representar el espectro Raman Stokes.

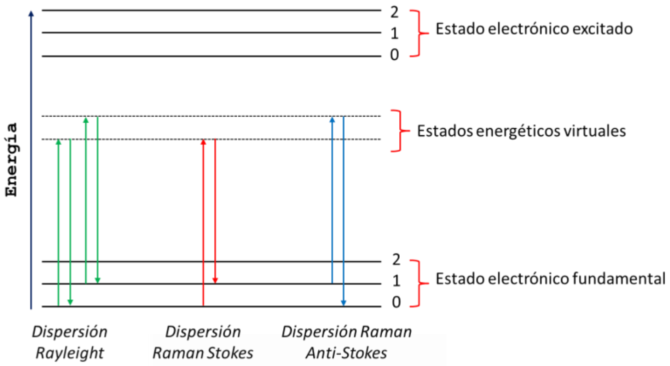

Figura III.12. Esquema energético de la dispersión Rayleigh y Raman no resonante.

La dificultad más destacable de la espectroscopía Raman es la interferencia entre la radiación Raman dispersada y la fluorescencia. El uso de láseres de longitud de onda larga evita este problema, ya que la radiación incidente no tiene suficiente energía como para producir fluorescencia; sin embargo, ello conlleva el aumento del nivel de ruido que se incorpora al espectro. Otra posible solución consiste en el empleo de la técnica de la transformada de Fourier, que permite liberar a los espectros de la componente de fluorescencia [30].

La frecuencia de la radiación que se emplea para inducir la dispersión Raman no tiene por qué corresponderse con una frecuencia de absorción de la muestra y, de hecho, es lo más favorable, dado que de esta forma se evitan posibles interferencias, tanto con la absorción como con la posterior fluorescencia. Sin embargo, cuando la longitud de onda del láser elegido se corresponde con una banda de absorción de la muestra, se produce el efecto Raman resonante. Al coincidir la frecuencia de la radiación incidente con la resonancia, se consiguen factores del orden de $10^5$ a $10^6$ sobre las intensidades de las transiciones Raman no resonantes. En este caso, ciertas transiciones que normalmente están prohibidas, ahora están permitidas y esto supone información adicional que va incluida en el espectro. Por ejemplo, en el caso de moléculas poliatómicas, en las que una banda de absorción electrónica puede estar asociada con un grupo cromóforo, las líneas Raman que experimentan el mayor crecimiento en la intensidad corresponderían a las vibraciones de los núcleos próximos al grupo cromóforo responsable de la resonancia [30].

La espectroscopía Raman proporciona información vibracional molecular complementaria a la de la espectroscopía infrarroja. Existe la llamada «regla de exclusión mutua», que establece que en una molécula que posea un centro de simetría, aquellas vibraciones activas en Raman serán inactivas en infrarrojo, y viceversa [29]. La espectroscopía Raman se lleva a cabo con excitación y detección en la región visible del espectro, por lo que se pueden emplear disoluciones acuosas, que absorben en la región del infrarrojo. Por tanto, la utilización de la espectroscopía Raman, es muy útil a la hora de seguir reacciones electroquímicas en fase acuosa *in situ*.

El esquema de la celda espectro-electroquímica de teflón empleada para los experimentos de espectroscopía Raman *in situ* se muestra en la Figura III.13. La ventana de cuarzo evita que el objetivo del microscopio pueda ser contaminado con productos generados durante el proceso o por evaporación del electrolito. La muestra se deposita sobre un soporte de teflón que contiene una barra de carbón vítreo (que actúa como contacto eléctrico).

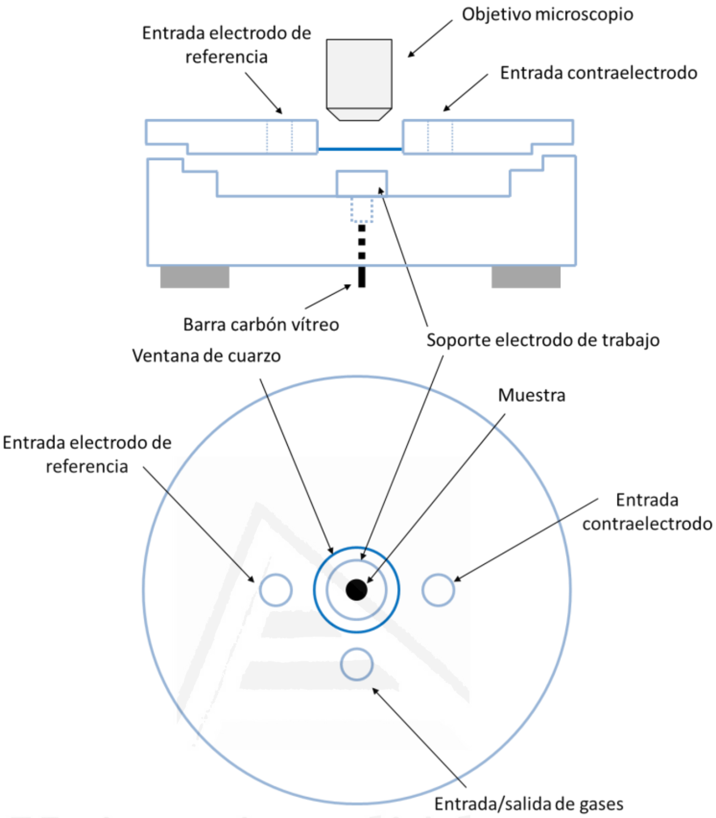

Figura III.13. Esquema de la celda espectro-electroquímica empleada para los experimentos de espectroscopía Raman *in situ*.

En la presente Tesis Doctoral se ha utilizado un espectrómetro Raman modelo LabRam (Jobin–Yvon Horiba) dotado de un microscopio confocal. Como detector se ha empleado un dispositivo de carga acoplada (CCD, del inglés *charge-couples device*) enfriado por efecto Peltier.

### III.3.5. Microscopía electrónica de barrido y espectroscopía de fluorescencia de rayos-X mediante análisis por dispersión de energía

La microscopía electrónica de barrido (SEM, del inglés *scanning electron microscopy*) constituye una técnica muy útil para la identificación y caracterización de sólidos, ya que permite conocer detalles microestructurales y de composición de las muestras [31,32].

En esta técnica se emplea un haz de electrones como fuente de radiación. Se puede utilizar un sistema termoiónico (calentamiento de un filamento de W o $LaB_6$) o de emisión de campo (FE, del inglés *field emission*) (cátodo frío). Los electrones emitidos se aceleran mediante una diferencia de potencial que oscila entre 2 y 40 kV [31]; los equipos de FE son capaces de trabajar a voltajes muy reducidos (de 0,02 kV a 30 kV) permitiendo observar muestras sensibles al haz de electrones sin dañarlas y minimizando los efectos de carga [33]. La columna del microscópico electrónico debe estar a vacío para evitar la interacción de los electrones con las moléculas de gas del aire y así evitar la dispersión de los electrones [31]. El haz de electrones emitidos es focalizado sobre la muestra con un sistema de lentes electromagnéticas. Cuando la muestra es irradiada con el haz de electrones (con energías de entre 5 y 30 keV) se producen diferentes fenómenos de dispersión elástica e inelástica. La emisión de electrones secundarios, de electrones retrodispersados y de rayos X permite obtener información sobre la morfología superficial y la composición química de la muestra [31].

La señal de electrones secundarios se forma en una delgada capa superficial, del orden de 50 a 100 Å. Son electrones de baja energía, menos de 50 eV, que permiten obtener información topográfica («en relieve») de la muestra [31]. Los electrones retrodispersados sin embargo, son electrones del haz incidente que han sido reflejado al interaccionar con la muestra. La emisión de electrones retrodispersados depende fuertemente del número atómico de la muestra, por lo que dos partes de la muestra que tengan distinta composición se revelan con distinta intensidad aunque no exista ninguna diferencia de topografía entre ellas [33]. El análisis SEM requiere que las muestras sean conductoras, por lo que, si no lo son, han de recubrirse con una película delgada de un material conductor como Au o C.

La emisión de rayos X característicos permite el análisis de la composición de la muestra. Esta radiación es producida por el retorno a su estado de equilibrio de átomos previamente excitados por el haz de electrones. Cuando un electrón pasa a ocupar una órbita más interna en el átomo, emite una radiación X de energía característica para cada elemento [31]. La espectroscopía de fluorescencia de rayos-X mediante análisis por dispersión de energía (EDX, del inglés *energy-dispersive X-ray spectroscopy*) permite conocer la composición elemental de distintas partes de la muestra, pudiendo realizar bien un barrido o bien análisis puntuales de las distintas zonas observadas.

En la presente Tesis Doctoral se ha empleado un FE-SEM marca ZEISS modelo Merlin VP Compact equipado con un sistema de microanálisis por EDX marca BRUKER modelo Quantax 400.

### III.3.6. Microscopía electrónica de transmisión

La microscopía electrónica de transmisión (TEM, del inglés *transmission electron microscopy*) permite obtener información sobre la naturaleza de la muestra (morfología, composición química, estructura cristalina) [31].

Esta técnica se basa en irradiar una fina película de muestra (~100 nm de grosor) con un haz de electrones de elevada energía (entre 100 y 300 keV [32]). El haz de electrones emitidos es focalizado sobre la muestra con un sistema de lentes electromagnéticas. Parte de esos electrones son transmitidos, otra parte son dispersados y otra parte da lugar a interacciones que producen distintos fenómenos como emisión de electrones secundarios y Auger, rayos X, etc. [31].

El microscopio TEM emplea la transmisión/dispersión de los electrones para formar imágenes, la difracción de los electrones para obtener información acerca de la estructura cristalina y la emisión de rayos X característicos para conocer la composición elemental de la muestra [31]. Los electrones que atraviesan la muestra pueden ser, o no, dispersados, y permiten obtener distintos tipos de información:

(i) Los electrones transmitidos no dispersados forman imágenes directas del material; mientras que los dispersados inelásticamente son los responsables del ruido de fondo presente en las imágenes de TEM.

(ii) Los electrones dispersados elásticamente son los responsables de la formación de las imágenes de difracción. A partir de estas imágenes se puede deducir la disposición de los átomos en el sólido. Dependiendo de la cristalinidad del material, se obtienen distintos tipos de diagramas de difracción. Un material amorfo o de tamaño de cristal muy pequeño genera diagramas formados por una serie de anillos difusos. Si la muestra consiste en varios cristales con distintas orientaciones, el diagrama presenta el aspecto de varios anillos concéntricos. Cuando se trata de un monocristal, el diagrama consta de puntos regularmente distribuidos. A partir de la medida de las distancias, bien entre los puntos o bien entre los anillos del diagrama, se obtiene información acerca de las distancias interatómicas de cada material.

Además, los rayos X emitidos permiten caracterizar la composición química de la muestra (EDX).

Para llevar a cabo los análisis de este trabajo se ha utilizado un TEM marca JEOL modelo JEM–2010. La cámara de adquisición de imágenes es de la marca GATAN modelo ORIUS SC600.

## Referencias

[1] Soneda Y, Kodama M. Effect of mesopore in MgO templated mesoporous carbon electrode on capacitor performance. Electrochemistry 2013;81:845-8.

[2] Rouquerol F, Rouquerol J, Sing K. Adsorption by powders and porous solids. Principles, methodology and applications. London: Academic Press, 1999.

[3] Lozano-Castelló D, Suárez-García F, Cazorla-Amorós D, Linares-Solano Á. Porous texture of carbons. In: Beguin F, Frackowiak E, editors. Carbons for electrochemical energy storage and conversion systems, Boca Raton (USA): CRC Press,Taylor & Francis Group; 2010, p. 115.

[4] Sing KSW, Everett DH, Haul RAW, Moscou L, Pierotti RA, Rouquerol J et al. Reporting physisorption data for gas solid systems with special reference to the determination of surface-area and porosity. Pure Appl Chem 1985;57(4):603-19.

[5] Lozano-Castelló D, Cazorla-Amorós D, Linares-Solano A. Usefulness of $CO_2$ adsorption at 273 K for the characterization of porous carbons. Carbon 2004;42:1233-42.

[6] Cazorla-Amorós D, Alcañiz-Monge J, de la Casa-Lillo M, Linares-Solano A. $CO_2$ as an adsorptive to characterize carbon molecular sieves and activated carbons. Langmuir 1998;14:4589-96.

[7] Linares-Solano A, Salinas-MarÍtnez de Lecea C, Alcañiz-Monge J, Cazorla-Amorós D. Further advances in the characterization of microporous carbons by physical adsorption of gases. Tanso 1998;1998:316-25.

[8] Brunauer S, Emmett PH, Teller E. Adsorption of gases in multimolecular layers. J Am Chem Soc 1938;60:309-19.

[9] Lowell S, Shields JE, Thomas MA, Thommes M. Characterization of porous solids and powders: surface area, pore size and density. The Netherlands: Kluwer Academic Publishers, 2004.

[10] Gregg, S.J., Sing,K.S.W. Adsorption, surface area, and porosity. London; New York: Academic Press, 1982.

[11] Dubinin MM. The potential theory of adsorption of gases and vapors for adsorbents with energetically nonuniform surfaces. Chem Rev 1960;60:235-41.

[12] Sing K. The use of nitrogen adsorption for the characterisation of porous materials. Colloid Surf A:Physicochem Eng Asp 2001;187:3-9.

[13] Centeno TA, Stoeckli F. The assessment of surface areas in porous carbons by two model-independent techniques, the DR equation and DFT. Carbon 2010;48:2478-86.

[14] Tarazona P. Free-energy density functional for hard-spheres. Phys Rev A 1985;31:2672-9.

[15] Tarazona P. Erratum. Free-energy density functional for hard-spheres. Phys Rev A 1985;31:2672-9.

[16] Tarazona P, Marconi U, Evans R. Phase-equilibria of fluid interfaces and confined fluids. Nonlocal *versus* Local Density Functionals. Mol Phys 1987;60:573-95.

[17] Ravikovitch P, Haller G, Neimark A. Density functional theory model for calculating pore size distributions: pore structure of nanoporous catalysts. Adv Colloid Interface Sci 1998;76:203-26.

[18] Ravikovitch P, Vishnyakov A, Russo R, Neimark A. Unified approach to pore size characterization of microporous carbonaceous materials from $N_2$, Ar, and $CO_2$ adsorption isotherms. Langmuir 2000;16:2311-20.

[19] Bleda-Martínez MJ, Maciá-Agulló JA, Lozano-Castelló D, Morallón E, Cazorla-Amorós D, Linares-Solano A. Role of surface chemistry on electric double layer capacitance of carbon materials. Carbon 2005;43:2677-84.

[20] Román-Martínez MC, Cazorla-Amorós D, Linares-Solano A. TPD and TPR characterization of carbonaceous supports and Pt/C catalysts. Carbon 1993;31:895-902.

[21] Figueiredo J, Pereira M, Freitas M, Orfao J. Modification of the surface chemistry of activated carbons. Carbon 1999;37:1379-89.

[22] Burg P, Cagniant D. Characterization of carbon surface chemistry. In: Radovic L, editor. Chemistry and physics of carbon, Boca Raton (USA): CRC Press-Taylor & Francis Group; 2008, p. 129-176.

[23] Bard AJ, Faulkner LR. Electrochemical methods. Fundamentals and applications. 2nd ed. New York: John Wiley & Sons, 2001.

[24] Béguin F, Raymundo-Piñero E, Frackowiak E. Electrical double-layer capacitors and pseudocapacitors. In: Béguin F, Frackowiak E, editors. Carbons for electrochemical energy storage and conversion systems, Boca Raton (USA): CRC Press,Taylor & Francis Group; 2010, p. 329.

[25] Buttry DA. Applications of the quartz crystal microbalance to electrochemistry. In: Bard AJ, editor. Electroanalytical Chemistry. A series of advances. Vol.17, New York: Marcel Dekker; 1991, p. 1-86.

[26] Buttry DA, Ward MD. Measurement of interfacial processes at electrode surfaces with the electrochemical quartz crystal microbalance. Chem Rev 1992;92:1355-9.

[27] Breuer K. Applications of the piezoelectric quartz crystal microbalance for microdevice development. In: Bender JW, Krim J, editors. Microscale diagnostic techniques, Germany: Springer; 2005, p. 227-259.

[28] Lucklum R, Soares D, Kanazawa K. Models for resonant sensors. In: Arnau Vives A, editor. Piezoelectric transducers and applications, Berlin (Germany): Springer; 2004, p. 69-99.

[29] Dieing T, Hollricher O, Toporski J. Introduction to the fundamentals of Raman spectroscopy. In: Dieing T, Hollricher O, Toporski J, editors. Confocal Raman microscopy, Berlin (Germany): Springer; 2011, p. 21-42.

[30] Requena Rodríguez A, Zúñiga Román J. Espectroscopía Raman. In: Requena Rodríguez A, Zúñiga Román J, editors. Espectroscopía, Madrid (Spain): Pearson Educación; 2004, p. 245-596.

[31] Herrero P, Baró A. Microscopia óptica, electrónica y por efecto túnel. In: Albella JM, Cintas AM, Miranda T, Serratosa JM, editors. Introducción a la ciencia de materiales: técnicas de preparación y caracterización, Madrid (España): Consejo Superior de Investigaciones Científicas; 1993, p. 553-590.

[32] Goodhew PJ, Humphreys J, Beanland R. The scanning electron microscope. In: Anonymous Electron microscopy and analysis, London and New York: Taylor & Francis; 2000, p. 122.

[33]http://sstti.ua.es/es/instrumentacion-cientifica/unidad-de-microscopia/microscopia-electronica-de-barrido.html.

# Chapter IV

# New insights on electrochemical hydrogen storage in nanoporous carbons by *in situ* Raman spectroscopy

## IV.1. Introduction

Carbon materials are widely studied as electrodes for energy storage devices (e.g. supercapacitors [1-5]), because of their high conductivity, low cost and versatility of structure/texture. A relevant electrochemical application of carbon materials is hydrogen storage by electro-reduction of water in alkaline and neutral media. This process entails storing electrical charge through water reduction and weak chemical bonding of hydrogen. Different carbon materials have been studied for this application, such as activated carbons (ACs) [6-12], carbon nanotubes (CNTs) [13-17], and others [18,19].

The values of electrochemical hydrogen storage capacity published with CNTs show a large dispersion [13-15,17], what can be justified by the different purity degree of CNTs, which always contain some amorphous material and metal catalyst used in the synthesis [13,20]. Taking into account theoretical calculations and experimental results, storage of a relatively high amount of hydrogen in CNTs is quite unlikely [13,20]. Porous carbons have been studied for this application, giving more effective electrochemical hydrogen storage and greater reproducibility [7].

In the literature, several studies discussing the role of porosity and unsaturated carbon atoms in electrochemical hydrogen storage can be found. Generally, they all conclude that the higher the narrow micropore volume (i.e. pore size smaller than around 0.7 nm), the higher the electrochemical hydrogen storage capacity [6,21,22], and that the later decreases with decreasing the number of dangling carbon atoms [7,9]. The presence of surface oxygen groups in the AC produces the saturation of the active sites (i.e. unsaturated carbon atoms), decreasing the amount of hydrogen electrochemically stored in alkaline solution [9]. The type of carbon-hydrogen bonds and the electrochemical hydrogen storage capacity depending on the electrolyte have been also studied. Hydrogen is weakly chemisorbed in alkaline medium [7], whereas electrochemical hydrogen storage efficiency is quite poor in acidic electrolyte [8].

Since carbon materials display characteristic vibrational modes by Raman spectroscopy [9,13,23,24], this technique has been used to *in situ* monitor the structural changes occurring during electrochemical conditions, and to characterize the type of carbon-hydrogen interaction under cathodic conditions [9,13,25].

The objective of the work developed in this chapter is to investigate the mechanism of electrochemical hydrogen storage, under cathodic conditions, comparing the behavior of two ACs, with different porosity and surface chemistry, in two different electrolytes (6 M KOH and 0.5 M $Na_2SO_4$). The ACs are electrochemically characterized by cyclic voltammetry (CV) and galvanostatic charge-discharge (GCD) techniques, and *in situ* Raman spectroscopy is employed to analyze the surface structural changes of ACs at different potentials, in both electrolytes.

## IV.2. Experimental

The materials used for the study were:

(i) A commercial AC (named as MWV-E510A)
(ii) An AC (named as ANK3) obtained following the procedure described in the next section.

### IV.2.1. Synthesis of the activated carbon

ANK3 was obtained by KOH activation of anthracite, following the procedure described elsewhere [26]. Chemical activation with KOH was carried out using an impregnation method. Anthracite precursor was mixed, by stirring, with a KOH aqueous solution (ratio 3:1; KOH:anthracite) for 2 h at 60 ºC. The resulting slurry was dried at 110 ºC overnight in an oven. Then, the resulting mixture was used for carbonization. It was heated up to 750 ºC during 2 h (ramp of 5 ºC min$^{-1}$). Afterwards, ANK3 was washed several times with a 5 M HCl solution and with distilled water until free of chloride ions. Finally, the sample was dried at 110 °C for 12 h.

### IV.2.2. Porous texture characterization

The porous texture of the two samples was determined by physical adsorption ($N_2$ at -196 ºC and $CO_2$ at 0 ºC) using an Autosorb–6 equipment (Quantrachrome) after samples out-gassing at 250 ºC under vacuum for 4 hours. The total micropore volume (i.e. pore size smaller than 2 nm) was calculated from the application of the Dubinin–Radushkevich (DR) equation to the $N_2$ adsorption data at -196 ºC ($0.005 < P\ P_0^{-1} < 0.17$). The narrow micropore volume (i.e. pore size smaller than around 1 nm) was estimated from $CO_2$ adsorption at 0 ºC using the DR equation and applied to the higher relative pressure region [27-29]. The apparent specific surface area was calculated by applying the Brunauer–Emmett–Teller (BET) theory to the $N_2$ adsorption data ($0.05 < P\ P_0^{-1} < 0.35$).

### IV.2.3. Surface chemistry characterization

Temperature programmed desorption (TPD) was performed in a DSC-TGA equipment (TA Instruments, SDT 2960 Simultaneous) coupled to a mass spectrometer (Thermostar, Balzers, GSD 300 T3), to characterize the surface chemistry of the samples. In these experiments, approximately 10 mg of the sample were heated up to 950 ºC (heating rate 20 ºC min$^{-1}$) under a helium flow rate of 100 ml min$^{-1}$.

### IV.2.3. Electrochemical characterization

Carbon electrodes were prepared by mixing the porous carbon powder, acetylene black and polytetrafluoroethylene as a binder (Polytetrafluoroethylene 60 wt % dispersion in $H_2O$, Sigma-Aldrich) in ratio 80:10:10, respectively. The mixture was dried under an infrared lamp and compressed (2 tons) during 10 minutes to prepare a monolith with a diameter of 13 mm. The total carbon electrode weight used for the measurements was about 50 mg. The monolith was introduced in a stainless steel mesh and compressed (2 tons) for 10 minutes. Lastly, the electrode was dried during 1.5 hours (under vacuum and 80 ºC). Before the experiments, the electrodes were soaked during 24 hours in the electrolyte.

Cyclic voltammograms were obtained at 1 mV s$^{-1}$ scan rate, and the specific capacitance (C in F g$^{-1}$) of the AC was calculated using Equation IV.1:

$$C = \frac{Q/2}{\Delta E} \qquad \textbf{Equation IV.1}$$

Where *Q* is the total electrical charge obtained by integration of the cyclic voltammogram (C $g^{-1}$) and $\Delta E$ is the potential window (V).

Hydrogen was electrochemically stored with a charge current of -500 mA $g_{electrode}^{-1}$ during 1 hour, and the amount stored was evaluated by applying a discharge current of 50 mA $g_{electrode}^{-1}$, until reaching the initial open circuit potential.

The total charge measured during the galvanostatic discharge ($Q_{total\ discharge}$ in C $g^{-1}$) was calculated with Equation IV.2:

$$Q_{total\ discharge} = I \cdot t \qquad \textbf{Equation IV.2}$$

Where *I* is the current density referred to the mass of AC (A $g^{-1}$) and *t* is the discharge time (s).

As expressed by Equation IV.3, $Q_{total\ discharge}$ includes a capacitive contribution, $Q_{EDL}$ (specific capacitance of the AC by the potential window of the discharge process), and the charge $Q_H$ related with hydrogen electrochemically stored:

$$Q_{total\ discharge} = Q_{EDL} + Q_H \qquad \textbf{Equation IV.3}$$

Hence, the amount of hydrogen stored (H in wt%) is calculated applying (Equation IV.4):

$$\left(Q_H \cdot \frac{M}{F}\right) * 100 = H \qquad \textbf{Equation IV.4}$$

Where *M* is the atomic mass of hydrogen (1 g $mol^{-1}$) and *F* is the Faraday constant (96,485 C $mol^{-1}$).

All the electrochemical measurements were performed in a typical pyrex three-electrode cell using a platinum wire as the counter-electrode and a reversible hydrogen electrode (RHE) as the reference electrode; all potentials were further referred to the normal hydrogen electrode (NHE). The temperature during all the electrochemical experiments was kept at 25 ºC.

The electrochemical characterization was carried out with an Autolab PGSTAT30 potentiostat.

### IV.2.4. *In situ* Raman characterization

*In situ* Raman characterization was done using a three-electrode spectro-electrochemical cell made of polytetrafluoroethylene (see Figure III.13 in Chapter III). A platinum wire was used as the counter-electrode, and Ag/AgCl (3 M KCl) (0.21 V vs NHE) was used as the reference electrode; the potentials were further referred to the NHE. The working electrode was prepared by depositing a small amount of the electrode mixture (prepared as described earlier) on a glassy carbon bar (which acts as the electric contact). The Raman spectra were obtained with a LabRam spectrometer (Jobin–Yvon Horiba) coupled to an upright microscope Olympus BX30. The excitation line was provided by a 9 mW He–Ne laser at 632.8 nm. The calibration of the spectrometer was performed with a Si slice (521 ± 2 $cm^{-1}$). The laser beam was focused through a 50 x long-working objective (0.5 NA) into a 2 µm spot at the electrode surface. The sample viewing system consisted of a television camera attached to the microscope. The spectrometer resolution was better than 3 $cm^{-1}$ and the detector was a Peltier cooled charge-couple device (CCD) (1064 x 256 pixels). It was used a 800 µm pinhole, a 200 µm slit and a 600 lines $mm^{-1}$ diffraction grating. The electrochemical conditions were applied using a DropSens portable bipotentiostat/galvanostat µstat 400.

The spectra were acquired during 30 seconds at each potential, after a steady state current was reached. Since the He-Ne laser power may degrade the sample during the Raman measurements, each spectrum has been recorded in a different zone of the carbon electrode. Several spectra have been acquired with different electrodes in order to ensure that the results are reproducible and representative of the samples behavior under the given electrochemical conditions. Furthermore, in some experiments, consecutive spectra have been recorded at each potential in different zones of the carbon electrode. In all cases, the evolution of hydrogen bubbles has been avoided.

## IV.3. Results and discussion

### IV.3.1. Porous texture and surface chemistry characterization results

Table IV.1 shows that both porous carbons have a highly developed porosity; ANK3 has higher BET surface area and total micropore volume than the commercial AC MWV-E510A.

Surface oxygen groups of ACs decompose upon heating producing CO and $CO_2$ at different temperatures [31,32]. The evolution of CO occurs at high temperatures as a consequence of the decomposition of basic or neutral groups such as phenols, ethers, carbonyls and quinones. $CO_2$ evolves generally at lower temperatures and it is mainly due to the decomposition of carboxylic groups and lactones. The decomposition of anhydride groups produces CO and $CO_2$. Table IV.1 includes the amounts desorbed in the TPD experiments and it shows a much higher content of surface oxygen groups for ANK3, which could be attributed, in part, to the activation method (KOH activation of anthracite) used for the preparation of this material. The lower oxygen content of the sample MWV-E510A, could be also explained considering that this is a commercial sample developed for supercapacitor application, which has been probably post-treated to eliminate functionalities.

Table IV.1. Porous texture and surface chemistry characterization results.

| Sample | ANK3 | MWV-E510A |
|---|---|---|
| **$S_{BET}$ ($m^2$ $g^{-1}$)** | 3165 | 2240 |
| **$V_{DR}$ ($N_2$) ($cm^3$ $g^{-1}$)** | 1.17 | 0.79 |
| **$V_{DR}$ ($CO_2$) ($cm^3$ $g^{-1}$)** | 0.81 | 0.83 |
| **μmolCO $g^{-1}$** | 2160 | 460 |
| **μmol$CO_2$ $g^{-1}$** | 590 | 160 |
| **μmolO $g^{-1a}$** | 3340 | 780 |

[a] μmolO $g^{-1}$ = μmolCO $g^{-1}$ + 2 · μmol$CO_2$ $g^{-1}$

### IV.3.2. Electrochemical characterization results

The cyclic voltammograms of ANK3 in 6 M KOH solution (Figure IV.1) show a quasi-rectangular shape between -0.67 V and -0.27 V (red line), typical of an essentially capacitive process associated with the formation of the electrical double-layer. If the potential window is broadened to more positive potential (i.e. anodic conditions) and more negative potentials (green line), an oxidation current appears at high potential which corresponds to the oxidation of the sample. Upon broadening the potential window to more negative potentials (blue and black lines) (i.e. cathodic conditions) a reduction current starts at -0.75 V which corresponds to incipient hydrogen evolution. During the positive scan from -1.27 V, a positive peak is clearly observed at -0.60 V (black line) which can be associated to the oxidation of hydrogen weakly chemisorbed during the negative scan [7]. The cyclic voltammograms of MWV-E510A in 6 M KOH solution (Figure IV.2) in the same potential range exhibit a similar behaviour.

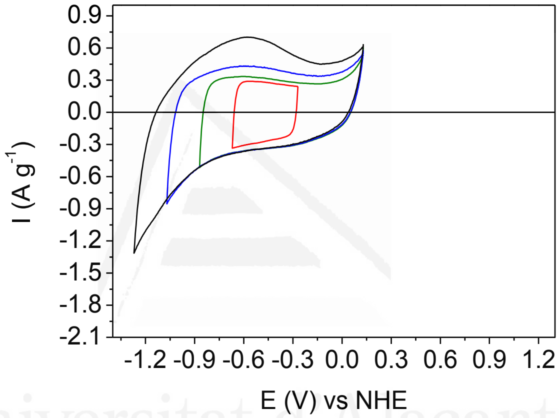

Figure IV.1. Cyclic voltammograms (1 mV s$^{-1}$) of ANK3 in 6 M KOH solution. Red line (-0.67 V / -0.27 V), green line (-0.87 V / 0.13 V), blue line (-1.07 V / 0.13 V), black line (-1.27 V / 0.13 V).

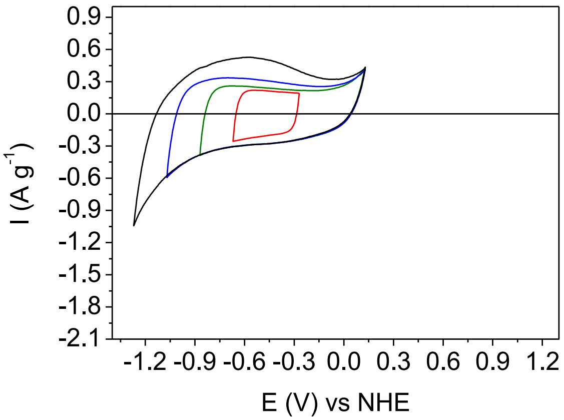

Figure IV.2. Cyclic voltammograms (1 mV s$^{-1}$) of MWV-E510A in 6 M KOH solution. Red line (-0.67 V / -0.27 V), green line (-0.87 V / 0.13 V), blue line (-1.07 V / 0.13 V), black line (-1.27 V / 0.13 V).

Figure IV.3 shows the cyclic voltammograms for the ANK3 sample in 0.5 M $Na_2SO_4$ solution. When the potential window is maintained between -0.14 V and 0.26 V (red line), the behavior corresponds mainly to a capacitive process. If the potential window is broadened to more positive and more negative values (green line) an oxidation current starts above 0.90 V which corresponds to the oxidation of the sample. A small reduction peak that could be related to this oxidation process is observed at around 0.40 V during the negative scan. When the potential window is broadened to more negative potentials (blue line) the reduction current associated with hydrogen evolution is observed. The peak related to the oxidation of the stored hydrogen is observed approximately at 0.85 V during the positive scan. If the potential window is broadened to even more negative potentials (black line), more hydrogen is chemisorbed as demonstrated by the increase in the oxidation peak at 0.85 V during the positive scan, but simultaneously hydrogen evolution takes place during the negative scan. The cyclic voltammograms for MWV-E510A in 0.5 M $Na_2SO_4$ solution (Figure IV.4) show a similar behavior. It is important to emphasize that the over-potentials for hydrogen evolution and hydrogen oxidation are much higher in $Na_2SO_4$ than in KOH medium for the two samples.

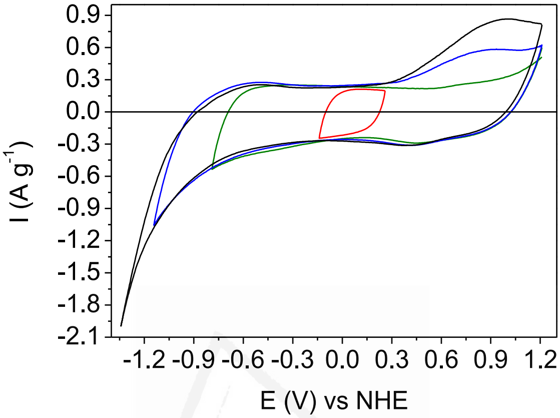

Figure IV.3. Cyclic voltammograms (1 mV $s^{-1}$) of ANK3 in 0.5 M $Na_2SO_4$ solution. Red line (-0.14 V / 0.26 V), green line (-0.79 V / 1.21 V), blue line (-1.14 V / 1.21 V), black line (-1.34 V / 1.21 V).

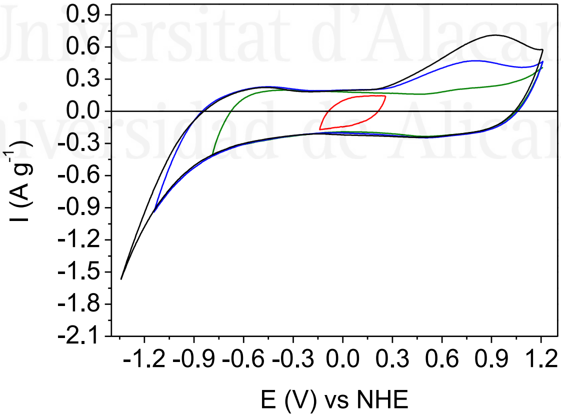

Figure IV.4. Cyclic voltammograms (1 mV $s^{-1}$) of MWV-E510A in 0.5 M $Na_2SO_4$ solution. Red line (-0.14 V / 0.26 V), green line (-0.79 V / 1.21 V), blue line (-1.14 V / 1.21 V), black line (-1.34 V / 1.21 V).

Table IV.2 includes the specific capacitance values calculated from the quasi-rectangular voltammograms for the two samples in both media. For the two samples, the specific capacitance is higher in KOH than in $Na_2SO_4$ medium, as already reported [3]. The specific capacitance values are higher for ANK3 in both electrolytes, in agreement with the higher development of porosity and the higher amount of surface oxygen groups of this sample (see Table IV.1) [1,2,22].

Table IV.2. Specific capacitance values obtained from the cyclic voltammograms at 1 mV $s^{-1}$.

| Sample | Solution | C (F $g^{-1}$) |
|---|---|---|
| **ANK3** | 6 M KOH | 260 |
| **MWV-E510A** | 6 M KOH | 194 |
| **ANK3** | 0.5 M $Na_2SO_4$ | 175 |
| **MWV- E510A** | 0.5 M $Na_2SO_4$ | 111 |

Figures IV.5 and IV.6 present the GCD curves for the two samples in KOH and in $Na_2SO_4$ medium, respectively. The samples are maintained during 1 hour at open circuit potential and, after this time, a negative current (-500 mA $g_{electrode}^{-1}$) is applied during 1 hour. During the charge process a very negative potential close to -1.30 V is reached for both samples and both electrolytes. As it has been previously seen in the cyclic voltammograms, at this potential value, electrochemical hydrogen storage takes place. The difference between the initial open circuit potential and the potential value reached during the charge process is higher in $Na_2SO_4$ medium for the two samples, and higher for the ANK3 sample in both electrolytes. Interestingly, it can be observed that the galvanostatic curves are different depending on the electrolyte, but they are qualitatively comparable in a given electrolyte for the two ACs. The long discharge times are related to the oxidation of chemisorbed hydrogen [12]. In KOH medium (see Figure IV.5), most of the charge is consumed approximately between -1.00 V and -0.50 V for the two samples, and it is related to the oxidation of weakly bonded hydrogen. By contrast, in $Na_2SO_4$ medium (see Figure IV.6), the main consumption of charge occurs at high potentials (it starts at around 0.00 V for ANK3 and at -0.20 V for MWV-E510A), and it is linked to the oxidation of strongly bonded hydrogen. These results correlate with the CV experiments where it has been seen that oxidation of adsorbed hydrogen occurs at higher potential in $Na_2SO_4$ than in KOH medium. This might explain the presence of two slopes in the discharge curves in $Na_2SO_4$ medium: the first part of the curves, where the potential is not high enough to cause the oxidation of adsorbed hydrogen, would be mainly related to a capacitive process; and the second part, at higher potential, corresponds to the oxidation of strongly bonded hydrogen. These data correlate with the CV experiments and they also are in agreement with previous observations that hydrogen may be stored in strongly and weakly bonded states, depending on the nature of electrolyte [7,8].

In the case of the two electrolytes herein investigated, one can conclude that weakly bonded hydrogen is the dominant form in KOH medium, whereas the strongly bonded one dominates in $Na_2SO_4$ medium.

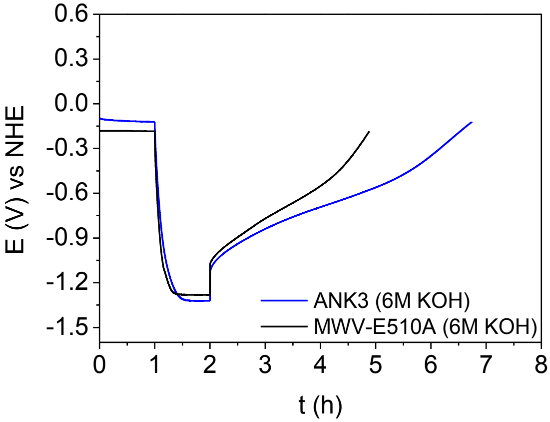

Figure IV.5. GCD curves in 6 M KOH solution. Charge -500 mA $g_{electrode}^{-1}$ during 1 hour, discharge +50 mA $g_{electrode}^{-1}$ until initial open circuit potential.

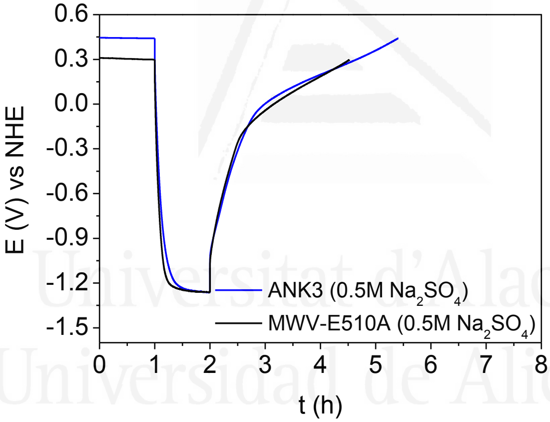

Figure IV.6. GCD curves in 0.5 M $Na_2SO_4$ solution. Charge -500 mA $g_{electrode}^{-1}$ during 1 hour, discharge +50 mA $g_{electrode}^{-1}$ until initial open circuit potential.

The total charge involved in the discharge process ($Q_{total\ discharge}$) and the hydrogen storage capacity obtained after subtracting the double-layer charging contribution are collected in Table IV.3. It can be seen that the electrochemical hydrogen storage capacity is higher in KOH than in $Na_2SO_4$ mainly for ANK3. The capacity is also higher for ANK3 in both electrolytes, which is in agreement with the higher porosity development of this material [6,9,21,22], even though it has a higher amount of surface oxygen groups.

Table IV.3. Hydrogen storage capacity estimated from the GCD experiments. Charge -500 mA $g_{electrode}^{-1}$ during 1 hour, discharge +50 mA $g_{electrode}^{-1}$ until initial open circuit potential.

| **Sample** | **Solution** | **$Q_{total\ discharge}$ (C $g^{-1}$)** | **H (wt.%)** |
|---|---|---|---|
| **ANK3** | 6 M KOH | 1060 | 0.78 |
| **MWV-E510A** | 6 M KOH | 659 | 0.46 |
| **ANK3** | 0.5 M $Na_2SO_4$ | 774 | 0.49 |
| **MWV- E510A** | 0.5 M $Na_2SO_4$ | 564 | 0.40 |

### IV.3.3. *In situ* Raman characterization results

In order to better understand the mechanism of hydrogen storage, *in situ* Raman spectroscopy has been used. Figures IV.7-IV.10 contain the *in situ* Raman spectra recorded at different potentials in the two electrolytes with the two carbon materials. The selection of the potentials used to collect *in situ* Raman spectra was based on the previous cyclic voltammograms.

In general, the D (1350 $cm^{-1}$) and G (1585 $cm^{-1}$) bands, which are characteristic of graphene based carbons [33], are observed in all the experiments. The G band corresponds to the graphitic lattice vibration mode, and the D band is related to the presence of defects. It should be mentioned that all the spectra shown were normalized versus the D band. When decreasing the potential, two bands at around 1110 and 1500 $cm^{-1}$ are observed, which are related to electrochemical hydrogen storage [9] and have been assigned to $Csp^2$–H and C=C stretching vibration, respectively, in amorphous carbon-hydrogen bonds [34,35].

These two bands appear simultaneously when the potential decreases, and disappear simultaneously when the potential goes to more positive values. This indicates that hydrogen chemisorption is reversible, which is in agreement with the results obtained by other authors [7,9].

In Figures IV.7 and IV.8, showing the spectra of the two ACs in KOH medium, it can be observed that the bands associated to the carbon-hydrogen bonds appear at -0.69 and -0.59 V for ANK3 and MWV-E510A, respectively, indicating that hydrogen storage proceeds more easily with MWV-E510A. These results suggest that the structural order of the carbon material and, especially, the surface functionality (both related with the raw material, the activation method and post-treatment) may have an influence on the rate of carbon atoms hydrogenation. As it can be seen in Table IV.1, the amount of surface oxygen groups in ANK3 is much larger than in MWV-E510A, what makes that carbon-hydrogen bonds in the former will be essentially formed through the reduction of carbon-oxygen surface complexes under cathodic conditions [36]. Such reaction is slower than the direct formation of carbon-hydrogen bonds with the unsaturated carbon atoms of MWV-E510A.

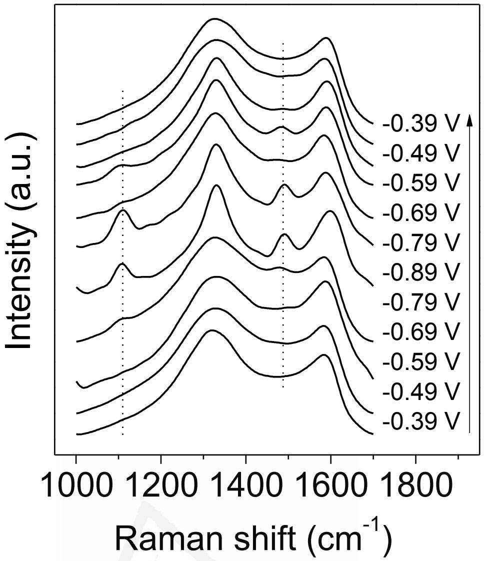

Figure IV.7. Raman spectra for the sample ANK3 at different potentials referred to NHE in 6 M KOH solution. Spectra normalized versus the D band.

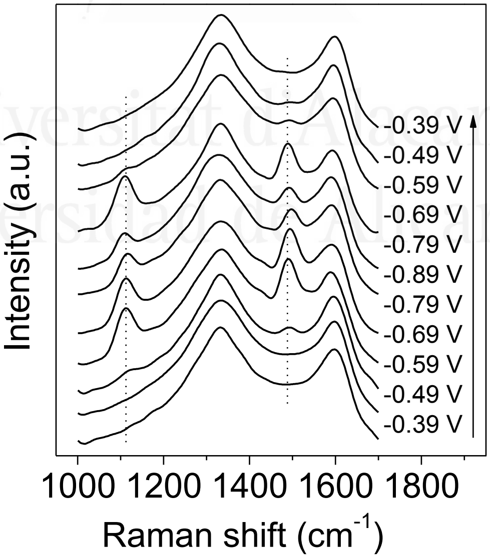

Figure IV.8. Raman spectra for the sample MWV-E510A at different potentials referred to NHE in 6 M KOH solution. Spectra normalized versus the D band.

The behaviour obtained in $Na_2SO_4$ medium is similar (see Figures IV.9 and IV.10), and carbon-hydrogen characteristic bands start to appear at -0.59 V for sample ANK3 and at -0.39 V for sample MWV-E510A.

However, there are interesting differences among both electrolytes regarding the potential at which the bands formation is observed compared to the thermodynamic potential values. Thus, in KOH medium, for the two samples, the formation of carbon-hydrogen bonds starts at more positive potential than the thermodynamic potential value for hydrogen evolution (-0.87 V), whereas in $Na_2SO_4$ medium the hydrogenation of carbon atoms begins at similar value of potential for MWV-E510A and at more negative potential for ANK3 than the thermodynamic potential value of hydrogen evolution (-0.34 V). This indicates that carbon-hydrogen bond formation is easier in KOH, what is in agreement with the results obtained from the GCD and CV experiments that suggest that weakly bonded hydrogen is dominant form in KOH medium and the strongly bonded one dominates in $Na_2SO_4$ medium.

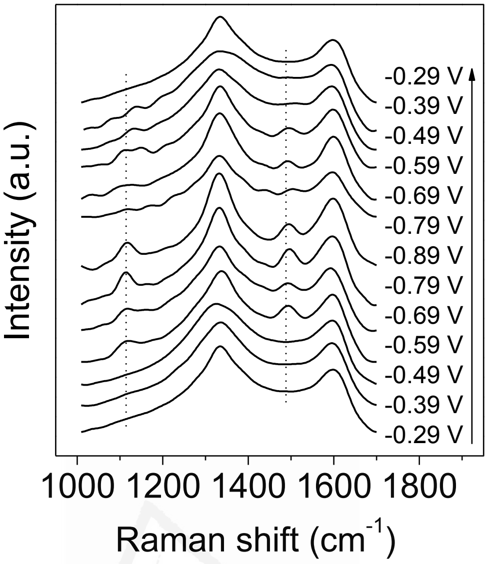

Figure IV.9. Raman spectra for sample ANK3 at different potentials referred to NHE in 0.5 M $Na_2SO_4$ solution. Spectra normalized versus the D band.

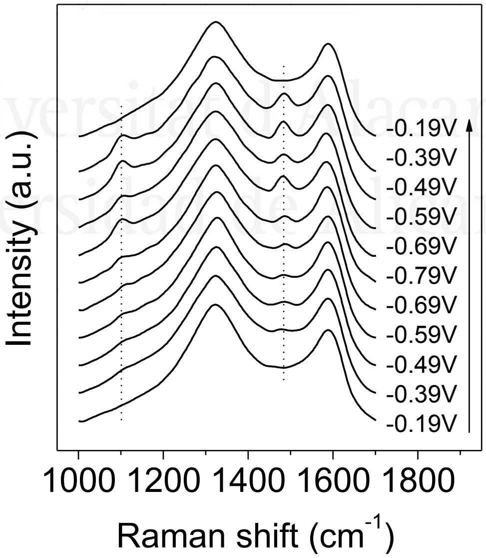

Figure IV.10. Raman spectra for sample MWV-E510A at different potentials referred to NHE in 0.5 M $Na_2SO_4$ solution. Spectra normalized versus the D band.

It should be noted that for the ANK3 sample, in both electrolytes, the shape of the D band changes when the bands associated with carbon-hydrogen bonds appear. The shape of the D band depends on the intensities of the D1 (1350 $cm^{-1}$), D3 (1500 $cm^{-1}$) and D4 (1200 $cm^{-1}$) bands [37]. When the D band narrows, the second order band of D1 (2720 $cm^{-1}$) appears in the full spectra (not shown here), meaning that hydrogenation of the carbon material leads to an intensity increase of the D1 band; this band is related with symmetry breaking of the graphite lattice by an edge [38]. In the case of the ANK3 sample, which structure may consist of small crystalline domains, the hydrogenation of carbon atoms seems to produce edges, increasing the intensity of the D1 band. The non-significant change of this band in case of MWV-E510A may be related to a more disordered structure of this material. Furthermore, it should be taken into account that each spectrum has been recorded in a different zone of the carbon electrode to avoid the degradation of the sample due to the laser power.

## IV.4. Conclusions

*In situ* Raman spectroscopy confirms that carbon-hydrogen bonds are formed during the charge process in both electrolytes. This hydrogen chemisorption is reversible, and the original Raman spectra of the samples are recovered after the discharge step. Comparing the two samples, it can be suggested that the surface functionality and porosity of the ACs have an important influence in the electrochemical hydrogen storage process. It is seen that hydrogen storage proceeds more easily for the sample with lower amount of surface oxygen groups. Moreover, the potential values corresponding to the starting of carbon-hydrogen bonds formation suggest that weakly bonded hydrogen is the dominant form in KOH medium, while strongly bonded hydrogen dominates in $Na_2SO_4$ medium. Furthermore, the hydrogenation of carbon atoms seems to produce edges in the small crystalline domains based structure of ANK3, as revealed by the intensity increase of the D1 band.

As general conclusions, it can be said that, both the characteristic of the ACs and the electrolyte used have an important influence in the electrochemical hydrogen storage process. It has been seen that the electrochemical hydrogen storage capacity is higher in KOH than in $Na_2SO_4$, mainly for ANK3. The capacity is also higher for ANK3 in both electrolytes, which is in agreement with the higher porosity development of this material, even though it has a higher amount of surface oxygen groups.

## References

[1] Bleda-Martínez MJ, Maciá-Agulló JA, Lozano-Castelló D, Morallón E, Cazorla-Amorós D, Linares-Solano A. Role of surface chemistry on electric double layer capacitance of carbon materials. Carbon 2005;43:2677-84.

[2] Jurewicz K, Vix-Guterl C, Frackowiak E, Saadallah S, Reda M, Parmentier J et al. Capacitance properties of ordered porous carbon materials prepared by a templating procedure. J Phys Chem Solids 2004;65:287-93.

[3] Bichat MP, Raymundo-Pinero E, Beguin F. High voltage supercapacitor built with seaweed carbons in neutral aqueous electrolyte. Carbon 2010;48:4351-61.

[4] Demarconnay L, Raymundo-Piñero E, Béguin F. A symmetric carbon/carbon supercapacitor operating at 1.6 V by using a neutral aqueous solution. Electrochem Commun 2010;12:1275-8.

[5] Hu C, Wang C, Wu F, Tseng R. Characterization of pistachio shell-derived carbons activated by a combination of KOH and $CO_2$ for electric double-layer capacitors. Electrochim Acta 2007;52:2498-505.

[6] Béguin F, Kierzek K, Friebe M, Jankowska A, Machnikowski J, Jurewicz K et al. Effect of various porous nanotextures on the reversible electrochemical sorption of hydrogen in activated carbons. Electrochim Acta 2006;51:2161-7.

[7] Béguin F, Friebe M, Jurewicz K, Vix-Guterl C, Dentzer J, Frackowiak E. State of hydrogen electrochemically stored using nanoporous carbons as negative electrode materials in an aqueous medium. Carbon 2006;44:2392-8.

[8] Jurewicz K, Frackowiak E, Béguin F. Towards the mechanism of electrochemical hydrogen storage in nanostructured carbon materials. Appl Phys A 2004;78:981-7.

[9] Bleda-Martínez MJ, Pérez JM, Linares-Solano A, Morallón E, Cazorla-Amorós D. Effect of surface chemistry on electrochemical storage of hydrogen in porous carbon materials. Carbon 2008;46:1053-9.

[10] Babel K, Janasiak D, Jurewicz K. Electrochemical hydrogen storage in activated carbons with different pore structures derived from certain lignocellulose materials. Carbon 2012;50:5017-26.

[11] Lota G, Fic K, Jurewicz K, Frackowiak E. Correlation of hydrogen capacity in carbon material with the parameters of electrosorption. Cent Eur J Chem 2011;9:20-4.

[12] Jurewicz K, Frackowiak E, Béguin F. Electrochemical storage of hydrogen in activated carbons. Fuel Process Technol 2002;77:415-21.

[13] Martin JB, Kinloch IA, Dryfe RA. Are carbon nanotubes viable materials for the electrochemical storage of hydrogen? J Phys Chem C 2010;114:4693-703.

[14] Dai G, Liu C, Liu M, Wang M, Cheng H. Electrochemical hydrogen storage behavior of ropes of aligned single-walled carbon nanotubes. Nano Lett 2002;2:503-6.

[15] Chen X, Zhang Y, Gao X, Pan G, Jiang X, Qu J et al. Electrochemical hydrogen storage of carbon nanotubes and carbon nanofibers. Int J Hydrogen Energy 2004;29:743-8.

[16] Yang C, Li YJ, Chen W. Electrochemical hydrogen storage behavior of single-walled carbon nanotubes (SWCNTs) coated with Ni nanoparticles. Int J Hydrogen Energy 2010;35:2336-43.

[17] Rajalakshmi N, Dhathathreyan K, Govindaraj A, Satishkumar B. Electrochemical investigation of single-walled carbon nanotubes for hydrogen storage. Electrochim Acta 2000;45:4511-5.

[18] Miranda-Hernández M, Ayala J, Rincón ME. Electrochemical storage of hydrogen in nanocarbon materials: electrochemical characterization of carbon black matrices. J Solid State Electr 2003;7:264-70.

[19] Miranda-Hernández M, Rincón ME. Carbon paste electrodes: correlation between the electrochemical hydrogen storage capacity and the physicochemical properties of carbon blacks. J Solid State Electr 2005;9:646-52.

[20] Niessen R, De Jonge J, Notten P. The electrochemistry of carbon nanotubes I. Aqueous electrolyte. J Electrochem Soc 2006;153:A1484-91.

[21] Fang B, Zhou H, Honma I. Ordered porous carbon with tailored pore size for electrochemical hydrogen storage application. J Phys Chem B 2006;110:4875-80.

[22] Vix-Guterl C, Frackowiak E, Jurewicz K, Friebe M, Parmentier J, Béguin F. Electrochemical energy storage in ordered porous carbon materials. Carbon 2005;43:1293-302.

[23] Wesełucha-Birczyńska A, Babeł K, Jurewicz K. Carbonaceous materials for hydrogen storage investigated by 2D Raman correlation spectroscopy. Vib Spectrosc 2012;60:206-11.

[24] Costa SD, Fantini C, Righi A, Bachmatiuk A, Rümmeli MH, Saito R et al. Resonant Raman spectroscopy on enriched $^{13}$C carbon nanotubes. Carbon 2011;49:4719-23.

[25] Colina A, Ruiz V, Heras A, Ochoteco E, Kauppinen E, Lopez-Palacios J. Low resolution Raman spectroelectrochemistry of single walled carbon nanotube electrodes. Electrochim Acta 2011;56:1294-9.

[26] Lozano-Castelló D, Lillo-Ródenas MA, Cazorla-Amorós D, Linares-Solano A. Preparation of activated carbons from Spanish anthracite: I. Activation by KOH. Carbon 2001;39:741-9.

[27] Lozano-Castello D, Cazorla-Amoros D, Linares-Solano A. Usefulness of $CO_2$ adsorption at 273 K for the characterization of porous carbons. Carbon 2004;42:1233-42.

[28] Cazorla-Amoros D, Alcaniz-Monge J, de la Casa-Lillo M, Linares-Solano A. CO2 as an adsorptive to characterize carbon molecular sieves and activated carbons. Langmuir 1998;14:4589-96.

[29] Ravikovitch P, Vishnyakov A, Russo R, Neimark A. Unified approach to pore size characterization of microporous carbonaceous materials from $N_2$, Ar, and CO2 adsorption isotherms. Langmuir 2000;16:2311-20.

[30] Rodríguez-Reinoso F, Linares-Solano A. Microporous structure of activated carbons as revealed by adsorption methods. In: Thrower PA,

editor. Chemistry and physics of carbon, New York: Marcel Dekker; 1989, p. 1-146.

[31] Román-Martínez MC, Cazorla-Amorós D, Linares-Solano A. TPD and TPR characterization of carbonaceous supports and Pt/C catalysts. Carbon 1993;31:895-902.

[32] Figueiredo J, Pereira M, Freitas M, Orfao J. Modification of the surface chemistry of activated carbons. Carbon 1999;37:1379-89.

[33] Tuinstra F, Koenig JL. Raman spectrum of graphite. J Chem Phys 1970;53:1126-30.

[34] Kuzmany H, Pfeiffer R, Salk N, Günther B. The mystery of the 1140 $cm^{-1}$ Raman line in nanocrystalline diamond films. Carbon 2004;42:911-7.

[35] Michaelson S, Hoffman A. Hydrogen bonding, content and thermal stability in nano-diamond films. Diam Relat Mater 2006;15:486-97.

[36] Morallón E, Arias-Pardilla J, Calo JM, Cazorla-Amorós D. Arsenic species interactions with a porous carbon electrode as determined with an electrochemical quartz crystal microbalance. Electrochim Acta 2009;54:3996-4004.

[37] Sadezky A, Muckenhuber H, Grothe H, Niessner R, Pöschl U. Raman microspectroscopy of soot and related carbonaceous materials: spectral analysis and structural information. Carbon 2005;43:1731-42.

[38] Wang Y, Alsmeyer DC, McCreery RL. Raman spectroscopy of carbon materials: structural basis of observed spectra. Chem Mater 1990;2:557-63.

# Chapter V

# Characterization of a zeolite-templated carbon by electrochemical quartz crystal microbalance and *in situ* Raman spectroscopy

## V.1.Introduction

Templated carbons have attracted much attention because the combination of both tailored and ordered porous network with a nano-sized structure could result in the development of unique features for their potential applications. Zeolite-templated carbon (ZTC) synthesized in the nanochannels of zeolite Y, is a good example of these materials. ZTC consists of buckybowl-like nanographenes ordered into a three-dimensional network [1,2], with a well-defined pore size of 1.2 nm [3,4], which preserves the long-range ordering with the same periodicity as the spacing (111) in zeolite Y of 1.4 nm [3-6]. In such a structure, the entire surface is fully exposed and, therefore, ZTC exhibits both a very large micropore volume [1,3,6] and apparent specific surface area (as high as 4000 $m^2$ $g^{-1}$ [1,3]). Equally, an extremely large number of reactive edge sites are exposed [2].

Recently, it has been observed that ZTC can be electrochemically oxidized and its unique buckybowl-like framework provides a large amount of highly reactive sites for this oxidation. This oxidized carbon material presents a high specific capacitance due to the contribution of the pseudocapacitance mainly derived from the hydroquinone-quinone redox couple and specific capacitances over 500 F $g^{-1}$ have been reported in 1 M $H_2SO_4$ solution [2]. The surface chemistry produced by the electrochemical treatment has been characterized by different techniques such as temperature programmed desorption (TPD) [2,7], Fourier-transform infrared spectroscopy [2] and X-ray photoelectron spectroscopy [2].

Electrochemical quartz crystal microbalance (EQCM) is a technique that allows the simultaneous measurement of electrochemical parameters (such as potential, current and charge) and mass changes in the nanogram range. This technique has been used to study different processes, such as electrochemical deposition and dissolution of metals [8,9], hydrogen adsorption on platinum electrodes [10], adsorption/desorption of anions on platinum electrodes [10] or ion exchange transport in polymer films [11]. Furthermore, the EQCM has been employed to monitor mass changes in carbon electrodes caused by both the electrochemical oxidation and degradation of the carbon material mainly in proton exchange membrane fuel cell electrocatalysts [12-14]. The behaviour of electroadsorbed ions and solvent molecules in activated carbons (ACs) and single-wall carbon nanotubes (SWCNTs) has been also studied in aqueous [15-19] and organic electrolytes [18,20].

Since carbon materials display characteristic vibrational modes by Raman spectroscopy, that provides information about their structural order, this technique has been widely used to study different carbon materials such as: graphitic materials [21-27], ACs [23,28,29], CNTs [30-35], fullerenes [36-40], peapods [31,41], soot [22,42] and templated carbons [2,43] among others. However, *in situ* Raman spectroscopy has been rarely applied for the characterization of carbon materials during electrochemical experiments [28,29,31,33,35,41].

The objective of the work presented in this chapter is to analyze the electrochemical behaviour of the ZTC focusing on both the surface chemistry and structural changes produced under different electrochemical conditions in 1M $H_2SO_4$ medium. EQCM allows simultaneous monitoring of the voltammetric and gravimetric responses of ZTC under electrochemical experimental conditions. Furthermore, in order to more accurately explain the EQCM results, the surface chemistry of the ZTC, before and after the electrochemical treatments, was analyzed by performing TPD experiments. Moreover, *in situ* Raman spectra at different potentials were collected to further elucidate the changes produced in the ZTC sample under electrochemical conditions. The unique buckybowl-like framework of ZTC, which is quite different in structure from that of ACs, makes these carbons an interesting example for demonstrating the usefulness of EQCM and *in situ* Raman spectroscopy techniques.

## V.2. Experimental

### V.2.1. Synthesis of the zeolite-templated carbon

ZTC sample was prepared using zeolite Y (Na-form, $SiO_2/Al_2O_3$ = 5.6, obtained from Tosoh Co. Ltd.) as hard template and following the procedure described in the literature [1,5]. Briefly, powdered zeolite Y was first dried at 150 ºC under vacuum and then impregnated with furfuryl alcohol at room temperature under reduced pressure. After washing with mesitylene, to remove furfuryl alcohol from the external surface of the zeolite powder, the furfuryl alcohol inside the zeolite channels was polymerized by heating the powder at 150 ºC for 8 hours under $N_2$ flow. The resulting composite was then heated at 5 ºC $min^{-1}$ under a flow of $N_2$ up to a temperature of 700 ºC. When the temperature reached 700 ºC, chemical vapor deposition (CVD) of propylene (7% in $N_2$) was accomplished for 2 hours. This CVD treatment is done because the amount of the carbon derived from furfuryl alcohol is not sufficient to form the self-supported, three-dimensional structure of ZTC. After CVD treatment, the zeolite/carbon composite was heat-treated at 900 ºC for 3 hours under a $N_2$ flow. Finally, the zeolite Y template was dissolved by HF treatment (47 % aqueous solution) and the resulting liberated carbon was washed with copious amounts of water and air-dried at 150 ºC overnight. As demonstrated by scanning electron microscopy elsewhere [6,43,44], the final carbon material is a powder made up of particles with submicrometer size (around 200 nm), which retains the morphology of the zeolite Y particles.

### V.2.2. Porous texture characterization

Porous texture of the ZTC powder was determined by $N_2$ adsorption at -196 ºC, using a volumetric sorption analyzer, after out-gassing the samples at 150 ºC under vacuum for 6 hours. The total pore volume ($V_T(N_2)$) was calculated from the $N_2$ adsorption amount at $P P_0^{-1} = 0.96$. The total micropore volume ($V_{DR}(N_2)$) was calculated from the Dubinin–Radushkevich (DR) equation using the same $P P_0^{-1}$ range as in Chapter IV (i.e. $0.005 < P P_0^{-1} < 0.17$). Also in this case, the apparent specific surface area was calculated by applying the Brunauer–Emmett–Teller (BET) theory to the $N_2$ adsorption data (but using the $P P_0^{-1}$ range between 0.01 and 0.05).

### V.2.3. Electrochemical and gravimetric characterization

ZTC electrodes for EQCM experiments were prepared by mixing the ZTC powder and polytetrafluoroethylene (PTFE) as binder (ratio 95:5, respectively). A small amount of the mixture was deposited on a piezoelectric quartz crystal just by pressing with a spatula, and it was used as working electrode. The total electrode mass used for the measurements was 45.0 - 90.0 µg, including both the carbon and PTFE materials. A new carbon electrode was prepared for each experiment. The piezoelectric quartz crystals were 9 MHz AT-cut, coated with Pt

(0.3 µm thick) on a Ti substrate (50 nm thick), with a geometrical area of 0.196 $cm^2$ (see Figure III.10 in Chapter III). The electrochemical experiments were performed in a three-electrode cell made of PTFE ((see Figure III.11 in Chapter III), which was specifically designed for this equipment, in which it is necessary that one side of the piezoelectric quart crystal covered with platinum is not in contact with the solution. A platinum wire was used as the counter-electrode and Ag/AgCl (KCl 3.5 M) was used as the reference electrode. Prior to perform the experiments, the 1M $H_2SO_4$ solution was purged with $N_2$ to remove the dissolved oxygen, and the cell was blanketed with $N_2$ flow during the measurements. Temperature was controlled at 25 ºC.

The electrochemical and gravimetric behaviour was studied by doing both cyclic voltammetry (CV) (at 5 mV $s^{-1}$ scan rate) and potentiostatic experiments (maintaining the potential constant during 2 hours).

From the 5th voltammogram of the CV experiments, the specific capacitance (C in F $g^{-1}$) was calculated using the equation indicated in Chapter IV:

$$C = \frac{Q/2}{\Delta E} \qquad \textbf{Equation V.1}$$

Where $Q$ is the total electrical charge obtained by integration of the cyclic voltammogram (C $g^{-1}$) and $\Delta E$ is the potential window (V).

The amount of electrochemically active oxygen groups introduced after a given electrochemical treatment (wt. % $g_O$ $g_{ZTC}^{-1}$) was calculated by applying the Faraday law (Equation V.2):

$$\text{wt.}\%\ g_o\, g_{ZTC}^{-1} = \frac{\left(\Delta Q/2\right)\cdot M}{z\cdot F}\cdot 100 \qquad \textbf{Equation V.2}$$

Where $\Delta Q$ is the electrical charge difference between the voltammetric profile after electrooxidation and the voltammetric profile corresponding to only EDL obtained by integration of the cyclic voltammograms

(C $g_{ZTC}^{-1}$), *M* is the atomic mass of oxygen (16 g mol$^{-1}$), *z* is the number of electrons involved in the redox reaction and *F* is the Faraday constant (96485 C mol$^{-1}$).

The relation between the resonance frequency change and the mass change on the piezoelectric quartz crystal electrode can be calculated by the Sauerbrey equation:

$$\Delta f = \frac{-2nf^2}{\sqrt{\mu_Q \rho_Q}} \frac{\Delta m}{A} \qquad \textbf{Equation V.3}$$

Where $\Delta f$ is the measured resonant frequency change (Hz), *n* is the fundamental mode of the crystal, *f* is the resonant frequency prior to deposition, $\mu_Q$ is the shear modulus of quartz ($2.947 \cdot 10^{10}$ N m$^{-2}$), $\rho_Q$ is the density of quartz (2651 kg m$^{-3}$), $\Delta m$ is the mass change, and *A* is the piezoelectrically active area. When the experiments involve only relative frequency changes which are measured in a given solution, the offset caused by the viscous loading has negligible effect on the accuracy of the Sauerbrey equation for the determination of small mass changes. Moreover, in these experiments less than 2 % change of frequency is produced by the deposition of the carbon electrode and, therefore, the Sauerbrey equation can be used accurately [45,46]. The value of sensitivity was $1.84 \cdot 10^8$ Hz cm$^2$ g$^{-1}$, and was determined by performing a potentiostatic platinum electrochemical deposition experiment.

Electrochemical measurements were carried out with a Wenking ST72 potentiostat with a EG&G PARC 175 generator or a EG&G potentiostat model 273. The EQCM was a EG&G PAR model QCA 917. A capacitance of 1 nF was used to isolate the EQCM from the potentiostat.

### V.2.4. Surface chemistry characterization

In order to quantify the surface chemistry changes under the electrochemical conditions studied with the EQCM, the same electrochemical treatments were performed to ZTC followed by TPD experiments. To carry out TPD analysis, around 10 mg of the carbon sample is required; therefore, the total carbon electrode weight used for the electrochemical treatments was about 15 mg. Even if the ZTC presents good conductivity, it is strongly recommended to use acetylene black to increase the conductivity of the working electrode and to get a homogeneous modification of the material. Accordingly, ZTC electrodes were prepared by mixing the ZTC powder, acetylene black and PTFE (ratio 90:5:5, respectively). The mixture was compressed (2 tons) during 5 minutes to prepare a monolith with a diameter of 13 mm. The monolith was introduced in a Ti mesh and compressed (4 tons) for 5 minutes. Since the working electrode mass in these experiments is higher than those used in the EQCM, and in this case the piezoelectric quartz crystal electrode is not needed, for simplicity we have used the typical pyrex three-electrode cell, using a platinum wire as the counter-electrode and Ag/AgCl (KCl 3.5 M) as the reference electrode.

In order to more accurately analyze the surface chemistry changes before and after the electrochemical treatments, a pristine ZTC electrode mixture was used since the electrochemically oxidized samples contain 5 wt. % of acetylene black and 5 wt. % of PTFE, even though the influence of these materials is small. In the case of the electrochemically oxidized samples, ZTC electrodes were recovered after the electrochemical experiments and washed with distilled water during 24 hours. For the TPD analysis, approximately 10 mg of the sample, previously dried in an oven during 6 hours (under vacuum and

80 ºC), were heated up to 900 ºC (heating rate 20 ºC min$^{-1}$) under a helium flow rate of 100 ml min$^{-1}$. A DSC–TGA equipment (TA Instruments, SDT 2960 Simultaneous) coupled to a mass spectrometer (Thermostar, Balzers, GSD 300 T3) was used, as previously described in Chapter IV.

### V.2.5. *In situ* Raman characterization

*In situ* Raman characterization was performed using the same three-electrode configuration and the same spectro-electrochemical cell as previously used in Chapter IV. Analogously, a platinum wire was used as the counter-electrode, and a Ag/AgCl (3 M KCl) was used as the reference electrode. The working electrode was also prepared by depositing a small amount of the electrode mixture on a glassy carbon bar (which acts as the electric contact) but, in this case, ZTC electrodes were prepared by mixing the ZTC powder and PTFE in ratio 95:5, respectively. Raman spectra were obtained using the same equipment and conditions. However, two different excitation lines were used, a 9 mW He–Ne laser at 632.8 nm and a 9 mW Diode laser at 782 nm. The spectra were acquired for 30 seconds for He–Ne laser and for 200 seconds for Diode laser at each potential, after a steady state current was reached.

## V.3. Results and discussion

### V.3.1. Porous texture and surface chemistry characterization results of powder ZTC

Porous texture and surface chemistry characterization results are presented in Table V.1. The synthesized ZTC has high $S_{BET}$ and large micropore volume, as already reported elsewhere [3,6]. As it has been previously said in Chapter IV, surface oxygen groups of carbon materials decompose upon heating producing CO and $CO_2$ at different temperatures which can be followed by the TPD experiments [47,48]. Evolution of CO occurs at high temperatures as consequence of the decomposition of basic or neutral groups such as phenols, ethers, carbonyls and quinones. $CO_2$ evolves generally at lower temperatures and it is mainly due to the decomposition of carboxylic groups and lactones. Decomposition of anhydride groups produces CO and $CO_2$. From the TPD profiles, the amount of CO and $CO_2$ evolved groups were estimated and included in Table V.1, showing that this carbon material presents a high total oxygen content, which was estimated to be 5.3 wt. %.

Table V.1. Porous texture and surface chemistry characterization results of powdered ZTC.

| $S_{BET}$ ($m^2$ $g^{-1}$) | $V_T$ ($N_2$) ($cm^3$ $g^{-1}$) | $V_{DR}$ ($N_2$) ($cm^3$ $g^{-1}$) | μmolCO $g^{-1}$ | μmol$CO_2$ $g^{-1}$ | μmolO $g^{-1}$ [a] |
|---|---|---|---|---|---|
| 3600 | 1.67 | 1.55 | 2362 | 474 | 3309 |

[a] μmolO $g^{-1}$ = μmolCO $g^{-1}$ + 2 · μmol$CO_2$ $g^{-1}$

### V.3.2. Electrochemical and gravimetric characterization results

Before each electrochemical experiment, ZTC electrodes were subjected to a high number of scans at 50 mV $s^{-1}$ between -0.20 V and 0.00 V to ensure that the carbon material is properly wet. Subsequently, 5 scans at 5 mV $s^{-1}$ were done from -0.10 V to 0.30 V in order to calculate the value of the initial specific capacitance of 175 F $g^{-1}$ (Figure V.1). It should be pointed out that under these potential ranges neither oxidation nor reduction processes take place.

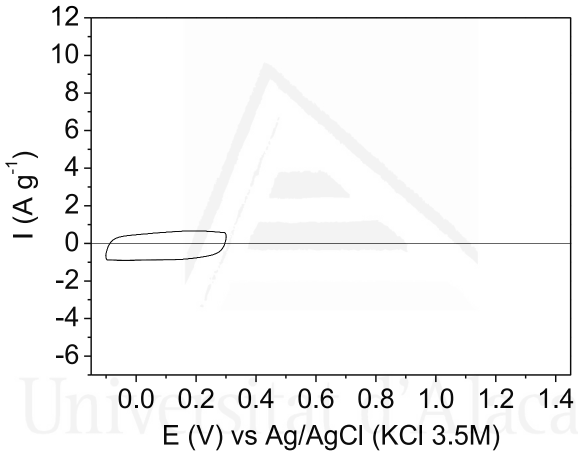

Figure V.1. Cyclic voltammograms obtained between -0.10 V and 0.30 V of ZTC at 5 mV $s^{-1}$ in 1M $H_2SO_4$ solution.

Cyclic voltammograms were obtained at 5 mV $s^{-1}$ scan rate under two subsequent potential ranges, from -0.10 V to 0.80 V and from -0.10 V to 1.20 V. It should be noted that 5 scans between -0.10 V and 0.60 V were done after each potential range in order to calculate the specific capacitance after the electrochemical oxidation. The values obtained were 353 and 468 F $g^{-1}$, respectively.

Figures V.2.a and V.2.b present the cyclic voltammograms and the gravimetric response, respectively, obtained during the five scans between -0.10 V and 0.80 V. The voltammetric behaviour shows an oxidation current at high positive potentials during the first positive cycle that decreases with the number of cycles. During the first negative sweep, a reduction process at 0.21 V is clearly observed in the cyclic voltammogram. The reverse process is produced during the subsequent positive cycle at, approximately, the same potential value (0.28 V). Then, the electrochemical oxidation of the carbon material (see Reactions V.1 and V.2 [19], where C() are carbon reactive sites) produces the appearance of a redox process that may be related to the surface oxygen groups produced during the voltammetric cycles up to 0.80 V. It has been previously reported that the CO-type groups related to the hydroquinone-quinone redox pair (see Reaction V.3 [49,50]) are responsible for this redox pair [2,13,51].

The gravimetric response (Figure V.2.b) shows a large mass increase during the first cycle at the same potential where the oxidation of the ZTC takes place. During the subsequent cycles an increase in mass is produced at the same potential, but to a lesser extent.

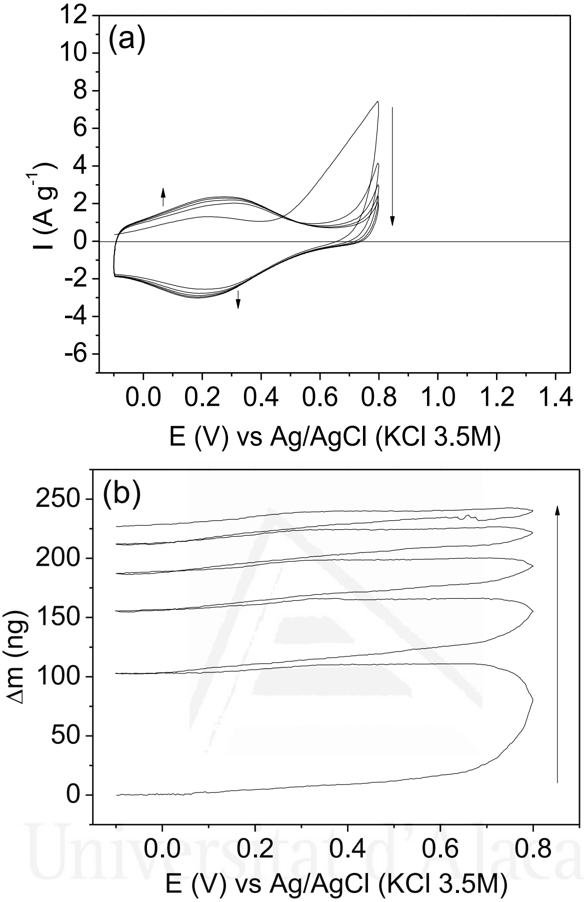

Figure V.2. Cyclic voltammograms (a) and gravimetric response (b) simultaneously obtained between -0.10 V and 0.80 V of ZTC at 5 mV s$^{-1}$ in 1M $H_2SO_4$ solution.

**Reaction V.1: electrochemical oxidation**

$$C() + H_2O \rightarrow C(O) + 2\ H^+ + 2\ e^-$$

**Reaction V.2: electrochemical oxidation**

$$C() + 2\ H_2O \rightarrow C(O_2) + C(H) + 3\ H^+ + 3\ e^-$$

**Reaction V.3: hydroquinone-quinone redox pair**

$$C_xOH \leftrightarrow C_xO + H^+ + e^-$$

The electrochemical oxidation of the ZTC under these electrochemical conditions produces the increase of the specific capacitance from the initial value of 175 F $g^{-1}$ up to 353 F $g^{-1}$ due to the contribution of the pseudocapacitance. From this increase, and considering that all the oxygen groups generated follows the hydroquinone-quinone redox mechanism, the amount of oxygen introduced was estimated to be 2.06 wt. % $g_O$ $g_{ZTC}^{-1}$.

TPD experiments (not shown here) were performed to calculate the increase of the amount of oxygen introduced under the electrochemical conditions applied. In general, an increase of the amount of oxygen groups when increasing electrochemical oxidation occurs, and no remarkable peak shifts are observed in any case. It should be pointed out, that the increase of the CO-type groups is higher than those of $CO_2$ for all the electrochemical treatments.

Regarding the experiment done between -0.10 and 0.80 V, the increase of the amount of oxygen calculated from the CO-profile (presumably due to the formation of oxygen groups that follows the hydroquinone-quinone redox mechanism) was 1.78 wt. % $g_O$ $g_{ZTC}^{-1}$, which is very similar to the value obtained from the increase of the specific capacitance.

It should be noted that net mass increase calculated from the gravimetric response is 0.28 wt. % $g_O$ $g_{ZTC}^{-1}$, which is much lower than those previously obtained; suggesting that electrochemical gasification of the carbon material is probably taking place. Under cathodic conditions, carbon-oxygen surface complexes, previously formed under anodic polarization, can be reduced according to Reactions V.4-V.7 [19]. In addition, electrochemical gasification of the carbon material may also happen under anodic conditions (see Reaction V.8 [49]).

**Reaction V.4: electrochemical gasification**

$$C(O) + 2H^+ + 2e^- \rightarrow CO + 2C(H)$$

**Reaction V.5: electrochemical gasification**

$$C(O) + 2H^+ + 2e^- \rightarrow CO + 2C() + H_2$$

**Reaction V.6: electrochemical gasification**

$$C(O_2) + 3H^+ + 3e^- \rightarrow CO_2 + 3C(H)$$

**Reaction V.7: electrochemical gasification**

$$C(O_2) + 3H^+ + 3e^- \rightarrow CO_2 + H_2 + C() + C(H)$$

**Reaction V.8: electrochemical gasification**

$$C() + 2H_2O \rightarrow CO_2 + 4\,H^+ + 4\,e^-$$

Figures V.3.a and V.3.b show the cyclic voltammograms and the gravimetric response simultaneously obtained during the experiment done between -0.10 V and 0.60 V after the electrochemical oxidation between -0.10 V and 0.80 V. The redox processes related with the hydroquinone-quinone redox pair can be seen. Over this potential range only a small net mass increase is observed, presumably due to additional electrooxidation of ZTC. However, in each cycle the mass increases during the anodic scan, and it decreases almost to the same extent during the cathodic scan. Going to more positive potential, the adsorption of $HSO_4^-$ ions and the oxidation of hydroquinones surface groups take place. Since $HSO_4^-$ ions are much heavier than protons involved in the redox reaction, a net mass increase is recorded. The formation of the EDL produces mass changes, as it has been seen in the literature for ACs [14-17], SWCNTs [18] and the bare piezoelectrically quartz crystal electrodes [10,13,14] with the EQCM. Interestingly, going to more negative potential, apart from the net mass decrease observed, a shoulder appears at 0.49 V that could be related to weight increase due to reduction of quinone surface groups that is produced together with the entrance of water molecules (the oxidation and reduction of redox groups could change the hydrophobicity of the carbon materials promoting the entrance or exit of water molecules [13,14]). This behaviour suggests that, at the beginning of the cathodic scan, the proton concentration in the electrode is very low, and this would inhibit protonation of the quinone groups that suddenly begins at 0.49 V (i.e. “double-layer induced inhibition of redox reaction”). Therefore, the reversible mass changes observed in each cycle are the sum of the contribution of the adsorption and desorption of ions and water molecules and also the proton involved in faradic reactions.

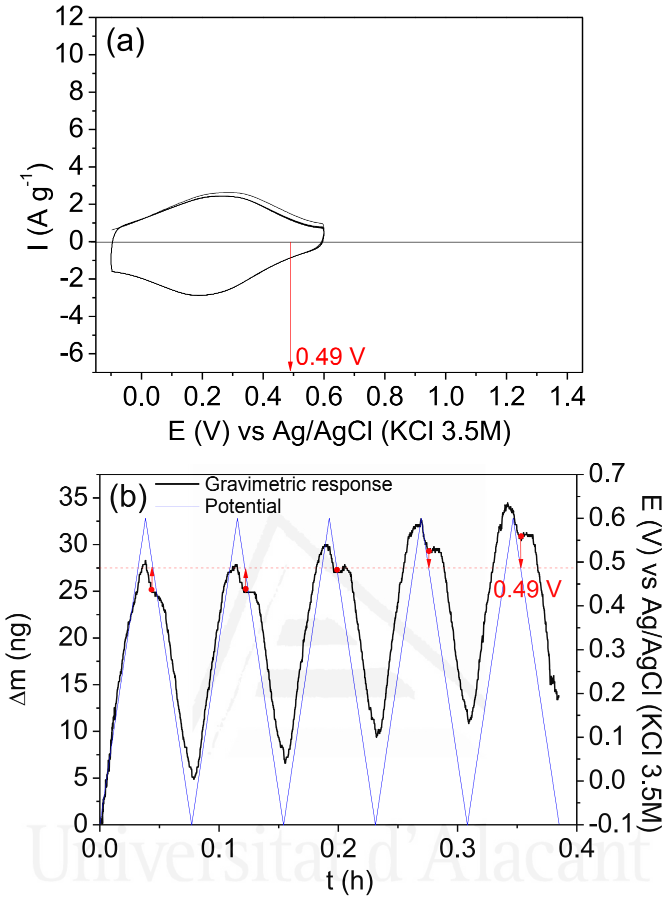

Figure V.3. Cyclic voltammograms (a) and gravimetric response (b) simultaneously obtained between -0.10 V and 0.60 V of ZTC at 5 mV $s^{-1}$ in 1M $H_2SO_4$ solution, after the electrochemical oxidation between -0.10 V and 0.80 V.

Figures V.4.a and V.4.b show the cyclic voltammograms and the gravimetric response, respectively, recorded when the potential is increased up to 1.20 V. The cyclic voltammogram obtained during the first cycle up to 1.20 V shows a higher anodic current corresponding to the electrochemical oxidation of the ZTC; the redox processes, at around 0.30 V, are also observed in the subsequent cycles and the specific capacitance, measured between -0.10 and 0.60 V, reaches the value of 468 F $g^{-1}$. However, this electrooxidation at 1.20 V makes the redox processes between -0.10 V and 0.60 V to be more irreversible (the anodic and cathodic peaks are located at 0.33 V and at 0.25 V, respectively). Thus, it seems that the surface oxygen groups electrochemically generated are different with respect to those generated between -0.10 V and 0.80 V and/or a decrease in the conductivity of the sample could also take place [7]. The amount of oxygen introduced (with respect to the previous experiment) calculated from the increase of the pseudocapacitance was 1.32 wt. % $g_O$ $g_{ZTC}^{-1}$; whereas the value calculated from the CO-TPD profile was higher (2.87 wt. % $g_O$ $g_{ZTC}^{-1}$). These results suggest that many oxygen groups generated are non-electrochemically active, at least in the potential range used.

Figure V.4.b shows the gravimetric response under these experimental conditions. It can be observed that the increase in mass starts at similar potential value as in Figure V.2.b but a higher mass increase is obtained. During the subsequent cycles, mass increases to a lesser extent. Moreover, the value calculated from the net mass increase shown from the EQCM response (0.56 wt. % $g_O$ $g_{ZTC}^{-1}$) is lower than the obtained from TPD experiments, suggesting that electrochemical gasification is taking place.

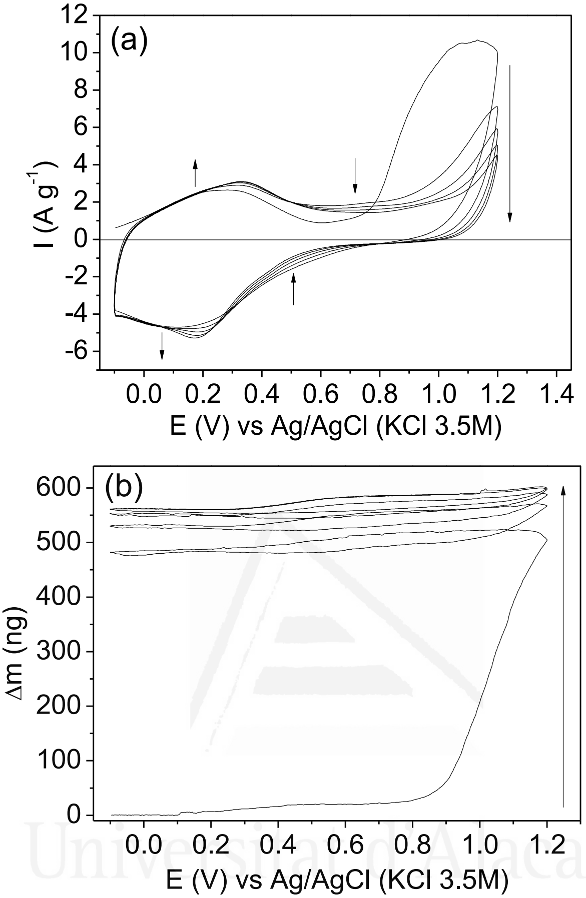

Figure V.4. Cyclic voltammograms (a) and gravimetric response (b) simultaneously obtained between -0.10 V and 1.20 V of ZTC at 5 mV s$^{-1}$ in 1M $H_2SO_4$ solution.

To further characterize the ZTC sample, more severe electrochemical conditions were applied. Firstly, 3 scans under two subsequent potential ranges (not shown here), from -0.10 V to 0.80 V (hereinafter 1st CV experiment) and from -0.10 V to 1.40 V (hereinafter 2nd CV experiment) were performed. In both potential ranges, a large electrochemical oxidation is observed mainly in the first cycle. Figure V.5 contains the 3rd voltammogram of the 2nd CV experiment done between -0.10 V and

1.40 V (dashed line), showing that when reaching the potential value of 1.40 V less reversible redox processes appear (the anodic and cathodic peaks are observed at around 0.37 V and 0.05 V, respectively).

After this experiment, the electrode was maintained at a constant potential value of 1.40 V during 2 hours. In this experiment (not shown here) only a slight mass increase of 40 ng is observed in spite of the high potential applied for quite long time. This result points out that both processes electrochemical oxidation and electrochemical gasification take place simultaneously. After that, 20 scans between -0.10 V and 1.40 V were done (hereinafter 3rd CV experiment, results not shown here). A large decrease in the current density is observed, that is probably due to loss of conductivity, since the degradation of the ZTC sample (that involves the decrease in size of graphene-like domains) presumably occurs under the electrochemical conditions applied so far. Subsequently, the electrode was maintained at a constant potential value of -0.10 V during 2 hours (experiment not shown here). In this case, a significant net mass change is also not observed. Finally, the electrode was submitted to 22 scans between -0.10 V and 1.40 V (Figure V.6) (hereinafter 4th CV experiment), the 22nd cyclic voltammogram is shown in Figure V.5 (solid line).

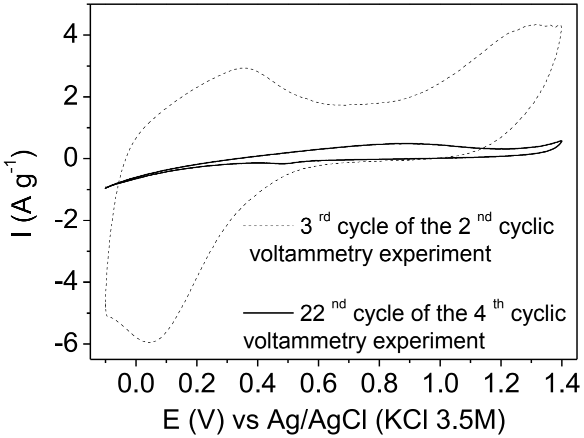

Figure V.5. Cyclic voltammograms between -0.10 V and 1.40 V of ZTC at 5 mV s$^{-1}$ in 1M $H_2SO_4$ solution. Dashed line (3rd scan of the 2nd CV experiment), solid line (22nd scan of the 4th CV experiment).

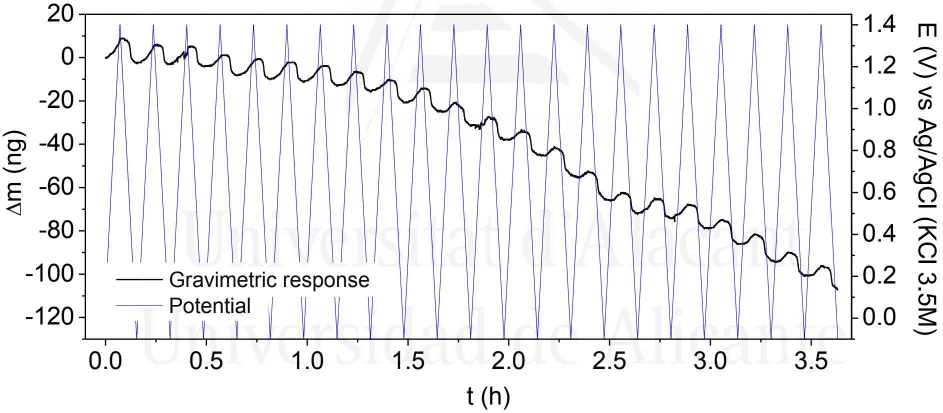

Figure V.6. Gravimetric response between -0.10 V and 1.40 V of ZTC at 5 mV s$^{-1}$ in 1M $H_2SO_4$ solution during the 22 cycles of the 4th CV experiment.

The large decrease in the current density demonstrates that the ZTC has suffered a remarkable degradation that involves a noticeable loss of conductivity and of the porous structure. In this case, in spite of the high increase of the total surface oxygen with respect to the pristine ZTC electrode (12.27 wt. % $g_O$ $g_{ZTC}^{-1}$, calculated from TPD experiments), a net mass decrease is observed (see Figure V.6), consistent with considerable mass loss due to electrochemical gasification. In fact, from the gravimetric response of the 22nd cycle (see Figure V.7) it can be clearly seen a sharp mass loss going from 0.56 V to 0.35 V. It seems that the carbon-oxygen groups, previously generated, are being reduced going to more negative potential, thus producing the electrochemical gasification of the carbon material. The net mass decrease in each cycle, of approximately 7 ng, is in the same order of magnitude as that previously reported for the electrochemical gasification of a porous carbon electrode [19].

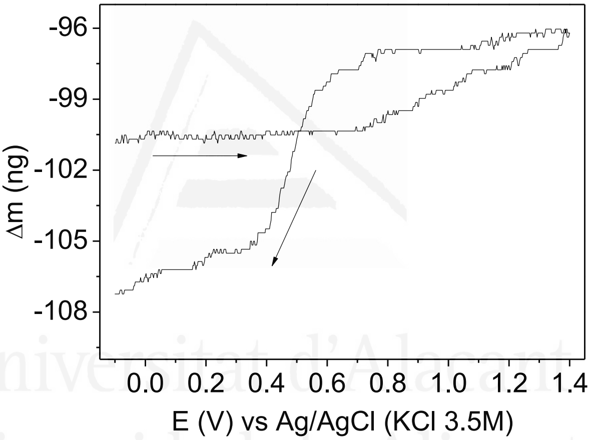

Figure V.7. Gravimetric response between -0.10 V and 1.40 V of ZTC at 5 mV $s^{-1}$ in 1M $H_2SO_4$ solution of the 22nd scan of the 4th CV experiment.

### V.3.3. *In situ* Raman characterization results

Raman spectroscopy is a useful technique for structural characterization of carbon materials. Consequently, *in situ* Raman spectroscopy was used in order to further elucidate the changes produced in ZTC due to the electrochemical oxidation and degradation processes. The potential applied to collect *in situ* Raman spectra has been based on the previous cyclic voltammograms. First of all, a spectrum at open circuit potential ($E_{oc}$) was recorded. Subsequently, the potential was varied from 0.30 V (which is the value of $E_{oc}$, approximately) to 1.20 V (where the electrochemical oxidation of ZTC is already produced) and returning to 0.30 V.

Figures V.8 and V.9 show the most revealing *in situ* Raman spectra recorded with He–Ne laser and Diode laser. In general, the first-order G and D bands (at around 1575 and 1355 cm$^{-1}$, respectively) are observed in all the spectra. These bands are characteristic of graphene based carbons, the G band corresponds to an ideal graphitic lattice vibration mode and the D band is related to the presence of defects [21,22,27,52,53]. Further analysis requires taking into account that the so called G and D bands include several bands [22,23,42,52,53]. The G band comprises not only the G band itself (1575 cm$^{-1}$) but also the D2 band (1620 cm$^{-1}$), that has been assigned to a lattice vibration analogous to that of the G band but involving graphene layers which are not directly sandwiched between two other graphene layers (i.e. 'boundary layer planes') [22,24,54]. In the case of the D band, the most intense one is the D1 band (1355 cm$^{-1}$), that is an inherent mode in the graphite lattice that becomes observable when symmetry is broken by an edge [21,27]. Furthermore, the wide D band involves the D4 band (1200 cm$^{-1}$), that has been observed for carbon film with high content of sp$^3$–carbon [54] and it has been assigned to mixed sp$^2$–sp$^3$ bonding or to C–C and C=C stretching vibration modes of polyene-like structures [55]. Moreover, the D3 band (1500 cm$^{-1}$), that seems to be related to interstitial defects either between the layers or the basic structural units of carbon films [56] or amorphous carbon [57], justifies the high signal intensity between the two peak maxima (i.e. the G and D bands).

In these experiments, the spectra shown are normalized versus the D band because the spectra are collected at different positions in the sample to avoid degradation that may be caused by the laser. It should be pointed out that, for both laser, the G band appears at 1595 $cm^{-1}$ which is a little higher wavenumber value than that of graphite, suggesting that graphene sheets in ZTC are not fully developed nanometer-sized sheets [1,43].

Spectra recorded with the He–Ne laser are presented in Figure V.8. The spectra registered at $E_{oc}$ and at 0.30 V are almost equal, as expected. In these spectra the G band is narrower than the D one. It seems that the D band has a remarkable contribution of the D4 band (see the shoulder at approximately 1200 $cm^{-1}$), suggesting that initially the ZTC contains some amount of $sp^3$–carbon atoms. Since the ZTC structure consists in a three-dimensional ordered network of buckybowl-like nanographenes, and taking into account that the main band of the $C_{60}$ fullerene appears at approximately 1469 $cm^{-1}$ (which has been assigned to pentagonal pinch mode [39-41,58]), the shoulder observed at around 1463 $cm^{-1}$ seems to be due to the presence of curved graphitic planes in ZTC [1,43].

Going to more positive potential values, significant changes are observed. The D band becomes narrower and the contribution of the D4 band seems to decrease with increasing electrochemical oxidation; i.e., the content of $sp^3$–carbon decreases, thus suggesting that $sp^3$–carbon are the most reactive carbon atoms where the electrochemical oxidation and gasification of the ZTC initially occurs (see Reactions V.1, V.2 and V.8). ZTC oxidation and gasification continues as detected by EQCM through other reactive carbon atoms or nascent reactive sites formed (see Reactions V.5 and V.7 as possible pathways). Furthermore, an upshift of the D band is observed that remains even returning to 0.30 V. For SWCNTs it has been previously reported that the D band strongly upshifts reversibly under anodic polarization presumably due to contraction and stiffening of C–C bonds produced by hole doping (and only a small variation is registered under cathodic conditions) [35]. Moreover, for graphite samples, an upshift of the D band has been observed under compressive strain [59]. Therefore the upshift of the D band may be due both to anodic polarization and compressive strain of the ZTC structure as a consequence of the electrochemical oxidation and gasification processes that take place under the electrochemical treatment applied (since the D band upshifts remains even returning to 0.30 V). It should be pointed out that in the spectrum recorded at 1.10 V, an intensity increase and upshift of the band related to pentagonal pinch mode is observed (see the peak at around 1489 cm$^{-1}$). The intensity increase of the Raman modes of $C_{60}$ fullerene peapods has been previously reported (‘anodic enhancement’) [41], and the upshift is generally attributed to the oxidation of $C_{60}$ to $C_{60}^{+}$, which is extremely difficult to achieve [31]. Here, the complex structure of the ZTC may explain these Raman shifts.

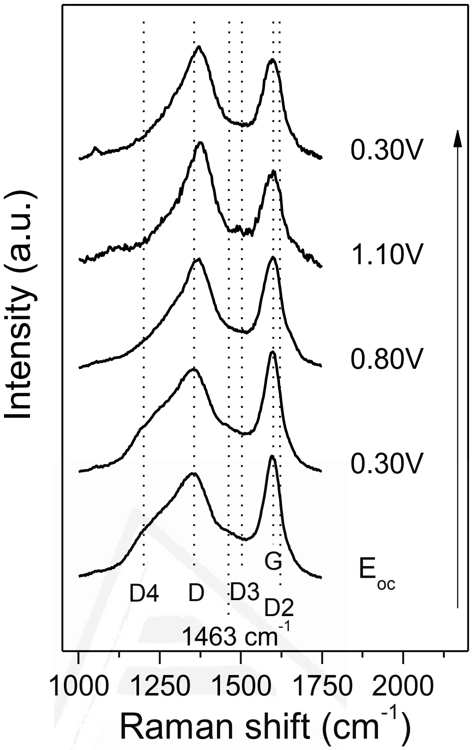

Figure V.8. Raman spectra recorded with He–Ne laser of the ZTC sample at different potentials referred to Ag/AgCl (KCl 3 M) in 1 M $H_2SO_4$ solution. Spectra normalized versus the D band.

Figure V.9 shows the spectra recorded using the Diode laser. As in the previous experiment, the spectra recorded at $E_{oc}$ and at 0.30 V are very similar. In these spectra, apart from the D and G bands described earlier, the main band of $C_{60}$ fullerene assigned to pentagonal pinch mode also appears at 1478 cm$^{-1}$. The intensity of this band also increases under anodic polarization. Furthermore, a shoulder in the G band between 1650 cm$^{-1}$ and 1750 cm$^{-1}$ is seen in the spectrum recorded at 1.00 V, which could be associated to the M band

(1750 $cm^{-1}$) that has been assigned to an overtone of the “out-of-plane” mode of 867 $cm^{-1}$ for graphite samples [30,60].

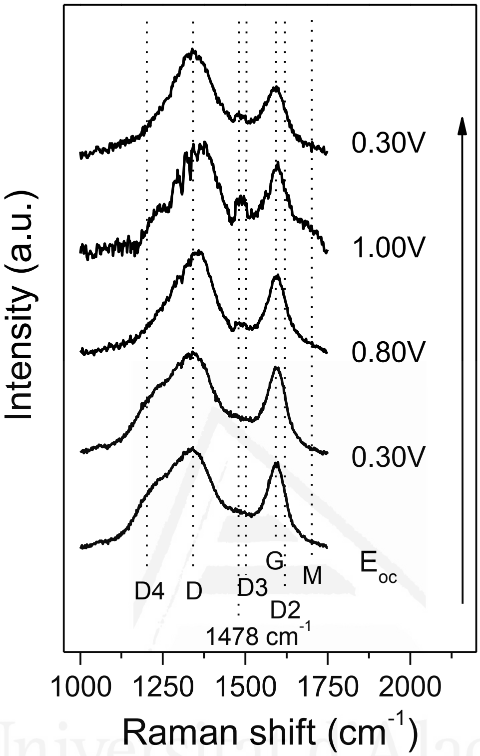

Figure V.9. Raman spectra recorded with Diode laser of the ZTC sample at different potentials referred to Ag/AgCl (KCl 3 M) in 1 M $H_2SO_4$ solution. Spectra normalized versus the D band.

The ratio between the D and G bands intensities ($I_D/I_G$) increases with the electrochemical treatment applied. Figure V.10 presents the variation of $I_D/I_G$ ratio for all the spectra recorded with the He–Ne laser. Since the increase of $I_D/I_G$ indicates higher degree of disorder in the graphitic structure [22,61,62], the electrochemical oxidation and gasification processes seem to produce the degradation of the sample, as it has been previously shown from the EQCM results because a decrease of the potential to the initial one (0.30 V) does not recover the

$I_D/I_G$ ratio. It should be pointed out that the $I_D/I_G$ at the potential value of 1.20 V gets out of the trend, that may be due to the high content of oxygen groups that the ZTC presents at this potential value, which produces a remarkable fluorescence effect [29] that hinders the definition of the baseline and may produce erroneous relative intensities of some Raman bands, thus explaining the behaviour observed.

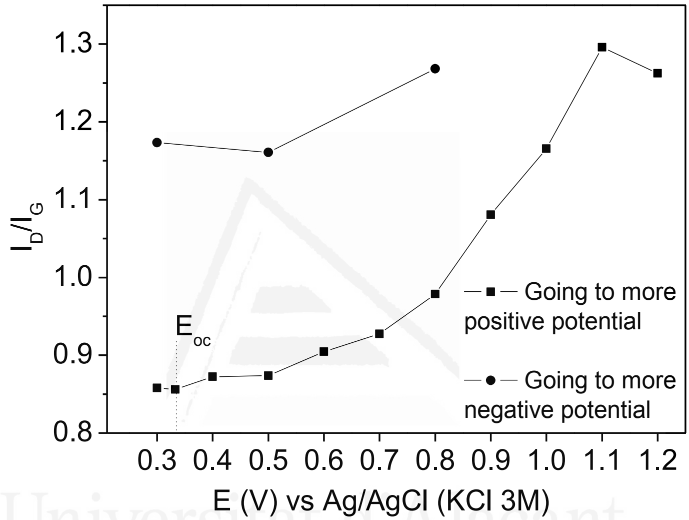

Figure V.10. ID/IG for He–Ne laser of the ZTC sample. Square symbol (■) going to more positive potential, circle symbol (●) going to more negative potential after the scan to positive potential.

According to previous research, the higher the excitation laser wavelength the higher the $I_D/I_G$ [21,22,53,63] (the change of relative signals intensities with excitation wavelength can be attributed to resonance effects [22,53]). In this case, from the Figures V.8 and V.9 it is shown that the $I_D/I_G$ ratio is higher for the Diode laser than for the He–Ne laser.

## V.4. Conclusions

EQCM allows the simultaneously monitoring of both voltammetric and gravimetric responses of ZTC under electrochemical conditions. ZTC is greatly electrochemically oxidized in the first voltammetric cycles under the potential intervals from -0.10 V up to 0.80 V, 1.20 V and 1.40 V as shown by the oxidation current and the large mass increase recorded at high potential values. Since the mass increase is lower than that expected from the increase in the specific capacitance value and from the TPD results, it seems that the electrochemical oxidation and gasification of the ZTC take place simultaneously. Under more severe electrochemical conditions (i.e. by performing large number of cyclic voltammograms between -0.10 V and 1.40 V and potentiostatic experiments at 1.40 V and -0.10 V), a large decrease in the current density demonstrates that the ZTC has suffered a remarkable degradation that involves a noticeable loss of conductivity and of the porous structure. Moreover, a net mass decrease is recorded, showing that electrochemical gasification of the sample occurs to a considerable extent. Analyzing a single voltammogram, a sharply net mass loss has been recorded going to more negative potential, showing that electrochemical gasification of the carbon material can occur not only under anodic conditions but also under cathodic conditions (i.e. by reducing carbon-oxygen groups generated under anodic conditions going to more negative potential). The gravimetric response has been demonstrated to be useful to further explain the electrochemical oxidation and gasification processes displayed by the voltammetric response. Furthermore, mass changes related to adsorption and desorption of ions and water molecules during the formation of the EDL can be detected.

Concerning *in situ* Raman spectroscopy, it has been shown that the complex structure of the ZTC requires detailed analysis of the characteristic first-order bands of graphene based carbons (i.e. the D and G bands). In addition, the spectra show bands related to $C_{60}$ fullerene, thus supporting that the ZTC comprises curved nanographenes sheets. Furthermore, it is shown that the electrochemical oxidation of ZTC under anodic conditions produces structural changes that involve the degradation of the three-dimensional regular network, as demonstrated by the increase of the $I_D/I_G$ (which indicates higher degree of disorder in the graphitic structure). Moreover, by increasing the potential to more positive values an intensity decrease of the band related to $sp^3$–carbon content (D4) is observed, thus suggesting that $sp^3$–carbon are reactive dangling carbon atoms where the electrochemical gasification of the carbon material occurs. Finally, the spectra obtained from the two lasers complement each other, allowing further explanation of the changes produced in the ZTC by varying the potential applied.

## References

[1] Nishihara H, Yang Q, Hou P, Unno M, Yamauchi S, Saito R et al. A possible buckybowl-like structure of zeolite templated carbon. Carbon 2009;47:1220-30.

[2] Itoi H, Nishihara H, Ishii T, Nueangnoraj K, Berenguer-Betrián R, Kyotani T. Large pseudocapacitance in quinone-functionalized zeolite-templated carbon. Bull Chem Soc Jpn 2014;87:250-7.

[3] Matsuoka K, Yamagishi Y, Yamazaki T, Setoyama N, Tomita A, Kyotani T. Extremely high microporosity and sharp pore size distribution of a large surface area carbon prepared in the nanochannels of zeolite Y. Carbon 2005;43:876-9.

[4] Nishihara H, Itoi H, Kogure T, Hou P, Touhara H, Okino F et al. Investigation of the ion storage/transfer behavior in an electrical double-layer capacitor by using ordered microporous carbons as model materials. Chem Eur J 2009;15:5355-63.

[5] Ma Z, Kyotani T, Tomita A. Preparation of a high surface area microporous carbon having the structural regularity of Y zeolite. Chem Commun 2000:2365-6.

[6] Ma Z, Kyotani T, Tomita A. Synthesis methods for preparing microporous carbons with a structural regularity of zeolite Y. Carbon 2002;40:2367-74.

[7] Berenguer R, Nishihara H, Itoi H, Ishii T, Morallón E, Cazorla-Amorós D et al. Electrochemical generation of oxygen-containing groups in an ordered microporous zeolite-templated carbon. Carbon 2013;54:94-104.

[8] Watanabe M, Uchida H, Ikeda N. Electrochemical quartz crystal microbalance study of copper ad-atoms on gold and platinum electrodes Part I. Adsorption of anions in sulfuric acid. J Electroanal Chem 1995;380:255-60.

[9] Inoue M, Nakazawa A, Umeda M. Study of Pt electrode dissolution in $H_2O_2$-containing $H_2SO_4$ solution using an electrochemical quartz crystal microbalance. J Power Sources 2011;196:4579-82.

[10] Gloaguen F, Léger J-, Lamy C. An electrochemical quartz crystal microbalance study of the hydrogen underpotential deposition at a Pt electrode. J Electroanal Chem 1999;467:186-92.

[11] Bruckenstein S, Brzezinska K, Hillman A. EQCM studies of polypyrrole films. 1. Exposure to aqueous sodium tosylate solutions under thermodynamically permselective conditions. Electrochim Acta 2000;45:3801-11.

[12] Dam VAT, Jayasayee K, de Bruijn FA. Determination of the potentiostatic stability of PEMFC electro catalysts at elevated temperatures. Fuel Cells 2009;9:453-62.

[13] Hung CC, Lim PY, Chen JR, Shih HC. Corrosion of carbon support for PEM fuel cells by electrochemical quartz crystal microbalance. J Power Sources 2011;196:140-6.

[14] Yadav AP, Sugawara Y, Nishikata A, Tsuru T. Electrochemical Stability and Oxidation Mechanism of Carbon Support for PEM Fuel cell. ECS Transactions 2008;16:2093-9.

[15] Levi MD, Levy N, Sigalov S, Salitra G, Aurbach D, Maier J. Electrochemical quartz crystal microbalance (EQCM) studies of ions and solvents insertion into highly porous activated carbons. J Am Chem Soc 2010;132:13220-2.

[16] Levi MD, Salitra G, Levy N, Aurbach D, Maier J. Application of a quartz-crystal microbalance to measure ionic fluxes in microporous carbons for energy storage. Nature Mater 2009;8:872-5.

[17] Sigalov S, Levi MD, Salitra G, Aurbach D, Maier J. EQCM as a unique tool for determination of ionic fluxes in microporous carbons as a function of surface charge distribution. Electrochem Commun 2010;12:1718-21.

[18] Barisci J, Wallace G, Baughman R. Electrochemical quartz crystal microbalance studies of single-wall carbon nanotubes in aqueous and non-aqueous solutions. Electrochim Acta 2000;46:509-17.

[19] Morallón E, Arias-Pardilla J, Calo JM, Cazorla-Amorós D. Arsenic species interactions with a porous carbon electrode as determined with an electrochemical quartz crystal microbalance. Electrochim Acta 2009;54:3996-4004.

[20] Kim I, Egashira M, Yoshimoto N, Morita M. On the electric double-layer structure at carbon electrode/organic electrolyte solution interface analyzed by ac impedance and electrochemical quartz-crystal microbalance responses. Electrochim Acta 2011;56:7319-26.

[21] Wang Y, Alsmeyer DC, McCreery RL. Raman spectroscopy of carbon materials: structural basis of observed spectra. Chem Mater 1990;2:557-63.

[22] Sadezky A, Muckenhuber H, Grothe H, Niessner R, Poschl U. Raman micro spectroscopy of soot and related carbonaceous materials: Spectral analysis and structural information. Carbon 2005;43:1731-42.

[23] Cuesta A, Dhamelincourt P, Laureyns J, Martínez-Alonso A, Tascón J. Raman microprobe studies on carbon materials. Carbon 1994;32:1523-32.

[24] Bowling RJ, Packard RT, McCreery RL. Activation of highly ordered pyrolytic graphite for heterogeneous electron transfer: relationship between electrochemical performance and carbon microstructure. J Am Chem Soc 1989;111:1217-23.

[25] Wang J, Zhu M, Outlaw R, Zhao X, Manos D, Holloway B et al. Free-standing subnanometer graphite sheets. Appl Phys Lett 2004;85:1265-7.

[26] Cançado L, Takai K, Enoki T, Endo M, Kim Y, Mizusaki H et al. General equation for the determination of the crystallite size La of nanographite by Raman spectroscopy. Appl Phys Lett 2006;88:163106.

[27] Tuinstra F, Koenig JL. Raman spectrum of graphite. J Chem Phys 1970;53:1126-30.

[28] Leyva-García S, Morallón E, Cazorla-Amorós D, Béguin F, Lozano-Castelló D. New insights on electrochemical hydrogen storage in nanoporous carbons by in situ Raman spectroscopy. Carbon 2014;69:401-8.

[29] Bleda-Martínez MJ, Pérez JM, Linares-Solano A, Morallón E, Cazorla-Amorós D. Effect of surface chemistry on electrochemical storage of hydrogen in porous carbon materials. Carbon 2008;46:1053-9.

[30] Brar V, Samsonidze G, Dresselhaus M, Dresselhaus G, Saito R, Swan A et al. Second-order harmonic and combination modes in graphite, single-wall carbon nanotube bundles, and isolated single-wall carbon nanotubes. Phys Rev B 2002;66:155418.

[31] Kalbáč M, Kavan L, Zukalova M, Dunsch L. In situ Raman spectroetectrochemical study of $C^{13}$-Labeled fullerene peapods and carbon nanotubes. Small 2007;3:1746-52.

[32] Costa SD, Fantini C, Righi A, Bachmatiuk A, Rümmeli MH, Saito R et al. Resonant Raman spectroscopy on enriched $^{13}C$ carbon nanotubes. Carbon 2011;49:4719-23.

[33] Corio P, Santos P, Brar V, Samsonidze G, Chou S, Dresselhaus M. Potential dependent surface Raman spectroscopy of single wall carbon nanotube films on platinum electrodes. Chem Phys Lett 2003;370:675-82.

[34] Dresselhaus M, Dresselhaus G, Saito R, Jorio A. Raman spectroscopy of carbon nanotubes. Phys Rep Rev Sec Phys Lett 2005;409:47-99.

[35] Ruch PW, Hardwick LJ, Hahn M, Foelske A, Koetz R, Wokaun A. Electrochemical doping of single-walled carbon nanotubes in double layer capacitors studied by *in situ* Raman spectroscopy. Carbon 2009;47:38-52.

[36] Falke S, Eravuchira P, Materny A, Lienau C. Raman spectroscopic identification of fullerene inclusions in polymer/fullerene blends. J Raman Spectrosc 2011;42:1897-900.

[37] Li G, Han Z, Piao G, Zhao J, Li S, Liu G. To distinguish fullerene C60 nanotubes and C60 nanowhiskers using Raman spectroscopy. Mater Sci Eng B 2009;163:161-4.

[38] Bethune DS, Meijer G, Tang WC, Rosen HJ. The vibrational Raman spectra of purified solid films of C60 and C70. Chemical Physics Letters 1990;174:219-22.

[39] Bethune DS, Meijer G, Tang WC, Rosen HJ, Golden WG, Seki H et al. Vibrational Raman and infrared-spectra of chromatographically separated C60 and C70 fullerene clusters. Chem Phys Lett 1991;179:181-6.

[40] Ikeda K, Uosaki K. Resonance hyper-Raman scattering of fullerene C-60 microcrystals. J Phys Chem A 2008;112:790-3.

[41] Kavan L, Dunsch L, Kataura H, Oshiyama A, Otani M, Okada S. Electrochemical tuning of electronic structure of C-60 and C-70 fullerene peapods: In situ visible near-infrared and Raman study. J Phys Chem B 2003;107:7666-75.

[42] Sze S, Siddique N, Sloan J, Escribano R. Raman spectroscopic characterization of carbonaceous aerosols. Atmos Environ 2001;35:561-8.

[43] Paredes J, Martinez-Alonso A, Yamazaki T, Matsuoka K, Tascon J, Kyotani T. Structural investigation of zeolite-templated, ordered microporous carbon by scanning tunneling microscopy and Raman spectroscopy. Langmuir 2005;21:8817-23.

[44] Hou P, Yamazaki T, Orikasa H, Kyotani T. An easy method for the synthesis of ordered microporous carbons by the template technique. Carbon 2005;43:2624-7.

[45] Buttry DA. Applications of the quartz crystal microbalance to electrochemistry. Bard editor ed. New York: Electroanalytical Chemistry. A series of advances, 1990.

[46] Buttry DA, Ward MD. Measurement of interfacial processes at electrode surfaces with the electrochemical quartz crystal microbalance. Chem Rev 1992;92:1355-9.

[47] Román-Martínez MC, Cazorla-Amorós D, Linares-Solano A. TPD and TPR characterization of carbonaceous supports and Pt/C catalysts. Carbon 1993;31:895-902.

[48] Figueiredo J, Pereira M, Freitas M, Orfao J. Modification of the surface chemistry of activated carbons. Carbon 1999;37:1379-89.

[49] Kinoshita K. Carbon: electrochemical and physicochemical properties. New York: Wiley, 1998.

[50] Leon y Leon CA, Radovic LR. Interfacial chemistry and electrochemistry of carbon surfaces. In: Thrower PA, editor. Chemistry and physics of carbon, New York: Marcel Dekker; 1994, p. 213-310.

[51] Bleda-Martínez MJ, Lozano-Castelló D, Morallón E, Cazorla-Amorós D, Linares-Solano A. Chemical and electrochemical characterization of porous carbon materials. Carbon 2006;44:2642-51.

[52] Jawhari T, Roid A, Casado J. Raman spectroscopic characterization of some commercially available carbon black materials. Carbon 1995;33:1561-5.

[53] Antunes EF, Lobo AO, Corat EJ, Trava-Airoldi VJ, Martin AA, Veríssimo C. Comparative study of first- and second-order Raman spectra of MWCNT at visible and infrared laser excitation. Carbon 2006;44:2202-11.

[54] Schwan J, Ulrich S, Batori V, Ehrhardt H, Silva S. Raman spectroscopy on amorphous carbon films. J Appl Phys 1996;80:440-7.

[55] Dippel B, Jander H, Heintzenberg J. NIR FT Raman spectroscopic study of flame soot. Phys Chem Chem Phys 1999;1:4707-12.

[56] Rouzaud JN, Oberlin A, Beny-Bassez C. Carbon films: Structure and microtexture (optical and electron microscopy, Raman spectroscopy). Thin Solid Films 1983;105:75-96.

[57] Ivleva NP, Messerer A, Yang X, Niessner R, Poeschl U. Raman microspectroscopic analysis of changes in the chemical structure and reactivity of soot in a diesel exhaust aftertreatment model system. Environ Sci Technol 2007;41:3702-7.

[58] Luo Z, Zhao YS, Yang W, Peng A, Ma Y, Fu H et al. Core-shell nanopillars of fullerene C-60/C-70 loading with colloidal an nanoparticles: a Raman scattering investigation. Journal of Physical Chemistry a 2009;113:9612-6.

[59] del Corro E, Otero de la Roza A, Taravillo M, Baonza VG. Raman modes and Gruneisen parameters of graphite under compressive biaxial stress. Carbon 2012;50:4600-6.

[60] McDonald-Wharry J, Manley-Harris M, Pickering K. Carbonisation of biomass-derived chars and the thermal reduction of a graphene oxide sample studied using Raman spectroscopy. Carbon 2013;59:383-405.

[61] Osswald S, Havel M, Gogotsi Y. Monitoring oxidation of multiwalled carbon nanotubes by Raman spectroscopy. J Raman Spectrosc 2007;38:728-36.

[62] Rozada R, Paredes JI, Villar-Rodil S, Martinez-Alonso A, Tascon JMD. Towards full repair of defects in reduced graphene oxide films by two-step graphitization. Nano Res 2013;6:216-33.

[63] Sood A, Gupta R, Asher S. Origin of the unusual dependence of Raman D band on excitation wavelength in graphite-like materials. J Appl Phys 2001;90:4494-7.

# Chapter VI

# Silica-templated ordered mesoporous carbon thin films as electrodes for micro-capacitors

## VI.1. Introduction

Supercapacitors (or electrochemical capacitors) are based on the formation of the electric double-layer (EDL) in the interphase electrode-electrolyte and the quick faradic charge transfer reactions between the electrolyte and the electrode (i.e. pseudocapacitance). Porous carbon materials have been intensely investigated as electrodes for supercapacitors because of their low-cost, versatility of structure/texture, good conductivity and high cycling life. Due to these mechanisms in supercapacitors based on carbon electrodes, porous structure and pore size distribution are key parameters to improve the capacitance of the electrodes [1-3]. It is well known that micropores provide abundant adsorption sites for the ions of the electrolyte, thus determining the capacitance values [3-6]. Furthermore, the presence of mesopores might be beneficial to interconnect the pore network, thus promoting fast diffusion of the electrolyte [7-11]. Accordingly, many studies on the synthesis of microporous, mesoporous and hierarchical ordered carbon materials can be found. Currently, there is an increasing interest on templated carbons because they combine both tailored and ordered porous network that could result in the development of unique features for energy storage applications [7-10,12-17]. Furthermore, in recent times, silica/carbon composites, which preserve the ordered pore structure of the silica, are being studied as electrodes for electrochemical capacitors [17-19].

The recent technological trend towards portable electronic devices has led to a strong interest in small-scale energy storage devices. The standard method to prepare carbon electrodes from powdered carbon materials presents some disadvantages e.g. the use of polymeric binders and conductive additives and the high electrical resistivity caused by the presence of macroporosity between the particles. Furthermore, the amount of the active material in the final electrode is between 80 and 90 wt %, which is also a significant drawback. Thin film capacitors (or micro-capacitors) have great potential to be used as power source in small-scale energy storage devices, because a continuous thin film of a carbon material with the proper porous texture directly synthesized on a suitable current collector could avoid some of the disadvantages associated with the standard preparation method of carbon electrodes. Taking into account that thickness of the electrode plays an important role in the path length for the ions, the thickness of micro-capacitors electrodes (ranging from nm [20] to few µm [21]) is a noticeable advantage compared to conventional supercapacitors electrodes (that show thickness of several hundreds of µm [22]). According to all the aforementioned, micro-capacitors may show high capacitance values and rate performance, which are required for high power density and energy density systems. In this regard, several studies can be found on electrochemical capacitors based on thin films made from: graphene and reduced graphene oxide (rGO) [20,23], carbon nanotubes (CNTs) [24,25], n-doped silicon nanowires [26] or conducting polymers e.g. polypyrrole [27]. Several works can also be found on interdigitated chips based on: transition metal oxides e.g. $MnO_2$ [28] or $RuO_x$ [29], $VS_2$ nanosheets [30], VN and NiO films [31], powdered activated carbon (ACs) [21] or composites containing e.g. rGO [32], graphene [33] and carbon fibres [34] among others.

Consequently, the objective of the work presented in this chapter is to synthesize a continuous thin film of a mesoporous carbon material directly on a graphite current collector, without the use of binders or conductivity promoters, and to study its potential application as electrodes for micro-capacitors. The carbon thin film was synthesized using an ordered mesoporous silica thin film as hard template and sucrose as carbon source. The nanostructure of the silica, the composite silica/carbon and the mesoporous carbon thin films was characterized by field emission scanning electron microscopy (FE-SEM) coupled to energy dispersive X-ray spectroscopy (EDX), transmission electron microscopy (TEM) and Raman spectroscopy. Furthermore, the electrochemical behaviour of mesoporous carbon and composite silica/carbon thin films was analysed in 1M $H_2SO_4$ by cyclic voltammetry (CV) and galvanostatic charge-discharge (GCD) techniques. The results show that both the mesoporous carbon thin film and composite silica/carbon thin film exhibit high specific capacitance and excellent rate performance and electrochemical stability, what make them excellent candidates as electrodes for micro-capacitors.

## VI.2. Experimental

### VI.2.1. Synthesis of ordered mesoporous silica thin films

To obtain both tailored and ordered mesoporous carbon thin film, a nanostructured silica thin film was successfully synthesized onto the graphite current collector and used as hard-template. Tetraethylorthosilicate (TEOS) was employed as the silica source and the tri-block co-polymer Pluronic® F127 was used as the structure directing agent. A commercial graphite current collector plate (POCO Graphite) of around 15 x 35 $mm^2$ was dip-coated in the precursor solution with molar ratio of 1 TEOS:$6.60\cdot10^{-3}$ F127:$6.66\cdot10^{-3}$ HCl:4.62 $H_2O$:22.6 EtOH (that has been previously used to synthesize a rombohedral silica thin film by spin-coating method [35]). The constant withdrawal rate was 60 mm $min^{-1}$ and the relative humidity was maintained at 50 %. The film was aged at room temperature and relative humidity of 50 % during 24 h and, then, it was heated at 80 ºC for 24 h. Finally, the synthesized thin film was calcined at 450 ºC (ramp of 1 ºC $min^{-1}$) for 5 h in air, in order to eliminate the Pluronic® F127.

### VI.2.2. Synthesis of mesoporous carbon thin films

Mesoporous carbon thin film was synthesized using sucrose ($C_{12}H_{22}O_{11}$) as carbon source and the nanostructured silica thin film as hard-template. The synthesis is similar to that reported by Ryoo et al. [36]. Briefly, the synthesized mesoporous silica thin film was dip-coated in an aqueous solution with molar ratio of $3.65\cdot10^{-3}$ $C_{12}H_{22}O_{11}$: $1.43\cdot10^{-3}$ $H_2SO_4$: 0.28 $H_2O$. The constant withdrawal rate was 9 mm $min^{-1}$. The film was then dried at 100 ºC for 4 h and, subsequently, pre-carbonized at 160 ºC for 4 h. After that, the silica thin film containing partially polymerized and carbonized sucrose, was dip-coated in a solution with molar ratio of $2.34\cdot10^{-3}$ $C_{12}H_{22}O_{11}$: $0.92\cdot10^{-3}$ $H_2SO_4$: 0.28 $H_2O$. Then, the composite was also dried and pre-carbonized at the same conditions formerly explained. After that, the composite was carbonized in an oven under a $N_2$ flow of 100 ml $min^{-1}$ at 900 ºC (ramp of 10 ºC $min^{-1}$) for 6 h. The mesoporous carbon thin film was obtained by removing the silica template with HF (40 %) for 4 h and subsequently washing with copious amounts of deionized water.

### VI.2.3. SEM, TEM and Raman characterization

FE-SEM (ZEISS, Merlin VP Compact model) coupled to EDX (BRUKER Quantax 400 model) equipment was used to analyse the distribution of the silica thin film onto the graphite plate surface.

The nanostructure of the synthesized samples (mesoporous silica, composite silica/carbon and mesoporous carbon thin films) was analysed by TEM (JEOL, JEM–2010 model). A small amount of the sample, obtained by scraping the surface of the graphite plate, was suspended in few drops of ethanol; and a drop of this suspension was then deposited onto a 300 mesh Lacey copper grid and left to dry at room temperature.

Raman spectroscopy (same equipment as used in the previous chapters, i.e. Jobin–Yvon Horiba LabRam model coupled to an upright microscope Olympus BX30) was employed to further characterize the nanostructure of the composite silica/carbon and mesoporous carbon thin films. Since the spectra obtained from these samples cannot be isolated from the graphite current collector background signal, the Raman spectra of the silica thin film and the bare graphite current corrector were also recorded to better explain the spectra collected from the mesoporous carbon and composite silica/carbon thin films. The excitation line was provided by a 9mW He–Ne laser at 632.8 nm. The laser beam was focused through a 100 x long-working objective. Each spectrum was acquired for 30 s.

### VI.2.4. Electrochemical characterization

Electrochemical characterization of the mesoporous carbon and the composite silica/carbon thin films was performed in 1M $H_2SO_4$ solution, using the three-electrode cell configuration. Furthermore, two-electrode cell configuration experiments were performed to study the electrochemical performance of the thin films synthesized in a capacitor. During the electrochemical measurements the temperature was controlled at 25 ºC.

A typical pyrex cell for the three-electrode cell configuration test was used. A platinum wire was used as the counter-electrode and Ag/AgCl (3.5 M KCl) as the reference electrode. A geometrical area of the synthesized thin film (of 15 x 35 $mm^2$) was immersed in the solution and used as the working electrode.

Two-electrode cells were built using the Swagelok® configuration and gold current collectors, with Nylon® separator between the thin films. The total geometrical area of the two electrodes used was around 50 $mm^2$.

Regarding the CV characterization, two cyclic voltammograms were performed at several scan rates ranging from 2 to 5000 mV $s^{-1}$. From the 2nd cyclic voltammogram the specific capacitance (C in F $cm^{-2}$) was calculated using the equation applied in the previous chapters:

$$C = \frac{Q/_2}{\Delta E} \qquad \textbf{Equation VI.1}$$

Where $Q$ is the total electrical charge obtained by integration of the cyclic voltammogram (C $cm^{-2}$) and $\Delta E$ is the potential window (V).

It should be pointed out that, hereafter, $cm^2$ refers to geometrical area of the working electrode in a three-electrode cell configuration and to the sum of the geometrical area of both electrodes in a two-electrode cell configuration.

After the CV characterization, GCD was performed at different current densities between 1 and 40 mA $cm^{-2}$. Additionally, durability test at 10 mA $cm^{-2}$ was performed for the two-electrode cell configuration. From the slope of the discharge galvanostatic curve, the specific capacitance (C in F $cm^{-2}$) was calculated using Equation 2:

$$C = \frac{I \cdot \Delta t}{\Delta E} \qquad \textbf{Equation VI.2}$$

Where $I$ is the discharge current density (mA $cm^{-2}$), $\Delta t$ is the discharge time (s) and $\Delta E$ is the potential range of the discharge (V).

All the electrochemical measurements were performed with potentiostat-galvanostats Biologic (VSP model) and Arbin (SCTS-TA-4 model).

## VI.3. Results and discussion

### VI.3.1. SEM, TEM and Raman characterization results

Figures VI.1.a and VI.1.b show the FE-SEM and the corresponding EDX silicon mapping analysis of the mesoporous silica thin film deposited onto the graphite current collector. Considering that the current collector is commercial graphite synthesized just by pressing graphite particles (randomly oriented in the plate), it presents macropores, that are clearly observed in Figure VI.1.a. From Figure VI.1.b, it can be seen that the silicon atoms are almost homogeneously distributed, demonstrating that the silica thin film is uniformly deposited onto the graphite current collector. It should be noted that the roughness of the current collector could hinder the registration of the X-ray signal depending on the orientation of the detector with respect to the surface plate, thus causing dark zones in the image recorded.

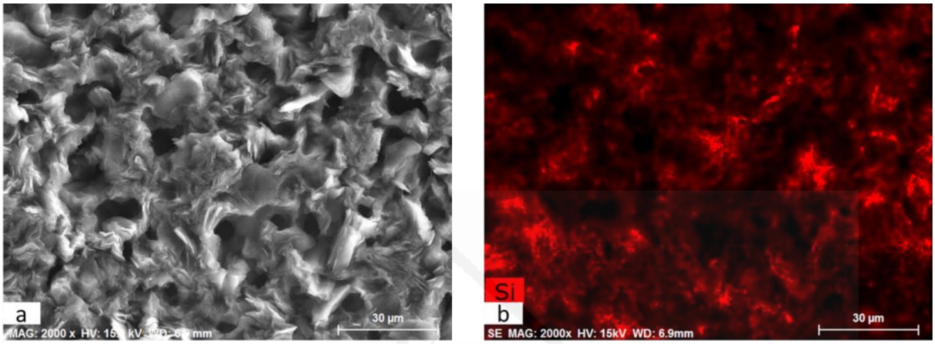

Figure VI.1. FE-SEM image (a) and corresponding EDX silicon mapping analysis (b) of the mesoporous silica thin film deposited onto the graphite current collector.

TEM images of the silica, the composite silica/carbon and the mesoporous carbon thin films are shown in Figures VI.2.a, VI.2.b and VI.2.c, respectively. From the TEM image of the silica, it can be seen that the thin film synthesized consists of ordered and homogeneous-size mesopores of around 8 nm, which are perpendicularly disposed to the graphite current collector. The TEM image of the composite silica/carbon thin film shows that the carbon thin film synthesized coats but does not fills the mesopores of the silica. The TEM image of the mesoporous carbon thin film shows that the carbon coating leads to a remarkable decrease of the pore size down to 2-3 nm. This decrease is partially related to the shrinkage of the silica structure due to thermal treatment during carbonization step [19]. Furthermore, it seems that by removing the silica template, a partial loss of structural order in the mesoporous carbon thin film occurs.

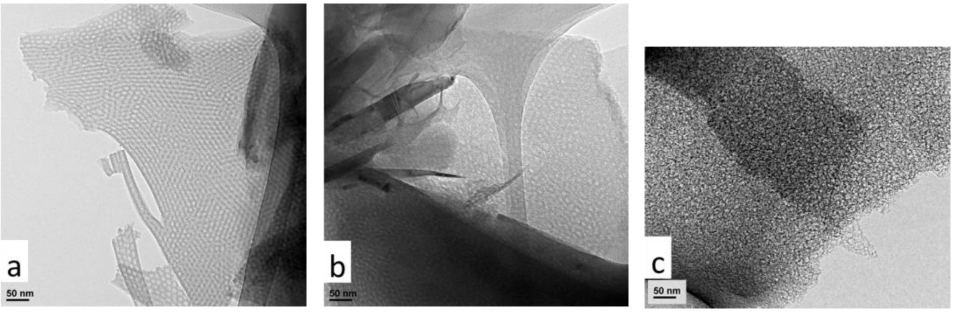

Figure VI.2. TEM image of: mesoporous silica thin film (a), composite silica/carbon thin film (b) and mesoporous carbon thin film (c).

Several studies found in the literature conclude that the best electrode performance is obtained with porous materials with pores of 2-6 nm [8,18], because mesopores with these sizes improve the kinetics of ion diffusion in the electrode, thus increasing the power performance at large current densities [1]. Accordingly, the mesoporous carbon thin film synthesized is expected to show excellent electrochemical behaviour regarding the specific capacitance and retained capacitance values.

Figure VI.3 contains the Raman spectra acquired for the bare graphite current collector, the mesoporous silica thin film, the composite silica/carbon thin film and the mesoporous carbon thin film. It should be noted that the thin films were directly analysed on the graphite current collector; therefore, the signal obtained for the samples cannot be isolated from the graphite current collector background signal. All the spectra were normalized versus the D band.

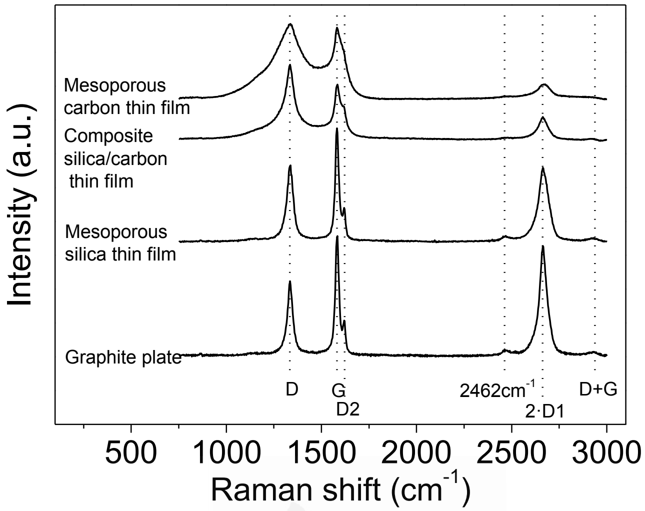

Figure VI.3. Raman spectra of the graphite plate and the mesoporous silica, composite silica/carbon and mesoporous carbon thin films. Spectra normalized versus the D band.

In general, first- and second-order characteristic bands of carbon materials are observed for all the spectra. Regarding the first-order bands, the G band (1578 cm$^{-1}$) corresponds to an ideal graphitic lattice vibration mode and the D band (1335 cm$^{-1}$) is related to the presence of defects [37-41]. It should be taken into account that the so called G and D bands include several bands [38,40-43]: the D1 band (that is an inherent mode in the graphite lattice that becomes observable when symmetry is broken by an edge [37,39]), the D2 band (1621 cm$^{-1}$), that has been assigned to a lattice vibration analogous to that of the G band but involving graphene layers which are not directly sandwiched between two other graphene layers (i.e. ‘boundary layer planes’) [38,44,45], the D3 band (at around 1500 cm$^{-1}$), that seems to be related to interstitial defects either between the layers or the basic structural units of carbon films [46] or to amorphous carbon [47] and the D4 band (at around 1200 cm$^{-1}$), that has been observed for carbon film with a high content of sp$^3$-carbon [45] and it has been assigned to mixed sp$^2$-sp$^3$ bonding.

Concerning the second-order bands (that are attributed to the combination of the first-order bands [37,38,41,42,48]), the main band appears at 2663 cm$^{-1}$ which is the first overtone of the D1 band (2·D1). It should be noted that the intensity of the 2·D1 relates to the G band intensity in graphite materials [49]. Furthermore, two less intense bands at around 2462 cm$^{-1}$ and 2937 cm$^{-1}$, that can be assigned to the first overtone of a Raman inactive graphitic lattice vibration mode at 1220 cm$^{-1}$ [37] and to the D+G band, respectively, are also observed.

The Raman spectrum of the bare graphite current collector shows the two typical intense bands of graphite, the first-order G band and the second-order 2·D1 band [50-52]. Moreover, the first-order D1 and D2 bands and the D+G second-order band and the one located at 2462 cm$^{-1}$ are also observed, as previously reported for graphite samples [38,49,53,54].

The analysis of the spectra of the thin films synthesized is not straightforward because these signals cannot be isolated from the background graphite plate signal, which, furthermore, may be slightly different depending on the illuminated zone owing to the randomly orientation of the graphite particles that comprise the graphite plate. The spectrum of the mesoporous silica thin film is almost equal to that from the graphite plate because the signal of the silica is much less intense than that of carbon materials [55,56]. From the spectra of the composite silica/carbon and mesoporous carbon thin films, the characteristic G and D bands of carbon materials are observed for the two samples. For the mesoporous carbon thin film, the D and G bands are wider than those from the composite silica/carbon, i.e. it seems that there are higher contributions from the D3 and D4 bands. Therefore, it seems that by removing the silica template the structure of the mesoporous carbon thin film relaxes, thus causing the increase of defects (as previously seen from TEM images, where it was shown that the removal of the silica template produces the partial loss of the mesoporosity order in the carbon thin film). Regarding the different intensity of the 2·D1 band between these two samples, it could be due to the different background of the graphite plate signal.

### VI.3.2. Three-electrode cell electrochemical characterization results

Both the mesoporous carbon and composite silica/carbon thin films were characterized by CV and subsequently by GCD experiments. It should be pointed out that, the bare graphite was also submitted to the same electrochemical treatment.

Prior to electrochemical characterization, the working electrode was subjected to 20 scans between 0.00 V and 0.60 V (where neither oxidation nor reduction took place) at 50 mV $s^{-1}$ to ensure that the electrode was properly wetted by the electrolyte. Then, the following procedure has been performed on the thin film electrodes. First of all, two cyclic voltammograms between 0.00 V and 0.60 V were performed at different scan rates: 2, 5, 10, 20, 50, 100, 200, 500, 1000, 2000 and 5000 mV $s^{-1}$. Subsequently, two cyclic voltammograms at 5 mV $s^{-1}$ were performed under three subsequent potential ranges going from -0.20 V to 0.80 V, from -0.40 V to 1.00 V and from -0.60 V to 1.00 V. After that, the same electrochemical treatment between 0.00 V and 0.60 V at different scan rates (between 2 and 5000 mV $s^{-1}$) was applied. Finally, the working electrode was submitted to four charge-discharge cycles between 0.00 and 0.60 V at different current densities: 2, 4, 6, 8, 10, 20 and 40 mA $cm^{-2}$.

Regarding the CV characterization results, the steady-state 2nd cyclic voltammogram of the experiments is presented. Figure VI.4.a shows the cyclic voltammograms between 0.00 V and 0.60 V for the mesoporous carbon thin film at different scan rates. The cyclic voltammograms show a quasi-rectangular shape, typical of an essentially capacitive process associated with the formation of the EDL, even at the high scan rate of 500 mV $s^{-1}$. It reveals a remarkable low inner resistance compared to conventional electrodes prepared from powdered carbon materials using binders, since even for mesoporous [7,15,57] and hierarchical [16] powdered carbon materials the shape of the cyclic voltammogram got distorted even at lower scan rate values. Figure VI.4.b shows the cyclic voltammograms done at 5 mV $s^{-1}$ under different potential windows. The cyclic voltammogram done between -0.20 V and 0.80 V (blue line) shows a quasi-rectangular shape, related to the formation of the EDL; however, during the positive cycle, an anodic current is observed going from 0.60 V to 0.80 V that is presumably related to the oxidation of the electrode material. After broadening the potential window from -0.40 V to 1.00 V (red line), several redox processes are observed. During the positive sweep a remarkable oxidation current related to the oxidation of the carbon material is recorded going from 0.60 V to 1.00 V, and the corresponding cathodic peak is observed during the subsequent negative cycle at approximately 0.37 V. Furthermore, a cathodic current, presumably related to the electrochemical hydrogen evolution process, is observed from -0.20 V to -0.40 V. Under the potential window between -0.60 V and 1.00 V (black line) a similar behaviour is observed. But, since the cathodic limit is less positive, higher reduction current associated to the electrochemical hydrogen evolution reaction is observed starting from -0.20 V to more negative potential. The peak related to the oxidation of the adsorbed hydrogen is observed at approximately 0.10 V during the subsequent positive scan [58]. In order to analyse the possible modification of the carbon thin film by the previous electrochemical treatment the potential range was changed again to 0.00 V and 0.60 V. Figure VI.4.c, shows the cyclic voltammograms done between 0.00 V and 0.60 V, at different scan rates, after opening the potential window. In this case, the cyclic voltammograms also show a quasi-rectangular shape even at high scan rate values. It should be pointed out that the specific capacitance values increase with respect to the cyclic voltammograms previously recorded (see Figure V.4.a). It seems that, by opening the potential window, the entrance of the ions of the electrolyte in all the porosity is promoted, resulting in an increase of the specific capacitance values. Moreover, some pseudocapacitance is observed at low scan rates as a consequence of the formation of oxygen surface groups during the characterization at high positive potential limit (Figure VI.4.b).

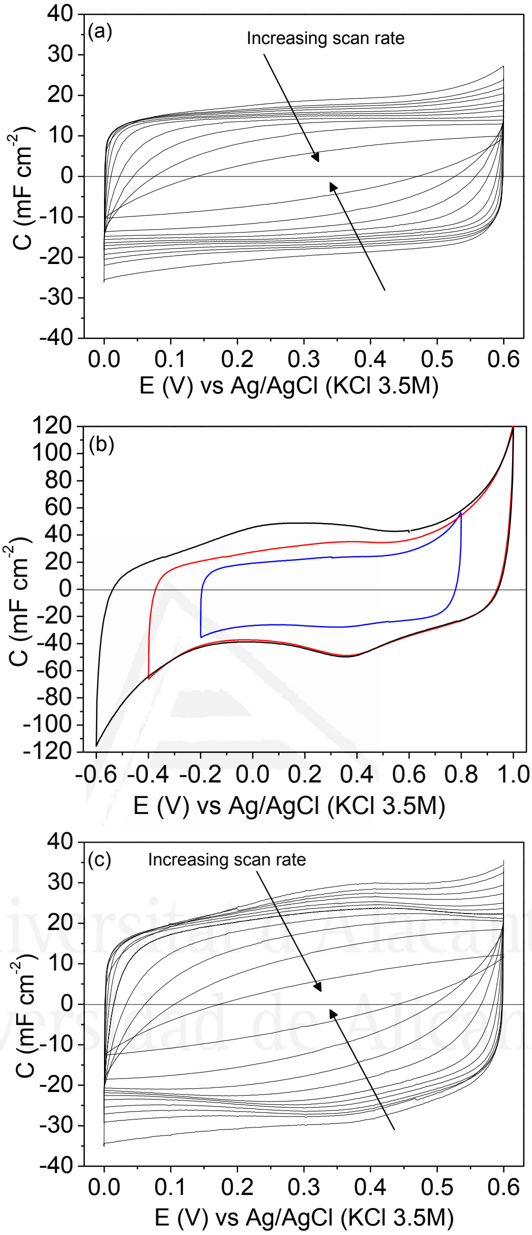

Figure IV.4. Cyclic voltammograms of the mesoporous carbon thin film in 1M $H_2SO_4$ solution: between 0.00 V and 0.60 V at 2, 5, 10, 20, 50, 100, 200, 500, 1000, 2000, 5000 mV $s^{-1}$ (a); between -0.20 V and 0.80 V (blue line), between -0.40 V and 1.00 V (red line) and between -0.60 V and 1.00 V (black line) at 5 mV $s^{-1}$ (b); between 0.00 V and 0.60 V at 2, 5, 10, 20, 50, 100, 200, 500, 1000, 2000, 5000 mV $s^{-1}$ after opening the potential window (c).

Concerning GCD characterization results, the 4th charge-discharge cycle at each current density between 2-40 mA $cm^{-2}$ is shown in Figure VI.5. It can be seen that the curves show a quasi-ideal triangular and symmetrical shape, and negligible ohmic drop, typical of a capacitive behaviour associated to the formation of the EDL.

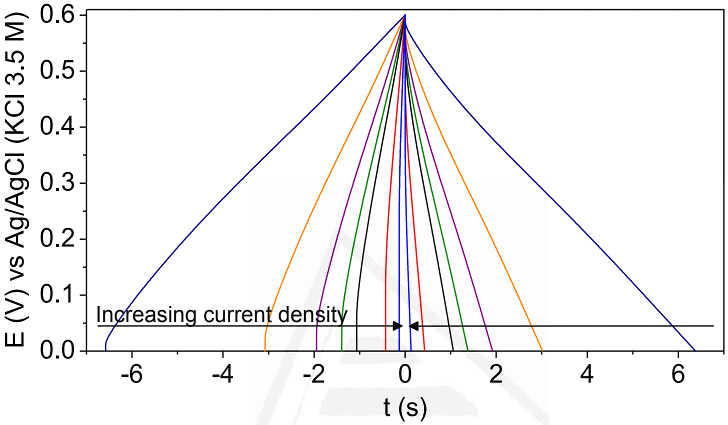

Figure VI.5. 4th chage-discharge cycle of the mesoporous carbon thin film in 1M $H_2SO_4$ solution at: 2 (blue line), 4 (red line), 6 (black line), 8 (green line), 10 (purple line), 20 (orange line), 40 (dark blue line) mA $cm^{-2}$.

In order to study the behaviour of the mesoporous carbon thin film without removal of the silica template, the same electrochemical treatment was applied to the composite silica/carbon thin film. Since electrochemical charge accommodation during the formation of the EDL takes place exclusively at the surface, the composite silica/carbon thin film is expected to act in a similar way to the mesoporous carbon thin film.

Figure VI.6.a shows the cyclic voltammograms done between 0.00 V and 0.60 V at different scan rates. The cyclic voltammograms show a quasi-rectangular shape even at high scan rate values. Figure VI.6.b shows the cyclic voltammograms done at 5 mV $s^{-1}$ under three subsequent potential windows: between -0.20 V and 0.80 V (blue line), between -0.40 V and 1.00 V (red line) and between -0.60 V and 1.00 V (black line). A similar behaviour to that observed for mesoporous carbon thin film is shown. Upon broadening the potential window several redox processes takes place. The oxidation of the carbon material from 0.60 V to more positive values and the corresponding cathodic peak at around 0.37 V are observed (see red and black lines). Furthermore, the electrochemical hydrogen evolution process (starting from -0.20 V to less positive potential values) and the oxidation of the adsorbed hydrogen in the subsequent positive sweep (at around 0.10 V), are also shown. Moreover, a well-defined oxidation peak at 0.72 V is observed during the positive sweep (see red and black lines). Since this peak does not appear in the mesoporous carbon thin film, it may be related to oxygen groups originated from remnant traces of the carbonized Pluronic® F127 surfactant used in the synthesis of the mesoporous silica thin film. It should be noted that this oxidation peak does not appear in the potential window between -0.20 V and 0.80 V, thus suggesting that the oxygen groups originated from these remnant traces of the carbonized Pluronic® F127 should be previously reduced (upon reaching more negative potential values) and then oxidized in the subsequent anodic sweep. Figure VI.6.c, shows the cyclic voltammograms done between 0.00 V and 0.60 V at different scan rates after opening the potential window. Likewise for mesoporous carbon thin film, the capacitance values increase with respect to the recorded before broadening the potential window.

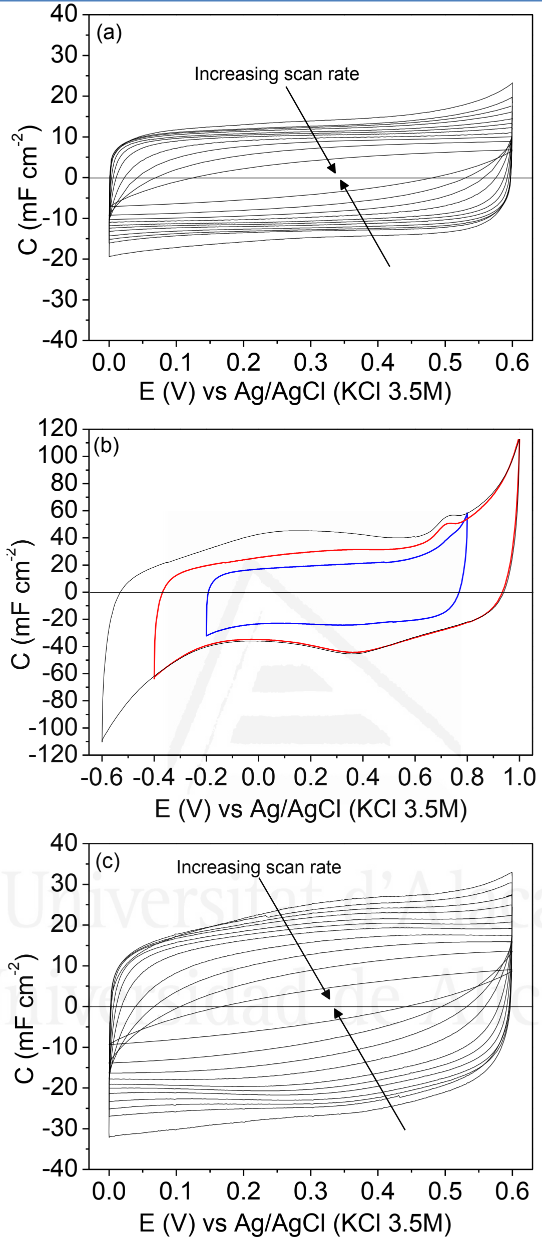

Figure VI.6. Cyclic voltammograms of the composite silica/carbon thin film in 1M $H_2SO_4$ solution: between 0.00 V and 0.60 V at 2, 5, 10, 20, 50, 100, 200, 500, 1000, 2000, 5000 mV s$^{-1}$ (a); between -0.20 V and 0.80 V (blue line), between -0.40 V and 1.00 V (red line) and between -0.60 V and 1.00 V (black line) at 5 mV s$^{-1}$ (b); between 0.00 V and 0.60 V at 2, 5, 10, 20, 50, 100, 200, 500, 1000, 2000, 5000 mV s$^{-1}$ after opening the potential window (c).

From GCD characterization results (Figure VI.7) it can be seen that the curves show a quasi-ideal triangular and symmetrical shape, and negligible ohmic drop, typical of a capacitive behaviour associated to the formation of the EDL.

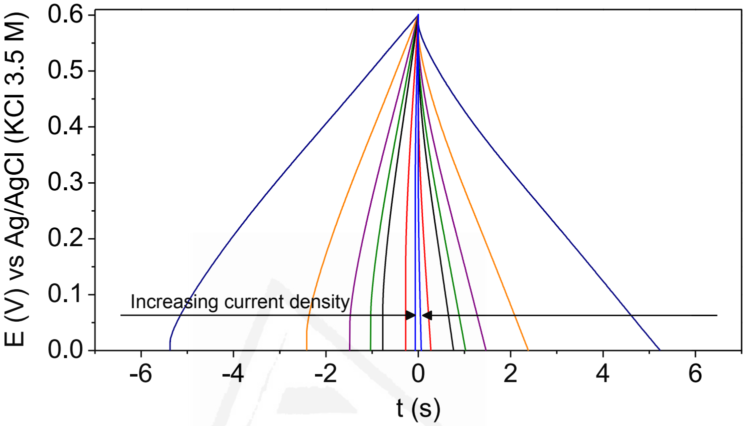

Figure VI.7. 4th chage-discharge cycle of the composite silica/carbon thin film in 1M $H_2SO_4$ solution at: 2 (blue line), 4 (red line), 6 (black line), 8 (green line), 10 (purple line), 20 (orange line), 40 (dark blue line) mA $cm^{-2}$.

The specific capacitance values for the mesoporous carbon and the composite silica/carbon thin films at each scan rate and at each current density were calculated from the CV and GCD experiments, respectively.

Figure VI.8 shows the specific capacitance at each scan rate value calculated before (empty circle symbols) and after (empty square symbols) opening the potential window. In order to show the small contribution of the current collector the specific capacitances for the graphite current collector after opening the potential window (empty triangle symbols), are also included. As has been previously shown from Figures VI.4.a and VI.4.c, the capacitance increases after opening the potential window, which is presumably due to the entrance of the electrolyte to all the pores, as a consequence of broadening the potential window, and to the formation of oxygen surface groups that contribute to pseudocapacitance and improve the wetting of the electrolyte. It should be remarked that the very high capacitance value of 26.7 mF cm$^{-2}$ was recorded at 2 mV s$^{-1}$ (after opening the potential window).

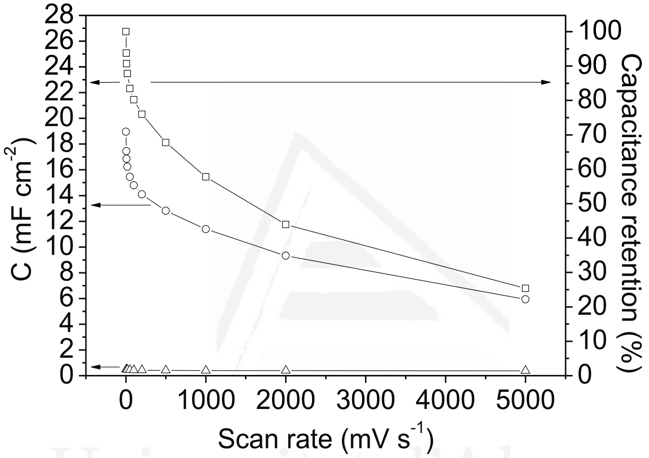

Figure VI.8. Specific capacitance *versus* scan rate plot for: graphite current collector after opening the potential window (-Δ- empty triangle symbols) and mesoporous carbon thin film before (-○-empty circle symbols) and after (-□-empty square symbols) opening the potential window. Note: the secondary axis of capacitance retention applies only to the mesoporous carbon thin film after opening the potential window.

It is well known that for materials that combine micro- and mesoporosity high capacitance and rate performance are obtained [11,16]. The results obtained, in terms of specific capacitance and capacitance retention, corroborate that the materials synthesized consist of a continuous and ordered thin film with the proper porous texture where the pathway for the electrolyte shows less tortuosity than that in electrodes made from powdery materials; as a result, the capacitance retention shown is higher than for electrodes made from powdered hierarchical porous carbon [16]. Therefore, the use of a continuous thin film carbon material improves the electrochemical performance of a carbon electrode prepared from a powdered material with regard to its use as an electrode in micro-capacitors.

Figures VI.9 and VI.10 show the specific capacitance values versus the scan rate (after opening the potential window) and the current density, respectively, for the mesoporous carbon thin film (empty symbols) and for the composite silica/carbon thin film (full symbols). The results obtained show that the electrochemical behaviour of the composite silica/carbon thin films is similar to that obtained from the mesoporous carbon thin film, confirming that the uniform carbon coating makes the composite possess excellent electrical conductivity. It should be remarked that the very high capacitance value of 24.3 mF cm$^{-2}$ at 2 mV s$^{-1}$ was recorded for the composite silica/carbon thin film (see full square symbols in Figure VI.9).

From the results shown in Figure VI.10, it should be pointed out that the high specific capacitance value of 22.3 mF cm$^{-2}$ at 2 mA cm$^{-2}$ for the mesoporous carbon thin film and the high capacitance retention (61 %) at the highest current density of 40 mA cm$^{-2}$ were achieved. These high specific capacitance values are in the same order of magnitude as that obtained for a zeolite-templated carbon thin film [59]. From the results for the composite silica/carbon thin film it should be pointed out that at 2 mA cm$^{-2}$ the capacitance is 18.4 mF cm$^{-2}$, and at the highest current density of 40 mA cm$^{-2}$ the electrode even retains 44 % of the initial capacitance (giving a capacitance of 8.2 mF cm$^{-2}$) (see full rhombus symbols).

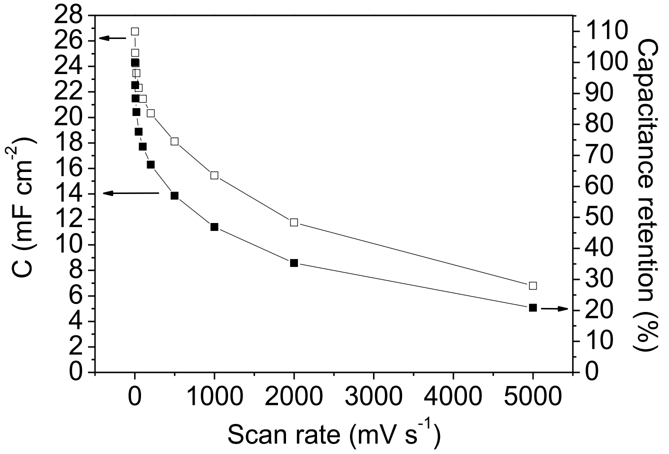

Figure VI.9. Specific capacitance *versus* scan rate plot for: mesoporous carbon thin film (-□- empty square symbols) and composite silica/carbon thin film (-■- full square symbols) after opening the potential window. Note: the secondary axis of capacitance retention applies only to the composite silica/carbon thin film.

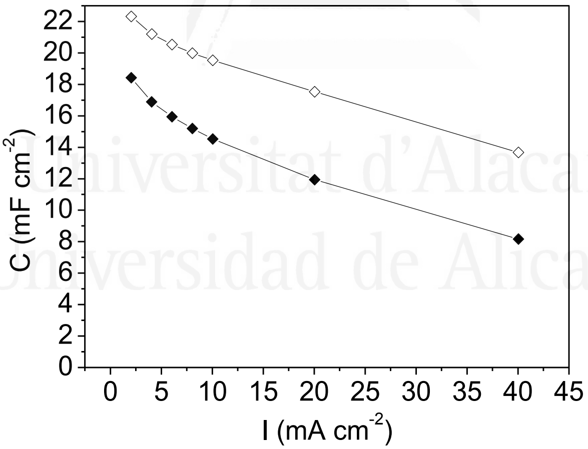

Figure VI.10. Specific capacitance *versus* current density plot for: mesoporous carbon thin film (-◊- empty rhombus symbols) and composite silica/carbon thin film (-♦- full rhombus symbols).

The electrochemical characterization results show the exceptional electrochemical properties of the mesoporous carbon thin film and that it may be a suitable candidate as electrode for micro-capacitors.

Furthermore, it has been shown that the formation of an uniform carbon coating over the silica template, makes the composite to have an excellent electrical conductivity despite the insulating nature of the silica [17-19,60,61]. Therefore, the composite silica/carbon thin film exhibits excellent electrical conductivity and electrochemical behaviour to be directly used as electrode for micro-capacitors, which is very interesting from an economical and environmental point of view.

### VI.3.3. Two-electrode cell electrochemical characterization results

It has been shown that both the mesoporous carbon and composite silica/carbon thin films show exceptional electrochemical properties to be used as electrodes for electrochemical micro-capacitors. Therefore, the thin films synthesized were characterized in a symmetric two-electrode cell. The symmetric electrochemical capacitor was characterized by CV and subsequently by GCD. After that, the capacitor was submitted to a durability test.

Regarding the CV characterization, two cyclic voltammograms between 0.00 V and 1.00 V were performed at different scan rates: 5, 10, 20, 50, 100, 200, 500, 1000, 2000 and 5000 mV $s^{-1}$. Subsequently, the GCD characterization was accomplished by performing four charge-discharge cycles between 0.00 and 1.00 V at different current densities: 1, 3, 5, 7, 9 and 11 mA $cm^{-2}$ (it should be reminded that for the two-electrode electrochemical characterization $cm^{-2}$ refers to the sum of the geometrical area of both the positive and negative electrodes). Finally, durability test was carried out, consisting of 25,000 GCD cycles, at 10 mA $cm^{-2}$, under two subsequent potential ranges (from 0.00 V to 1.00 V and from 0.00 V to 1.20 V).

Figures VI.11 and VI.12 show the steady-state 2nd cyclic voltammogram at each scan rate value for the symmetric electrochemical capacitor made from the mesoporous carbon and the composite silica/carbon thin films, respectively. The cyclic voltammograms show a quasi-rectangular shape even at high scan rate values, thus improving the electrochemical behaviour of conventional electrochemical capacitors made from powdered carbon materials using binders [62,63] or micro-devices based on carbon fibres [34], where the shape of the cyclic voltammogram gets distorted even at lower scan rate values.

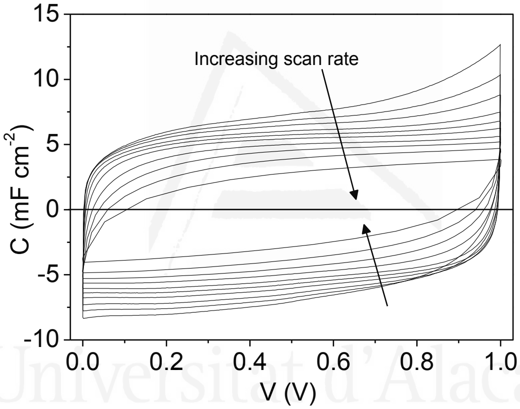

Figure VI.11. Cyclic voltammograms of the symmetric electrochemical capacitor from the mesoporous carbon thin film in 1M $H_2SO_4$ solution between 0.00 V and 1.00 V at: 5, 10, 20, 50, 100, 200, 500, 1000, 2000, 5000 mV $s^{-1}$.

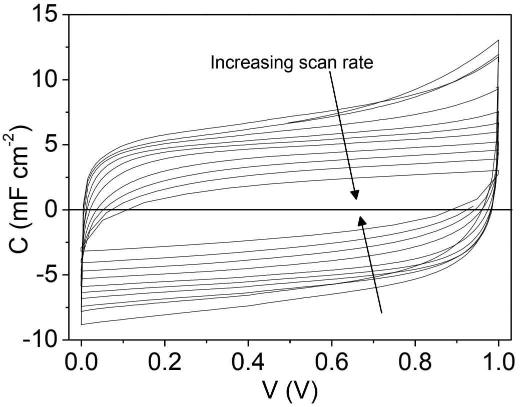

Figure VI.12. Cyclic voltammograms of the symmetric electrochemical capacitor from the composite silica/carbon thin film in 1M $H_2SO_4$ solution between 0.00 V and 1.00 V at: 5, 10, 20, 50, 100, 200, 500, 1000, 2000, 5000 mV $s^{-1}$.

Figure VI.13 shows the specific capacitance versus the scan rate for the symmetric electrochemical capacitor made from the mesoporous carbon thin film (empty square symbols) and from the composite silica/carbon thin film (full square symbols). Analogously, in Figure VI.14 the specific capacitance is presented versus the current density (calculated from the GCD experiments, not shown here) for the mesoporous carbon thin film (empty rhombus symbols) and from the composite silica/carbon thin film (full rhombus symbols) symmetric capacitors. In general, the results obtained show similar electrochemical behaviour for both the mesoporous carbon and the composite silica/carbon thin films symmetric electrochemical capacitor, as previously seen from the three-electrode cell configuration characterization results.

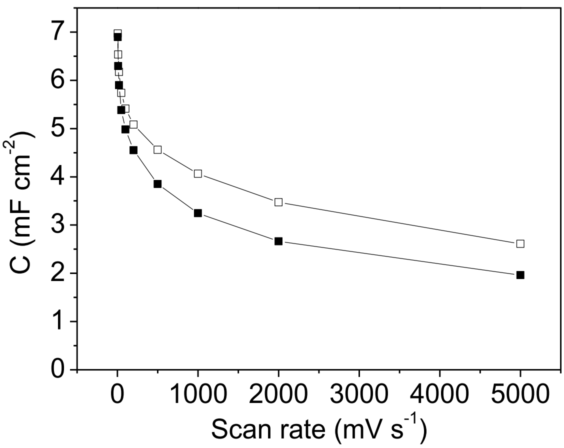

Figure VI.13. Specific capacitance *versus* scan rate plot for the symmetric electrochemical capacitor made from: the mesoporous carbon thin film (-□- empty square symbols) and the composite silica/carbon thin film (-■- full square symbols).

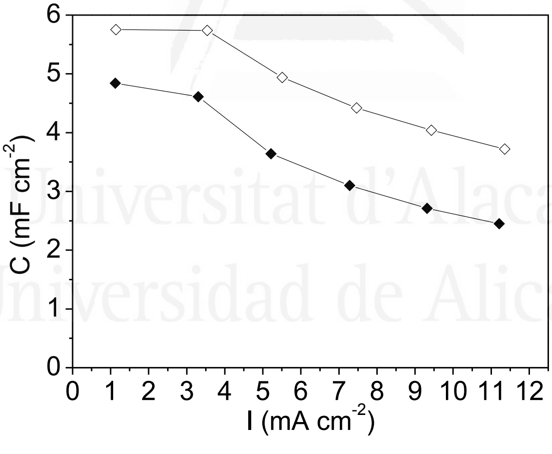

Figure VI.14. Specific capacitance *versus* current density plot for the symmetric electrochemical capacitor made from: the mesoporous carbon thin film (-◊- empty rhombus symbols) and the composite silica/carbon thin film (-♦- full rhombus symbols).

It should be remarked that the very high capacitance values of 7.0 mF cm$^{-2}$ and 6.9 mF cm$^{-2}$ were recorded at 5 mV s$^{-1}$ for the mesoporous carbon and the composite silica/carbon thin film symmetric capacitors, respectively (Figure VI.13). Even though the comparison is not straightforward (because of the different experimental assembly and electrochemical conditions), the results obtained improve the value reported for an interdigitated micro-capacitor based on powdered ACs (2.1 mF cm$^{-2}$) [21]. By increasing the scan rate up to 5000 mV s$^{-1}$ the capacitance retention values of the electrochemical capacitor is 37 % and 28 % for the mesoporous carbon and the composite silica/carbon thin film electrodes, respectively; what is a remarkable result considering that the microelectrode assembly is not the most adequate one. Even then, the specific capacitance values are comparable to that found in the literature for interdigitated micro-capacitors based on reduced graphene oxide or graphene composites [32,33] and onion-like carbon [64], and for micro-capacitors made of rGO thin films [20].

From Figure VI.14, it should be remarked the high specific capacitance values obtained at low current densities (1 and 3 mA cm$^{-2}$), of around 5.7 mF cm$^{-2}$ and 4.7 mF cm$^{-2}$ for the mesoporous carbon thin film and the composite silica/carbon thin film symmetric electrochemical capacitor, respectively, which are similar to that obtained for micro-capacitors based on rGO–CNT composites [32].

Figure VI.15 shows the durability test results for the mesoporous carbon thin film symmetric electrochemical capacitor. This figure includes the first 25,000 cycles performed between 0.00 V and 1.00 V and the 25,000 cycles subsequently performed between 0.00 V and 1.20 V. A slight decrease can be seen in the specific capacitance even after the high number of cycles performed (more pronounced in the first 25,000 cycles), which indicates a very low degradation of the mesoporous carbon thin film electrodes. A very similar behaviour, i.e. low decrease of the specific capacitance value even after very high number of cycles, was observed for durability test done for the composite silica/carbon thin film (results not shown here). Even though straightforward comparison is not fair, these results point out the superior durability of capacitors made from the thin films synthesized compared to conventional electrochemical capacitors made from powdered carbon materials that are not usually subjected to such a high number of GCD cycles and also they show a decrease of the capacitance retention even after less number of cycles applied [65-67].

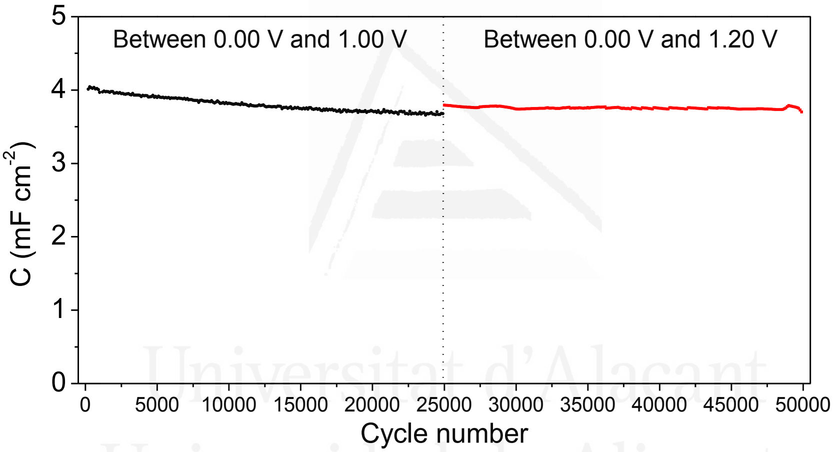

Figure VI.15. Specific capacitance versus cycle number plot for the symmetric electrochemical capacitor made from the mesoporous carbon thin film: between 0.00 V and 1.00 V (-■- black square symbols) and between 0.00 V and 1.20 V (-■- red square symbols). Current density: 10 mA cm$^{-2}$.

Thus, both the mesoporous carbon thin film and the composite silica/carbon thin film show exceptional electrochemical properties, in terms of capacitance, rate performance and stability, making them promising candidates as electrodes for micro-capacitors.

## VI.4. Conclusions

Continuous mesoporous carbon thin film was successfully synthesized onto a graphite current collector using an ordered mesoporous silica thin film as the hard-template. The nanostructure of the silica, the composite silica/carbon and the mesoporous carbon thin films was characterized by microscopy and spectroscopy techniques. FE-SEM and corresponding EDX silicon mapping analysis of the mesoporous silica thin film demonstrated that it is uniformly deposited onto the graphite current collector. From TEM images it was shown that the silica template presents ordered mesopores of around 8 nm perpendicularly disposed to the graphite current collector. From the image of the composite silica/carbon thin film it was shown that the carbon material covers the nanostructure of the template and it maintains the structural order of the silica thin film. A TEM image of the mesoporous carbon thin film demonstrated that the order partially decreases by removing the silica template and that the mesopore size is around 2-3 nm. Mesoporous carbon thin film Raman spectrum shows an increment of the D and G bands width with respect to the composite silica/carbon thin film spectrum, pointing out that the removal of the silica template produces a relaxation of the mesoporous carbon thin film structure: the structural order of the carbon materials decreases, that entails the appearance of defects. This result is in agreement with the partial loss of the mesoporosity order previously observed from TEM images. Concerning the electrochemical characterization, it should be pointed out that the very high capacitance values of 7.0 mF cm$^{-2}$ and 6.9 mF cm$^{-2}$ were recorded at 5 mV s$^{-1}$ for the mesoporous carbon and the composite silica/carbon thin films symmetric capacitors, respectively, that improve the values reported for other carbon-based electrode devices. The very similar electrochemical results (high specific capacitance and high rate performance) obtained for both thin films (mesoporous carbon and silica/carbon composite) demonstrate that the uniform carbon coating make the composite possess excellent electrical conductivity. Furthermore, the durability test has shown that the thin films synthesized show low degradation, even after a high number of cycles are applied, since the specific capacitance remains almost constant. Therefore, both the mesoporous carbon thin film and the composite silica/carbon thin film show exceptional electrochemical properties, in terms of capacitance, rate performance and stability, making them promising candidates as electrodes for micro-capacitors.

## References

[1] L.L. Zhang, Z. Lei, J. Zhang, X. Tian, X.S. Zhao, Supercapacitors: electrode materials aspectsIn: Crabtree RH, (Ed), Energy production and storage. Inorganic chemical strategies for a warming world, John Wiley & Sons, New Haven, 2010, pp. 341.

[2] F. Béguin, E. Raymundo-Piñero, E. Frackowiak, Electrical double-layer capacitors and pseudocapacitorsIn: Béguin F, Frackowiak E, (Eds), Carbons for electrochemical energy storage and conversion systems, CRC Press, Pennsylvania, 2010, pp. 329.

[3] M.J. Bleda-Martínez, D. Lozano-Castelló, D. Cazorla-Amorós, E. Morallón,Kinetics of double-layer formation: influence of porous structure and pore size distribution Energ.Fuel. 24 (2010) 3378-3384.

[4] M. Liu, J. Qian, Y. Zhao, D. Zhu, L. Gan, L. Chen,Core-shell ultramicroporous@microporous carbon nanospheres as advanced supercapacitor electrodes J.Mater.Chem.A. 3 (2015) 11517-11526.

[5] Y. Zhao, M. Liu, X. Deng, L. Miao, P.K. Tripathi, X. Ma, D. Zhu, Z. Xu, Z. Hao, L. Gan,Nitrogen-functionalized microporous carbon nanoparticles for high performance supercapacitor electrode Electrochim.Acta. 153 (2015) 448-455.

[6] Y. Zhao, M. Liu, L. Gan, X. Ma, D. Zhu, Z. Xu, L. Chen,Ultramicroporous carbon nanoparticles for the high-performance electrical double-layer capacitor electrode Energ.Fuel. 28 (2014) 1561-1568.

[7] H. Liu, K. Wang, H. Teng,A simplified preparation of mesoporous carbon and the examination of the carbon accessibility for electric double layer formation Carbon. 43 (2005) 559-566.

[8] A. Fuertes, G. Lota, T. Centeno, E. Frackowiak,Templated mesoporous carbons for supercapacitor application Electrochim.Acta. 50 (2005) 2799-2805.

[9] K. Kim, M. Choi, R. Ryoo,Ethanol-based synthesis of hierarchically porous carbon using nanocrystalline beta zeolite template for high-rate electrical double layer capacitor Carbon. 60 (2013) 175-185.

[10] S. Yoon, J. Lee, T. Hyeon, S.M. Oh,Electric double-layer capacitor performance of a new mesoporous carbon J.Electrochem.Soc. 147 (2000) 2507-2512.

[11] R. Ruiz-Rosas, M.J. Valero-Romero, D. Salinas-Torres, J. Rodriguez-Mirasol, T. Cordero, E. Morallon, D. Cazorla-Amoros,Electrochemical Performance of Hierarchical Porous Carbon Materials Obtained from the Infiltration of Lignin into Zeolite Templates ChemSusChem. 7 (2014) 1458-1467.

[12] D.W. Wang, F. Li, H.T. Fang, M. Liu, G.Q. Lu, H.M. Cheng,Effect of pore packing defects in 2-D ordered mesoporous carbons on ionic transport J Phys Chem B. 110 (2006) 8570-8575.

[13] A. Fuertes, F. Pico, J. Rojo,Influence of pore structure on electric double-layer capacitance of template mesoporous carbons J.Power Sources. 133 (2004) 329-336.

[14] H. Nishihara, T. Kyotani,Templated nanocarbons for energy storage Adv Mater. 24 (2012) 4473-4498.

[15] H. Zhou, S. Zhu, M. Hibino, I. Honma,Electrochemical capacitance of self-ordered mesoporous carbon J.Power Sources. 122 (2003) 219-223.

[16] K. Xia, Q. Gao, J. Jiang, J. Hu,Hierarchical porous carbons with controlled micropores and mesopores for supercapacitor electrode materials Carbon. 46 (2008) 1718-1726.

[17] T. Kwon, H. Nishihara, Y. Fukura, K. Inde, N. Setoyama, Y. Fukushima, T. Kyotani,Carbon-coated mesoporous silica as an electrode material Microporous Mesoporous Mat. 132 (2010) 421-427.

[18] J. Zhi, Y. Wang, S. Deng, A. Hu,Study on the relation between pore size and supercapacitance in mesoporous carbon electrodes with silica-supported carbon nanomembranes RSC Adv. 4 (2014) 40296-40300.

[19] S.M. Filonenko, N.D. Shcherban, P.S. Yaremov, V.S. Dyadyun,Sorption and electrochemical properties of carbon-silica composites and carbons from 2,3-dihydroxynaphthalene J.Porous Mat. 22 (2015) 21-28.

[20] J.J. Yoo, K. Balakrishnan, J. Huang, V. Meunier, B.G. Sumpter, A. Srivastava, M. Conway, A.L.M. Reddy, J. Yu, R. Vajtai, P.M. Ajayan,Ultrathin planar graphene supercapacitors Nano Lett. 11 (2011) 1423-1427.

[21] D. Pech, M. Brunet, P. Taberna, P. Simon, N. Fabre, F. Mesnilgrente, V. Conedera, H. Durou,Elaboration of a microstructured inkjet-printed carbon electrochemical capacitor J.Power Sources. 195 (2010) 1266-1269.

[22] F. Béguin, V. Presser, A. Balducci, E. Frackowiak,Carbons and electrolytes for advanced supercapacitors Adv.Mater. 26 (2014) 2219-2251.

[23] L. Oakes, A. Westover, J.W. Mares, S. Chatterjee, W.R. Erwin, R. Bardhan, S.M. Weiss, C.L. Pint,Surface engineered porous silicon for stable, high performance electrochemical supercapacitors Sci Rep. 3 (2013) 1-7.

[24] J. Kim, K. Nam, S. Ma, K. Kim,Fabrication and electrochemical properties of carbon nanotube film electrodes Carbon. 44 (2006) 1963-1968.

[25] M. Kaempgen, C.K. Chan, J. Ma, Y. Cui, G. Gruner,Printable thin film supercapacitors using single-walled carbon nanotubes Nano Lett. 9 (2009) 1872-1876.

[26] F. Thissandier, N. Pauc, T. Brousse, P. Gentile, S. Sadki,Micro-ultracapacitors with highly doped silicon nanowires electrodes Nanoscale Res.Lett. 8 (2013) 1-5.

[27] W. Sun, R. Zheng, X. Chen,Symmetric redox supercapacitor based on micro-fabrication with three-dimensional polypyrrole electrodes J.Power Sources. 195 (2010) 7120-7125.

[28] I. Nam, G. Kim, S. Park, J. Park, N.D. Kim, J. Yi,Fabrication and design equation of film-type large-scale interdigitated supercapacitor chips Nanoscale. 4 (2012) 7350-7353.

[29] S. Makino, Y. Yamauchi, W. Sugimoto,Synthesis of electro-deposited ordered mesoporous RuOx using lyotropic liquid crystal and application toward micro-supercapacitors J.Power Sources. 227 (2013) 153-160.

[30] J. Feng, X. Sun, C. Wu, L. Peng, C. Lin, S. Hu, J. Yang, Y. Xie,Metallic few-layered $VS_2$ ultrathin nanosheets: high two-dimensional conductivity for in-plane supercapacitors J.Am.Chem.Soc. 133 (2011) 17832-17838.

[31] E. Eustache, R. Frappier, R.L. Porto, S. Bouhtiyya, J. Pierson, T. Brousse,Asymmetric electrochemical capacitor microdevice designed with vanadium nitride and nickel oxide thin film electrodes Electrochem.Commun. 28 (2013) 104-106.

[32] M. Beidaghi, C. Wang,Micro-supercapacitors based on interdigital electrodes of reduced graphene oxide and carbon nanotube composites with ultrahigh power handling performance Adv. Func. Mater. 22 (2012) 4501-4510.

[33] Y.S. Moon, D. Kim, G. Lee, S.Y. Hong, K.K. Kim, S.M. Park, J.S. Ha,Fabrication of flexible micro-supercapacitor array with patterned graphene foam/MWNT-COOH/MnOx electrodes and its application Carbon. 81 (2015) 29-37.

[34] W. Liu, N. Liu, Y. Shi, Y. Chen, C. Yang, J. Tao, S. Wang, Y. Wang, J. Su, L. Li, Y. Gao,A wire-shaped flexible asymmetric supercapacitor based on carbon fiber coated with a metal oxide and a polymer J.Mater.Chem.A. 3 (2015) 13461-13467.

[35] H. Lee, J. Yang, H. Lee, J. Park, K. Lee, Y. Kwon,Facile and adaptable synthesis method of mesostructured silica thin films J.Mater.Chem. 18 (2008) 1881-1888.

[36] R. Ryoo, S. Joo, S. Jun,Synthesis of highly ordered carbon molecular sieves via template-mediated structural transformation J Phys Chem B. 103 (1999) 7743-7746.

[37] Y. Wang, D.C. Alsmeyer, R.L. McCreery,Raman spectroscopy of carbon materials: structural basis of observed spectra Chem Mater. 2 (1990) 557-563.

[38] A. Sadezky, H. Muckenhuber, H. Grothe, R. Niessner, U. Poschl,Raman micro spectroscopy of soot and related carbonaceous materials: Spectral analysis and structural information Carbon. 43 (2005) 1731-1742.

[39] F. Tuinstra, J.L. Koenig,Raman spectrum of graphite J.Chem.Phys. 53 (1970) 1126-1130.

[40] T. Jawhari, A. Roid, J. Casado,Raman spectroscopic characterization of some commercially available carbon black materials Carbon. 33 (1995) 1561-1565.

[41] E.F. Antunes, A.O. Lobo, E.J. Corat, V.J. Trava-Airoldi, A.A. Martin, C. Veríssimo,Comparative study of first- and second-order Raman spectra of MWCNT at visible and infrared laser excitation Carbon. 44 (2006) 2202-2211.

[42] A. Cuesta, P. Dhamelincourt, J. Laureyns, A. Martínez-Alonso, J. Tascón,Raman microprobe studies on carbon materials Carbon. 32 (1994) 1523-1532.

[43] S. Sze, N. Siddique, J. Sloan, R. Escribano,Raman spectroscopic characterization of carbonaceous aerosols Atmos.Environ. 35 (2001) 561-568.

[44] R.J. Bowling, R.T. Packard, R.L. McCreery, Activation of Highly Ordered Pyrolytic Graphite for Heterogeneous Electron Transfer: Relationship between Electrochemical Performance and Carbon Microstructure, J. Am. Chem. Soc. 111 (1989) 1217-1223.

[45] J. Schwan, S. Ulrich, V. Batori, H. Ehrhardt, S. Silva,Raman spectroscopy on amorphous carbon films J.Appl.Phys. 80 (1996) 440-447.

[46] J.N. Rouzaud, A. Oberlin, C. Beny-Bassez,Carbon films: Structure and microtexture (optical and electron microscopy, Raman spectroscopy) Thin Solid Films. 105 (1983) 75-96.

[47] N.P. Ivleva, A. Messerer, X. Yang, R. Niessner, U. Poeschl,Raman microspectroscopic analysis of changes in the chemical structure and reactivity of soot in a diesel exhaust aftertreatment model system Environ.Sci.Technol. 41 (2007) 3702-3707.

[48] A. Sood, R. Gupta, S. Asher,Origin of the unusual dependence of Raman D band on excitation wavelength in graphite-like materials J.Appl.Phys. 90 (2001) 4494-4497.

[49] E. Del Corro, M. Taravillo, V.G. Baonza,Stress-dependent correlations for resonant Raman bands in graphite with defects J.Raman Spectrosc. 45 (2014) 476-480.

[50] R. Krishna, A.N. Jones, R. Edge, B.J. Marsden,Residual stress measurements in polycrystalline graphite with micro-Raman spectroscopy Radiat.Phys.Chem. 111 (2015) 14-23.

[51] A.C. Ferrari,Raman spectroscopy of graphene and graphite: disorder, electron-phonon coupling, doping and nonadiabatic effects Solid State Commun. 143 (2007) 47-57.

[52] A.C. Ferrari, J.C. Meyer, V. Scardaci, C. Casiraghi, M. Lazzeri, F. Mauri, S. Piscanec, D. Jiang, K.S. Novoselov, S. Roth, A.K. Geim,Raman spectrum of graphene and graphene layers Phys.Rev.Lett. 97 (2006) 187401.

[53] R. Krishna, A.N. Jones, B.J. Marsden,Transmission electron microscopy, Raman and X-ray photoelectron spectroscopy studies on neutron irradiated polycrystalline graphite Radiat.Phys.Chem. 107 (2015) 121-127.

[54] Y. Kawashima, G. Katagiri,Observation of the out-of-plane mode in the Raman scattering from the graphite edge plane Phys.Rev.B. 59 (1999) 62-64.

[55] M. Laskowska, Ł Laskowski, K. Dzilinski,Mesoporous silica functionalized by nickel-cyclam molecules: preparation and resonance Raman study Curr.Top.Biophys. 35 (2012) 11-18.

[56] D. Carboni, B. Lasio, V. Alzari, A. Mariani, D. Loche, M.F. Casula, L. Malfatti, P. Innocenzi,Graphene-mediated surface enhanced Raman scattering in silica mesoporous nanocomposite films Phys.Chem.Chem.Phys. 16 (2014) 25809-25818.

[57] G.Q. Lu, Z.F. Yan, W. Xing, S.Z. Qiao, R.G. Ding, F. Li, H.M. Cheng,Superior electric double layer capacitors using ordered mesoporous carbons Carbon. 44 (2006) 216-224.

[58] K. Jurewicz, E. Frackowiak, F. Béguin,Towards the mechanism of electrochemical hydrogen storage in nanostructured carbon materials Appl Phys A. 78 (2004) 981-987.

[59] A. Berenguer-Murcia, R.R. Ruiz-Rosas, J. Garcia-Aguilar, K. Nueangnoraj, H. Nishihara, E. Morallon, T. Kyotani, D. Cazorla-Amoros,Binderless thin films of zeolite-templated carbon electrodes useful for electrochemical microcapacitors with ultrahigh rate performance Phys.Chem.Chem.Phys. 15 (2013) 10331-10334.

[60] H. Nishihara, Y. Fukuraa, K. Inde, K. Tsuji, M. Takeuchi, T. Kyotani,Carbon-coated mesoporous silica with hydrophobicity and electrical conductivity Carbon. 46 (2008) 48-53.

[61] H. Nishihara, T. Kwon, Y. Fukura, W. Nakayama, Y. Hoshikawa, S. Iwamura, N. Nishiyama, T. Itoh, T. Kyotani,Fabrication of a highly conductive ordered porous electrode by carbon-coating of a continuous mesoporous silica film Chem.Mat. 23 (2011) 3144-3151.

[62] Y. Gao, L. Li, Y. Jin, Y. Wang, C. Yuan, Y. Wei, G. Chen, J. Ge, H. Lu,Porous carbon made from rice husk as electrode material for electrochemical double layer capacitor Appl.Energy. 153 (2015) 41-47.

[63] E.J. Lee, Y.J. Lee, J.K. Kim, M. Lee, J. Yi, J.R. Yoon, J.C. Song, I.K. Song,Oxygen group-containing activated carbon aerogel as an electrode material for supercapacitor Mater.Res.Bull. 70 (2015) 209-214.

[64] D. Pech, M. Brunet, H. Durou, P. Huang, V. Mochalin, Y. Gogotsi, P. Taberna, P. Simon,Ultrahigh-power micrometre-sized supercapacitors based on onion-like carbon Nat.Nanotechnol. 5 (2010) 651-654.

[65] I.I.G. Inal, S.M. Holmes, A. Banford, Z. Aktas,The performance of supercapacitor electrodes developed from chemically activated carbon produced from waste tea Appl.Surf.Sci. 357 (2015) 696-703.

[66] V. Khomenko, E. Raymundo-Pinero, E. Frackowiak, F. Béguin,High-voltage asymmetric supercapacitors operating in aqueous electrolyte Appl.Phys.A:Mater.Sci.Process. 82 (2006) 567-573.

[67] G. Huang, W. Kang, B. Xing, L. Chen, C. Zhang,Oxygen-rich and hierarchical porous carbons prepared from coal based humic acid for supercapacitor electrodes Fuel Process Technol. 142 (2016) 1-5.

# Chapter VII

# Electrochemical performance of a superporous activated carbon in ionic liquid-based electrolytes

## VII.1. Introduction

Electrochemical double-layer capacitors (EDLCs), or supercapacitors, based on the formation of the electric double-layer (EDL) in the interphase electrode-electrolyte and the quick faradic charge transfer reactions between the electrolyte and the electrode (i.e. pseudocapacitance), are currently considered one of the most promising electrochemical energy storage devices [1,2]. Presently, the main goal of the studies dedicated to these devices is to design high energy (>10 Wh kg$^{-1}$) devices displaying the high power of state-of-the art EDLCs [3].

The energy density of an EDLC is described by Equation VII.1,

$$E = \frac{1}{2} \cdot C \cdot V^2 \quad \textbf{Equation VII.1}$$

Where *E* is the energy, *C* is the capacitance and *V* is the operating voltage.

Thus the increase of both the capacitance and the operating voltage are the two strategies to improve the energy stored.

Porous carbon materials and, in particular, activated carbons (ACs) are one of the most suitable electrode materials for EDLCs because of their low-cost, versatility of both structure/texture and surface chemistry, good conductivity and high cycling life [4,5]. Regarding the carbon material properties, the surface chemistry plays a key role because it can affect the wettability of the electrode and contribute to the pseudocapacitance, but also it has a strong influence on the stability of the capacitor upon cycling [6,7]. Furthermore, due to the EDL mechanisms in supercapacitors based on carbon electrodes, porous structure and pore size distribution are key parameters to improve the capacitance of the electrodes [1,5,8]. It is now well known that pores with diameters comparable to the effective ion size are optimal for high specific capacitance [9]; however, extremely narrow pores may present sieving effect and, in consequence, they do not contribute to the charge stored [2,6,10-12].

Aqueous solution, organic solution and ionic liquids (ILs) are currently used as electrolytes for supercapacitors. Aqueous electrolytes display high capacitance values but a relatively low operating voltage of around 1 V, though an operating voltage up to 1.8 V can be reached using neutral aqueous solution [4,13]. Organic electrolytes, typically based on quaternary ammonium salt dissolved in an organic solvent, usually propylene carbonate (PC) or acetonitrile (ACN), provide a stability window in the range of 2.5-2.7 V [10,14] that display a higher specific energy than aqueous systems (even though they show less ionic conductivity and capacitance values). However, ILs are currently considered one of the most interesting electrolytes because they show non-flammability and negligible vapour pressure (and thus, high safety), high thermal stability and a wide electrochemical stability window that provides operative voltage higher than 3 V [15]. The main drawback of ILs is the high viscosity and low conductivity compared to electrolytes based on PC and ACN that might affect the capacitance values displayed by electrode materials [16]. To overcome this limitation, mixtures of ILs and organic solvents have been proposed and they are now considered as a convenient strategy to merge the favourable properties of these two classes of electrolytes.

Supercapacitors and batteries are mainly used for applications where the electronic systems have to operate at a wide range of temperatures (i.e. between -30 ºC and +60 ºC) [17] thus several works studying the electrochemical behaviour of these devices using IL-based electrolytes at different temperatures can be found in the literature [8,18,19].

In the past years the large majority of the investigated ACs have been developed for use in either aqueous or conventional organic electrolytes for EDLCs. Only few studies have been dedicated to the development of ACs tailored for alternative electrolytes, e.g. IL-based one. For this reason, this latter investigation appears of importance to take fully advantage of the favourable features of IL-based electrolytes.

The main objective of the work presented in this chapter is to characterize an AC with tailored porosity (high apparent specific surface area and a high volume of micropores with an average pore size of around 1.4 nm) for innovative electrolytes (solvent-free and solvent-based) for high voltage EDLCs. The influence of the ion/pore size ratio and the electrolyte characteristics (i.e. viscosity and conductivity) on the electrochemical behaviour of the investigated AC was studied in three PC-based electrolytes (1M tetraethylammonium tetrafluoroborate in PC (1M $Et_4N$ $BF_4$/PC), 1M 1-butyl-1-methylpyrrolidinium tetrafluoroborate in PC (1M $PYR_{14}$ $BF_4$/PC) and 1M 1-butyl-1-methylpyrrolidinium bis-(trifluoromethylsulfonyl)imide in PC (1M $PYR_{14}$ TFSI/PC)), and in the IL $PYR_{14}$ TFSI at different temperatures (20, 40 and 60 ºC).

## VII.2. Experimental

### VII.2.1. Synthesis of the activated carbon

The superporous AC (named as ANK3) was obtained following the procedure described in Chapter IV. It should be pointed out that synthesis conditions were selected in order to obtain both high apparent specific surface area and high micropore volume.

### VII.2.2. Porous texture characterization

The porous texture of the ANK3 was determined following the procedure described in Chapter IV. It should be noted that Brunauer–Emmett–Teller theory is commonly used to calculate the apparent specific surface area ($S_{BET}$) of the materials despite BET analysis could be inadequate for some microporous materials [20]. Thus, specific surface area was also calculated by applying non-local density functional theory ($S_{NLDFT}$) to the $N_2$ adsorption data. Furthermore, pore size distribution (PSD) was calculated by applying the NLDFT model to the $N_2$ adsorption data [21,22] as applied by the Solution of Adsorption Integral Equation Using Splines Software (SAIEUS, available online at http://www.nldft.com/), using Heterogeneous Surface Model.

### VII.2.3. Surface chemistry characterization

Temperature programmed desorption (TPD) was performed using the equipment described in Chapter IV. To carry out the analysis, approximately 10 mg of the ANK3 were heated up to 950 ºC (heating rate 20 ºC min$^{-1}$) under a helium flow rate of 100 ml min$^{-1}$.

### VII.2.4. Electrolytes preparation

Before preparing the electrolytes the conductive salts were pre-treated. The IL $PYR_{14}$ TFSI (IoLiTec, 99.5 %) was dried over molecular sieve (3 Å) until the water content was below 20 ppm. $Et_4N$ $BF_4$ (Sigma-Aldrich ≥ 99 %) was also dried under vacuum. $PYR_{14}$ $BF_4$ (IoLiTec, 99 %) was purified as described elsewhere [23]. PC (Sigma–Aldrich 99.7 %) was used as organic solvent. Both the storing of the salts, IL and PC as well as the preparation of the electrolytes were done in a dry room (relative humidity < 0.2 %).

### VII.2.5. Electrochemical characterization

ANK3 electrodes were composed of 90 wt. % of ANK3 powder as active material, 5 wt. % of carbon black (SUPER C65) as conductivity promoter and 5 wt. % of sodium carboxymethylcellulose as binder (CMC from Walocel CRT 2000 GA). First of all, 0.025 g of CMC was dissolved in 1.6 mL of ultrapure water by magnetic stirring for 1 h. Afterwards, a mixture composed of 0.450 g of ANK3 and 0.025 g of carbon black was added and it was kept 30 min stirring at 5000 rpm using a rotary disk (Dremel 4000, Dremel Europe). Subsequently, the homogenous slurry was casted on aluminium foil (30 µm, purity > 99.9 %, etched by immersion in 5 wt. % KOH at 60 ºC for 60 s) by using a laboratory scale doctor blade coater. The casted electrodes were left drying overnight at room temperature. After drying, electrodes with a diameter of 12 mm were cut from the coated sheets. The ANK3 electrodes prepared showed thickness values between 150 and 300 µm and average mass values between 1.5 and 6.0 mg.

Free standing electrodes (named as NORIT) with mass loadings over 40 mg were prepared using a different binder (polytetrafluoroethylene, PTFE, 60 wt. % dispersion in $H_2O$, Sigma–Aldrich) and a microporous commercial AC (NORIT DLC Super 30, with a $S_{BET}$ of 1618 $m^2\ g^{-1}$) as an active material, with a final ratio of 85:10:5 (AC:carbon black:PTFE). The PTFE aqueous dispersion, the AC and the carbon black were dispersed in an excess amount of EtOH and stirred until viscous slurry was obtained. Then, the slurry was rolled and electrodes of 12 mm diameter were cut and left dried at 80 ºC overnight.

Both the ANK3 and NORIT electrodes were dried under vacuum at 120 ºC overnight before using them.

Electrochemical tests were carried out using the Swagelok®-type configuration. The cells were assembled in an argon-filled glove box with oxygen and water contents <1 ppm. Whatman GF/D glass microfiber filter of 675 µm in thickness and 13 mm in diameter was used as separator. Before assembly the cell, the separator was drenched with 140 µL of electrolyte and carbon electrodes were soaked under vacuum during 5 min. All the electrochemical tests were performed using a VMP multichannel potentiostatic-galvanostatic system (Biologic Science Instruments). Electrochemical cells were placed in an oven to keep a constant temperature during the measurements.

Electrochemical characterization of ANK3 in different electrolytes and at different temperatures was performed by using a standard three-electrode configuration. NORIT electrodes were used as counter-electrode so as not to limit the capacitive response of the working electrode, while Ag wire was used as quasi-reference electrode. For EDLC characterization, asymmetric (in mass) supercapacitors were assembled to maximise the specific energy [24,25], ANK3 electrodes were used both as positive and negative electrode.

Prior to electrochemical characterization, the assembled cells remained 24 h at the selected temperature and, afterwards, 30 scans at 5 mV s$^{-1}$ were performed to ensure that the electrode was properly wetted by the electrolyte.

Cyclic voltammograms were obtained at 1 mV s$^{-1}$ using three-electrode configuration. Cyclic voltammograms were recorded at different potential ranges by broadening 0.10 V the potential limit of every cycle with respect to the previous one. Regarding cyclic voltammetry (CV) characterization of the EDLC, Cyclic voltammograms were carried out at different scan rates ranging from 1 to 200 mV s$^{-1}$ at a given potential window. In both experiments, three scans were recorded at each condition.

From the 3rd steady-state cyclic voltammograms capacitance values were calculated using Equations VII.2-VII.4:

$$C_s = \frac{Q/2}{\Delta E} \quad \textbf{Equation VII.2}$$

Where $C_s$ is the specific capacitance (F g$^{-1}$), $Q$ is the total electrical charge obtained by integration of the cyclic voltammogram (C g$^{-1}$) and $\Delta E$ is the potential window (V).

$$C_{n,BET} = \frac{C_S}{S_{BET}} \cdot 1000 \qquad \textbf{Equation VII.3}$$

Where $C_{n,BET}$ is the normalized capacitance (mF m$^{-2}$) and $S_{BET}$ is the apparent specific surface area of ANK3 calculated by applying the BET theory (m$^2$ g$^{-1}$).

$$C_{n,NLDFT} = \frac{C_S}{S_{NLDFT}} \cdot 1000$$ **Equation VII.4**

Where $C_{n,NLDFT}$ is the normalized capacitance (mF m$^{-2}$) and $S_{NLDFT}$ is the specific surface area of ANK3 calculated by applying the NLDFT method (m$^2$ g$^{-1}$).

## VII.3. Results and discussion

### VII.3.1. Porous texture and surface chemistry characterization

Figures VII.1 and VII.2 show the $N_2$ adsorption isotherm and PSD of ANK3, respectively. The $N_2$ isotherm is of type I, according to the IUPAC classification [26], typical of microporous materials. The PSD plot shows that ANK3 is an essentially microporous material with a wide micropore size distribution and a mean pore size of around 1.4 nm.

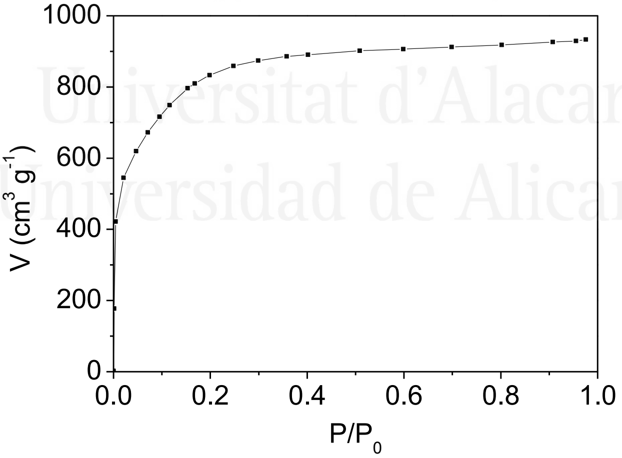

Figure VII.1. $N_2$ adsorption isotherm at 77 K of ANK3.

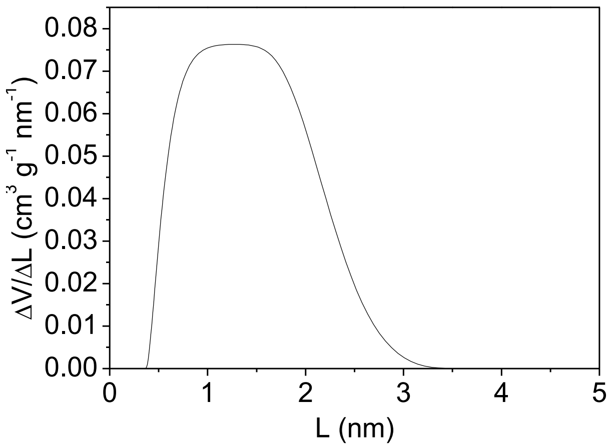

Figure VII.2. PSD of ANK3 obtained from the $N_2$ isotherm at 77 K by applying NLDFT method.

Table VII.1 shows the porous texture and surface chemistry characterization of ANK3. It can be seen that the ANK3 shows high apparent specific surface area and large micropore volume. $V_{DR}$ ($CO_2$) also indicates that the AC presents narrow microporosity (i.e., micropores less than 1 nm, approximately).

As it has been previously said in Chapter IV and V surface oxygen groups of carbon materials decompose upon heating producing CO and $CO_2$ at different temperatures which can be followed by the TPD experiments [27,28]. Evolution of CO occurs at high temperatures as consequence of the decomposition of basic or neutral groups such as phenols, ethers, carbonyls and quinones. $CO_2$ evolves generally at lower temperatures and it is mainly due to the decomposition of carboxylic groups and lactones. Decomposition of anhydride groups produces CO and $CO_2$. From the TPD profiles (not shown here), the amount of CO and $CO_2$ evolved groups were estimated and included in Table VII.1.

Table VII.1. Porous texture and surface chemistry characterization results of ANK3.

| **Sample** | **ANK3** |
|---|---|
| **$S_{BET}$ ($m^2$ $g^{-1}$)** | 3165 |
| **$S_{NLDFT}$ ($m^2$ $g^{-1}$)** | 2130 |
| **$V_{DR}$ ($N_2$) ($cm^3$ $g^{-1}$)** | 1.17 |
| **$V_{DR}$ ($CO_2$) ($cm^3$ $g^{-1}$)** | 0.81 |
| **µmolCO $g^{-1}$** | 2160 |
| **µmol$CO_2$ $g^{-1}$** | 590 |
| **µmolO $g^{-1}$ [a]** | 3340 |

[a] µmolO $g^{-1}$ = µmolCO $g^{-1}$ + 2 · µmol$CO_2$ $g^{-1}$

### VII.3.2. Electrochemical characterization in three-electrode configuration

Steady-state cyclic voltammograms performed in three-electrode configuration in the electrolytes 1M $Et_4N$ $BF_4$/PC, 1M $PYR_{14}$ $BF_4$/PC and 1M $PYR_{14}$ TFSI/PC are shown in Figure VII.3.

First of all, it should be remarked that, for the three electrolytes, black cyclic voltammograms show a quasi-rectangular shape, typical of an essentially capacitive process associated with the formation of the EDL.

Concerning the more positive potential window, red and blue cyclic voltammograms show an anodic current at high potential values, for the three electrolytes. It should be noted that this anodic current is higher for the experiments performed in 1M $Et_4N$ $BF_4$/PC medium. The corresponding cathodic peak is observed at around 0.80 V both in 1M $Et_4N$ $BF_4$/PC and 1M $PYR_{14}$ TFSI/PC and at approximately 1.00 V in 1M

$PYR_{14}$ $BF_4$/PC. As it will be discussed below, several parameters influence the electrochemical behaviour of the ANK3 in the three electrolytes, justifying the potential values registered for the cathodic process even though both anions and cations of the 1M $Et_4N$ $BF_4$/PC and 1M $PYR_{14}$ TFSI/PC electrolytes are different while, 1M $PYR_{14}$ $BF_4$/PC presents the same $BF_4^-$ anion that 1M $Et_4N$ $BF_4$/PC.

Regarding the less positive potential window, it seems that reduction processes take place at negative potential values (see red, blue, green and purple cyclic voltammograms); in fact, a cathodic current is recorded starting from -1.20, -1.70 and -2.00 V to less positive potential in 1M $Et_4N$ $BF_4$/PC, 1M $PYR_{14}$ $BF_4$/PC and 1M $PYR_{14}$ TFSI/PC media, respectively. The corresponding anodic peak is observed during the positive scan at around -0.61, -0.30 and -0.44 V for 1M $Et_4N$ $BF_4$/PC, 1M $PYR_{14}$ $BF_4$/PC and 1M $PYR_{14}$ TFSI/PC, respectively (see red, blue, green and purple cyclic voltammograms). It should be noted that the anodic peak is shifted to more positive potentials, and its intensity increases when increasing the negative potential limit down to -2.10 V (see purple cyclic voltammogram), for the three electrolytes. These redox processes may be related both to faradic charge transfer reactions (i.e. pseudocapacitance) due to the presence of surface oxygen groups in the ANK3 [6,16] and/or to decomposition of PC [8,29]. It has been shown that the aging rate of symmetric EDLC is dominated by the aging of the negative electrode, in PC-based electrolytes [30]. It is known that the electrochemical decomposition of PC can be promoted by the presence of the surface functionalities, that is to say, the solvent can react with functional groups on the ACs. Furthermore inorganic impurities of ACs that could remain after chemical activation may facilitate the irreversible decomposition of PC (in this case, ANK3 shows a residual potassium content below 1 wt. % [31]). The degradation of the PC might produce a blockage of the porosity [8,29]; it has been suggested that propene and $H_2$ come from PC reduction and $CO_2$ is produced by PC oxidation [29].

It should be noted that, when broadening the potential window, both the anodic and cathodic currents registered seems to indicate that the operative potential window increases as follows: 1M $Et_4N$ $BF_4$/PC < 1M $PYR_{14}$ $BF_4$/PC < 1M $PYR_{14}$ TFSI/PC, that is in agreement with the literature [10,14,16].

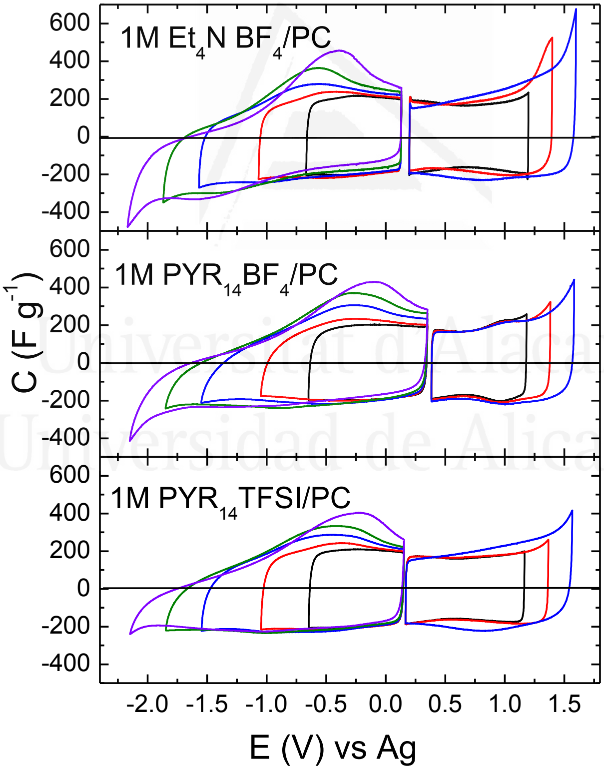

Figure VII.3. Cyclic voltammograms in three-electrode configuration in: 1M $Et_4N$ $BF_4$/PC, 1M $PYR_{14}$ $BF_4$/PC and 1M $PYR_{14}$ TFSI/PC. 1 mV $s^{-1}$ scan rate. 20 ºC.

From the cyclic voltammograms performed between the open circuit potential ($E_{oc}$) and -0.65 V and from $E_{oc}$ to 1.20 V, the capacitance values displayed by cations and anions of the electrolytes were calculated (see Table VII.2).

Table VII.2. Capacitance values calculated for the ions of the three electrolytes (1M $Et_4N$ $BF_4$/PC, 1M $PYR_{14}$ $BF_4$/PC and 1M $PYR_{14}$ TFSI/PC) in three-electrode configuration.

| | $C_s$ (F $g^{-1}$) | | $C_{n,BET}$ (mF $m^{-2}$) | | $C_{n,NLDFT}$ (mF $m^{-2}$) | |
|---|---|---|---|---|---|---|
| | Anion | Cation | Anion | Cation | Anion | Cation |
| **1M $Et_4N$ $BF_4$/PC** | 179 | 197 | 57 | 62 | 84 | 93 |
| **1M $PYR_{14}$ $BF_4$/PC** | 187 | 185 | 59 | 58 | 88 | 87 |
| **1M $PYR_{14}$ TFSI/PC** | 168 | 195 | 53 | 62 | 79 | 92 |

As shown in the table, the ANK3-based electrodes are displaying specific capacitance values which are exceeding 180 F $g^{-1}$. To the best of our knowledge, these values are among the highest so far reported for AC-based electrodes in non-conventional electrolyte. The $C_s$ for $TFSI^-$ is slightly lower than that shown by $BF_4^-$. The ion size of $BF_4^-$ has been estimated to be 0.46 nm [10] (considering that it has a spherical shape), while ion dimensions of $TFSI^-$ are, approximately, 0.79 nm and 0.29 nm [9]. Both shape and ion size with respect to the pore size, influence the adsorption in the micropores. If only one layer of ions was adsorbed in the pores, the smaller the distance between the pore wall and the centre of the ion, the higher the capacitance, what could provide higher specific capacitance for $TFSI^-$. However, when increasing the pore size, if a second layer could be accommodated, the capacitance would increase [32]. In this case, the activated carbon used has a wide micropore size distribution and an average pore size of 1.4 nm that can accommodate at least two layers of spherical $BF_4^-$ anions with a more efficient packing than $TFSI^-$. Other parameters should be taken into account such as ion solvation, conductivity and viscosity. It has been shown that for the entrance of the ions into the pores they have to be at least partially desolvated [2,9,32,33]. Also the lower conductivity and higher viscosity of 1M $PYR_{14}$ TFSI/PC compared to both 1M $Et_4N$ $BF_4$/PC and 1M $PYR_{14}$ $BF_4$/PC (see Table VII.3) explains the lower $C_s$ of $TFSI^-$ compared to that displayed by $BF_4^-$. Even though viscosity and conductivity of 1M $Et_4N$ $BF_4$/PC and 1M $PYR_{14}$ $BF_4$/PC are quite similar, the fact that both ions, and not only the counterions (with the opposite charge as that of the charged electrode) are involved in the EDL formation [12] may justify the different $C_s$ values calculated for $BF_4^-$ in these two electrolytes.

Table VII.3. Viscosity and conductivity of the electrolytes at 20 ºC [10].

| | **Viscosity (mPa s)** | **Conductivity (mS $cm^{-1}$)** |
|---|---|---|
| **1M $Et_4N$ $BF_4$/PC** | 4.0 | 10.7 |
| **1M $PYR_{14}$ $BF_4$/PC** | 4.2 | 9.8 |
| **1M $PYR_{14}$ TFSI/PC** | 5.1 | 7.3 |

The $C_s$ of $Et_4N^+$ (calculated from 1M $Et_4N$ $BF_4$/PC) is slightly higher than that shown by $PYR_{14}^+$ (calculated from 1M $PYR_{14}$ $BF_4$/PC) but almost equal to that shown by $PYR_{14}^+$ (calculated from 1M $PYR_{14}$ TFSI/PC). In this case, the diameter of $Et_4N^+$ is 0.69 nm [10] (considering that it has a spherical shape), while the dimensions of $PYR_{14}^+$, which has been estimated using the Avogadro software, are around 1.10 nm and 0.65 nm (see Figure VII.4). If $PYR_{14}^+$ is adsorbed with the longest dimension perpendicular to the pore wall, both $Et_4N^+$ and $PYR_{14}^+$ would have similar distance between the pore wall and the centre of the ion and, then, similar $C_s$. Since the activated carbon used has a wide micropore size distribution with an average pore size of 1.4 nm, the pores are wide enough to accommodate the larger cations giving similar capacitances.

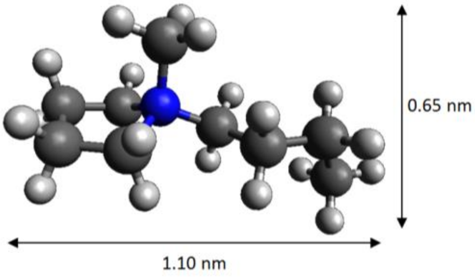

Figure VII.4. Avogadro software model of the structure of $PYR_{14}^{+}$.

It is well known, that not only the apparent specific surface area but also PSD and surface chemistry affects to the capacitance displayed by carbon materials both in aqueous and non-aqueous electrolytes [6,7,9,12,34]. The ratio between the pore width and the ion size is a key parameter that strongly affects the electrochemical behaviour. It has been demonstrated that pore size very close to the ion size leads to the maximum capacitance [9], however ion access to very narrow micropores (i.e. non-accessible pores) may be hindered (thus showing sieving effect) [6,12].

In this study, the porosity of the AC has been tailored in order to obtain a high apparent specific surface area and a high volume of micropores with an average pore size of around 1.4 nm. This tailored porosity makes possible to reach very high $C_s$ values, in the three electrolytes, since this material provides wider micropores for an efficient adsorption and accommodation of ions for the different ion sizes studied in this work. For this reason, these results improve those found in the literature for other ACs in non-aqueous electrolytes (using both ACN and PC as solvent) [10,35-37]. $C_{n,NLDFT}$ values are comparable to that showed for

ACs that do not present sieving effect [10], thus suggesting that most of the porosity is fully accessible to the ions of the electrolytes, because the pore size (of around 1.4 nm) is higher than the ion size of the electrolytes used.

Cyclic voltammograms obtained for the pure IL $PYR_{14}$ TFSI at three different temperatures (20, 40 and 60 ºC) are shown in Figure VII.5. Cyclic voltammograms performed in the pure $PYR_{14}$ TFSI at 20 ºC show distorted shape compared to that recorded at 40 and 60 ºC, that exhibit a quasi-rectangular shape typical of an essentially capacitive process associated with the formation of the EDL. The increase of conductivity and decrease of viscosity when increasing temperature [15,38,39] may explain these results. Furthermore, $PYR_{14}^+$ cation seems to present diffusional problems at 20 ºC, presumably due both to: (i) the higher size of $PYR_{14}^+$ (1.10 and 0.65 nm, see Figure VII.4) compared to $TFSI^-$ (0.79 and 0.29 nm [9]) with respect to the mean pore size of ANK3 (around 1.4 nm) and (ii) the characteristics of the electrolyte at this temperature (i.e. conductivity and viscosity) [16]. On the other hand, the comparison of cyclic voltammograms performed at 20 ºC in the pure $PYR_{14}$ TFSI (Figure VII.5) and in 1M $PYR_{14}$ TFSI/PC (Figure VII.3), reveals that conductivity increases and viscosity decreases when using the PC-containing electrolyte, as it has been previously seen [16,39]. Thus, it seems that electrochemical behaviour is affected not only by ion/pore size ratio and ion shape but also by viscosity and conductivity of the IL (that vary both by diluting the IL with organic solvents and by changing IL temperature) [40].

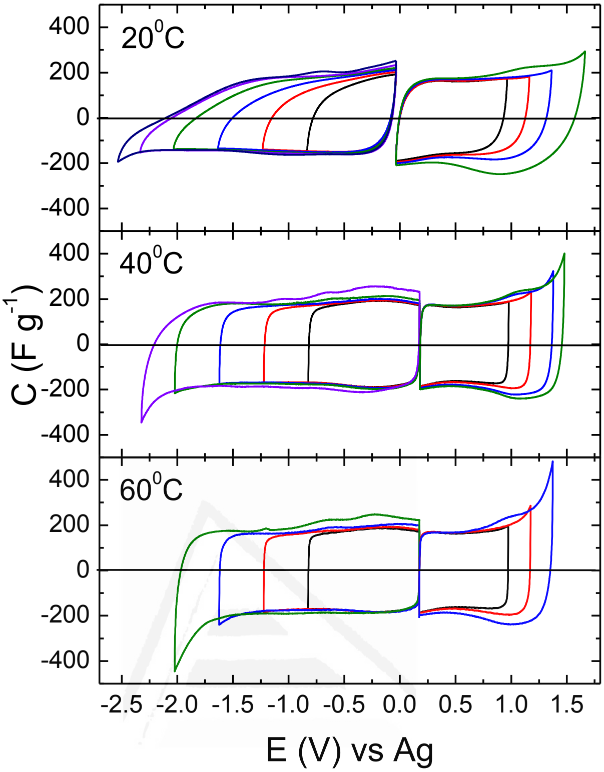

Figure VII.5. Cyclic voltammograms in three-electrode configuration in $PYR_{14}$ TFSI at 20, 40 and 60 ºC. 1 mV $s^{-1}$ scan rate.

It should be noted that by increasing the potential limits (both positive and negative window) several redox peaks are observed for the three temperatures. At 20 ºC, an anodic peak is observed at approximately 1.15 V and the corresponding cathodic peak is seen at around 0.95 V. These redox processes are observed at 1.00 V (anodic peak) and at 1.10 V (cathodic peak) for the cyclic voltammograms performed at 40 and 60 ºC. Furthermore, three oxidation peaks are observed at around -0.22, -0.67 and -1.10 V for the cyclic voltammograms performed at 40 and 60 ºC, when reaching potential limits down to -2.30 and -2.00 V, respectively. Even at 20 ºC, a slight anodic peak is observed at -0.70 V after reaching the negative potential of -2.50 V. These redox peaks may be due both to faradic charge transfer reactions (i.e. pseudocapacitance), due to the presence of surface oxygen groups in the ANK3 [16], and/or to the degradation of the $PYR_{14}$ TFSI. It should be noted that the remarkable anodic peak observed at around -0.44 V for 1M $PYR_{14}$ TFSI/PC (see Figure VII.3) is not observed in the cyclic voltammograms performed in the pure $PYR_{14}$ TFSI, thus it is reasonable to suppose that decomposition of PC might take place at potentials lower than -1.20 V. Regarding potential stability window it seems to decrease when increasing temperature: a negative current is recorded starting from -2.30 V, -1.80 V and -1.50 V to more negative values and a positive current starts at, approximately, 1.50 V, 1.40 and 1.20 V for the cyclic voltammograms done at 20, 40 and 60 ºC, respectively. These latter findings are in line with results already reported in the literature [2, 43].

Table VII.4 shows capacitance values of $PYR_{14}^+$ and $TFSI^-$ calculated from the cyclic voltammograms performed between $E_{oc}$ and -0.82 V and between $E_{oc}$ and 0.97 V. Values obtained from the experiments performed at 40 and 60 ºC are quite similar. Capacitance displayed by $PYR_{14}^+$ is slightly higher than that shown by the $TFSI^–$ anion; furthermore, the same trend was observed from 1M $PYR_{14}$ TFSI/PC (see Table VII.2). However, this trend is not observed from the experiment done at 20 ºC, where the higher size of $PYR_{14}^+$ cation leads to diffusional problems at this temperature.

Table VII.4. Capacitance values calculated for the ions of $PYR_{14}$ TFSI in three-electrode configuration.

| | $C_s$ (F $g^{-1}$) | | $C_{n,BET}$ (mF $m^{-2}$) | | $C_{n,NLDFT}$ (mF $m^{-2}$) | |
|---|---|---|---|---|---|---|
| | $TFSI^-$ | $PYR_{14}^+$ | TFSI- | $PYR_{14}^+$ | TFSI- | $PYR_{14}^+$ |
| **20 ºC** | 149 | 132 | 47 | 42 | 70 | 62 |
| **40 ºC** | 167 | 176 | 53 | 56 | 78 | 83 |
| **60 ºC** | 167 | 174 | 53 | 55 | 78 | 82 |

It should be pointed out that the tailored porosity of ANK3 (high apparent specific surface area and a high volume of micropores with an average pore size of around 1.4 nm) allows to obtain very high $C_s$ values of around 170 F $g^{-1}$ in solvent-free electrolytes (showed by for both ions of $PYR_{14}$ TFSI at 40 and 60 ºC). These values improve those found in the literature for high surface area carbon materials in $PYR_{14}$ TFSI [41,42] and in other IL [43] and for AC-based solid state supercapacitors [44] at 60 ºC.

### VII.3.3. EDLC characterization

To complete the electrochemical characterization of the ANK3 in the PC-containing electrolytes studied, ANK3-based EDLCs were assembled and preliminary investigations were performed. The mass loadings of the active materials were balanced, according to the electrochemical stability limits and the $C_s$ values showed in each electrolyte, in order to avoid the premature aging of the cell and to enhance the electrochemical performance of the EDLCs [24,25,45,46]. The ratio of mass was calculated using Equation VII.5:

$$\frac{m_+}{m_-} = \frac{C_{S-} \cdot \Delta E_-}{C_{S+} \cdot \Delta E_+} \qquad \textbf{Equation VII.5}$$

Where $m_+/m_-$ is the mass ratio between the positive and the negative electrode, $C_{s+}/C_{s-}$ is the respective $C_s$ and $\Delta E_+/\Delta E_-$ is the respective maximum operating potential window (calculated from three-electrode configuration experiments).

Three cyclic voltammograms were performed at 1, 2, 5, 20, 50, 100 and 200 mV s$^{-1}$ scan rates. Operative potential windows of 2.7, 3.2 and 3.5 V were reached for 1M $Et_4N$ $BF_4$/PC, 1M $PYR_{14}$ $BF_4$/PC and 1M $PYR_{14}$ TFSI/PC, respectively. The 3$^{rd}$ steady cyclic voltammograms at 5 mV s$^{-1}$, for the three electrolytes, are presented in Figure VII.6. The cyclic voltammograms show a quasi-rectangular shape, typical of an essentially capacitive process associated with the formation of the EDL.

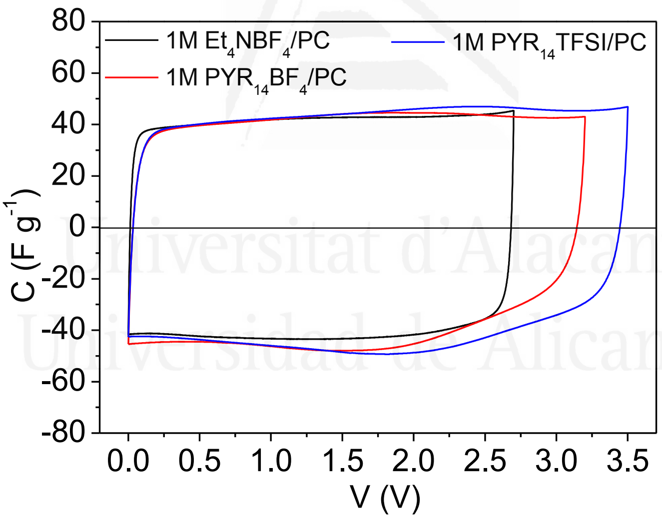

Figure VII.6. Cyclic voltammograms at 5 mV s$^{-1}$ in two-electrode configuration in: 1M $Et_4N$ $BF_4$/PC, 1M $PYR_{14}$ $BF_4$/PC and 1M $PYR_{14}$ TFSI/PC. 20 ºC.

$C_s$ values, at each scan rate, were also calculated and they are shown in Figure VII.7. It should be remarked the high $C_s$ value, of around 45 F g$^{-1}$ at 1 mV s$^{-1}$ scan rate, shown by ANK3 in the three electrolytes.

Even though the comparison is not straightforward (because of the different electrochemical conditions), capacitance values obtained improve the results reported for different ACs in several non-aqueous electrolytes [8,10,16,23,30,47]. In 1M $Et_4N$ $BF_4$/PC, the percentage value of retained capacitance at 200 mV $s^{-1}$ is 56%, which is higher than for the other two electrolytes. These results suggest that ion/pore size ratio, ion shape and viscosity and conductivity of the electrolyte have a strong influence on the electrochemical behaviour at higher scan rate.

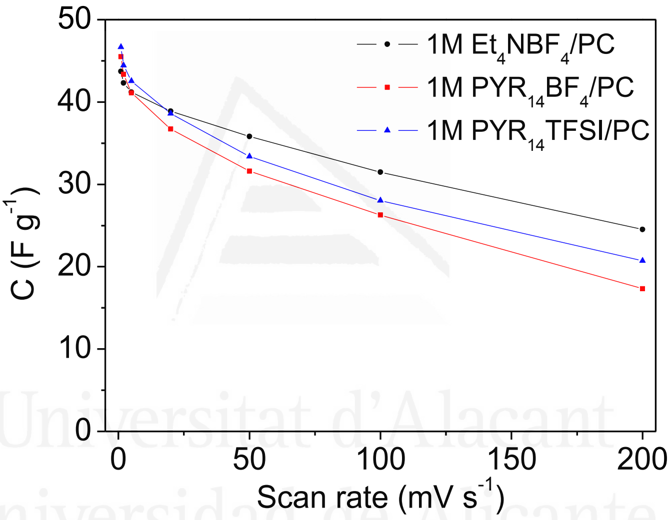

Figure VII.7. $C_s$ values *versus* scan rate plot for: 1M $Et_4N$ $BF_4$/PC, 1M $PYR_{14}$ $BF_4$/PC and 1M $PYR_{14}$ TFSI/PC.

The excellent electrochemical behaviour shown by ANK3 (in terms of specific capacitance and retained capacitance) due to the tailored porosity of this AC makes it a promising candidate as electrode for EDLC both in organic and IL electrolytes.

## VII.4. Conclusions

Tailoring the porosity of the AC is one of the key to take fully advantages of the features of innovative electrolytes. We showed that using AC with high apparent specific surface area and high micropore volume with an average pore size of 1.4 nm it is possible to obtain very high capacitance values in the pure $PYR_{14}$ TFSI at three different temperatures (20, 40 and 60 ºC) as well as in 1M $Et_4N$ $BF_4$/PC, 1M $PYR_{14}$ $BF_4$/PC and 1M $PYR_{14}$ TFSI/PC at 20 ºC, using a three-electrode configuration. Excellent electrochemical behaviour (in terms of capacitance and retained capacitance) was also shown by ANK3-based EDLC in 1M $Et_4N$ $BF_4$/PC, 1M $PYR_{14}$ $BF_4$/PC and 1M $PYR_{14}$ TFSI/PC at 20 ºC.

These results pointed out that the tailored porosity of the ANK3 makes it an excellent candidate to be used as electrode for the realization of high voltage, high energy EDLC containing non-conventional electrolytes.

Furthermore, it was confirmed that several parameters, such as the ion/pore size ratio, the ion shape, the ion solvation and the characteristics of the electrolyte (i.e. conductivity and viscosity) have a strong influence on the electrochemical behaviour shown by ANK3.

## References

[1] Béguin F, Raymundo-Piñero E, Frackowiak E. Electrical double-layer capacitors and pseudocapacitors. In: Béguin F, Frackowiak E, editors. Carbons for electrochemical energy storage and conversion systems, Boca Raton (USA): CRC Press,Taylor & Francis Group; 2010, p. 329.

[2] Béguin F, Presser V, Balducci A, Frackowiak E. Carbons and electrolytes for advanced supercapacitors. Adv Mater 2014;26:2219-51.

[3] Miller JR, Simon P. Materials science - Electrochemical capacitors for energy management. Science 2008;321:651-2.

[4] Frackowiak E, Béguin F. Carbon materials for the electrochemical storage of energy in capacitors. Carbon 2001;39:937-50.

[5] Bleda-Martínez MJ, Lozano-Castelló D, Cazorla-Amorós D, Morallón E. Kinetics of double-layer formation: influence of porous structure and pore size distribution. Energ Fuel 2010;24:3378-84.

[6] Lozano-Castelló D, Cazorla-Amorós D, Linares-Solano A, Shiraishi S, Kurihara H, Oya A. Influence of pore structure and surface chemistry on electric double layer capacitance in non-aqueous electrolyte. Carbon 2003;41:1765-75.

[7] Bleda-Martínez MJ, Lozano-Castelló D, Morallón E, Cazorla-Amorós D, Linares-Solano A. Chemical and electrochemical characterization of porous carbon materials. Carbon 2006;44:2642-51.

[8] Cazorla-Amorós D, Lozano-Castelló D, Morallón E, Bleda-Martínez MJ, Linares-Solano A, Shiraishi S. Measuring cycle efficiency and capacitance of chemically activated carbons in propylene carbonate. Carbon 2010;48:1451-6.

[9] Largeot C, Portet C, Chmiola J, Taberna P, Gogotsi Y, Simon P. Relation between the ion size and pore size for an electric double-layer capacitor. J Am Chem Soc 2008;130:2730.

[10] Pohlmann S, Kuehnel R, Centeno TA, Balducci A. The Influence of Anion-Cation Combinations on the Physicochemical Properties of Advanced Electrolytes for Supercapacitors and the Capacitance of Activated Carbons. ChemElectroChem 2014;1:1301-11.

[11] Frackowiak E, Abbas Q, Beguin F. Carbon/carbon supercapacitors. J Energy Chem 2013;22:226-40.

[12] Lazzari M, Mastragostino M, Pandolfo AG, Ruiz V, Soavi F. Role of Carbon Porosity and Ion Size in the Development of Ionic Liquid Based Supercapacitors. J Electrochem Soc 2011;158:A22-5.

[13] Bichat MP, Raymundo-Pinero E, Beguin F. High voltage supercapacitor built with seaweed carbons in neutral aqueous electrolyte. Carbon 2010;48:4351-61.

[14] Brandt A, Balducci A. Theoretical and practical energy limitations of organic and ionic liquid-based electrolytes for high voltage electrochemical double layer capacitors. J Power Sources 2014;250:343-51.

[15] Galinski M, Lewandowski A, Stepniak I. Ionic liquids as electrolytes. Electrochim Acta 2006;51:5567-80.

[16] Pohlmann S, Lobato B, Centeno TA, Balducci A. The influence of pore size and surface area of activated carbons on the performance of ionic liquid based supercapacitors. Phys Chem Chem Phys 2013;15:17287-94.

[17] Simon P, Gogotsi Y. Materials for electrochemical capacitors. Nat Mater 2008;7:845-54.

[18] Huang P, Pech D, Lin R, McDonough JK, Brunet M, Taberna P et al. On-chip micro-supercapacitors for operation in a wide temperature range. Electrochem Commun 2013;36:53-6.

[19] Kado Y, Imoto K, Soneda Y, Yoshizawa N. Highly enhanced capacitance of MgO-templated mesoporous carbons in low temperature ionic liquids. J Power Sources 2014;271:377-81.

[20] Rouquerol J, Llewellyn P, Rouquerol F. Is the BET equation applicable to microporous adsorbents? Stud Surf Sci Catal 2007;160:49-56.

[21] Lozano-Castelló D, Suárez-García F, Cazorla-Amorós D, Linares-Solano Á. Porous texture of carbons. In: Beguin F, Frackowiak E, editors. Carbons for electrochemical energy storage and conversion

systems, Boca Raton (USA): CRC Press,Taylor & Francis Group; 2010, p. 115.

[22] Jagiello J, Olivier JP. 2D-NLDFT adsorption models for carbon slit-shaped pores with surface energetical heterogeneity and geometrical corrugation. Carbon 2013;55:70-80.

[23] Schütter C, Ramírez-Castro C, Oljaca M, Passerini S, Winter M, Balducci A. Activated carbon, carbon blacks and graphene based nanoplatelets as active materials for electrochemical double layer capacitors: a comparative study. J Electrochem Soc 2015;162:A44-51.

[24] Snook GA, Wilson GJ, Pandolfo AG. Mathematical functions for optimisation of conducting polymer/activated carbon asymmetric supercapacitors. J Power Sources 2009;186:216-23.

[25] Peng C, Zhang S, Zhou X, Chen GZ. Unequalisation of electrode capacitances for enhanced energy capacity in asymmetrical supercapacitors. Energy Environ Sci 2010;3:1499-502.

[26] Sing KSW, Everett DH, Haul RAW, Moscou L, Pierotti RA, Rouquerol J et al. Reporting physisorption data for gas solid systems with special reference to the determination of surface-area and porosity. Pure Appl Chem 1985;57(4):603-19.

[27] Román-Martínez MC, Cazorla-Amorós D, Linares-Solano A. TPD and TPR characterization of carbonaceous supports and Pt/C catalysts. Carbon 1993;31:895-902.

[28] Figueiredo J, Pereira M, Freitas M, Orfao J. Modification of the surface chemistry of activated carbons. Carbon 1999;37:1379-89.

[29] Hahn M, Würsig A, Gallay R, Novák P, Kötz R. Gas evolution in activated carbon/propylene carbonate based double-layer capacitors. Electrochem Commun 2005;7:925-30.

[30] Ruch PW, Cericola D, Foelske A, Koetz R, Wokaun A. A comparison of the aging of electrochemical double layer capacitors with acetonitrile and propylene carbonate-based electrolytes at elevated voltages. Electrochim Acta 2010;55:2352-7.

[31] Lozano-Castelló D, Lillo-Ródenas MA, Cazorla-Amorós D, Linares-Solano A. Preparation of activated carbons from Spanish anthracite: I. Activation by KOH. Carbon 2001;39:741-9.

[32] Fedorov MV, Kornyshev AA. Ionic Liquids at Electrified Interfaces. Chem Rev 2014;114:2978-3036.

[33] Jiang D, Jin Z, Henderson D, Wu J. Solvent Effect on the Pore-Size Dependence of an Organic Electrolyte Supercapacitor. J Phys Chem Lett 2012;3:1727-31.

[34] Bleda-Martínez MJ, Maciá-Agulló JA, Lozano-Castelló D, Morallón E, Cazorla-Amorós D, Linares-Solano A. Role of surface chemistry on electric double layer capacitance of carbon materials. Carbon 2005;43:2677-84.

[35] Vix-Guterl C, Frackowiak E, Jurewicz K, Friebe M, Parmentier J, Béguin F. Electrochemical energy storage in ordered porous carbon materials. Carbon 2005;43:1293-302.

[36] Raymundo-Piñero E, Kierzek K, Machnikowski J, Béguin F. Relationship between the nanoporous texture of activated carbons and their capacitance properties in different electrolytes. Carbon 2006;44:2498-507.

[37] Kumagai S, Tashima D. Electrochemical performance of activated carbons prepared from rice husk in different types of non-aqueous electrolytes. Biomass Bioenerg 2015;83:216-23.

[38] Bonhote P, Dias A, Papageorgiou N, Kalyanasundaram K, Gratzel M. Hydrophobic, highly conductive ambient-temperature molten salts. Inorg Chem 1996;35:1168-78.

[39] Kuehnel R-, Boeckenfeld N, Passerini S, Winter M, Balducci A. Mixtures of ionic liquid and organic carbonate as electrolyte with improved safety and performance for rechargeable lithium batteries. Electrochim Acta 2011;56:4092-9.

[40] Fuertes AB, Sevilla M. High-surface area carbons from renewable sources with a bimodal micro-mesoporosity for high-performance ionic liquid-based supercapacitors. Carbon 2015;94:41-52.

[41] Balducci A, Dugas R, Taberna PL, Simon P, Plee D, Mastragostino M et al. High temperature carbon-carbon supercapacitor using ionic liquid as electrolyte. J Power Sources 2007;165:922-7.

[42] Tooming T, Thomberg T, Kurig H, Jaenes A, Lust E. High power density supercapacitors based on the carbon dioxide activated D-glucose derived carbon electrodes and 1-ethyl-3-methylimidazolium tetrafluoroborate ionic liquid. J Power Sources 2015;280:667-77.

[43] Balducci A, Bardi U, Caporali S, Mastragostino M, Soavi F. Ionic liquids for hybrid supercapacitors. Electrochem Commun 2004;6:566-70.

[44] Ayalneh Tiruye G, Munoz-Torrero D, Palma J, Anderson M, Marcilla R. All-solid state supercapacitors operating at 3.5 V by using ionic liquid based polymer electrolytes. J Power Sources 2015;279:472-80.

[45] Cericola D, Koetz R, Wokaun A. Effect of electrode mass ratio on aging of activated carbon based supercapacitors utilizing organic electrolytes. J Power Sources 2011;196:3114-8.

[46] Khomenko V, Raymundo-Pinero E, Beguin F. A new type of high energy asymmetric capacitor with nanoporous carbon electrodes in aqueous electrolyte. J Power Sources 2010;195:4234-41.

[47] Orita A, Kamijima K, Yoshida M. Allyl-functionalized ionic liquids as electrolytes for electric double-layer capacitors. J Power Sources 2010;195:7471-9.

# Chapter VIII

## General conclusions

Advanced nanostructured carbon materials have been synthesized and chemically and electrochemically characterized with the purpose of being used for electrochemical energy storage applications. Carbon materials with tailored porosity were revealed as promising candidates to be used as electrodes for electrochemical capacitors. Further studies were also performed in order to deepen into the knowledge of the electrochemical behaviour of the selected porous carbon materials under different electrochemical conditions and using different electrolytes.

The results obtained from the PhD Thesis led to the following general conclusions:

➢ Regarding the electrochemical hydrogen storage in nanoporous carbons, it has been shown that:

- Both the characteristics of the ACs and the electrolyte used have an important influence in the electrochemical hydrogen storage process. The electrochemical hydrogen storage capacity was higher in basic medium than in neutral medium. The capacity was also higher for the AC with the higher porosity development in both electrolytes.
- *In situ* Raman spectroscopy confirmed that chemical carbon-hydrogen bonds are formed during the charge process in both electrolytes and that this hydrogen chemisorption is reversible.
- Weakly bonded hydrogen was the dominant form in basic medium, while strongly bonded hydrogen dominated in neutral medium.

➢ With respect to the characterization of a ZTC by using the EQCM and *in situ* Raman spectroscopy techniques, the main conclusions are as follows:

- ZTC was greatly electrochemically oxidized in the first voltammetric cycles under the potential intervals studied (i.e. from -0.10 V up to 0.80 V, 1.20 V and 1.40 V). Under more severe electrochemical conditions, ZTC suffered a remarkable degradation that involves a noticeable loss of conductivity and of the porous structure.
- *In situ* Raman spectroscopy showed that electrochemical oxidation of ZTC under anodic conditions produced structural changes that involved the degradation of the three-dimensional regular network.
- Both the EQCM and the TPD results obtained suggested that the electrochemical oxidation and gasification of the ZTC takes place simultaneously. It was shown that electrochemical gasification of the carbon material can occur not only under anodic conditions but also under cathodic conditions (i.e. by reducing carbon-oxygen groups generated under anodic conditions going to more negative potential). The gravimetric response recorded with the EQCM demonstrated to be useful to further explain the electrochemical oxidation and gasification processes displayed during the voltammetric measurements.

➢ Concerning the synthesis and characterization of silica-templated ordered mesoporous carbon thin films, the main conclusions can be summarized as follows:

- Continuous mesoporous carbon thin film was successfully synthesized onto a graphite current collector using an ordered mesoporous silica thin film as the hard-template. Structural characterization of the thin films synthesized showed that: (i) the silica template presented ordered mesopores of around 8 nm perpendicularly disposed to the graphite current collector, (ii) the carbon material covered the nanostructure of the template and it maintained the structural order of the silica thin film, (iii) the order of the mesoporous carbon thin film partially decreased by removing the silica template and the mesopore size was around 2-3 nm.

- Very high capacitance values were recorded for the mesoporous carbon and the composite silica/carbon thin films symmetric capacitors, thus improving the values reported for other carbon-based devices. The very similar electrochemical results obtained for both thin films demonstrated that the uniform carbon coating makes the composite to have excellent electrical conductivity. Furthermore, the durability test performed demonstrated that the thin films synthesized showed low degradation, even after a high number of cycles are applied.
- Both the mesoporous carbon thin film and the composite silica/carbon thin film showed exceptional electrochemical properties, in terms of capacitance, rate performance and stability, making them promising candidates as electrodes for micro-capacitors.

➢ The main conclusions extracted from the study of the electrochemical performance of a superporous activated in ionic liquid-based electrolytes are:

- Very high capacitance values in the pure $PYR_{14}$ TFSI at three different temperatures (20, 40 and 60 ºC) as well as in 1M $Et_4N$ $BF_4$/PC, 1M $PYR_{14}$ $BF_4$/PC and 1M $PYR_{14}$ TFSI/PC at 20 ºC were shown by ANK3 using a three-electrode configuration. Furthermore, excellent electrochemical behaviour (in terms of capacitance and retained capacitance) was also shown by ANK3-based supercapacitors in 1M $Et_4N$ $BF_4$/PC, 1M $PYR_{14}$ $BF_4$/PC and 1M $PYR_{14}$ TFSI/PC at 20 ºC.

- It was demonstrated that several parameters, such as the ion/pore size ratio, the ion shape, the ion solvation and the characteristics of the electrolyte (i.e. conductivity and viscosity) have a strong influence on the electrochemical behaviour shown by ANK3.
- The tailored porosity of the ANK3 makes it an excellent candidate to be used as electrode for the design of high voltage, high energy supercapacitors containing non-conventional electrolytes.

# *Capítulo VIII*

## Conclusiones generales

En la presente Tesis Doctoral, diferentes materiales carbonosos nanoestructurados han sido sintetizados y caracterizados química y electroquímicamente para aplicaciones de almacenamiento electroquímico de energía. Los materiales carbonosos con porosidad diseñada han mostrado ser excelentes candidatos para su uso como electrodos en condensadores electroquímicos. Además, se han realizado estudios adicionales con el fin de profundizar en el conocimiento del comportamiento electroquímico de los materiales carbonosos porosos seleccionados, bajo distintos condiciones electroquímicas y usando diferentes electrolitos.

Así pues, el trabajo desarrollado en la presente Tesis Doctoral permite extraer las siguientes conclusiones generales:

➢ En relación al estudio del almacenamiento electroquímico de hidrógeno en materiales carbonosos nanoporosos son:

- Las propiedades de los carbones activados así como el tipo de electrolito utilizado mostraron una gran influencia en el almacenamiento electroquímico de hidrógeno. El porcentaje de hidrógeno almacenado electroquímicamente fue mayor para la muestra con una porosidad más desarrollada, en ambos medios. Además, el hidrógeno almacenado electroquímicamente fue mayor en medio básico que en medio neutro.
- La técnica de espectroscopía Raman *in situ* confirmó que se forman enlaces químicos entre el hidrógeno y el carbono durante el proceso de carga, en ambos electrolitos, y que la quimisorción de hidrógeno es reversible.

- Se observó que en medio básico predomina el hidrógeno enlazado más débilmente, mientras que en medio neutro predomina el hidrógeno enlazado más fuertemente.

➢ Las conclusiones generales extraídas de la caracterización del ZTC mediante el uso de técnicas como la EQCM y la espectroscopía Raman *in situ* son:

- El ZTC se oxida electroquímicamente en los primeros ciclos de voltamperometría cíclica bajo los intervalos de potencial estudiados (de -0,10 V a 0,80 V, 1,20 V y 1,40 V). Bajo condiciones electroquímicas más severas, el ZTC sufre una degradación importante que implica la pérdida significativa de conductividad eléctrica y degradación de la estructura porosa.
- La técnica de espectroscopía Raman *in situ* mostró, también, que la oxidación electroquímica del ZTC, bajo condiciones anódicas, produce cambios estructurales (degradación de la estructura porosa tridimensional y ordenada).
- Los resultados obtenidos de la caracterización realizada con las técnicas EQCM y TPD sugirieron que los procesos de oxidación y gasificación electroquímica del ZTC tienen lugar de forma simultánea. Se mostró que la gasificación del material carbonoso puede tener lugar no sólo bajo condiciones anódicas, sino también bajo condiciones catódicas (es decir, reduciendo los grupos oxigenados, generados previamente bajo condiciones anódicas).

  La respuesta gravimétrica proporcionada por la técnica EQCM demostró ser útil para explicar más profundamente los procesos de oxidación y gasificación electroquímica que se producen durante la caracterización voltamperométrica.

➢ Respecto a la síntesis y caracterización de películas delgadas de un material carbonoso mesoporoso sintetizado por nanomoledo, las principales conclusiones extraídas son:

- Se ha conseguido sintetizar una película delgada y continua de un material carbonoso mesoporoso, directamente sobre un colector de corriente de grafito, utilizando como plantilla una película delgada de sílice mesoporosa ordenada. La caracterización de la estructura de las películas sintetizadas mostró que: (i) la película delgada de sílice presenta mesoporos ordenados de, aproximadamente, 8 nm dispuestos perpendicularmente al colector de corriente de grafito, (ii) el material carbonoso cubre la nanoestructura de la plantilla, manteniendo el orden estructural de la película delgada de sílice mesoporosa, (iii) el orden de la película delgada de material carbonoso mesoporoso disminuye parcialmente al eliminar la plantilla de sílice, además, el tamaño de los mesoporos del material carbonoso está en torno a 2-3 nm.
- Los condensadores electroquímicos simétricos preparados a partir de las películas delgadas del material carbonoso mesoporoso y del material compuesto sílice/carbón han mostrado valores elevados de capacidad, mejorando los resultados reportados en la bibliografía para otros dispositivos basados en materiales carbonosos. El comportamiento electroquímico mostrado por estos dos materiales demuestra que el depósito de la lámina delgada de material carbonoso sobre la sílice hace que el material compuesto posea una excelente conductividad eléctrica. Además, los experimentos de

durabilidad realizados mostraron que ambos materiales sufren una baja degradación, incluso después de ser sometidos a un elevado número de ciclos.

- Tanto las películas delgadas del material carbonoso mesoporoso como del material compuesto sílice/carbón mostraron excelentes propiedades electroquímicas (capacidad, retención de capacidad y estabilidad) lo que hace que sean candidatos prometedores para su uso como electrodos en micro-condensadores.

➢ Las conclusiones principales del estudio del comportamiento electroquímico de un carbón activado superporoso en electrolitos basados en líquidos iónicos son:

- El carbón activado ANK3 mostró elevados valores de capacidad en el líquido iónico $PYR_{14}$ TFSI a tres temperaturas (20, 40 y 60 ºC) y en los medios 1M $Et_4N$ $BF_4$/PC, 1M $PYR_{14}$ $BF_4$/PC y 1M $PYR_{14}$ TFSI/PC a 20 ºC (en configuración de tres electrodos). Además, los supercondensadores basados en los electrolitos 1M $Et_4N$ $BF_4$/PC, 1M $PYR_{14}$ $BF_4$/PC y 1M $PYR_{14}$ TFSI/PC mostraron, también, un excelente comportamiento electroquímico (elevados valores de capacidad y de retención de capacidad).
- Se ha visto que el comportamiento electroquímico mostrado por el ANK3 está influenciado por diferentes parámetros, tales como: la relación entre el tamaño del ión y el tamaño del poro, la forma de los iones, la solvatación de éstos y otras características del electrolito (conductividad y viscosidad).
- La porosidad diseñada del ANK3 hace que sea un excelente candidato para su uso como electrodo en supercondensadores basados en electrolitos no convencionales, haciendo que estos

dispositivos puedan alcanzar elevados valores de voltaje de trabajo así como de energía almacenada.

# Summary

The main objective of this PhD Thesis is the synthesis and characterization of advanced nanostructured carbon materials for energy storage applications.

Porous carbon materials have been intensely investigated as electrodes for energy storage applications because of their low-cost, versatility of structure/texture, good conductivity and high cycling life. A relevant electrochemical application of carbon materials is hydrogen storage by electro-reduction of water in alkaline and neutral media. Two activated carbons (ACs), with different porous texture and surface chemistry, were used and characterized by different electrochemical techniques in two electrolytes (6 M KOH and 0.5 M $Na_2SO_4$). Comparing the two samples, it was suggested that the surface functionality and porosity of the activated carbons have an important influence in the electrochemical hydrogen storage process. From the galvanostatic charge-discharge (GCD) curves, it was shown that the electrochemical hydrogen storage capacity was higher in basic medium than in neutral medium. The capacity was also higher for the AC with the higher porosity development in both electrolytes. The *in situ* Raman spectra collected showed that carbon-hydrogen bonds are formed reversibly in both electrolytes during cathodic conditions. It was confirmed that, in both electrolytes, the hydrogenation of carbon atoms was produced more easily for the sample with lower amount of surface oxygen groups. In basic medium, for the two samples, the formation of carbon-hydrogen bonds proceeded at more positive potential with respect to the thermodynamic potential value for hydrogen evolution.

Currently, templated carbons have attracted much attention because the combination of both tailored and ordered porous network with a nano-sized structure could result in the development of unique features for their potential applications. The zeolite-templated carbon (ZTC) synthesized in the nanochannels of zeolite Y is a promising candidate as electrode for electric double-layer capacitors because of its unique structure consisting of buckybowl-like nanographenes assembled into a three-dimensional regular network with a well-defined pore size of 1.2 nm and large surface area. The electrochemical behaviour of the ZTC, focusing on both the surface chemistry and structural changes produced under different electrochemical conditions in 1M $H_2SO_4$ medium, was studied. The electrochemical quartz crystal microbalance (EQCM) allowed simultaneous monitoring of the voltammetric and gravimetric responses of ZTC. Under electrochemical oxidation conditions, a high anodic current and a net mass increase were recorded, resulting in the increase of the specific capacitance owing to the contribution of the pseudocapacitance, mainly derived from the hydroquinone-quinone redox couple. Under more severe electrochemical conditions, a net mass loss was observed, revealing that electrochemical gasification took place. Surface chemistry, before and after the electrochemical treatments, was analyzed through temperature programmed desorption (TPD) experiments. Both the EQCM and the TPD experimental results obtained suggested that the electrochemical oxidation and gasification of the ZTC took place simultaneously. Furthermore, *in situ* Raman spectroscopy was used to further characterize the structural changes produced in ZTC under the electrochemical conditions applied, supporting that high potential values produced the electrochemical oxidation and degradation of the carbon material.

Furthermore, the recent technological trend towards portable electronic devices has leaded a strong interest in small-scale energy storage devices. Thin film capacitors have great potential to be used as power source in small-scale energy storage devices. In this PhD Thesis, a silica-templated ordered mesoporous carbon thin film was directly synthesized on a graphite current collector using an ordered mesoporous silica thin film as hard-template. The nanostructure of the silica, the composite silica/carbon and the mesoporous carbon thin films was characterized by field emission scanning electron microscopy coupled to energy-dispersive X-ray spectroscopy microanalysis system, transmission electron microscopy and Raman spectroscopy. Silica thin film, which was uniformly deposited onto the graphite plate surface, presented mesopores of around 8 nm perpendicularly disposed to the current collector. Carbon thin film, which almost replicates the nanostructure of the silica thin film, showed mesopores of around 2-3 nm. Electrochemical behaviour of both the mesoporous carbon and the composite silica/carbon thin films was analyzed by cyclic voltammetry and GCD in 1 M $H_2SO_4$ solution, demonstrating that the thin films synthesized show exceptional properties in terms of specific capacitance, rate performance and electrochemical stability to be used as electrodes for micro-capacitors.

The use of ionic liquid and organic-based electrolytes for supercapacitors is being widely studied in recent years, because they allow increasing the operating voltage with respect to the aqueous electrolytes that leads to an increase of the energy density of the device. In the present PhD Thesis, the electrochemical behaviour of a superporous AC with a tailored porosity (high apparent specific surface area and a high volume of micropores with an average pore size of around 1.4 nm) was analyzed in different non-aqueous electrolytes. The AC showed very high capacitance (higher than 160 F $g^{-1}$) values in the $PYR_{14}$ TFSI at different temperatures (20, 40 and 60 ºC) as well as in 1M $Et_4N$ $BF_4$/PC, 1M $PYR_{14}$ $BF_4$/PC and 1M $PYR_{14}$ TFSI/PC. The tailored porosity of the AC made possible to obtain very high capacitance values, making this carbon material a promising candidate to be used as electrode for electrochemical capacitors using non-conventional electrolytes. It was also confirmed that several parameters, such as the ion/pore size ratio, the ion shape, the ion solvation and the conductivity and viscosity of the electrolyte have a strong influence on the electrochemical behaviour of the AC.

# Resumen

El objetivo principal de la presente Tesis Doctoral se centra en la síntesis y caracterización de materiales carbonosos avanzados para aplicaciones en el almacenamiento de energía.

Los carbones activados han sido ampliamente investigados para su uso como electrodos en dispositivos de almacenamiento de energía debido a sus propiedades: bajo coste, versatilidad de la estructura/textura, buena conductividad eléctrica y elevada durabilidad. Una aplicación importante, basada en procesos farádicos, es el almacenamiento electroquímico de hidrógeno por electrodescomposición del agua en condiciones catódicas. En la presente Tesis Doctoral, se ha analizado el comportamiento electroquímico de dos carbones activados, con diferente textura porosa y química superficial, en dos electrolitos (6 M KOH y 0,5 M $Na_2SO_4$). Comparando los resultados obtenidos para ambas muestras, se observó que la química superficial y la textura porosa de los carbones activados utilizados tienen una gran influencia en el proceso de almacenamiento electroquímico de hidrógeno. Las curvas de carga-descarga galvanostática (GCD del inglés *galvanostatic charge-discharge*), mostraron que la capacidad de almacenamiento electroquímico de hidrógeno en ambos medios fue mayor para la muestra con una porosidad más desarrollada. Además, el hidrógeno almacenado electroquímicamente fue mayor en medio básico que en medio neutro. La técnica de espectroscopía Raman *in situ* confirmó que se forman enlaces químicos reversibles entre el hidrógeno y el carbono, bajo condiciones catódicas. Además, se observó que, en ambos electrolitos, la hidrogenación de los átomos de carbono sucede más fácilmente para la muestra con menor cantidad de grupos oxigenados superficiales. Respecto a la influencia del electrolito, en medio básico la formación de enlaces carbono-hidrógeno se produjo a potenciales más

positivos que el potencial termodinámico de formación de hidrógeno molecular.

La síntesis de materiales carbonosos nanomoldeados se ha convertido en una línea de investigación puntera debido a que permite producir materiales carbonosos con estructuras y texturas controladas a escala nanométrica, lo que resulta en el desarrollo de propiedades únicas para su uso en diferentes aplicaciones. El material carbonoso sintetizado utilizado zeolita Y como plantilla (ZTC, del inglés *zeolite-templated carbon*), es un material prometedor para su uso como electrodo en supercondensadores debido a que posee una elevada área superficial aparente y elevado volumen de microporos, un tamaño de poro bien definido, en torno a 1,2 nm, y una estructura porosa tridimensional y ordenada. En la presente Tesis Doctoral, se ha analizado el comportamiento electroquímico del ZTC en medio 1M $H_2SO_4$, prestando especial atención a la química superficial y a los cambios estructurales que se producen bajo las condiciones electroquímicas aplicadas. Se ha utilizado la microbalanza electroquímica de cristal de cuarzo (EQCM, del inglés *electrochemical quartz crystal microbalance*) para analizar el comportamiento electroquímico y gravimétrico del ZTC. Bajo condiciones de oxidación electroquímica, se registró una elevada corriente anódica y un gran aumento neto de masa. La electrooxidación del material carbonoso produjo un incremento de la capacidad específica del ZTC debido a la contribución de la pseudocapacidad, principalmente derivada de la formación del par hidroquinona-quinona. Bajo condiciones electroquímicas más severas, se observó una pérdida neta de masa, lo que sugirió que la gasificación electroquímica del material carbonoso se produce bajo dichas condiciones. Los experimentos de desorción a temperatura programada (TPD, del inglés *temperature programmed desorption*) permitieron analizar la química superficial del ZTC, antes y después de someter a la muestra a las diferentes condiciones electroquímicas estudiadas. Los resultados obtenidos tanto de la caracterización con la EQCM como de los experimentos de TPD sugirieron que los procesos de oxidación y gasificación electroquímica del ZTC se producen simultáneamente. La espectroscopía Raman *in situ* permitió caracterizar, más detalladamente, los cambios estructurales que se producen en el ZTC bajo las condiciones electroquímicas aplicadas. Los resultados mostraron, también, que a elevados valores de potencial se produce la oxidación y degradación simultánea del material carbonoso.

En la actualidad existe una creciente demanda de dispositivos de almacenamiento de energía miniaturizados, debido al incremento de la producción dispositivos electrónicos portátiles. En la presente Tesis Doctoral, se ha llevado a cabo la síntesis de películas delgadas de un material carbonoso mesoporoso, directamente sobre un colector de corriente de grafito, utilizando como plantilla una lámina delgada de sílice mesoporosa. La nanoestructura de las películas sintetizadas ha sido analizada mediante técnicas como: microscopía electrónica de barrido de emisión de campo acoplada a un sistema de microanálisis por espectroscopía de fluorescencia de rayos-X, microscopía electrónica de transmisión y espectroscopía Raman. Se ha visto que la película de sílice, depositada uniformemente sobre la lámina de grafito, presenta mesoporos ordenados de, aproximadamente, 8 nm dispuestos perpendicularmente al colector de corriente. El material carbonoso que cubre la nanoestructura de la plantilla, manteniendo el orden estructural de la película delgada de sílice mesoporosa, presenta mesoporos de un tamaño entre 2 y 3 nm. La caracterización electroquímica tanto de la película delgada del material carbono mesoporoso como del material compuesto sílice/carbón se llevó a cabo mediante experimentos de voltamperometría cíclica y GCD en medio 1 M $H_2SO_4$. El excelente comportamiento electroquímico mostrado por las películas delgadas sintetizadas (en términos de capacidad, retención de capacidad y estabilidad) hace que estos materiales sean candidatos prometedores para su uso como electrodos en micro-condensadores.

Los electrolitos basados en líquidos iónicos o sales disueltas en disolventes orgánicos están siendo ampliamente estudiados para su uso en supercondensadores debido a que permiten aumentar el voltaje de trabajo, respecto a los electrolitos acuosos, lo que resulta en un incremento de la energía que puede almacenar el dispositivo. En la presente Tesis Doctoral, se ha analizado el comportamiento electroquímico de un carbón activado con porosidad diseñada (elevada área superficial aparente, elevado volumen de microporos y un tamaño de microporos de, aproximadamente, 1,4 nm) en diferentes electrolitos no acuosos. El carbón activado presentó valores elevados de capacidad específica (superando, incluso, los 160 F $g^{-1}$), tanto en el $PYR_{14}$ TFSI a tres temperaturas diferentes (20, 40 y 60 ºC) como en los electrolitos 1M $Et_4N$ $BF_4$/PC, 1M $PYR_{14}$ $BF_4$/PC y 1M $PYR_{14}$ TFSI/PC a 20 ºC. La porosidad diseñada del carbón activado hace que sea un excelente candidato para su uso como electrodo en supercondensadores basados en electrolitos no convencionales. Se confirmó, además, que el comportamiento electroquímico mostrado por el carbón activado está influenciado por diferentes parámetros, como: la relación entre el tamaño del ión y el tamaño del poro, la forma de los iones, la solvatación iónica, así como la conductividad y viscosidad del electrolito.